University of Strathclyde

Strathclyde Institute of Pharmacy and Biomedical Sciences

Effects of OGG1 Activation on Mitochondrial Function in Response to Oxidative Stress

by

Steven R. Katchur

A thesis presented in fulfillment of the requirements for the degree of

Doctor of Philosophy

2016

This thesis if the result of the author's original research. It has been composed by the author and has not been previously submitted for examination which has led to the award of a degree.

Signed: 

Date: 19 May 2016

Acknowledgements

I would like to first thank GlaxoSmithKline for granting me this amazing opportunity. Thank-you to The University of Strathclyde for their efforts in helping me to learn and grow as a scientist.

I would like to especially thank my supervisor and mentor Dr. William Rumsey, for his patience, knowledge, and hard work in guiding my education. Thank-you to Dr. Ruth Mayer, Dr. Yolanda Sanchez, and Dr. Harry Kelly for their support throughout the program. A special thank-you to my coworkers at GlaxoSmithKline for their support and for cheering me on as I completed my degree.

Finally I would like to thank my mom, brother, and friends without their love and support none of this would have been possible.

In memory of Dr. Elizabeth Ellis, 2015

Table of Contents

Title I

Declaration of author's rights II

Acknowledgements III

Table of Contents IV

List of Figures IX

List of Tables XIII

Abbreviations XIV

Abstract XVIII

CHAPTER 1 General Introduction: 1

1. Introduction 2

1.1 Chronic obstructive pulmonary disease 2

1.2 ROS 5

1.3 Cigarette Smoke 8

1.4 Paraquat 11

1.5 Mitochondria 14

1.5.1 Mitochondrial Function 14

1.5.2 Mitochondrial DNA 14

1.5.3 Mitochondrial DNA damage 16

1.6 DNA Repair Mechanisms 19

1.6.1 Base Excision Repair Pathway 19

1.6.2 Mismatch repair 22

1.6.3 Nucleotide excision repair 23

1.7 Glycosylases 24

1.7.1 OGG1 24

1.7.1.1 Isoforms 27

1.7.2 NEIL1, NEIL2, and NEIL3 28

1.8 Mitochondrial Dynamics 29
1.9 Aims 34

CHAPTER 2: Materials and Methods 36

2. Materials and Methods 37
2.1 Cell Culture 37
2.2 Cell Treatment 37
2.2.1 Cigarette smoke exposure 37
2.2.2 Paraquat exposure 38
2.2.3 Baculovirus transduction 38
2.2.4 OGG1 siRNA Transfection 39
2.2.5 OGG1 activators 40
2.3 Image acquisition 41
2.4 Detection of reactive oxygen species (ROS) 43
2.5 Detection of mitochondrial ROS 43
2.6 Immunofluorescence assays 45
2.6.1 Oxidative DNA damage marker 8-oxoguanine 45
2.6.2 8-oxoguanine glycosylase 1 (OGG1) 49
2.6.3 Manganese superoxide dismutase (MnSOD) 50
2.6.4 Cytochrome c 50
2.6.5 phosphorylated-Histone 2-AX (pSer140) 51
2.6.6 Translocase outer membrane (TOM20) 52
2.6.7 Dynamin related protein-1 (DRP1) 52
2.6.8 Mitofusin-1 (MFN1) 53
2.6.9 DNA Ligase III 54
2.7 Mitochondrial membrane integrity 54
2.8 Mitochondrial membrane potential 57
2.9 ATP and ADP quantification 57
2.10 Glutathione determination 58

2.11 Western analysis 58
2.12 Statistical Analysis 60

CHAPTER 3: Development of a cell model of oxidant-induced mitochondrial DNA damage 61

3. Development of a cell model of oxidant-induced mitochondrial DNA damage 62
3.1 Introduction 62
3.2 Results 64
3.2.1 Cigarette smoke exposure increases ROS and oxidative DNA damage 64
3.2.2 Effect of paraquat on total and mitochondrial ROS 68
3.2.3 Time and concentration-dependent effect of paraquat on mitochondrial oxidative DNA damage 70
3.2.4 Effects of paraquat on inducing dsDNA breaks 75
3.2.5 Effects of paraquat on mitochondrial membrane potential and membrane integrity 77
3.2.6 Effects of paraquat on cytochrome c translocation 82
3.2.7 Effects of paraquat on DNA repair and the anti-oxidant response 82
3.2.8 Effects of mtDNA deletion on paraquat-induced oxidative DNA damage 90
3.3 Discussion 94

CHAPTER 4: Characterization of Modulating OGG1 Enzyme Activity 97

4. Characterization of modulating OGG1 enzyme activity 98
4.1 Introduction 98
4.2 Results 100
4.2.1 Effect of OGG1 BacMam on paraquat-induced mitochondrial DNA 8-oxoguanine 100
4.2.2 Effect of OGG1 siRNA on paraquat-induced 8-oxoguanine 104
4.2.3 Effect of small molecule OGG1 activators on paraquat-induced mitochondrial DNA 8-oxoguanine 105

4.2.4 Effect of small molecule OGG1 activators on paraquat-induced mitochondrial membrane depolarization 118

4.2.5 Effect of OGG1 activators on paraquat-induced changes on down-stream base excision repair proteins 118

4.2.6 Effect of OGG1 activators on paraquat-induced changes in mitochondrial OGG1 protein content 123

4.3 Discussion 126

CHAPTER 5: Examination of the Role of Mitochondrial DNA Damage on Cellular Energy Production and on Mitochondrial Dynamics 129

5. Examination of the role of mitochondrial DNA damage on cellular energy production and on mitochondrial dynamics 130

5.1 Introduction 130

5.2 Results 132

5.2.1 Effect of cigarette smoke on cellular energetic state. 132

5.2.2 Effect of paraquat on cellular energetic state over time. 132

5.2.3 Effect of OGG1 activators on paraquat-induced loss of ATP. 135

5.2.4 Effect of paraquat and OGG1 activators on mitochondrial mass. 143

5.2.5 Effect of paraquat and the OGG1 activators on mitochondrial fission. 147

5.2.6 Effect of paraquat and the OGG1 activators on mitochondrial fusion. 152

5.3 Discussion 158

CHAPTER 6: General Discussion 161

6.1 General Discussion 162

6.2 Activation of Base excision repair 164

6.3 Effects of OGG1 activation on mitochondrial function 166

6.4 Potential therapeutic options for OGG1 activators 168

6.5 Summary 170

CHAPTER 7: References 171

7. References 172

APPENDIX: Supplemental Data 186

APPENDIX: SUPPLEMENTAL DATA 187

List of Figures

CHAPTER 1

Figure 1.1 Schematic of alveoli from a healthy patient and the underlying structural cells of the lung. 3
Figure 1.2 Schematic of ROS production and enzymatic remediation. 6
Figure 1.3 Diagram of cigarette smoke-induced mitochondria damage/dysfunction on aging and disease. 10
Figure 1.4 A depiction of paraquat and its effects on the electron transport chain. .. 12
Figure 1.5 Structures of oxidized nucleotides repaired through base excision repair. 20
Figure 1.6 Base excision repair pathway depicting the short-patch repair. 22
Figure 1.7 Schematic of mitochondrial fission and fusion. 30

CHAPTER 1

Figure 2.1 Cigarette smoke exposure chamber. 38
Figure 2.2 Sequence and predicted secondary structure of the 8-OxoG-containing OGG1 DNA substrate. 41
Figure 2.3 Representative image of segmentation from ROS stained A549 cells 44
Figure 2.4 Single cell analysis for 8-oxoguaine in a high responder population. 47
Figure 2.5 Identification of changes in mitochondrial membrane integrity. 56

CHAPTER 3

Figure 3.1 Effects of cigarette smoke exposure on ROS production over time in A549 cells. 65
Figure 3.2 Effects of cigarette smoke exposure on oxidative DNA damage. 67
Figure 3.3 Effects of paraquat exposure on ROS production in A549 cells. 69
Figure 3.4 Effects of paraquat exposure on mitochondrial-specific ROS production in A549 cells. 71
Figure 3.5 Effects of 24 and 48 hr paraquat exposure on mitochondrial oxidative DNA damage content in A549 cells. 73

Figure 3.6 Effects of 48 hr paraquat exposure on induction of dsDNA breaks in A549 cells. 76
Figure 3.7 Effects of 24 and 48 hr paraquat exposure on mitochondrial membrane potential in A549 cells. 78
Figure 3.8 Effects of 24 hr paraquat exposure on mitochondria membrane integrity on A549 cells. 80
Figure 3.9 Effects of paraquat exposure on intrinsic apoptosis initiation: cytochrome c translocation. 83
Figure 3.10 Effects of 24 and 48 hr paraquat exposure on mitochondrial OGG1 content in A549 cells. 86
Figure 3.11 Effects of 24 hr paraquat exposure on MnSOD content in the mitochondria. 88
Figure 3.12 Effects of 24 and 48 hr paraquat exposure on total glutathione in A549 cells. 91
Figure 3.13 Effects of deleting mitochondrial DNA on paraquat-induced 8-oxoguanine. 93

CHAPTER 4

Figure 4.1 Effects of OGG1-BacMam following 24 hr paraquat-induced changes on cell number and 8-oxoguanine in A549 cells. 101
Figure 4.2 Effects of MnSOD-OGG1-GFP BacMam following paraquat exposure on 8-oxoguanine content in A549 cells. 102
Figure 4.3 Effects of OGG1 siRNA on 8-oxoguanine content following paraquat exposure in A549 cells. 106
Figure 4.4 Effects of OGG1 small molecule activators on paraquat-induced 8-oxoguanine in A549 cells. 109
Figure 4.5 Sample images of paraquat-exposed A549 cells following 4 hr pre-treatment with OGG1 activators. 112
Figure 4.6 Effects of small molecule OGG1 activators on nuclear area in A549 cells. 114
Figure 4.7 Effects of small molecule OGG1 activators on percent of A549 cell population classified as high responders. 116
Figure 4.8 Effects of OGG1 activators on mitochondrial membrane potential in A549 cells. 119

Figure 4.8 Effects of OGG1 activators on mitochondrial membrane potential in A549 cells. 120
Figure 4.9 Effects of OGG1 tool activators on DNA Ligase III in A549 cells. 121
Figure 4.10 Effects of OGG1 activators on OGG1 in A549 cells. 124

CHAPTER 5

Figure 5.1 Effects of cigarette smoke-induced changes in ATP/ADP ratio over time. 134
Figure 5.2 Effects of paraquat-induced changes in ATP/ADP ratio over time. 136
Figure 5.3 Effects of OGG1 activators on paraquat-induced changes in ATP/ADP ratio. 141
Figure 5.3 Effects of OGG1 activators on paraquat-induced changes in ATP/ADP ratio. 142
Figure 5.4 Effects of paraquat and OGG1 activators on mitochondrial mass in A549 cells. 144
Figure 5.4 Effects of paraquat and OGG1 activators on mitochondrial mass in A549 cells. 146
Figure 5.5 Effects of paraquat on mitochondrial fission in A549 cells over time. 148
Figure 5.6 Effects of OGG1 activators on paraquat-induced changes on mitochondrial fission in A549 cells. 149
Figure 5.7 Effects of paraquat on mitochondrial fusion in A549 cells over time. 153
Figure 5.8 Effects of OGG1 activators on paraquat-induced changes on mitochondrial fusion in A549 cells. 155

Appendix

Figure S1 Effects of OGG1 siRNA on OGG1 gene expression. 187
Figure S2 Validation of OGG1 antibody detection of appropriate protein band. 188
Figure S3 Examination of co-localization of paraquat-induced 8-oxogaunine to the mitochondria. 189
Figure S4 Effects of paraquat on mitochondrial DNA damage in A549 cells. 190
Figure S5 Effects of OGG1 activators on OGG1 incision activity. 191
Figure S6 Effects of paraquat on markers of inflammation – NF-κB translocation.. 192
Figure S7 Effects of OGG1 small molecule activators on paraquat-induced 8-oxoguanine in A549 cells. 194

Figure S8 Effects of time of addition of OGG1 small molecule activators on paraquat-induced 8-oxoguanine in A549 cells. 196

List of Tables

CHAPTER 1

Table 1.1 Evaluation of sputum cell mRNA from ECLIPSE study comparing Stage II vs. Stage III disease severity. 9
Table 1.2 Summary of alternative spliced isoforms of OGG1. 28

CHAPTER 2

Table 2.1 Excitation and Emission spectra for fluorescent stains and antibodies. 42

CHAPTER 4

Table 4.1 Tool OGG1 small molecule activators. 108
Table 4.2 Summary of activity for OGG1 activators. 128

CHAPTER 5

Table 5.1 Summary of ATP and ADP concentrations 24 and 48 hr post air or cigarette smoke exposure. 133
Table 5.2 Summary of ATP and ADP concentrations 24 and 48 hr post paraquat exposure. 137
Table 5.3 Summary of ATP and ADP concentrations following pre-treatment with an OGG1 activator in the presence of varying concentrations of paraquat for 48 hr. 139

Abbreviations

A	adenine
ADP	adenosine diphosphate
ALS	amyotrophic lateral sclerosis
AP	apyrinic/ apyrimidinic
APE	AP endonuclease
ASK1	apoptosis signal-regulating kinase-1
ATP	adenosine triphosphate
BER	base excision repair
BSA	bovine serum albumin
C	cytosine
CHOP	C/EBP homologous protein
COPD	chronic obstructive pulmonary disease
CSA/CSB	Cockayne syndrome complementation group A/B
DAMPs	damage associated molecular patterns
DCF	chloromethyl derivative of 2'7'-dichlorodihydrofluorescein diacetate
DMSO	dimethyl sulfoxide
DRP1	dynamin related protein 1
DSB	double strand break
EC_{50}	half-maximal effective concentration
ER	endoplasmic reticulum
ERK1	extra-cellular signal-regulated kinase
ETC	electron transport chain

FADH	flavin adenine dinucleotide
FBS	fetal bovine serum
G	guanine
GFP	green fluorescent protein
GG-NER	global genome-nucleotide excision repair
GSH	reduced glutathione
GSSG	oxidized glutathione
HBSS	Hank's balanced salt solution
HhH	helix-hairpin-helix
HO-1	heme oxygenase-1
IC_{50}	half-maximal inhibition concentration
IL	interleukin
JNK	c-Jun N-terminal kinase
MAPK	mitogen activated protein kinase
MFN1	mitofusion1
MFN2	mitofusion2
MMR	mismatch repair
MnSOD	manganese superoxide dismutase
mtDNA	mitochondrial DNA
NADH	nicotinamide adenine dinucleotide
NEIL	endonuclease eight-like
NER	nucleotide excision repair
NF-KB	nuclear factor kappa-light-chain-enhancer of activated B cells

NRF2	nuclear factor (erythroid-derived 2)-like 2
NQO-1	NAP(P)H quinine dehydrogenase-1
OGG1	8-oxoguanine glycosylase 1
OPA1	optic atrophy 1
PBMC	peripheral blood mononuclear cells
PBS	phosphate buffered saline
PCR	polymerase chain reaction
pH2AX	phosphorylated-histone 2-AX (pSer140)
PINK1	PTEN-induced kinase 1
PKA	protein kinase A
PVDF	polyvinyl difluoride
ROS	reactive oxygen species
rRNA	ribosomal ribonucleic acid
RT-PCR	reverse transcription polymerase chain reaction
siRNA	small interfering ribonucleic acid
SNP	small nucleotide polymorphism
T	thymidine
TBS	tris buffered saline
TC-NER	transcription coupled-nucleotide excision repair
TFAM	transcription factor A mitochondrial
TNF-α	tumor necrosis factor-α
TOM20	translocase outer membrane 20kDa subunit
tRNA	transfer ribonucleic acid

WT	wild type
XRCC1	X-ray repair cross-complementing protein 1

Abstract

Chronic obstructive pulmonary disease (COPD) is characterized by progressive airflow limitation, loss of the alveolar unit, and increased levels of oxidative damage to macromolecules, including DNA. 8-oxoguanine (8-OG) is the most common oxidative DNA lesion and its removal and repair is executed through the base excision repair pathway. The purpose of these studies was to determine whether enhancing the activity of the DNA glycosylase, OGG1, would benefit epithelial cell health by maintaining mitochondrial function following an oxidative challenge. Cigarette smoke exposure, a risk factor for COPD, enhanced oxidative DNA damage content. However, paraquat was chosen as a more specific stimulus as it intercalates within the inner mitochondrial membrane to produce excessive amounts of mitochondrial reactive oxygen species. Levels of 8-OG were measured in A549 cells using immunofluorescence and single cell phenotypic analysis was undertaken by a high content imaging platform. Transduction of A549 cells with full length-OGG1 baculovirus lowered the maximal levels of 8-OG in mtDNA compared to null virus control cells. Conversely, administration of *OGG1* siRNA rendered the cells more vulnerable to paraquat, increasing 8-OG content. Exemplars of small molecule OGG1 activators identified through a high-throughput-screen were shown to reduce paraquat-induced 8-OG formation. Moreover, OGG1 activators improved paraquat-induced loss of mitochondrial membrane potential, while paraquat-induced cytochrome *c* translocation to the nucleus was blocked. The paraquat-stimulated decline in the cellular energy state, i.e., the ATP/ADP ratio, was prevented in the presence of the OGG1 activators. Paraquat-induced changes in mitochondrial dynamics were blocked with the OGG1 activators, but did not affect mitochondrial mass. These data provide evidence of cytoprotection from oxidant-induced mtDNA damage when OGG1 protein is increased or activated, suggesting that the base excision repair pathway may be a target for potential small molecule intervention in COPD.

CHAPTER 1:

General Introduction

1. Introduction

1.1 Chronic obstructive pulmonary disease

Chronic obstructive pulmonary disease or COPD encompasses emphysema, chronic bronchitis, and small airway disease. This illness is characterized as a shortness of breath, chronic cough and a decline in a patient's quality of life. These symptoms are derived from chronic inflammation within the lung tissue that is associated with tissue destruction and a loss of surface area required for oxygen transfer to the circulation (Fig. 1.1) (Kirkham and Barnes, 2013). COPD is currently the third leading cause of death in the United States and according to the World Health Organization, will be the third leading cause of death in the world by 2020. Unfortunately, it is one of the only major causes of death still steadily increasing (Rycroft et al., 2012; Tuder and Petrache, 2012). Other chronic diseases such as diabetes, heart failure, and cancer are co-morbidities and greatly enhance the risk of mortality in COPD patients (Kim and Criner, 2013; Tuder and Petrache, 2012).

One shortcoming to the current management of this disease is the lack of complete understanding of the heterogeneity and etiology of COPD (Barker and Brightling, 2013). Although smoking cigarettes greatly increases the likelihood for developing COPD, only 15% of smokers will develop this disease. It is not perfectly understood what it is that protects the remaining 85% of smokers who do not develop this disease (Taylor et al., 2010). There are other contributing factors to COPD; however, many of them are poorly characterized, but these could factors include occupational exposure to dust or gases, age, genetics, environmental factors, and asthmatics who smoke (Berndt et al., 2012; Gould et al., 2010).

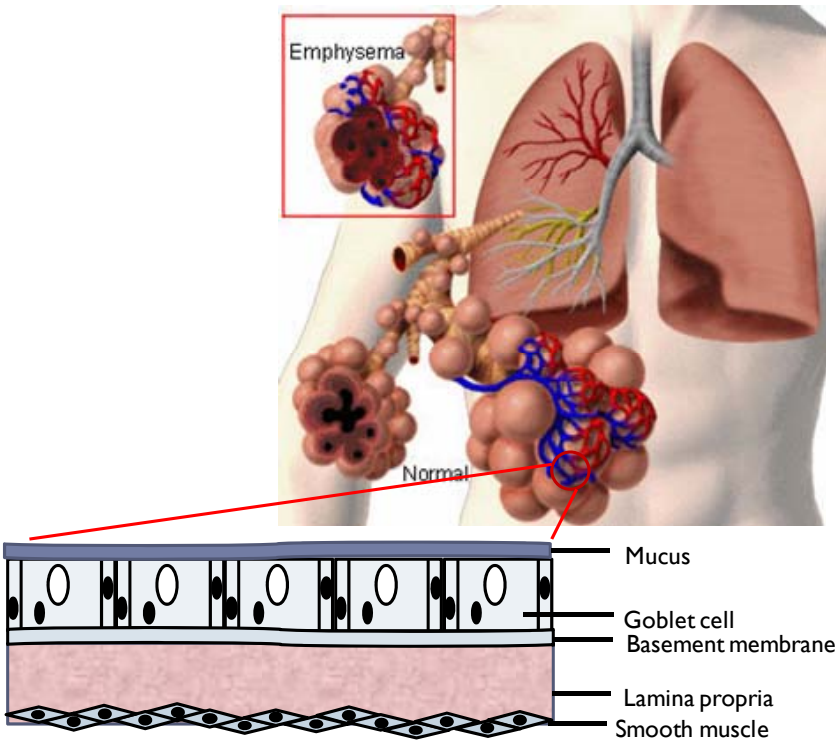

Figure 1.1 Schematic of alveoli from a healthy patient and the underlying structural cells of the lung.

(adapted from "Medical Look", "www.slideteam.net" 2015)

The image illustrates the lung, which terminates at the alveolar unit, where gas exchange occurs. The structure of the lung is such as to protect the cells from damage. At the surface of the cellular layer is mucus or surfactant; this provides the initial line of defense and aids in the maintenance of surface tension. Next is the epithelial cell layer, which lines the lung and protects the airways from pathogens, while enabling diffusion of oxygen into the body and excretion of carbon dioxide. Mucus-secreting goblet cells are present in this layer as well. Below this is the basement membrane, a layer of connective tissue that attaches the epithelial cell layer to the underlying supporting cells of the lamina propria. The lamina propria is the next cellular layer and provides the lung with structure and contains myriad cells including immune cells and macrophages. These cells remove foreign pathogens and cellular debris from the lung, and supply the epithelial cell layer with nutrients. This is where the capillaries necessary for gas exchange reside as well. Finally, the smooth muscle layer forms the contractile tissue that enables the lung to expand for inhaling and to contract for exhaling. In COPD patients, normal cellular function within the alveolar unit is impaired, which results in a loss of the alveolar unit.

Cigarette smoke contains thousands of compounds within the vapor phase of the smoke including lipopolysaccharide, cadmium, arsenic, cyanide, oxygen free radicals, and other organic compounds (Birben et al., 2012). The schematic in Fig 1.1 highlights the gross cellular structure of the lung and the importance of the epithelial cells as a barrier for toxins and other irritants present in cigarette smoke. It is well known that exposure to reactive oxygen species (ROS) can damage the macromolecules within lung cells, including the oxidation of lipid membranes, proteins, and damage to nucleic acids (Barker and Brightling, 2013). In addition to the load of ROS in cigarette smoke, there are endogenous sources of ROS, for example from normal cellular respiration, inflammatory cells (e.g. oxidative burst), and other oxygen consuming reactions. To offset these adverse responses the cell has several defense mechanisms such as enzymatic (catalase, superoxide dismutase and thioredoxin reductase) and non-enzymatic methods (vitamin C, vitamin E, and glutathione) that scavenge detrimental oxygen species (Birben et al., 2012). Oxidative stress, i.e. an imbalance in the level of oxidant relative to antioxidant defense, is now considered a major component of the etiology of COPD (MacNee, 2005).

While inflammation is considered a major contributor to COPD pathology, however, the inflammation observed in COPD is unlike asthma as it remains largely unresponsive to anti-inflammatory therapy. Despite smoking cessation, this abnormal and exaggerated inflammatory response continues. One benefit of inhaled corticosteroid treatment, is that acute COPD exacerbations are reduced by up to 20-25% in patients with the most severe form of this disease (Barnes, 2010; Gross, 2012). COPD exacerbations are primarily driven by bacterial and viral infections and they remain a major unmet need in the management of the disease (Hurst et al., 2010; Sethi et al., 2012). Cigarette smoke may impair the immune system within the lung, thereby promoting a microenvironment conducive to rapid bacterial colonization (Ishida et al., 2009). Inflammation in conjunction with an unaltered ROS burden is associated with a decline in antibacterial clearance by alveolar macrophages (Thimmulappa et al., 2012; Tuder and Petrache, 2012; Vlahos and Bozinovski, 2014).

There is increased evidence of DNA instability in lungs of COPD patients, and telomere shortening has been demonstrated within the lungs of patients with emphysema, leading to the suggestion that the COPD phenotype strongly resembles premature aging (Agustí and Barnes, 2012). Agusti and Barnes noted that shortened telomeres can contribute to the chronic inflammatory state in COPD by increasing the release of pro-inflammatory cytokines such as interleukin 8 (IL-8) and tumor necrosis factor-α (TNF-α). A recent study has shown that COPD patients experience a higher incidence of oxidative DNA damage within their circulating peripheral blood mononuclear cells (PBMCs) compared to healthy controls (Lúcia G da Silva et al., 2013). Moreover, the level DNA oxidation damage within the airway epithelium has been shown to correlate with disease severity (Deslee et al., 2010).

1.2 ROS

Reactive oxygen species or oxygen radicals comprise superoxide anion (O_2^-), hydroxyl radicals (OH^-), hydrogen peroxide (H_2O_2), peroxynitrite ($ONOO^-$), and ozone (O_3) (Xiang et al., 2010). Two predominant forms of free radicals are produced within mammalian cells, superoxide and nitric oxide (Powers and Jackson, 2008). Inside the mitochondria, and in a tightly-controlled process, electrons are transferred down the electron transport chain with molecular oxygen as the final acceptor. However, about 1-2% of these electrons leak out of the reaction and interact with molecular oxygen to form superoxide anions (Mittal et al., 2014; Persson and Vainikka, 2010). Superoxide is created either through the incomplete reduction of oxygen in the mitochondria or generated as a byproduct from enzymatic reactions (Powers and Jackson, 2008). Superoxide is produced by NADPH oxidases (NOX) to serve both in signaling pathways and as effector molecules (Nauseef, 2014). Nitric oxide is formed through specific enzymes within the body, and under controlled conditions has a number of biological functions (Powers and Jackson, 2008). The remaining aforementioned radicals can be generated either enzymatically through oxidoreductases or by non-enzymatic mechanisms involving the transfer of electrons produced under normal cellular metabolism (Forman and Torres, 2001; Xiang et al., 2010). A schematic shown in Fig. 1.2 depicts some of the pathways that produce ROS and specific enzymes involved in their conversion to non-harmful moieties (Kyaw et al., 2004). The schematic illustrates the steps involved in converting

superoxide by superoxide dismutase to hydrogen peroxide, followed by conversion by catalase to water and oxygen.

Superoxide radicals are especially damaging because they have the longest half-life compared to other ROS species, enabling diffusion of the free radical within the cell (Powers and Jackson, 2008). However, their negative charge prevents them from passively diffusing through the lipid bi-layer of the plasma membrane or through the outer mitochondrial membrane. In contrast, hydroxyl radicals are so reactive they typically damage molecules in close proximity to their formation and can only be

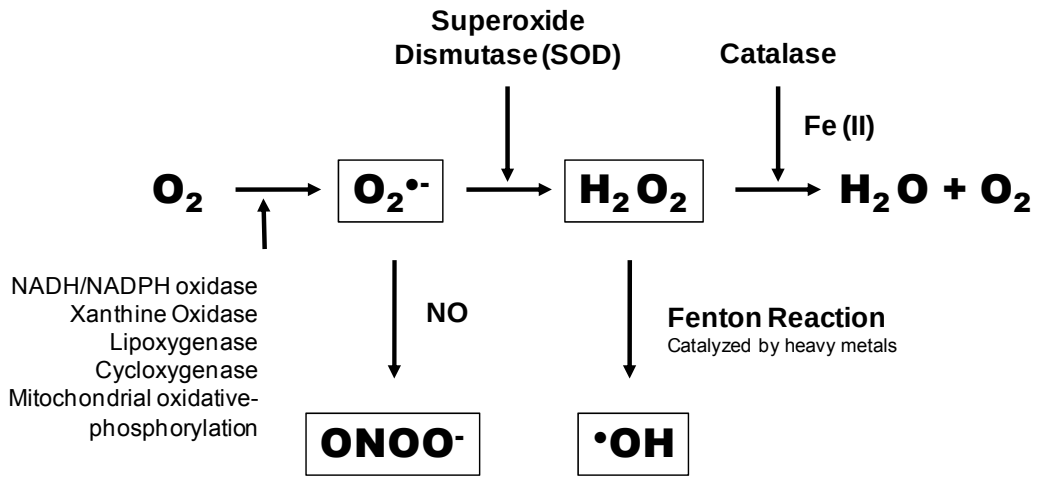

Figure 1.2 Schematic of ROS production and enzymatic remediation.

NO, nitric oxide; SOD; superoxide dismutase; O_2, molecular oxygen; H_2O_2, hydrogen peroxide; OH, hydroxyl radical; O_2^-, superoxide anion; ONOO, peroxynitrite; H_2O, water (Adapted from Kyaw et al., 2004)

confirmed to be present by the damage they inflict. The negative charge associated with hydroxyl radicals makes them unable to traverse cell membranes. Similarly to superoxide radicals, hydrogen peroxide is a stable, relatively long-lived molecule. A major difference is its ability to passively move through various cell membranes. Singlet oxygen, while it does not have a charge, has a large potential for damage due

to not having any electron spin restrictions, which greatly enhances its oxidizing ability (Powers and Jackson, 2008).

ROS can be produced within cells by several different routes, but the largest amounts are derived from molecular oxygen at the site of cellular metabolism in the mitochondria (Birben et al., 2012). Additionally, endogenous enzymes use ROS as a primary signaling molecule. For example, enzymes such as NADPH oxidases (NOX) produce ROS to mediate various biological functions such as bacterial clearance, angiogenesis, and cell migration (Lee et al., 2010). Once referred to as the "respiratory burst", neutrophils and macrophages produce reactive oxygen species (ROS) to eliminate invading bacteria (Forman and Torres, 2002). The defending macrophage both releases the ROS and responds to them by clearing the invading bacteria from the tissue (Bauer et al., 2011). The prevailing theory was initially that only neutrophils and macrophages produced ROS. However it has been shown that ROS are used in a variety of signaling pathways in all cells, ranging in effects from proliferation to apoptosis (Finkel, 2011; Forman and Torres, 2001). Sometimes referred to as redox signaling, is the process by which cells under low levels of ROS or non-lethal amounts signal in growth factor and other receptor-mediated cell signaling processes (Forman and Torres, 2001). Finally, exogenous sources such as cigarette smoke, ozone, air pollution, and pesticides bring various toxic oxidants into cells, and once brought into the cell, they can go on to cause uncontrolled ROS formation (Birben et al., 2012; Lascano et al., 2012).

Endogenous or exogenously generated ROS are capable of exerting damage on macromolecules such as proteins, lipids, and DNA when the anti-oxidant capacity is inadequate. This excessive ROS burden goes on unchecked and induces macromolecule damage, which is referred to as oxidative stress (Morreall et al., 2014). Enzymes such as superoxide dismutase (SOD), glutathione peroxidase, and catalase are used by the cell to degrade and dispose of the free radicals. These enzymes work in concert to convert the ROS into the non-harmful moieties, water and molecular oxygen (Powers and Jackson, 2008). Recent data have demonstrated the ability of ROS and oxidative stress to trigger the inflammasome response and the release of pro-inflammatory cytokines (Rovina et al., 2013). These

observations are consistent with data suggesting ROS can induce and perpetuate lung injury (Xiang et al., 2010).

1.3 Cigarette Smoke

With each puff from a cigarette, about 5000 toxic compounds are brought into the lungs including various free radicals such as hydrogen peroxide and hydroxyl radicals (Yang et al., 2014). As mentioned above, cigarette smoking is the primary cause of COPD in developed countries (Kelsen, 2012). This toxic irritant shifts the delicate balance between oxidants and anti-oxidants toward an oxidative microenvironment both within the lungs and systemically as well. Effectively, there are ROS species within the particulate phase and hundreds of different chemicals found within the vapor phase that can enter the cell to induce ROS generation with each puff of a cigarette (Fischer et al., 2015). For example, cyanide is a component of cigarette smoke, which binds to cytochrome oxidase and blocks electron transport thereby limiting ROS removal through the inhibition of catalase, an enzyme involved in the removal of hydrogen peroxide (Cooper and Brown, 2008; Vinnakota et al., 2012). Other chemicals such as arsenic, which interferes with the electron transfer within mitochondria, have also been shown to be present in cigarette smoke (Flora, 2011). Data generated from sputum samples by the ECLIPSE (Evaluation of COPD Longitudinally to Identify Predictive Surrogate Markers) study indicated that there was a significant down-regulation of many of the genes encoding the complexes in the electron transport chain in COPD patients (Table 1.1) (Rumsey et al., 2013). These data suggest there is an association with COPD disease severity progression with the down-regulation of the genes encoding the many of the sub-units for the complexes of the electron transport chain.

The airway epithelium responds to cigarette smoke by activating multiple damage response pathways (Pickett et al., 2010; Steiling et al., 2013). Alveolar macrophages have a decreased antigen presentation response and clearance of apoptotic cells and bacteria, due in part to ROS-mediated DNA oxidation damage (Grabiec and Hussell, 2016; Hodge et al., 2007). Altogether, these data suggest a possible

Stage II vs. Stage III	Up 1.2-fold p<0.0001	Down 1.2-fold p<0.0001	Total genes
Complex I subunits	0	29	37
Complex II subunits	0	1	4
Complex III subunits	1	5	6
Complex IV subunits	0	10	21
Complex V subunits	0	12	19

Table 1.1 Evaluation of sputum cell mRNA from ECLIPSE study comparing Stage II vs. Stage III disease severity.

Table depicting the number of nuclear and mitochondrial encoded genes involved in the electron transport chain complexes that are impacted in patients as they transition in disease severity from Stage II to Stage III of COPD (adapted from Rumsey et al., 2013).

association between cigarette smoke induced DNA oxidation damage and increased susceptibility to acute lung infections (Ishida et al., 2009). *In vitro* studies have shown that epithelial cells experienced increased nuclear swelling and cell death within 24 hr of exposure to cigarette smoke extract (Kovacs et al., 2012). Increased apoptosis is associated with cigarette smoke exposure and COPD disease progression as a result of increased alveolar cell death leading to a loss of the alveolar unit (Mizumura et al., 2014).

With each cigarette, ROS are inhaled into the lung, where they frequently will target the DNA and induce oxidative damage to the base pairs (Neofytou et al., 2012). Smokers with low levels of DNA base repair enzyme OGG1 have been shown to have a higher risk for the development of lung cancer compared to smokers with elevated levels of the enzyme (El-Zein et al., 2010). These authors examined patients with elevated levels of 8-oxoguanine, enabling them to identify a sub-

population of patients who might benefit from a therapeutic intervention aimed at reducing DNA damage (El-Zein et al., 2010). Yamamoto and colleagues demonstrated a four-fold increase in double strand DNA breaks compared to air controls in *ogg1-/-* lymphocytes exposed to cigarette smoke extract compared to air controls (Yamamoto et al., 2013). Additional studies have demonstrated increased levels of oxidative stress markers in various macromolecules including DNA damage that was found in both blood and lung derived samples from smokers (Ben Anes et al., 2014; Pierrou et al., 2007; Wiegman et al., 2015; Yang et al., 2014).

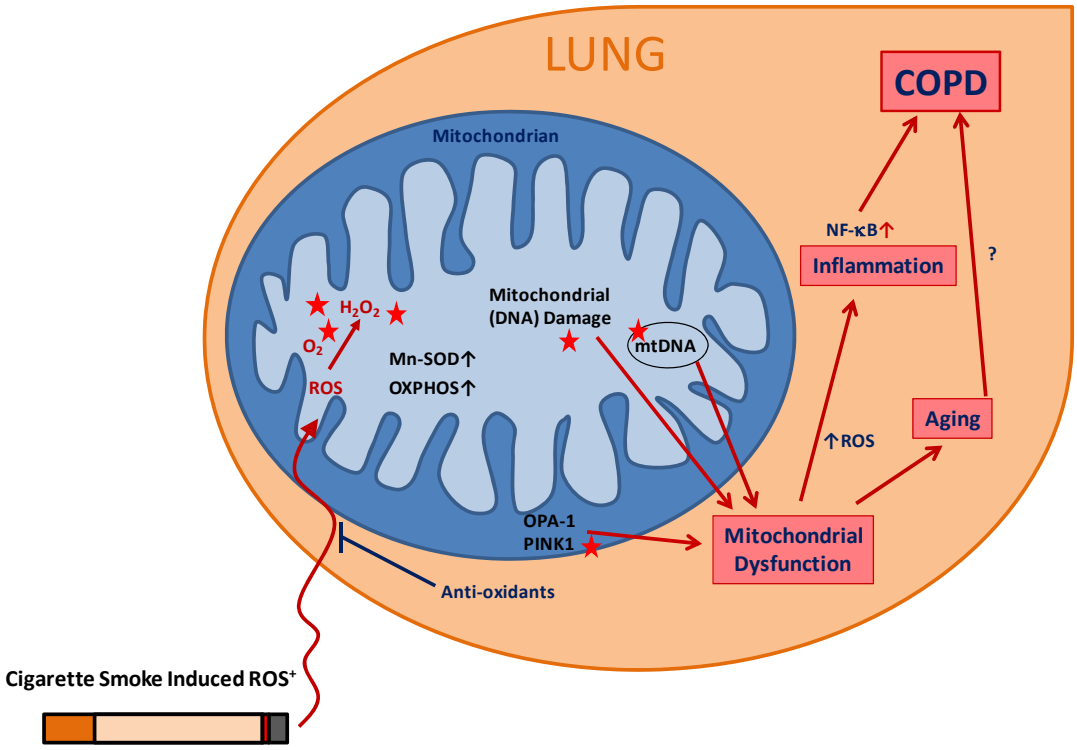

Figure 1.3 Diagram of cigarette smoke-induced mitochondria damage/dysfunction on aging and disease.

MnSOD, manganese superoxide dismutase; NF-κB, nuclear factor kappa-light-chain-enhancer of activated B cells; OPA-1, optic atrophy protein 1; OXPHOS, oxidative phosphorylation; PINK1, PTEN-induced putative kinase-1; ROS, reactive oxygen species (adapted from Brooks et al., 2013)

Based on observations by Gould et al. the expression of key anti-oxidant proteins is reduced in cigarette smoke exposed old mice, compared to similarly exposed younger mice (Gould et al., 2010). These pre-clinical observations are consistent with the patterns observed in diseases associated with aging like COPD, where there is an imbalance between oxidants and anti-oxidants within the lung (MacNee, 2005). Moreover, air pollution can produce a similar effect, with airway epithelial cells exhibiting increased levels of 8-oxoguanine and a decline in mitochondrial membrane potential, leading to a rise in mitochondrial dysfunction (Yang et al., 2015). These data suggest that cigarette smoke is not the only inhaled irritant capable of inducing oxidative DNA damage. As illustrated in Fig. 1.3, cigarette smoke impacts the mitochondria through increased ROS generation through potential alterations in the electron transport chain by some of the many chemicals found in cigarette smoke. This increase in ROS can go on and induce mitochondrial DNA oxidation leading to dysfunction and changes in how the mitochondria could signal for its destruction through PINK1 expression. The figure finally highlights how the changes in mitochondrial function could impact inflammation and the aging process and be just one aspect that could influence COPD disease progression.

1.4 Paraquat

Paraquat (1,1-dimethyl-4,4-biprridiunium dichloride) is a non-selective herbicide introduced commercially in 1962 (Lascano et al., 2012; Mainwaring et al., 2006). It is a quaternary amine with a positive charge, which would prohibit transport across lipid-containing animal and plant cell membranes. To cross the cell membrane, paraquat is transported by the same active transport system used by polyamines, which share a similar structure. In plants, paraquat binds to the cell wall and is reduced within chloroplasts by acting as an electron acceptor (Lascano et al., 2012). It has been shown that paraquat-induced toxicity in humans or animals is due to a similar process. In mammalian cells, paraquat is taken-up across the inner-mitochondrial membrane based on a carrier-mediated and mitochondrial membrane potential dependent process (Cochemé and Murphy, 2008). Once inside the mitochondria, the herbicide is reduced at complex I of the electron transport chain to generate ROS (Fig. 1.4). In the presence of oxygen, this free radical forms the superoxide anion and results in the regeneration of paraquat (Fig. 1.4) (Dinis-Oliveira et al., 2006).

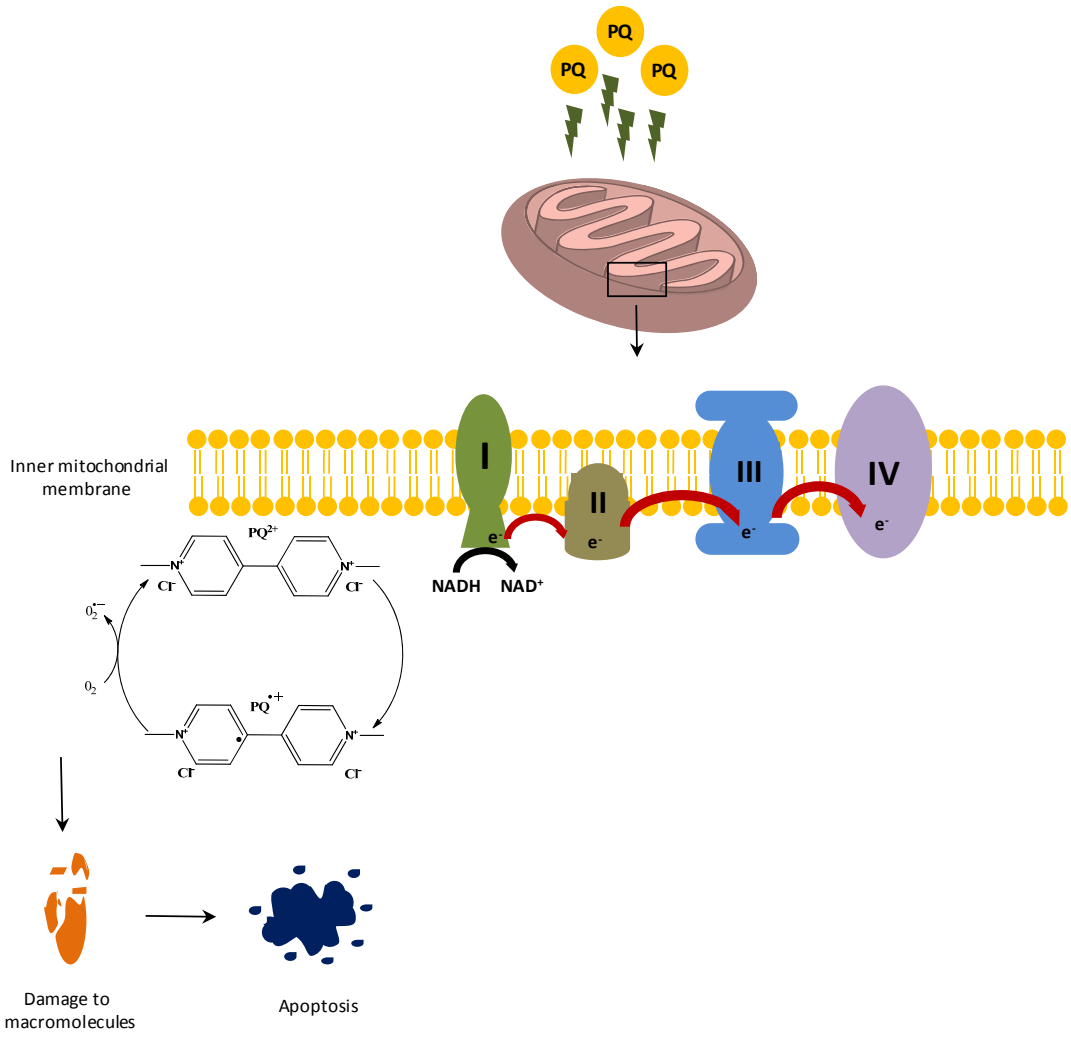

Figure 1.4 A depiction of paraquat and its effects on the electron transport chain.

(adapteded from Flora 2011)

The figure generally depicts paraquat inducing ROS production, thereby enabling electron leakage out of the electron transport chain. Specifically, paraquat is reduced as electrons are shuttled between complex I and III and generates a superoxide anion as paraquat is oxidized in the presence of oxygen. These ROS species if left unchecked by the cell can induce damage to macromolecules, eventually leading to apoptosis.

Since its discovery, paraquat has caused thousands of deaths both from accidental and voluntary exposure (Zhi et al., 2011). There is no antidote and the high mortality rate is primarily due to the inability to halt the rapid development and progression of pulmonary fibrosis (Zhi et al., 2011). Although, paraquat will affect the kidneys, thymus, and liver, it also concentrates within alveolar type II epithelial cells of the lung (Mainwaring et al., 2006). These structural cells are rich in mitochondria and are particularly important for surfactant production, which controls surface tension in the alveolar space (Miller et al., 1995).

One of the early hallmark signs of *in vivo* paraquat exposure or toxicity is mitochondrial swelling (Cochemé and Murphy, 2008). Paraquat lowers Complex I activity of the electron transport chain, which regulates Ca^{2+} flux through the mitochondrial membrane transition pore, which in turn causes the mitochondrial membrane potential to decrease and could lead to cell death (Dinis-Oliveira et al., 2006). Elevated ROS levels have been shown to be the first step in paraquat-induced complex I mediated cell death. This elevation in ROS induces oxidative DNA damage within the mitochondrial DNA, eventually leading to damage within the nuclear genome (Marella et al., 2007). Analysis of the molecular pathways leading to paraquat toxicity demonstrates that the lung epithelium may adapt by increasing the expression of key anti-oxidant and detoxifying enzymes such as heme oxygenase 1 (HO-1) and NAD(P)H quinone oxido-reductase-1 (NQO-1) in paraquat exposed rats (Mainwaring et al., 2006).

In addition to mitochondrial damage, paraquat activates endoplasmic reticulum (ER) stress. When exposed to paraquat, the neuroblastoma cell line SH-SY5Y experienced an increase in cell death and activation of the ER stress protein C/ERB homologous protein (CHOP) after 48 hr of exposure. This rise in cell death was associated with an increase in genomic DNA fragmentation (Yang et al., 2009). Furthermore, this toxin has been shown to induce autophagy via endoplasmic reticulum (ER) stress in the same neuroblastoma cell line (Niso-Santano et al., 2011). The autophagic response appeared to be mediated via signaling through the mitogen- activated protein kinase (MAPK) pathway specifically at the level of

apoptosis signal-regulating kinase 1 (ASK1) enzyme, which directly phosphorylates c-jun N-terminal kinase (JNK) and p38. These signaling molecules activate their respective stress response pathways and may lead to activation of an immune response (Niso-Santano et al., 2011).

1.5 Mitochondria

1.5.1 Mitochondrial Function

Mitochondria are believed to be the consequence of an ancient parasitic symbiosis between eukaryotic cells and aerobic bacteria (Green et al., 2011). Consistent with this hypothesis, mitochondria contain a double lipid bi-layer membrane and their own genome and protein translation machinery (Aravamudan et al., 2013). Within the mitochondrial matrix, which is enclosed by the inner mitochondrial membrane, key metabolic "feeder" pathways take place such as the Krebs cycle, amino acid catabolism, and β-oxidation of fatty acids. The electron transport chain, is situated in the inner membrane and accepts reducing equivalents (NADH, FADH) from the feeder pathways (Dolle et al., 2013). In so doing, the mitochondria function as the powerhouse of the cell and produce energy in the form of ATP via oxidative phosphorylation (Aravamudan et al., 2013; Sureshbabu and Bhandari, 2013). Mitochondrial dysfunction has long been considered a major player in the aging process. It is becoming increasing apparent that this organelle plays an important role in the chronic diseases of aging (Schumacker et al., 2014). However, and as a consequence of the aerobic lifestyle, it is estimated that between 1 and 3% of oxygen brought into the mitochondrial for oxidative phosphorylation is not completely reduced to water and can form the ROS species superoxide anion (Green et al., 2011).

1.5.2 Mitochondrial DNA

Mitochondrial DNA (mtDNA) is circular and double stranded, encompassing about 16,569 base pairs. The DNA is organized into two strands based on their nucleotide composition; the heavy strand which is relatively guanine rich and the light strand which is cytosine rich. Each of the hundreds of mitochondria present in each cell, can contain between 100 and 1000 copies of the mitochondrial DNA (Chinnery and

Hudson, 2013). The DNA is organized within structures called nucleoids and each nucleoid contains a single circular piece of DNA (Prakash and Doublie, 2015). The nucleoids are tethered to the inner mitochondrial membrane and they are rather evenly spaced across the mitochondria (Chinnery and Hudson, 2013).

There are 37 genes encoded by the mtDNA with 28 encoded on the heavy chain and 9 genes on the light chain. Of these 37 genes, 22 encode for mitochondrial transfer RNAs (tRNA), a 16S ribosomal RNA (rRNA), and a 12S rRNA. The remaining 13 genes encode specific subunits of the oxidative phosphorylation complexes. The majority of the DNA (93%) codes for specific genes; however, there is one significant region referred to as the displacement loop (D-loop) that is a non-coding region (Chinnery and Hudson 2013).

Guanine is especially susceptible to oxidation due to having the lowest reduction potential of the nucleic acid bases (Luo et al., 2014). The most common mutagenic DNA lesion is 8-oxoguanine, which because of its ability to bind with adenine instead of cytosine, initiates a somatic mutation with a G:C to A:T transversion (Cooke et al., 2003). Recently it has been demonstrated that the respiratory chain complexes are structurally interdependent. If there is a structural defect in one complex this will have a deleterious effect on the remaining complexes, thereby adversely impacting the integrity of the energy producing machinery (Morán et al., 2012). This observation suggests that maintaining the integrity of mtDNA is paramount to avoid reductions in energy production, which could result in a decline in cell health ultimately leading to cell death.

The mutation rate from mtDNA replication is believed to be higher than that of the nuclear genome, in part because of its proximity to the site of primary ROS generation, but also due to the lack of histones associated with mtDNA, which serve to protect the nuclear DNA from ROS-mediated DNA damage (S.-J. Kim et al., 2015; Pinto and Moraes, 2015). Mitochondria consume 85-95% of inspired oxygen and the close proximity of its genome to the electron transport chain, where electrons can leak from predominately complex I, makes mtDNA susceptible to oxidation (Hegde et

al., 2012; Jaeschke et al., 2012; Morán et al., 2012). The mitochondrial genome replicates at the site of the nucleoids in a process that involves several key proteins all of which are nuclear encoded. The polymerase specific for mtDNA replication is polymerase-γ, which has 3'-5' exonuclease activity but unlike other polymerases also contains proofreading activity. However, it is believed that mtDNA replication is less efficient than nuclear DNA, because degradation is an option afforded to the mtDNA and not the nuclear DNA (Pinto and Moraes, 2015). It was not clearly understood until recently how degradation of the mtDNA constituted a specific repair process afforded to the mitochondria in response to oxidative stress (Akhmedov and Marin-Garcia, 2015). Work by Furda and colleagues demonstrated that a short exposure to an oxidant induced a rapid loss of mtDNA, where as a persistent exposure did not have the same effect on a transformed mouse fibroblast cell line (Furda et al., 2012). The authors go on to suggest that following an oxidant-induced stress, it is the reduction of the mtDNA copy number and not the frequency of the mtDNA lesions or the persistent mtDNA damage that initially induces mitochondrial dysfunction.

1.5.3 Mitochondrial DNA damage

Predominately, research into DNA repair has focused on nuclear DNA with little emphasis placed on the mitochondrial genome or on the ability of the mitochondria to execute DNA repair (Cline, 2012; Liu and Demple, 2010). Recently however, it was revealed that mtDNA has an extensive repair capability including base excision repair (BER), mismatch repair (MMR) and double strand break (DSB) repair (Liu and Demple, 2010). It is estimated that the average cell produces between 10^3 and 10^5 DNA lesions each day through normal daily life, with the majority of this damage observed as single strand breaks and oxidized base pairs (Hegde et al., 2012).

As described above, superoxide anions are unable to diffuse out of the inner mitochondrial space due to the hydrophobic environment of the mitochondrial lipid bi-layer membrane; instead they are converted to hydrogen peroxide (by manganese superoxide dismutase, MnSOD), which can diffuse out of the mitochondria (Cline, 2012). If the hydrogen peroxide remains within the mitochondria matrix, it can yield hydroxyl radicals which are highly reactive to DNA (Cline, 2012). Oxidative DNA damage or mutations affecting any of the 13 genes encoding electron transport chain

by the mtDNA can affect the transfer of electrons along the respiratory chain leading to elevated superoxide production (Morán et al., 2012). It is these damaged mitochondria that permit the release of uncontrolled ROS, pro-inflammatory signals, or the release of the inner contents of the mitochondria, thereby signaling cells to initiate cell death (Green et al., 2011). There is growing evidence that demonstrates a feed forward mechanism, where cellular structures and macromolecules are continuously damaged by superoxide radicals not managed by the cellular anti-oxidant and defense capacity, resulting in elevated levels of oxidative stress, mitochondrial dysfunction and finally cell death (Morán et al., 2012; Wallace et al., 1997).

Recent evidence has revealed that the accumulation of somatic mutations in mitochondrial DNA leads to abnormalities and a decline in tissue function (Safdar et al., 2011). Ineffective repair of DNA damage in mitochondria has been linked to a number of chronic diseases including cancer, Alzheimer's disease, Parkinson's disease, amyotrophic lateral sclerosis (ALS), as well as aging (Hegde et al., 2012). Based on comparative studies examining methods to increase life span, it has been suggested in these studies using *Caenorhabaditis elegans* which are commonly used in ageing studies, and *Drosophila melanogaster* (fruit flies) that reducing electron leakage from complex I of the respiratory chain can have a beneficial impact (Stefanatos and Sanz, 2011; Tissenbaum, 2015). In the review, the authors noted that lower levels of electron leak in these animals, lead to a drop-off in production of superoxide radicals capable of macromolecule oxidation and mitochondrial DNA damage, suggesting that this may lead to an increased lifespan (Stefanatos and Sanz, 2011). It has also been demonstrated that the key event in mitochondrial dysfunction is oxidative damage to its DNA (Wallace et al., 1997). Many diseases associated with increased oxidative stress have increased levels of the damage marker 8-oxoguanine in the affected tissues, correlated with decreased levels of the enzyme responsible for repair of the damage, OGG1 (Hill et al., 2008). Interestingly, caloric restriction has been linked to mitochondrial efficiency and energy production, along with decreased levels of DNA damage and reduced levels of oxidative stress (Pinto and Moraes, 2015). This potentially indicates how energy production impacts mitochondrial function, and suggests that decreasing DNA damage enables the longer life span in certain species (Pinto and Moraes, 2015).

Growing evidence implicates mitochondrial dysfunction in COPD. There is a change in the stability of the mitochondria and in the number of proteins responsible for mitochondrial anti-oxidant capacity in this disease (Soulitzis et al., 2012). In COPD patients the mitochondrial dysfunction is not only localized within the lung, but also manifested as additional complications in their skeletal muscle leading to a decrease in strength and endurance, and an increase in fatigue (Meyer et al., 2013). While it is still poorly understood how chronic diseases of the lung such as COPD, asthma, cystic fibrosis, and cancer are associated to mitochondrial dysfunction, it has been shown that mitochondrial dysfunction can lead to the progression or is a key feature of the pathophysiology of these diseases (Sureshbabu and Bhandari, 2013). In certain cell based assays, anti-oxidants and ROS scavengers are effective at reducing cellular ROS levels and can have an impact on lowering oxidative DNA damage as assessed by the marker, 8-oxoguanine (Ma et al., 2013). More recently, it was demonstrated that cigarette smoke exposure affected mitochondrial morphology in airway epithelial cells and led to changes in metabolic activity and mitochondrial membrane potential (Ballweg et al., 2014). These cells were also shown to have elevated expression levels of mitofusion 2 (MFN2), a protein involved in merging mitochondria (Ballweg et al., 2014). These data confirm previous reports that demonstrated in cigarette smoke exposed epithelial cells, the mitochondria will begin to exhibit morphologic changes similar to the ones observed during the aging process (Hoffmann et al., 2013).

In addition to changes in mitochondrial function, cigarette smoke exposed epithelial cells have also been linked to changes in the autophagic response, specifically, mitophagy (Mizumura et al., 2014). Mitophagy is characterized as the process by which aged or dysfunctional mitochondria are degraded to protect the cell from un-controlled mitochondrial metabolism and release of pro-apoptotic factors, such as cytochrome c (Kim et al., 2007). The mitochondria are removed by the autophagosome, which delivers them to the lysosome for degradation (Kim et al., 2007). Similarly, defective mitophagy was observed in cigarette smoke exposed mice as well as in COPD patient samples (Ahmad et al., 2015). This loss of cigarette smoke extract-induced mitophagy was restored *in vitro* through the over expression of Parkin, a key protein involved in mitophagy, suggesting restoration of this cellular

function to remove damaged mitochondria avoids senescence, which has been shown to be increased in some patients with COPD. For instance, epithelial cells exposed to cigarette smoke extract were shown to have defective mitochondria due in part to ineffective clearing of damaged mitochondria through mitophagy (Ahmad et al., 2015). These data highlight the sequence of events noted in Fig. 1.4, and suggest that the mitochondria may play a significant part of the overall disease pathobiology of COPD.

1.6 DNA Repair Mechanisms

The study of DNA repair is a growing field and a thorough review is beyond the scope of the current manuscript. However, for completeness, each of the major DNA repair processes will be briefly described.

1.6.1 Base Excision Repair Pathway

DNA repair through the base excision repair (BER) pathway is a highly evolutionary conserved process from bacteria to humans (Liu et al., 2013; Mandal et al., 2012). This process is responsible for repairing small covalent modifications that do not distort the DNA structure, but if left unchecked can lead to G:C to T:A somatic mutations (Karahalil et al., 2010). mtDNA is 50-fold more sensitive to oxidative damage compared to nuclear DNA damage (Ruchko et al., 2011).

DNA glycosylases (see 1.7 Glycosylases) are continually scanning DNA to identify lesions that they are capable of repairing (Fig. 1.5). The lesion is initially flipped out by the glycosylase facilitating it to bind into the binding pocket of the enzyme (Liu et al., 2013). Next, the damaged base is removed by the glycosylase and the resulting apurinic/ apyrimidine (AP) site is cleaved and processed by AP endonuclease (APE) to yield a 3' hydroxyl adjacent to a 5' deoxyribosephosphate. The new base is inserted by DNA polymerase-β in the nucleus and polymerase-γ in the mitochondria (Liu et al., 2013). Finally, the DNA strand is sealed by DNA Ligase (Ruchko et al., 2011). This type of repair is typically referred to as short-patch BER (Fig. 1.6) (Karahalil et al., 2010). Sometimes, several nucleotides are removed due to

incompatibility of the 5` end so a flap is processed by a specific endonuclease FEN-1. This type of BER is referred to as long-patch BER and can involve up to about 7 nucleotides (Karahalil et al., 2010).

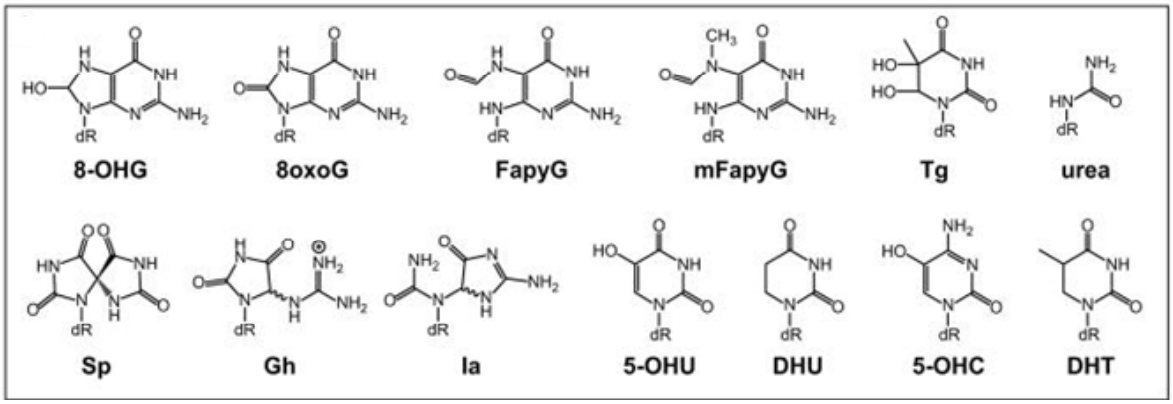

Figure 1.5 Structures of oxidized nucleotides repaired through base excision repair.

8-OHG, 7,8-dihydro-8-hydroxyguanine, 8oxoG, 7,8-dihydro-8oxoGuanine; FapyG, 2,6-diamino-4-hydroxy-5-formamidopyrimidine; mFapyG, N7-methylFapyG; Tg, thymine glycol; Sp, spiroiminodihydantoin; Gh, guanidinohydantion; Ia, iminoallantion; 5-OHU, 5-hydroxyuracil; DHU, dihydrouracil; 5-OHC, 5-hydroxycytosine; DHT, dihydrothymine (Brooks et al., 2013)

There are two major families of DNA glycosylases responsible for BER; they are the helix-hairpin-helix (HhH) super family and the Fpg/Nei family. Endonuclease III was originally discovered in *Eschericha coli* and is the founding member of the HhH family (Liu et al., 2013). This family primarily recognizes oxidized pyrimidines and only removes damaged bases from double-stranded DNA (Liu et al., 2013; Mandal et al., 2012). OGG1 is a member of the HhH super family, and in eukaryotes it identifies and removes oxidized purine base pairs (Liu et al., 2013). Another highly conserved glycosylase, MutY, is responsible for removing adenine residues that are incorrectly inserted opposite of an oxidized guanine residue (Liu et al., 2013).

The second family is the Fpg/Nei family, until recently it was only identified in bacteria, but Neil 1-3 have now been found in mammalian cells (Liu et al., 2013). With over 20 different types of oxidized base damage and only four or five DNA glycosylases responsible for repairing these lesions, there is broad specificity amongst them to correct damaged base pairs (Hegde et al., 2012). For instance, while OGG1 primarily excises 8-oxoguanine, it has been demonstrated that NEIL1 and NEIL2 (see 1.6.2 NEIL1, NEIL2, and NEIL3) are also efficient at removing 8-oxoguanine damage from DNA (Hegde et al., 2012). It is not surprising that the glycosylases have overlapping activity, since this helps to ensure genome stability (Chakraborty et al., 2015). The proximity of the mitochondrial DNA to electron leak from the electron transport chain and the lack of histones to protect the DNA from oxidative damage make it particularly susceptible to damage (Bacsi et al., 2013; Mandal et al., 2012). This is especially true for guanine, because it has the lowest redox potential of the four different bases (Bacsi et al., 2013; Mandal et al., 2012).

As shown in Fig. 1.6, once the glycosylase removes the damaged base, the remaining AP site is processed by APE1 (Siggens et al., 2012). X-ray repair cross-complementing protein 1 (XRCC1) is present as a scaffolding protein and facilitates processing and repair of the single-nucleotide gap by DNA polymerase-β (Siggens et al., 2012). In mitochondria, the polymerase involved with insertion of an intact base pair is polymerase- γ. Interestingly, this polymerase includes additional proofreading activity enabling DNA replication with a higher fidelity and reducing the necessary repair mechanisms (Scheibye-Knudsen et al., 2015). The final step in the process is ligation of the single strand DNA break with DNA Ligase I (nucleus) or DNA Ligase III (mitochondria, Fig. 1.6). Originally it was believed OGG1 was the rate limiting step in base excision repair, because increased OGG1 content suppressed oxidant-induced mtDNA damage (Ruchko et al., 2011). However, recent work by Bohr and colleagues suggests that the ligation of the repaired DNA strand with DNA Ligase III could be rate limiting as well (Akbari et al., 2014). Importantly, many of the steps detailed in this pathway are ATP dependent and are impacted by ATP depletion (Siggens et al., 2012).

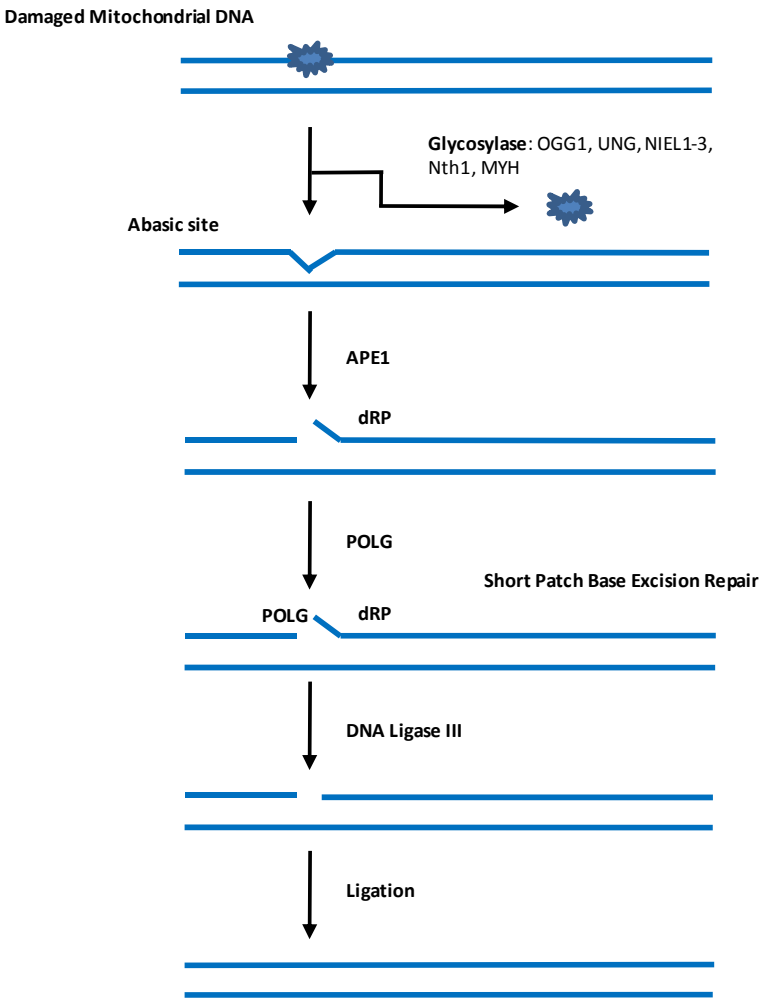

Figure 1.6 Base excision repair pathway depicting the short-patch repair.

A damaged base pair is detected by the glycosylase. The enzyme removes the damaged base pair and the resulting AP site is prepared by APE1 or in the case of OGG1 is bifunctional and the enzyme prepares the DNA strand for insertion of the correct base. In mitochondria polymerase-γ inserts the correct nucleotide and the single strand breaks are sealed by DNA Ligase III in the mitochondria (adapted from Martin, 2011).

1.6.2 Mismatch repair

Base-to-base mismatches or small insertion and deletions by the DNA polymerases are repaired through the evolutionarily conserved DNA mismatch repair pathway (Reyes et al., 2015). As DNA replicates, any mismatches that do occur are typically

corrected during proofreading and it is only in rare instances when this action fails that mismatch repair steps in and repairs the genome (Kunkel and Erie, 2015). The importance of mismatch repair is highlighted by the observation that the repair machinery for this pathway is located at the replication fork to ensure genome integrity as the DNA replicates (Kunkel and Erie, 2015).

Mismatch DNA repair has been extensively studied in *Escherichia coli* (Kunkel and Erie, 2015). The primary proteins involved in this pathway are MutS and MutL, where ATP binds to MutS inducing a conformational change allowing the proteins to slide down the newly synthesized DNA strand to identify DNA mismatches. MutL is recruited to the site of a mismatch, where it then recruits MutH, which has latent endonuclease activity and can nick the newly synthesized strand of DNA (Reyes et al., 2015). The DNA is then unwound by DNA helicase II and the error is degraded by a specific endonuclease, followed by the re-synthesis of the damaged DNA by DNA polymerase III (Reyes et al., 2015). Mammalian mismatch repair is very similar; however, instead of one protein there are several protein complexes responsible for the actions of the MutS and MutL proteins (Reyes et al., 2015). It was only recently confirmed that the mitochondria possess the ability to repair DNA mismatches (Akhmedov and Marin-Garcia, 2015). In the mitochondria, the MutS homologue has been identified as MSH5 while the homologue for MutL is MLH1 (Akhmedov and Marin-Garcia, 2015).

1.6.3 Nucleotide excision repair

Oxidized DNA bases can undergo a more complex repair mechanism than the previously described base excision repair (Section 1.6.1). This process is referred to as nucleotide excision repair (NER) and involves the removal of a lesion-containing oligonucleotide (Cooke et al., 2003). There are two sub-pathways for this type of repair, namely global genome NER (GG-NER) and transcription-coupled NER (TC-NER) (Marteijn et al., 2014). The two different subtypes of NER differ based on how the DNA damage is recognized, but these two pathways converge for the repair of the DNA damage (Melis et al., 2013).

The GG-NER probes the genome for bulky, helix-distorting DNA damage and TC-NER removes DNA damage from transcription-blocking lesions avoiding cell death (Marteijn et al., 2014). With TC-NER, the stalled RNA polymerase II signals to the NER machinery to remove and repair the blocking lesion (Melis et al., 2013). There are several proteins involved in the initiation of and repair by this pathway. One such class of proteins is Cockayne syndrome complementation group A and B (CSA and CSB). These two proteins have been shown to interact with OGG1, coinciding with evidence indicating these Cockayne syndrome proteins help to stabilize the repair complex at the mitochondrial membrane (Melis et al., 2013). While NER is absent from mitochondria, CSB has been shown to have a regulatory effect on OGG1, with decreased CSB associated with decreased OGG1 (Melis et al., 2013). Melis et al. suggest in their review that the interaction may play a role in stabilizing mitochondrial OGG1-mediated DNA repair, since the proteins are found to be up-regulated in the mitochondria in response to oxidative stress (Melis et al., 2013). Removal of either CSA or CSB has been shown to be associated with increased oxidative DNA damage and an altered redox state. Patients without these crucial enzymes display a premature aging phenotype, associated with deregulated mitochondrial activity (Kamenisch et al., 2010; Melis et al., 2013).

1.7 Glycosylases

1.7.1 OGG1

8-oxoguanine DNA glycosylase 1 or OGG1 is a major glycosylase for base excision repair, where the enzyme primarily recognizes the oxidized guanine base pair 8-oxo-7,8-dihydroguanine (8-oxoguanine) (Ba et al., 2014; Su et al., 2013). The *OGG1* gene is located on the human chromosome 3p25.2 and contains eight exons, enabling the formation of a number of different isoforms (see 1.7.1.1 Isoforms) (Ishida et al., 1999). The enzyme is located both within the nucleus and the mitochondria and is primarily tasked with the repair of 8-oxoguanine, thereby preventing a mismatch with adenine. This would result in a G:C to T:A transversion during replication, leading to somatic mutations (Ba et al., 2014). These somatic mutations if not avoided through efficient DNA repair, can result in genetic instability (Bauer et al., 2011).

OGG1 preferentially recognizes the damaged base pair 8-oxoguanine. To distinguish which base to remove, the enzyme binds to the strand of DNA through the formation of non-covalent hydrogen bonds between the enzyme and 8-oxoguanine and to the opposing cysteine residue on the opposite DNA strand. This mechanism ensures the identification and removal of only damaged bases (Klungland and Bjelland, 2007). Within the mitochondria, the primary repair mechanism for the DNA is base excision repair, with OGG1 the primary glycosylase (Fig. 1.7) (Scheibye-Knudsen et al., 2015; Su et al., 2013). OGG1 is a bifunctional glycosylase, where the enzyme excises the damaged base and then the resulting AP site is removed from the DNA backbone (Klungland and Bjelland, 2007; Su et al., 2013). OGG1 is three times more active in the mitochondria compared to the nucleus (S.-J. Kim et al., 2015). Finally, polymerase-γ is the enzyme responsible for both mtDNA replication and for executing repair of the mitochondrial genome within the base excision repair pathway (Liu and Demple, 2010).

While the mtDNA lacks histones to shield the DNA from damage, the mitochondrial nucleoid is associated with various proteins such as aconitase, which is an enzyme involved in the Krebs cycle (S.-J. Kim et al., 2015; Panduri et al., 2009). Under conditions of oxidative stress, aconitase has been shown to co-precipitate with mitochondrial OGG1. Independent of its 8-oxoguanine excision role, OGG1 was shown to protect aconitase activity in conditions of oxidant-induced mitochondrial dysfunction and apoptosis (Panduri et al., 2009). The functional association of OGG1 and aconitase is not completely elucidated and requires additional assessment. Kim and colleagues have put forth the hypothesis supporting the interaction of aconitase with mitochondrial OGG1 in the preservation of airway epithelial cell mtDNA to prevent downstream mitochondrial dysfunction and apoptosis (Kim et al., 2014).

OGG1 is regulated through p300/CBP-mediated acetylation (Radak et al., 2011). Acetylation of OGG1 increases its 8-oxoguanine excision activity by 10-fold compared to un-acetylated OGG1. Acetylated OGG1 is inversely correlated with the presence of 8-oxoguanine lesions, and declines with age (Radak et al., 2011). This observation lends support to the free radical theory of aging, where uncontrolled

oxidant-induced damage to macromolecules may underlie many of today's chronic diseases (Morán et al., 2012). Interestingly, there is mounting evidence of an epigenetic mechanism associated with OGG1. The interaction of OGG1 with an 8-oxoguanine lesion contained within the promoter sequence of pro-inflammatory genes can recruit additional transcription factors to up-regulate the innate immune response (Ba et al., 2014; H. S. Kim et al., 2015).

An allelic variant of OGG1, where serine 326 is switched with a cysteine, is found in about 50% of the Asian and about 25% of the Caucasian population (Morreall et al., 2014). It has been shown that this polymorphism of Ogg1 is repair deficient, and its reduced capacity for DNA repair is exacerbated under conditions of oxidative stress (Kaur et al., 2014). This amino acid substitution can have a negative impact on the function of the enzyme in part due to mis-folding of the protein at (Kaur et al., 2014). Recent studies have also shown that this specific form of OGG1 is susceptible to inactivation under inflammatory conditions (Morreall et al., 2014). Further, there is mounting evidence suggesting an association between the function of OGG1 and the processes involved in organ remodeling that is observed in chronic disease (Luo et al., 2014). Moreover, patients with this variant have a higher risk for developing certain cancers under conditions of oxidative stress (Morreall et al., 2014). It has been proposed that the decreased activity of the OGG1 Ser326Cys variant may contribute to the elevated risk of tobacco related lung cancer observed in patients with low levels of OGG1 (Morreall et al., 2014; Paz-Elizur et al., 2003).

Deletion of *ogg1* in mice is not embryonic lethal and no outward phenotypic change is present. *Ogg1*$^{-/-}$ mice are characterized by having abnormally high levels of 8-oxoguanie under non-stressed conditions (Klungland et al., 1999). However, these animals have reduced tolerance for oxidative stress conditions (Sampath et al., 2012). This observation suggests that while OGG1 is the primary enzyme responsible for detection and removal of the mutagenic lesion, a second glycosylase substitutes for Ogg1 to remove the oxidized guanine base pair from the genome, albeit at a diminished rate (Klungland et al., 1999). It is important to note that there was not an increased incidence in tumors in the Ogg1 knockout mouse compared to wild-type control mice (Klungland et al., 1999). It has also been reported that *ogg1*$^{-/-}$

mice have elevated levels of oxidative DNA damage and begin to develop features of metabolic syndrome when fed a high fat diet (Sampath et al., 2012). These data suggest an association of loss of Ogg1 activity, increased levels of the oxidative DNA lesion 8-oxoguanine and deleterious consequences related to abnormal metabolism.

Additional evidence demonstrates the potential positive impact of modulating OGG1 activity. The addition of an OGG1 plasmid construct containing a mitochondrial targeting sequence resulted in decreased oxidant-induced mitochondrial DNA damage and cell death in isolated perfused lungs challenged with hydrogen peroxide (Hashizume et al., 2013). Studies in animal models of sepsis suggest that the augmentation of OGG1 levels or activity leads to a potential therapeutic benefit resulting in decreased oxidative stress-induced mitochondrial DNA damage (Kuck et al., 2015). Kuck et al. examined the role of mitochondrial DNA as a damage-associated molecular pattern (DAMP) and how effective repair could reduce bacteria-induced efflux of DAMPs into the tissue (Kuck et al., 2015). In their study the authors demonstrated that a mitochondrial-targeted OGG1 fusion protein was protective against ROS-mediated intratracheally-instilled bacteria. Similar work by Hashizume and colleagues demonstrated that addition of human OGG1 protein conferred an increase in survivability from a ventilator-induced lung injury model in mice (Hashizume et al., 2013). Recently, it was reported that there is a link between mtDNA damage and cancer metastasis and progression; data have shown a possible therapeutic benefit for breast cancer in a transgenic human OGG1 mouse model (Yuzefovych et al., 2016). Altogether these data strongly suggest that there is a potential therapeutic benefit of increasing OGG1 content or modulating the catalytic activity of this enzyme in certain diseases.

1.7.1.1 Isoforms

There are eight spliced isoforms of OGG1 (Table 1.2). While there are two major groups of OGG1 isoforms based on the last exon included in the sequence at the C-terminal region, all of the enzyme isoforms share the same N-terminal or mitochondrial targeting sequence (Ogawa et al., 2015). Two predominant forms of OGG1, known as α-OGG1 and β-OGG1, are produced from the major alternatively spliced *OGG1* mRNA, with the first 316 amino acids in common between the two

types (Cheresh et al., 2013; Hashiguchi et al., 2004). The alpha form of the enzyme is believed to reside predominately in the nucleus, with some expression within the mitochondria, while the beta form is believed to reside entirely in the mitochondria. Previous reports had shown that OGG1β resided in the mitochondria, but did not have the capability to excise the oxidative lesion 8-oxoguanine (Hashiguchi et al., 2004). However, the OGG1β enzyme was recently purified from several lung cell lines, including A549 cells, and was shown to have the same excision capabilities as the alpha isoform, with only minor differences with respect to DNA AP lyase specificity (Ogawa et al., 2015). It has been suggested that OGG1-2α is the isoform that can chaperone aconitase in the mitochondria and prevent oxidant induced mitochondrial dysfunction (Panduri et al., 2009).

Type	Name	mRNA Accession	Nucleotide (base pairs)	DNA Coding Sequence	Number of Amino Acids	Protein Accession	Identical to OGG1-1a	Identical to OGG1-2a	Nuclear Localization sequence	Mitochondrial Targeting sequence
1	OGG1-1a	NM_002542	1652	344-1381	345	NP_002533	-	1-316	positive	positive
1	OGG1-1b	NM_016819	1896	344-1341	324	NP_058212	1-317	1-316	negative	positive
1	OGG1-1c	NM_016820	1669	344-1576	410	NP_058213	1-316	1-316	negative	positive
2	OGG1-2a	NM_016821	2158	344-1618	424	NP_058214	1-316	-	negative	positive
2	OGG1-2b	NM_016826	1957	344-1417	358	NP_058434	1-249	1-249, 250-357, 317-424	negative	positive
2	OGG1-2c	NM_016827	1775	344-931	195	NP_058436	1-190	1-190	negative	positive
2	OGG1-2d	NM_016828	2258	344-1414	356	NP_058437	1-316	1-316	negative	positive
2	OGG1-2e	NM_016829	2211	344-1312	322	NP_058438	1-316	1-316	negative	positive

Table 1.2 Summary of alternative spliced isoforms of OGG1.

*Table of the splice variant**s for human OGG1** (adapted from Ogawa et al., 2015).*

.

1.7.2 NEIL1, NEIL2, and NEIL3

Endonuclease eight-like 1, 2, and 3 or NEIL1, 2, and 3 are DNA glycosylases involved in the repair of the oxidized pyrimidine bases thymine (T), cytosine (C), and uracil (U) (Taricani et al., 2010). In contrast to OGG1, the NEIL glycosylases are capable of excising oxidized base pairs from both double and single stranded regions of DNA (Chakraborty et al., 2015).

NEIL1 has been shown to be primarily involved in DNA repair as the genome replicates; therefore, its repair activity is exerted within the nucleus (Chakraborty et

al., 2015; Mandal et al., 2012). NEIL1 is cell-cycle dependent, thereby supporting its primary activity in genomic DNA replication (Liu et al., 2013). NEIL2 has a preference for single-stranded DNA in a bubble structure and is involved in repair of damaged base pairs during transcription (Liu et al., 2013), and has been confirmed to repair oxidized DNA damage to transcribed genes (Chakraborty et al., 2015). Mice that were deficient in *neil2* exhibited no phenotypic changes when young, but the amount of oxidized DNA damage began to accumulate significantly in these knockout mice (Chakraborty et al., 2015).

The role of NEIL2 in mitochondrial DNA repair is supported by immunofluorescence studies carried out in a human cell line (Mandal et al., 2012). In this study, *NEIL2* depleted cells accumulated single strand DNA breaks with oxidized mitochondrial DNA damage. These data supports the previous observation of the lack of lethality in *ogg1-/-* mice and demonstrates the compensatory mechanisms at work between OGG1 and the NEIL glycosylases (Klungland et al., 1999). While the exact role for NEIL3 is still under investigation, recent evidence supports a preference for single stranded DNA repair based on the structure of the glycosylase (Liu et al., 2013).

One significant difference between the NEIL and OGG1 glycosylase enzymes appears to be their relationship to inflammatory pathways. Association of OGG1 with 8-oxoguanine damage elicits a pro-inflammatory response, signaling through the MAPK pathway (Ba et al., 2014; Chakraborty et al., 2015). However, *neil2*-null mice are highly susceptible to injury produced by pro-inflammatory cytokines suggesting that NEIL2 is involved in the anti-inflammatory defense response (Chakraborty et al., 2015).

1.8 Mitochondrial Dynamics

Mitochondria are present in almost all cells of the body and to maintain their health they are dynamic organelles that undergo fission (splitting apart) and fusion (merging) (Chauhan et al., 2014; Mishra and Chan, 2016; Willems et al., 2015). Fission and fusion are regulated processes designed to maintain cellular ATP concentrations (Sureshbabu and Bhandari, 2013). Due to the critical role

mitochondria play in normal cellular function, they have the ability to adapt to various biochemical challenges in an effort to maintain homeostasis (Chauhan et al., 2014). Mitochondria organize themselves into an inter-connected network surrounding the nucleus within a tightly controlled balance between fission and fusion (Fig. 1.7) (Chauhan et al., 2014; Trian et al., 2007). Reviewed by Aravamudan and colleagues, mitochondria will use the cytoskeletal structure connecting them to the endoplasmic reticulum to move within the cell; it is thought that this movement is motivated by the energy demands signaled by Ca^{+2} or other signaling intermediates (Aravamudan et al., 2013). Mitochondria receive signals from the nucleus to undergo fission and fusion in an effort to maintain normal cellular function, predominately energy production (Chauhan et al., 2014). Defects in fission and fusion can prevent mitochondria from re-organizing themselves adequately to maintain cell health (Chen and Chan, 2015).

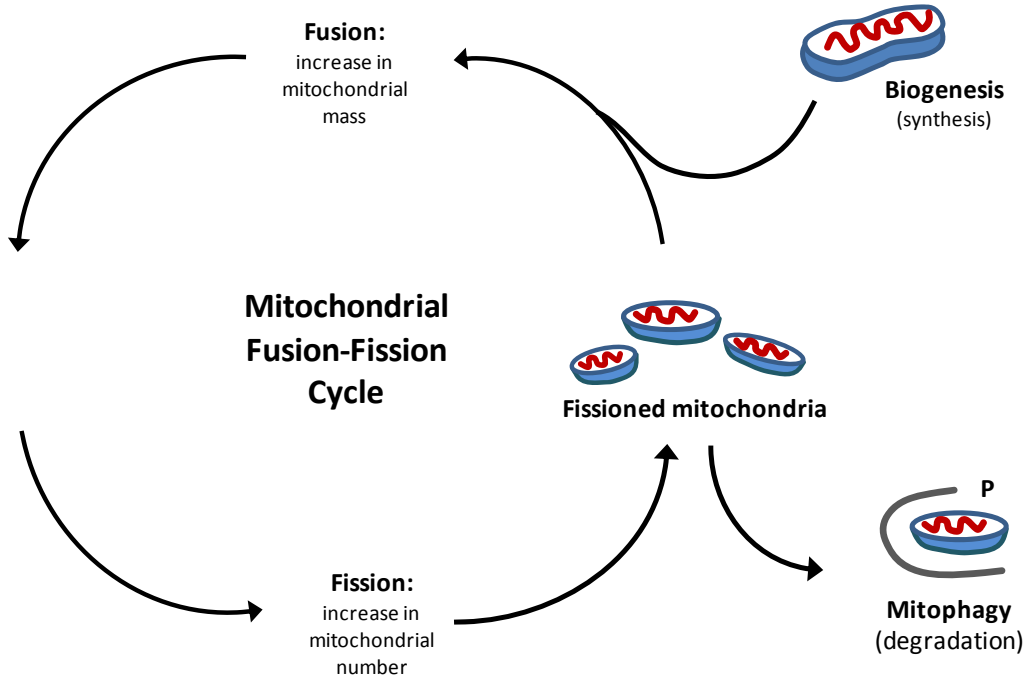

Figure 1.7 Schematic of mitochondrial fission and fusion.

The figure illustrates the cycle of fission and fusion as part of mitochondrial dynamics. Also represented is how mitogenesis feeds into fusion and how fission can lead to mitophay (adapted from Seo et al., 2010).

When the cell senses a loss of mitochondrial membrane potential, fission is activated. However, the daughter mitochondria are typically damaged and are more prone to enter mitophagy for clearance from the cell (Sureshbabu and Bhandari, 2013). Studies examining fission have shown that the mitochondrial nucleoid can freely diffuse between dividing mitochondria. This supports the hypothesis that fission plays an important role in the maintenance of normal cellular function (Muftuoglu et al., 2014). In this manner, fission concentrates the mutated or damaged DNA in an ATP dependent manner to minimize the number of mitochondria with mutated mtDNA (Chauhan et al., 2014; Sureshbabu and Bhandari, 2013). Elevated dynamin related protein-1 (DRP1) levels initiate fission enabling a dilution of DNA damage, which can lead to increased mitophagy in an effort to clear damaged mitochondria from the cell (Pinto and Moraes, 2015).

As just described, fission can be regulated by changes in the mitochondrial membrane potential. However, events such as exercise and periods of fasting or starvation can also activate DRP1 through phosphorylation at a specific serine residue (serine 637) by protein kinase A (PKA). This phosphorylation blocks fission in the cell to maintain larger mitochondria preventing their removal through mitophagy. The cell removes unnecessary organelles to avoid cell death due to limited resources. Conversely, this inhibition of fission can be reversed by removal of the phosphate group by calcineurin, which can be activated for example by changes in cytosolic calcium levels. Moreover, fission can be activated by phosphorylation at serine 616 by extra-cellular signal-regulated kinase (ERK1), which is part of the mitogen activated protein kinase family (MAPK), and ERK1 is activated by the oncogenic protein Ras. It remains unclear what the exact role fission may play in tumorgenesis (Mishra and Chan, 2016). Un-couplers of oxidavtive phosphorylation such as CCCP and FCCP have been shown to enhance fission, leading to fragmentation of the mitochondrial network (Mishra and Chan, 2016). While phosphorylation of DRP1 is described, the protein can undergo additional post-transcritional modifications such as acetylation, SUMOylation, ubiquitination, and s-nitrosylation that would impact its activity (Ishihara et al., 2015).

While fission has been typically associated with apoptosis, fusion is usually associated with cell proliferation as fusing mitochondria are important for energy production through oxidative phosphorylation (Aravamudan et al., 2013; Mishra and Chan, 2016). It has been suggested through observations that elongated mitochondria contained elevated levels of ATP and were more efficient at energy generation (Mishra and Chan, 2016). Further, the authors of the review describe conditions where fusion was eliminated, resulted in a dramatic decrease in mtDNA content, loss of membrane potential and reduced respiratory chain function. These data suggest if mitochondrial fusion is impaired, not only would there be an impact on ATP levels, but also an impact on mtDNA content (Mishra and Chan, 2016). Fusion is characterized as the process whereby mitochondria dilute their mtDNA damage to prevent it from reaching a certain threshold, after which the mitochondria would be marked for removal (Chauhan et al., 2014). In contrast to fission which is ATP dependent, fusion is the process the mitochondria utilize to ramp-up their ATP quantity and in this process both mtDNA mutations and ATP levels can affect these two dynamic processes (Chauhan et al., 2014).

In contrast to fission, fusion can be in-activated by loss of the mitochondrial membrane potential and under periods of metabolic stress, which results in cleavage of optic atrophy 1 (OPA1) from the inner mitochondrial membrane (Mishra and Chan, 2016). However, fusion can be activated in response to increased concentrations of the oxidized form of the anti-oxidant glutathione GSSG (Mishra and Chan, 2016). This molecule is elevated in cells as a result of increased ROS and other free radicals. Finally, changes in oxidative phosphorylation and ATP can activate fusion, where a rise in oxidative phosphorylation activity enables proteolytic cleavage of OPA1 into its active-soluble form promoting inner mitochondrial membrane fusion (Mishra and Chan, 2016). Further, changes in ATP enables GTP-loading of OPA1 by a specific kinase that phosphorylated GDP to GTP in the presence of ATP (Mishra and Chan, 2016). This demonstrates that while ATP is required for fission, ATP is critically linked to the regulation of fusion.

Damage or depletion of one of the key proteins involved in fission or fusion, such as DRP1, mitofusion 1 or 2 (MFN1 and MFN2), OPA1, and transcription factor A,

mitochondrial (TFAM), can lead to mitochondrial dysfunction, disorganized cristae formation, and ROS release (Hoffmann et al., 2013). In response to ROS, mitochondria will redistribute using the cytoskeletal structure of the cell to move from the central cytoplasmic region to the peri-nuclear region (Ahmad et al., 2015; Bardwell et al., 2013). Once the level of mutational damage in mtDNA reaches a certain threshold, the organelle is targeted for destruction through mitophagy (Chauhan et al., 2014). Hoffman and colleagues demonstrated that the mitochondrial structure and function of airway epithelial cells exposed to chronic cigarette smoke extract experienced significant changes. Exposed to certain concentrations of extract, the cells responded by increasing the levels of the anti-oxidant MnSOD enzyme and elevating the concentrations of various electron transport chain complexes (Hoffmann et al., 2013). Mitochondria can determine their own fate; if their mtDNA becomes too damaged or they become dysfunctional, damaged mitochondria will be removed by mitophagy. During mitophagy, PTEN-induced kinase 1 (PINK1) is expressed on the surface of mitochondria, where it signals for ubiquination by an E3 ubiquitin ligase, Parkin. This process of ubiquination signals for the mitochondria to be consumed by the autophagosome for removal from the cell (Matsuda et al., 2013). In Beas-2B airway epithelial cells, genetic deletion of PINK1 coupled with treatment with the fission inhibitor Mdivi-1, resulted in decreased levels of necrosis upon exposure to cigarette smoke (Mizumura et al., 2014). COPD patients show elevated levels of PINK1 expression within the lung tissue, suggesting increased mitophagy is associated with the pathogenesis of this disease (Mizumura et al., 2014). These data suggest that necrosis is also elevated in COPD lungs due to increased levels of mitochondrial dysfunction as reflected by elevated mitophagy.

Other chronic diseases have been shown to be impacted by mutations in the genes that regulate mitochondrial dynamics. Fragmented mitochondria as well as reduced quantities of mtDNA copy numbers, have been observed in chronic diseases such as Parkinson's and Alzheimer's disease (Pinto and Moraes, 2015; Willems et al., 2015). These neurodegenerative diseases are also negatively impacted by deletions of DRP1, MFN1, MFN2, or OPA1 suggesting the crucial importance of these proteins in maintaining normal cell health (Aravamudan et al., 2014). Additional evidence has shown that mechanisms such as mitophagy and autophagy along with fission and

fusion decline with age thereby enabling these damaged mitochondria to accumulate (Chauhan et al., 2014; Pinto and Moraes, 2015). Interestingly, activities such as calorie restriction, which has been to be linked to increased life span in mice, can activate the mitophagic/ autophagic response in cells (Pinto and Moraes, 2015). These data support the concept that increased oxidative DNA damage in the mitochondria is present in chronic diseases related to aging and that restoration of normal mitochondrial dynamics may provide a therapeutic option for disease.

1.9 Aims

As described above, there is growing evidence suggesting an association between increased oxidative stress-induced mtDNA damage with COPD disease severity and progression. The potential impact for effective mtDNA repair was partially described by Kirkham and Barnes, where it was their belief that there are many potential effects of ROS mediated carbonyl damage impacting COPD (Kirkham and Barnes, 2013). The focus of this work sought to elucidate the relationship between oxidant induced mitochondrial DNA damage and how effective repair of this damage could impact disease. The working hypothesis is that decreased mtDNA damage facilitated by an OGG1 activator may have a functional outcome and could be utilized as a potential therapeutic option for patients with COPD or other age-related diseases.

Airway epithelial type II cells, A549, were used as a model system to study the effects of exposure to cigarette smoke or to paraquat, which was used as a more specific stimulus, on mitochondrial localized ROS production on the mtDNA. Methods employed included measurements of the energy state (ATP/ADP ratio), mitochondrial membrane potential, and glutathione assessment. High content imaging assays were developed to assess the levels of ROS, 8-oxoguanine, OGG1 and DNA Ligase III (a proxy measure of base excision repair), MFN1 (a proxy measure for mitochondrial fusion), DRP1 (a proxy measure of mitochondrial fission), TOM20 (a proxy measure of mitochondrial mass), and pH2AX (a proxy measure of dsDNA breaks). Small molecule activators of OGG1 were assessed for their ability to execute base excision repair following an increase in the 8-oxoguanine lesion to block or alter paraquat-induced changes in mitochondrial membrane potential. These compounds and the manipulation of mitochondrial OGG1 were used to

quantify changes in mitochondrial mass, mitofusion, and mitofission with a view to ultimately developing a novel therapeutic approach to COPD.

The aim was to first develop and optimize a cell based assay to examine the effects of oxidative stress induced mitochondrial DNA damage and to monitor the cellular response to the ROS-mediated DNA damage. Second, the cellular assay was used to examine the effects of OGG1 BacMam, OGG1 siRNA, and small molecule OGG1 activators on paraquat-induced mitochondrial DNA damage and paraquat-induced alterations in base-excision repair. Finally, the OGG1 activators were examined for their effect on paraquat-induced changes in the energy state and on the mitochondrial dynamics as a representative measure of mitochondrial function.

CHAPTER 2:

MATERIALS and METHODS

2. Materials and Methods

2.1 Cell Culture

A549 cells (ATCC; Manassas, VA), adherent type II alveolar epithelial cells, were grown to sub-confluence using complete medium (Ham's F12, 10% heat inactivated fetal bovine serum (FBS), and 1X GlutaMAX supplement, Life Technologies; Carlsbad, CA). Cells were maintained in a humidified incubator at 5% CO_2, 37°C; the medium was replaced every two to three days. To sub-culture, A549 cells were subjected to trypsinization using Trypsin/EDTA (Lonza Inc.; Walkersville, MD), counted using Trypan blue (Life Technologies; Carlsbad, CA) exclusion, and were seeded at a density of 100,000 cells/mL with 100 µL/ well of a 96-well black micro-clear bottom plates. Cells were incubated for one day then medium was exchanged, and the cells placed back into the incubator. The cells were exposed to assorted stimuli (paraquat or cigarette smoke as detailed in figure legends), after which the cell plates were placed back into the incubator for varying amounts of time, depending on the individual marker of interest.

To generate *rho*$^{\varphi}$ cells, A549 cells were treated with ethidium bromide as described previously (Brar et al., 2012; Holmuhamedov et al., 2002). A549 cells were cultured in cell culture medium described above with the addition of ethidium bromide (50 ng/mL, Life Technologies; Carlsbad, CA), 100 µg/mL pyruvate (Life Technologies; Carlsbad, CA), and 50 µg/mL uridine (Sigma; St. Louis, MO). The cells were sub-cultured through 14 population doublings (about 30 days) and A549 *rho*$^{\varphi}$ were seeded into 96-well plates as described above.

2.2 Cell Treatment

2.2.1 Cigarette smoke exposure

Smoke from one unfiltered cigarette (Kentucky reference cigarette code 4A1 data 7/89; University of Kentucky, KY) was drawn using a peristaltic pump at 0.38 L/min into an 8 L chamber containing the cell plates, where a small fan was used to evenly distribute the smoke throughout the chamber (Fig. 2.1). One cigarette took approximately 2.5 min to burn at which point the pump was turned off and the cells

were kept in the box for an additional 2.5 min for a total smoke exposure of 5 min. A similar, separate apparatus was used for normal air exposed cells to avoid cross-contamination between the two treatment groups.

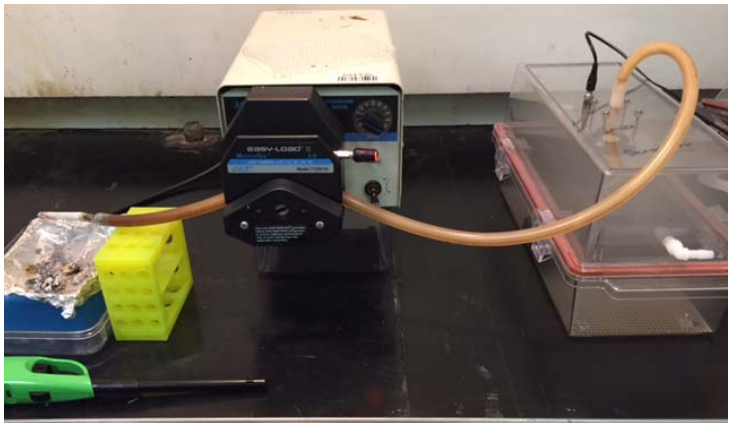

Figure 2.1 Cigarette smoke exposure chamber.

Picture of cigarette smoke exposure chamber, with the cigarette lit on the left, the peristaltic pump in the center and the chamber to the right for the cell plates. This system was adapted over the years and chambers such as this were reviewed by Thorne and Adamson (Thorne and Adamson, 2013).

2.2.2 Paraquat exposure

Paraquat (*N,N′*-dimethyl-4,4′-bipyridinium dichloride; Sigma; St. Louis, MO) was dissolved in Dulbecco's phosphate buffered saline (PBS) and stored as aliquots (1M, -20°C) for future use. An aliquot of paraquat was thawed for each experiment, and diluted in cell culture medium. The paraquat was added to the cells at varying final concentrations (0.01 to 3 mM) and for varying amounts of time (4 to 48 hr). Replicates were performed in triplicate for untreated and treated cells.

2.2.3 Baculovirus transduction

BacMam virus was constructed to insert differing copies of OGG1 into A549 cells. The virus was generated within the Biological Sciences group at GlaxoSmithKline.

Briefly, to generate the OGG1 BacMam expression vector, the vector pDONRhumanOGG1v1a_FL (GeneCopoeia; Rockville, MD) was purchased. This was a Gateway PLUS shuttle clone containing full-length human OGG1 transcript variant 1a (8-oxoguanine DNA glycosylase, OGG1, nuclear gene encoding mitochondrial protein, transcript variant 1a, reference sequence NM_002542.5). The cDNA of OGG1v1a fl was sub-cloned into a pFNCMV-DEST vector using a LR clonase reaction. The resulting expression OGG1v1a construct was transfected into SF9 insect cells for BacMam virus production according to Life Technologies Bac-to-Bac Baculovirus Expression Systems manual version 1.2 (Life Technologies; Carlsbad, CA)(Kost et al., 2007; Vogel et al., 2008). A549 cells were seeded into 96 well plates and incubated overnight. Cell culture medium was removed and fresh complete medium was added containing (volume: volume percentage) full length OGG1 BacMam virus, MnSOD-OGG1-GFP, or null virus. Based on initial transduction experiments conducted, A549 cells were successfully transduced following 48 hr incubation with the baculovirus. The cells were then exposed to various concentrations of paraquat for 24 hr.

2.2.4 *OGG1* siRNA Transfection

A549 cells were plated as previously described and incubated overnight. *OGG1* SMARTpool siRNA (Thermo Scientific; Waltham, MA) was stored at -20°C until ready for use. The siRNA was re-suspended in 5X siRNA buffer (Thermo Scientific; Waltham, MA) to a final concentration of 100 µM and incubated at room temperature for 30 min to ensure complete dissolution per the manufacturer's instructions. The siRNA was stored as aliquots at -20°C for future use. Frozen siRNA was thawed on wet ice and diluted in 1X siRNA buffer for a final concentration of 20 µM. The siRNA was diluted further 1:20 in Opti-MEM® I buffer (Life Technologies; Carlsbad, CA) and incubated at room temperature for 5 min. Dharmafect® 1 (Thermo Scientific; Rockford, IL) was diluted 1:75 in Opti-MEM® I buffer and incubated at room temperature for 5 min. The Dharmafect® 1 was then mixed with an equal volume of the diluted siRNA. This mixture was incubated for an additional 20 min at room temperature and then diluted 1:5 in Ham's F12 medium containing no additional supplements. The medium was then exchanged on the cell plates and replaced with

serum-free medium containing 100 nM human *OGG1* SMARTpool siRNA. Controls were included on each cell plate with cells treated with Dharmafect® 1 transfection reagent or media and siRNA buffer. A scrambled non-targeting siRNA and a non-affected gene control (GAPDH) were included to test for non-specific and off target effects of the siRNA treatment. These controls were added under the same conditions and concentrations as used for the *OGG1* siRNA. The cells were placed back into the incubator for 48 hr (determined based on earlier assay optimizations), and then the serum-free medium was exchanged for complete culture medium. These conditions were shown to be effective by measuring down-regulation of *OGG1* gene expression (Appendix S1).

2.2.5 OGG1 activators

Activators of OGG1 were identified from a high-throughput screen of the GlaxoSmithKline compound collection using a fluorescent OGG1 enzymatic assay. Briefly, a hairpin oligonucleotide (Fig. 2.2) containing an 8-oxoguanine base pair was used as a fluorescence substrate. The assay measured an increase in fluorescence as a result of dissociation of the 5'FAM (fluoroscein) from the FRET (fluorescence resonance energy transfer) quench pair with the 3' DAB (Dabcyl) fluorescent quencher (Fig. 2.2) upon cleavage of the DNA substrate at the nucleobase 8-oxoguanine by purified OGG1. In the presence of an activator, the very low basal catalytic activity of OGG1 was accelerated by 1-2 orders of magnitude, enabling this assay to detect activators present in the compound collection. 8-bromoguanine was run as a positive control on each plate along with negative (buffer only) controls (Lukina et al., 2013). All of the compounds used in this report were shown to positively bind purified OGG1 through an SPR (surface plasmon resonance) assay (data not shown).

The compounds tested were dissolved in 100% dimethyl sulfoxide (DMSO) (Thermo Scientific; Rockford, IL), and diluted to a final concentration of 0.1% DMSO in the cell well. Treatment groups without compound had 0.1% DMSO added as a control. Compound or the control were added 4 hr prior to paraquat exposure.

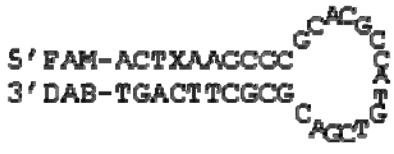

Figure 2.2 Sequence and predicted secondary structure of the 8-OxoG-containing OGG1 DNA substrate.

Picture of the hairpin-loop structure of the DNA substrate containing the oxidative DNA damage lesion 8-oxoguanine, which is marked in the sequence with an X.

2.3 Image acquisition

Cells in black, micro-clear bottom 96-well plates were imaged using an Operetta Imaging platform (Perkin Elmer; Waltham, MA) with the following settings: four fields per well, 20X, long-working distance objective, and in wide-field mode. Each image contains a bar as a reference for spatial resolution. The cell plates were exposed to varying excitation spectra depending on the dyes in each well, and the emission spectrum for each dye was detected (See Table 2.1). Each dye was added to untreated cells individually to be used as controls to adjust for background staining and to test for stain or dye interference from each color overlay. Cells intersecting the border of each image were excluded from the data analysis.

	Detects	Excitation	Emission
Hoechst 33342	nuclear DNA	360-400 nm	410-480 nm
CM-H2DCFDA	ROS	460-490 nm	500-550 nm
MitoSOX™	mitochondrial specific ROS	520-550 nm	560-630 nm
MitoTracker® Orange	mitochondria	520-550 nm	560-630 nm
DyLight™ 550	labeled secondary antibody	520-550 nm	560-630 nm
Alexa Fluor® 488	labeled secondary antibody	460-490 nm	500-550 nm
Alexa Fluor® 647	labeled secondary antibody	620-640 nm	650-700 nm
JC-1 aggregate	mitochondria membrane polarization	490-510 nm	585-605 nm
JC-1 monomer	mitochondria membrane polarization	490-510 nm	520-560 nm
CellMask™ Deep Red	Plasma membrane detection/ cell	620-640 nm	650-760 nm

Table 2.1 Excitation and Emission spectra for fluorescent stains and antibodies.

2.4 Detection of reactive oxygen species (ROS)

A549 cells were exposed to paraquat for 4 to 48 hr, after which the complete medium was replaced with warm PBS containing calcium (0.9 mM) and magnesium (0.5 mM) along with 5 µM CM-H_2DCFDA (DCF, Life Technologies; Carlsbad, CA). The cells were incubated for 30 min at 37°C in 5% CO_2. The buffer was aspirated and was replaced with warm Ham's F12 medium without supplements, 5 µg/mL Hoechst 33342, and 250 nM MitoTracker® orange (Life Technologies; Carlsbad, CA). Again, the cells were incubated for an additional 30 min (37°C), and the buffer was exchanged for live cell imaging solution (Life Technologies; Carlsbad, CA). To evaluate the immunofluorescence staining, image acquisition and high content analysis were performed as described in section 2.3. As shown in Fig. 2.3, the black and white images were segmented using the Hoechst stain and MitoTracker® orange for identification of the nucleus and mitochondria/ cytoplasm region, respectively. Once segmented, the mean fluorescence intensity of the CM-H2DCFDA stain was quantified from the entire cell region. A sum was calculated across all of the images from the well and then divided by the number of cells imaged across the 4 fields tested.

2.5 Detection of mitochondrial ROS

For the detection of mitochondria specific ROS, MitoSOX™ Red Mitochondrial Superoxide Indicator (Life Technologies; Carlsbad, CA) was added according to the manufacturer suggested protocol to untreated and treated A549 cells. Cell culture medium was aspirated from the cells and warm basal medium without supplements, 5 µM MitoSOX™, 5 µg/mL Hoechst 33342, and 5 µg/mL CellMask™ deep red was added. The dyes were incubated on the cells for 10 min, and then the medium was aspirated and replaced with live cell imaging solution. Cell plates were imaged as described previously. After the cells were classified and segmented (Hoechst 33342 for the nuclear region and CellMask™ deep red for cytoplasm), MitoSOX™ fluorescence intensity was quantified within the cytoplasm region of the cell. The sum fluorescence intensity was determined across all images in a particular well, and was corrected for the number of cells imaged per well.

(a)

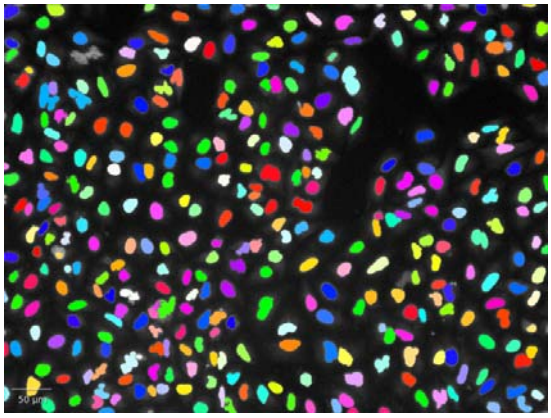

(b)

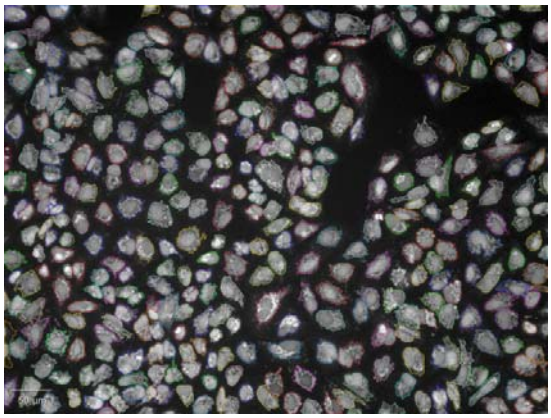

Figure 2.3 Representative image of segmentation from ROS stained A549 cells

A549 cells stained for ROS detection were imaged using the Operetta with Harmony v3.5.2 software (Perkin Elmer; Waltham, MA). The nucleus (a) was identified using the Hoechst 33342 dye for nuclear identification. Once the nucleus was classified, the software identified the cytoplasm region (b) of the cell using the MitoTracker® orange stain. A similar analysis paradigm was used for the subsequent imaging studies unless indicated otherwise.

2.6 Immunofluorescence assays

2.6.1 Oxidative DNA damage marker 8-oxoguanine

Cell culture medium from A549 cells was aspirated and replaced with 250 nM MitoTracker® orange in serum-free medium, and incubated for 30 min (37°C, 5% CO_2). Fixation of the cells was accomplished by the addition of an equal volume of 8% paraformaldehyde (4% final concentration, Electron Microscopy Sciences; Hatfield, PA). The cell plates were incubated for 20 min at room temperature in the dark. Cells were washed and stained for 8-oxoguanine using methods adapted from previously published methods (Marella et al., 2007; Moiseeva et al., 2009; Richardson et al., 2009). The fixative was aspirated, and the cells were washed once with PBS. RNase A (100 µg/mL in PBS, Qiagen; Valencia, CA) was added to the cells and incubated for 1 hr at 37°C, and washed once more with PBS. Hydrochloric acid (2M) was added to each well. The cells were incubated for 20 min at room temperature in the dark, the acid was aspirated from the cells and 0.1 M sodium borate, pH 8.5 was added for 2 min. A549 cells were washed and blocked in PBS containing 3% bovine serum albumin (BSA, Sigma; St. Louis, MO), 5% donkey serum (Millipore; Billerica, MA), and 0.1% Triton X-100 (Sigma; St. Louis MO). The block buffer remained on the cells for 5 min at room temperature and was then exchanged with additional block buffer containing diluted mouse anti-8-oxoguanine antibody (1:100, Millipore; Billerica, MA). Wells containing mouse IgM were included as an isotype control on each cell plate.

Following overnight incubation at 4°C in the dark, the cell plates were brought out to room temperature, washed once with PBS plus 0.1% Tween-20 (Bio-Rad; Hercules, CA), and followed by a single wash with PBS containing 3% BSA. This buffer was aspirated and diluted labeled goat-anti-mouse IgG (H &L)-Alexa Fluor® 647 (1:500, Life Technologies; Carlsbad, CA) and 5 µg/mL Hoechst 33342 in PBS containing 3% BSA was added for 1 hr at room temperature. Afterward, the cells were washed again with PBS plus 0.1% Tween-20 followed by a final single PBS wash. Hank's balanced salt solution (HBSS) was added and the plates were sealed with foil, and then imaged and analyzed using the Operetta Imaging system as described above. Segmentation was performed using the Hoechst 33342 and MitoTracker® orange dyes, and the fluorescence intensity of 8-oxoguanine was quantified in the cytoplasm region of the cells. Single cell analysis was performed and the cells were classified and selected based on their initial un-corrected mean cytoplasmic region intensity of 8-oxoguanine. As shown in Fig. 2.4, the number of cells with 8-oxoguanine intensity

above the peak mean distribution from the untreated control was characterized as a high responding cell, with several experiments used in establishing the threshold settings. The percentage of cells in this group was calculated based on the total number of cells imaged in each well. The shape and size of both the nuclear and the cellular regions were measured for area, width/length, and roundness as part of the morphological assessment. Finally, the mean fluorescence intensity for the isotype control was subtracted from each treatment group, correcting the value based on non-specific binding.

(a)

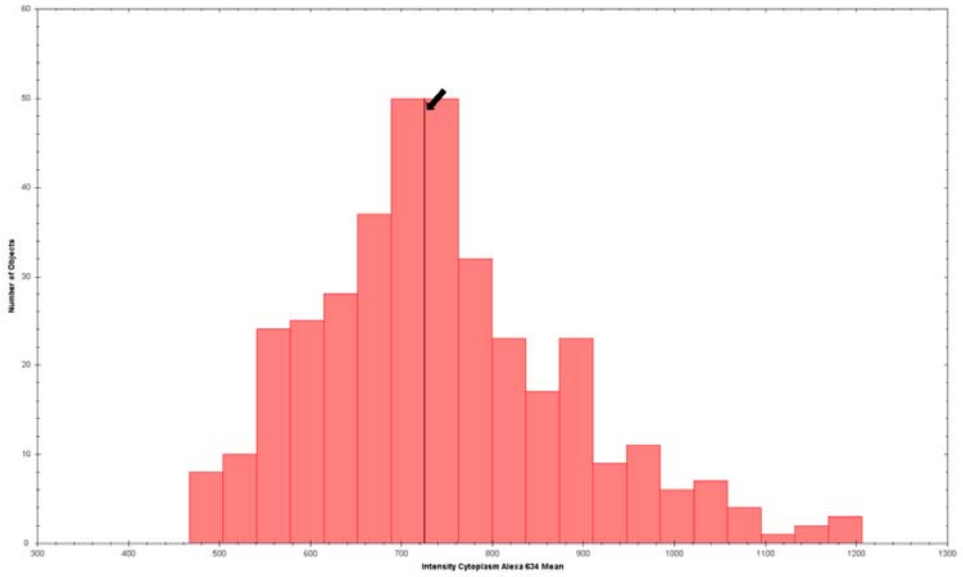

(b)

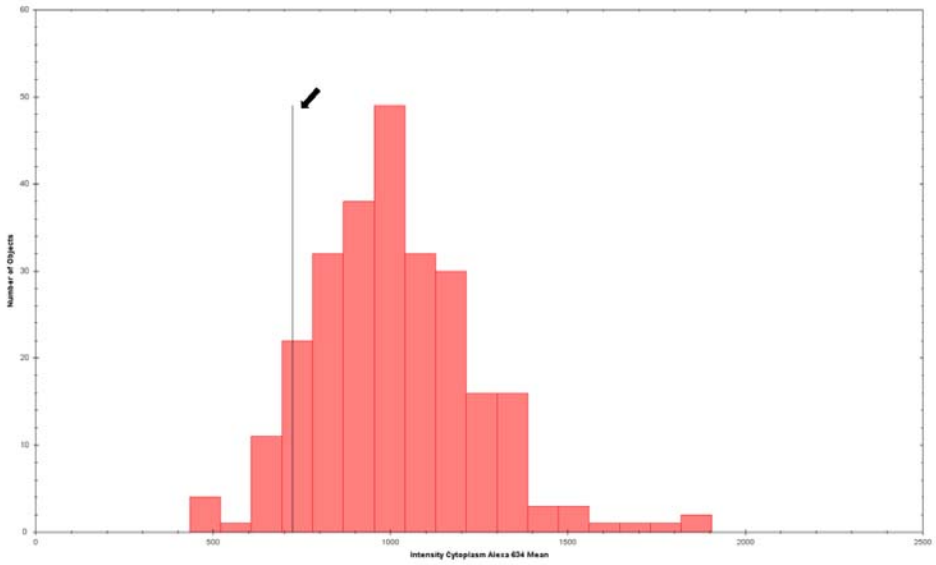

Figure 2.4 Single cell analysis for 8-oxoguaine in a high responder population.

Figure 2.4 Single cell analysis for 8-oxoguaine in a high responder population.

A549 cells were either (a) untreated or (b) exposed to 3 mM paraquat for 48 hr and followed by staining for 8-oxoguanine. In panel A the untreated cells are shown as a histogram representing the mean fluorescence intensity of 8-oxoguanine in the mitochondria of the cell (x-axis), relative to cell number (y-axis). The back line (indicated by the arrow) in the center of the central peak represents the threshold set for 8-oxoguanine. For panel B, the distribution shifts to the right for cells exposed to paraquat, indicating these cells have increased levels of mtDNA 8-oxoguanine.

2.6.2 8-oxoguanine glycosylase 1 (OGG1)

After exposure of A549 cells to mitochondrial toxin, the culture medium was replaced with 250 nM MitoTracker® orange in serum-free culture medium. Methods for staining were adapted from previous work utilizing manufacturer suggested methods (Abcam; Cambridge, MA). The cell plates were incubated for 30 min (37°C, 5% CO_2) and were fixed with 8% paraformaldehyde as described above. Following fixation, the buffer was aspirated, and the cells were permeabilized by the addition of PBS containing 0.1% Triton X-100 for 15 min at room temperature. The medium was exchanged and non-specific binding sites were blocked with PBS containing 10% goat serum (Life Technologies; Carlsbad, CA), 1% BSA, and 0.1% Tween-20 for 1 hr at room temperature. Buffer was aspirated and the cells were incubated overnight at 4°C in the dark in PBS containing 1% BSA, and 0.1% Tween-20, with diluted rabbit anti-OGG1 antibody (1:500, Cambridge Research Biologicals; Cleveland, UK), or rabbit IgG for the isotype control.

The cell plates were brought to room temperature and were washed twice (PBS and 0.05% Tween-20). Labeled goat-anti-rabbit IgG (H &L)-Alexa Fluor® 488 (Life Technologies; Carlsbad, CA) and 5 µg/mL Hoechst 33342 diluted in PBS, 1% BSA, and 0.1% Tween-20 was added to the wells. The cells were then incubated for 1 hr at room temperature in the dark. Following an additional two washes, HBSS was added to the cells, and the plates were sealed with foil for image acquisition and analysis as described above. As for 8-oxoguanine, the cells were segmented utilizing Hoechst 33342 and MitoTracker® orange nuclear and cytoplasmic region identification, respectively. The fluorescence intensity of the OGG1-Alexa Fluor® 488 was quantified in the cytoplasm region of the cell. The average of the mean fluorescence intensity of the isotype control was subtracted from each treatment group, which corrected the fluorescence intensity due to non-specific binding of the labeled goat anti-rabbit IgG secondary antibody. The percent change was then calculated for each treatment group relative to the average untreated control fluorescence intensity.

2.6.3 Manganese superoxide dismutase (MnSOD)

MnSOD was determined according to methods made available by the commercial source (Cellomics, Thermo Scientific; Rockford, IL). In brief, cell culture medium was aspirated from A549 cells, and 4% paraformaldehyde was added as the fixative. Following 20 min incubation at room temperature, the cells were washed twice with PBS, then permeabilized with 0.1% Triton X-100 in PBS. After 15 min, the cells were washed again twice with PBS, and blocking buffer (PBS, 0.3% BSA and 5% FBS) was added for 15 min at room temperature. The blocking buffer was aspirated and 2 µg/mL rabbit-anti-MnSOD (Thermo Scientific; Rockford, IL) in PBS and 0.3% BSA or 2 µg/mL rabbit IgG (isotype control) were added and maintained for 1 hr at room temperature. The cells were washed once (0.1% Tween-20 in PBS) followed by two washes with PBS. The cells were incubated with blocking buffer (PBS, 0.3% BSA, and 2% FBS) for 15 min at room temperature, and then the buffer was removed and diluted labeled goat-anti-rabbit IgG-DyLight® 550 (1:500, Thermo Scientific; Rockford, IL) in PBS containing 0.3% BSA, and 5 µg/mL Hoechst 33342 was added. The dye solution was maintained on the cells for 60 min at room temperature in the dark. After 45 min, 5 µg/mL CellMask™ deep red was added to the cells. Finally, the cells were washed two times with 0.1% Tween-20 in PBS, and HBSS was then added to the cells. The plates were sealed with foil for image acquisition and analysis as described above. The images were analyzed by first segmenting the cells using Hoechst 33342 for nuclear identification, then CellMask™ deep red for cytoplasmic region identification. The fluorescence intensity of the MnSOD-DyLight™-550 was quantified in the cytoplasm region of the cell. The average of the mean fluorescence intensity of the isotype control was subtracted from each treatment group.

2.6.4 Cytochrome *c*

Cytochrome *c* was determined according to methods made available by the commercial source (Cellomics, Thermo Scientific; Rockford, IL). After aspiration of the cell culture medium from the cells, 2% paraformaldehyde was added and incubated at room temperature for 15 min. The fixative was removed and the cells were permeabilized with 0.1% Triton X-100 in PBS. After 15 min, the cells were washed twice with PBS and non-specific binding sites were blocked (PBS, 0.3% BSA and 2% FBS) for 15 min at room temperature. The blocking buffer was aspirated, and mouse-anti-cytochrome *c* (2.5 µg/mL, Thermo Scientific; Rockford, IL) diluted in

PBS and 0.3% BSA or mouse IgG (Thermo Scientific; Rockford, IL) was added to the cells. Following 1 hr incubation at room temperature, the cells were washed twice (PBS plus 0.1% Tween-20), and then incubated with diluted labeled goat-anti-mouse IgG-DyLight™ 550 (1:500, Thermo Scientific; Rockford, IL) in PBS, 0.3% BSA, and 5 µg/mL Hoechst 33342. This cocktail was incubated on the cells for 60 min at room temperature in the dark, after 45 min, 5 µg/mL CellMask™ deep red was added and the incubation continued. The cells were washed twice with PBS plus 0.1% Tween-20, and then HBSS was added. The plates were sealed with foil for image acquisition as described above using the Operetta Imaging platform. The images were analyzed with the cells identified and segmented using Hoechst 33342 and CellMask™ deep red for nuclear and cytoplasmic region identification, respectively. The fluorescence intensity of the cytochrome *c*-DyLight™-550 was quantified in the cytoplasm as well as in the nuclear region of the cell. Translocation of cytochrome *c* from the mitochondria to the nucleus was calculated based on the fluorescence intensity of cytochrome *c* detected in the nucleus divided by the sum of the cytochrome c detected in both the cytoplasm and nuclear regions.

2.6.5 phosphorylated-Histone 2-AX (pSer140)

Commercially available methods were used for the detection of phosphorylated-histone 2-AX (pH2AX) (Cellomics, Thermo Scientific; Rockford, IL). Briefly, cell culture medium was aspirated from A549 cells and fixative (2% paraformaldehyde) was incubated at room temperature for 15 min. The fixative was removed and the cells were permeabilized (0.1% Triton X-100 in PBS). After 15 min, the cells were washed twice with PBS and non-specific binding sites were blocked (PBS, 0.3% BSA and 2% FBS) for 15 min at room temperature. The blocking buffer was aspirated, and mouse-anti-pH2AX diluted in PBS and 0.3% BSA (2 µg/mL, Thermo Scientific; Rockford, IL) or mouse IgG (Thermo Scientific; Rockford, IL) was added to the cells. Following 1 hr incubation at room temperature, the cells were washed twice (PBS plus 0.1% Tween-20), and then incubated with diluted labeled goat-anti-mouse IgG-DyLight® 550 (1:500, Thermo Scientific; Rockford, IL) in PBS, 0.3% BSA, and 5 µg/mL Hoechst 33342. This cocktail was incubated on the cells for 45 min at room temperature in the dark. The cells were washed twice (PBS plus 0.1% Tween-20), followed by two washes with PBS. HBSS was added and the plates were sealed with foil for image acquisition as described above using the Operetta Imaging platform. The images were analyzed with the cells identified and segmented using

Hoechst 33342 for nuclear region identification. The fluorescence intensity of the pH2AX-DyLight™-550 was quantified in the nuclear region of the cell.

2.6.6 Translocase outer membrane (TOM20)

Cell culture medium from treated and untreated A549 cells was aspirated, and replaced with serum-free cell culture medium containing 250 nM MitoTracker® orange. The cell plates were incubated for 20 min, and fixed as described above for 8-oxoguanine. TOM20 immunofluorescence staining was adapted from published methods (Dai et al., 2014). Briefly, following fixation the cells were permeabilized (PBS plus 0.1% Triton X-100) for 15 min at room temperature and were then washed once with PBS. Non-specific binding sites were blocked (PBS, 10% goat serum (Life Technologies; Carlsbad, CA), and 1% BSA) for 30 min at room temperature in the dark. The buffer was aspirated and rabbit-anti-TOM20 (4 µg/mL, Santa Cruz; Dallas, TX) or rabbit IgG as an isotype control were diluted in block buffer was added to the cell plates. The antibody remained on the cells overnight at 4°C in the dark, and the cell plates were then brought to room temperature the next day. The plates were washed twice (PBS plus 0.05% Tween-20), and diluted labeled goat-anti-rabbit IgG (H &L)-Alexa Fluor® 647 (1:500, Life Technologies; Carlsbad, CA) in PBS, 3% BSA, and 5 µg/mL Hoechst 33342 was added to the cells. The solution was incubated for 1 hr at room temperature in the dark, at which point the cells were washed twice as before and HBSS was added to the cells. The plates were sealed with foil, and then imaged as described above. Image analysis was carried out as described above for 8-oxoguanine. The fluorescence intensity of the TOM20-Alexa Fluor® 647 was quantified in the cytoplasm region of the cell and the average of the mean fluorescence intensity of the isotype control was subtracted from each treatment group. The percent change was calculated for each treatment group relative to the average fluorescence intensity for the untreated control.

2.6.7 Dynamin related protein-1 (DRP1)

Cell culture medium from treated and untreated A549 cells was aspirated and replaced with 250 nM MitoTracker® orange diluted in serum-free cell culture medium. The cell plates were incubated for 20 min and fixed as described for TOM-20. The methods for DRP1 detection were adapted and optimized from manufacturer suggested methods (Abcam; Cambridge, MA). Briefly, following fixation the cells

were permeabilized (PBS containing 0.1% Triton X-100) for 15 min at room temperature and then washed once with PBS. Block buffer was added (PBS containing 5% BSA) for 1 hr incubation at room temperature in the dark, and was aspirated from the cells. Diluted rabbit-anti-DRP1 (2 µg/mL, Thermo Scientific; Rockford, IL) or rabbit IgG (PBS and 0.3% BSA) was incubated on the cells overnight at 4°C. The cell plates were brought to room temperature, and then washed twice (0.1% Tween-20 in PBS). Diluted labeled goat-anti-rabbit IgG (H &L)-Alexa Fluor® 488 (1:500) in PBS, 0.3% BSA, and 5 µg/mL Hoechst 33342 were added and incubated for 1 hr at room temperature in the dark, after which the cells were washed again and HBSS was added. The plates were sealed with foil, and then imaged as described above. Image analysis was performed as described above for TOM-20. The fluorescence intensity of the DRP1-Alexa Fluor® 488 was quantified in the cytoplasm region of the cell. The average of the mean fluorescence intensity of the isotype control was subtracted from each treatment group. The percent change was calculated for each treatment group relative to the average untreated control fluorescence intensity.

2.6.8 Mitofusin-1 (MFN1)

Cell culture medium from treated and untreated A549 cells was aspirated and replaced with 250 nM MitoTracker® orange diluted in serum-free cell culture medium. The cell plates were incubated for 20 min and fixed as described for TOM-20, with methods for the detection of Mfn1 adapted and optimized from manufacturer suggested methods (Abcam; Cambridge, MA). Following fixation, the cells were permeabilized (0.1% Triton X-100 in PBS) for 15 min at room temperature and the buffer was exchanged for blocking buffer (5% horse serum (Life Technologies; Carlsbad, CA) in PBS). Following a 1 hr incubation at room temperature in the dark, the buffer was aspirated and diluted chicken-anti-MFN1 or chicken-IgG (10 µg/mL, Abcam; Cambridge, MA) in PBS containing 0.3% BSA was added. The antibody incubated overnight at 4°C in the dark. Cell plates were equilibrated to room temperature and washed twice (0.1% Tween-20 in PBS), and labeled goat-anti-chicken IgG (H &L)-Alexa Fluor® 488 (1:250, Life Technologies; Carlsbad, CA) diluted in PBS, 0.3% BSA, and 5 µg/mL Hoechst 33342 were then added and incubated for 1 hr at room temperature in the dark. Afterward the cells were washed again and HBSS was added. As described above the plates were sealed, imaged, and analyzed as described above. Fluorescence intensity of the MFN1-Alexa Fluor® 488 was quantified in the cytoplasm region of the cell. The average of the mean

fluorescence intensity of the isotype control was subtracted from each treatment group, and the percent change was calculated for each treatment group relative to the average untreated control.

2.6.9 DNA Ligase III

To determine changes in DNA Ligase III content, treated and untreated cells were fixed in 4% paraformaldehyde, and permeabilized as described above. DNA Ligase III staining methods were adapted from commercial manufacturer (Abcam; Cambridge, MA), and from published methods detailing mitochondrial DNA Ligase III staining (Mortusewicz et al., 2006). Briefly, the cells were washed twice with PBS and non-specific binding sites were blocked (5% BSA in PBS) for 1 hr at room temperature. The buffer was removed and a polyclonal rabbit anti-DNA Ligase III antibody (5 µg/mL, Novus Biological; Littleton, CO) or rabbit IgG diluted with 0.3% BSA in PBS was incubated overnight at 4°C. The cells were washed twice (0.05% Tween-20 in PBS) and diluted labeled goat-anti-rabbit IgG (H &L)-DyLight 550 (1:500, Thermo Scientific; Rockford, IL) and 5 µg/mL Hoechst 33342 in PBS with 0.3% BSA were incubated for 45 min at room temperature. CellMask™ deep red (5 µg/mL) was added to each well. And incubated for 15 min at room temperature. The cells were washed twice as described above and HBSS was added to each well. The plates were then sealed with foil, and imaged and analyzed as described above. Fluorescence intensity of the DNA Ligase III-DyLight™ 550 was quantified in the cytoplasm region of the cell. The average of the mean fluorescence intensity of the isotype control was subtracted from each treatment group. Finally, the percent change was calculated for each treatment group, relative to the average fluorescence intensity of the untreated control.

2.7 Mitochondrial membrane integrity

For mitochondrial dysfunction, texture analysis was performed in conjunction with the images acquired for ROS determination. The MitoTracker® orange staining pattern was analyzed using the smart learning features of PhenoLOGIC enabled Harmony software (Perkin Elmer; Waltham, MA). The chemistry of the stain works as follows, when the MitoTracker® stain is added to healthy cells with functional mitochondria, the stain will appear to be punctate in discrete compartments when imaged. However, in cells with dysfunctional or non-intact mitochondria the stain will diffuse out of the mitochondrial compartment; appearing as diffuse, non-specific staining

throughout the cytoplasm of the cell. Through the smart learning feature of the Harmony software, these two different phenotypes can be recognized and quantified as shown in Fig. 2.5. The software quantifies the intensity of the MitoTracker® orange stain in each region. This was reported as the fluorescence intensity mean for each region of mitochondrial staining in the cells, enabling quantification of the change in the staining pattern of the MitoTracker® dye.

(a) **(b)**

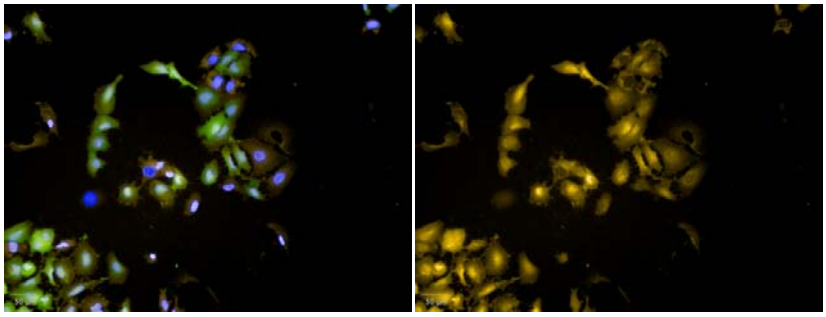

(c)

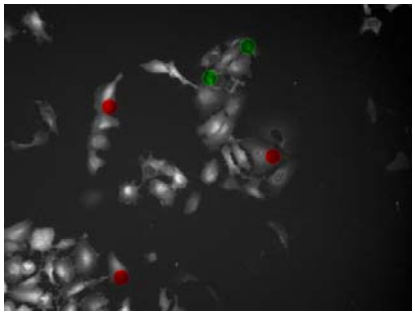

Figure 2.5 Identification of changes in mitochondrial membrane integrity.

A549 cells exposed to 1 mM paraquat for 48 hr were stained for ROS detection then imaged using Harmony v3.5.2. (a) Merged image from 48 hr paraquat exposure (blue – Hoechst 33342, green – ROS, orange – MitoTracker® orange). (b) Same image, with the Hoechst 33342 and ROS color overlays removed, leaving only the MitoTracker® orange. (c) Demonstrates how with the MitoTracker® orange image the software was trained in PhenoLOGIC enabling the smart learning portion of the Harmony software, by placing green or red regions on the image to classify the different staining patterns present within the cell.

2.8 Mitochondrial membrane potential

The cationic carbocyanine, ratiometric dye JC-1 (5,5',6,6'-tetrachloro-1,1',3,3'-tetraethylbenzimidazolycarbocyanine iodide; Life Technologies; Carlsbad, CA) was used to measure mitochondrial membrane potential (Torres-Gonzalez et al., 2014). Cell culture medium from treated and untreated A549 cells was removed, and JC-1 (2 µg/mL, Life Technologies; Carlsbad, CA) was added to the cells in serum-free A549 cell culture medium. The dye was incubated for 30 min (37°C, 5% CO_2) and then 5 µg/mL Hoechst 33342 and 5 µg/mL CellMask™ deep red were added to the cells. Following an additional 30 min (37°C, 5% CO_2) incubation, the medium was exchanged for live cell imaging solution. The cells were imaged as described above. Image analysis was performed with Hoechst 33342 and CellMask™ deep red stain for nuclear and cytoplasmic region identification, respectively. When the dye exists at low concentrations throughout the cell it will emit green fluorescence, but when concentrated within mitochondria with an intact membrane potential the dye forms J-aggregates and will emit red fluorescence when excited. Mean fluorescence intensity of the JC-1 aggregate and the JC-1 monomer were each quantified within the cellular region and the data was reported as a ratio of the average fluorescence intensity of the monomer relative to the aggregate.

2.9 ATP and ADP quantification

A549 cells were tested in 6-well tissue culture plates to ensure enough total protein was collected for testing. Cell culture medium was removed from treated and untreated cells and ice cold assay buffer from adenosine triphosphate (ATP, BioVision; Milpitas, CA) or adenosine diphosphate (ADP, Abcam; Cambridge, MA) kits was added to induce cell lysis per the manufacturer's suggested protocol. The plates were incubated for 15 to 20 min on a plate shaker at 4°C. The cells were scraped, and the lysate collected. Then the sample was stored at -80°C for future testing. To ensure total cell lysis, the sample was subjected to a freeze-thaw step, with the samples thawed on wet ice and then clarified through centrifugation (10,000 x g for 5 min at 4°C). The clarified lysate was collected and the protein concentration of each sample was determined using Bradford dye reagent (Bio-Rad; Hercules, CA). The protein concentration was determined relative to a linear regression analysis of a standard curve prepared in BSA.

For ATP, protein was removed with the addition of 4M perchloric acid precipitation, followed by neutralization with 2 M potassium hydroxide. ATP and ADP were then quantified in the test samples using the more sensitive fluorescence intensity option for both kits. The fluorescence intensity was quantified using the manufacturer suggested excitation and emission filters on the Envision Multi-label plate reader (Perkin Elmer; Waltham, MA). A linear regression analysis was performed on the standard curve to calculate the relative ATP and ADP concentrations in each sample. Each test sample fell within the linear range of the ATP or ADP standard curve and was corrected for protein concentration.

2.10 Glutathione determination

The cell culture media was removed from treated and untreated A549 cells and 5% sulfosalicylic acid (Sigma; St. Louis, MO) was added to the cells. The cells were then frozen at -80°C, and subjected to two-freeze/thaw cycles to induce cellular lysis. Cellular debris was spun down and the supernatant was quantified for glutathione content using the fluorescent assay from a commercially available kit (Arbor Assays; Atlanta, GA). The manufacturer suggested protocol was followed and the fluorescence intensity using the suggested excitation and emission filters was measured using the Envision Multi-label plate reader as described above. The assay measured total and reduced glutathione, where oxidized GSSG was calculated relative to these two parameters by subtracting free GSH from total glutathione and then dividing the quantity by two (dilution factor).

2.11 Western analysis

A549 cells were tested in 6-well tissue culture plates to ensure enough total protein was collected for testing. Cell culture medium was removed and the cells were lysed using ice cold buffer containing 50 mM Tris-HCl, 150 mM sodium chloride, 1% nonident P-40, 100 mM sodium fluoride, 50 mM β-glycerophosphate, 0.5 mM sodium vanadate, 1 mM phenylmetylsulfonyl fluoride, and EDTA-free cOmplete mini protease tablet (Sigma; St. Louis, MO). The plates were incubated for 15 to 20 min on a plate shaker at 4°C, the cells were scraped and the lysate collected. The lysate was clarified through centrifugation (10,000 x g for 5 min at 4°C), and the protein concentration of each sample was determined using Bradford dye reagent (Bio-Rad;

Hercules, CA). The protein concentration was determined relative to a linear regression analysis of a standard curve prepared in BSA.

Each sample was diluted with water and 4X loading buffer (Life Technologies; Carlsbad, CA) and 50 µg of protein was loaded in each well of a 4-12% Criterion XT Bis-Tris gel (Bio-Rad; Hercules, CA). The proteins were separated through electrophoresis and then transferred to a polyvinyl difluoride (PVDF) membrane. The membrane was rinsed with tris-buffered saline (TBS) and then incubated with block buffer (2% ECL Advance Blocking Agent, GE Healthcare Life Sciences; Marlborough, MA) for 1 hr at room temperature on a shaker. The block buffer was removed and replaced with rabbit-anti-human OGG1 (1 µg/mL, Cambridge Research Biologicals; Cleveland, UK) diluted in 0.5% block buffer and incubated overnight at 4°C. The membrane was quickly rinsed and then washed three times (TBS containing 0.1% Tween-20), followed by addition of diluted donkey anti-rabbit IgG-horse radish peroxidase (1:5000, GE Healthcare Life Sciences; Marlborough, MA). The antibody was incubated on the blot for 1 hr in the dark at room temperature on a shaker. The blot was then rinsed and washed as before with a final wash absent of Tween-20. Developer was added to the blot (ECL Prime, GE Healthcare Life Sciences; Marlborough, MA) and incubated for 1 min at room temperature and the enhanced chemiluminescence (ECL) was detected on autoradiography film.

To test for equal gel loading, the blot was stripped with commercially available stripping buffer (Thermo Scientific; Rockford, IL) for 30 min at 37°C, followed by an additional incubation for 30 min at room temperature. The blot was rinsed and washed (TBS plus 0.1% Tween-20) and anti-actin-horseradish peroxidase (1:10,000, Santa Cruz; Dallas, TX) was diluted in blocking buffer and incubated on the blot for 1 hr at room temperature on a shaker. The blot was rinsed and washed as described above with the final wash absent of Tween-20. The blot was then developed as described above.

2.12 Statistical Analysis

Data analysis was performed using GraphPad Prism version 6.04. Concentration response curves were analyzed for half maximal response (EC_{50}) using a non-linear, Sigmoid dose-response with a variable slope. The results were evaluated for significance using 1-way ANOVA with a Dunnett's post test comparing treatment groups to untreated control with significance determined as follows: * $p < 0.05$, ** $p < 0.01$, *** $p < 0.001$, **** $p < 0.0001$.

CHAPTER 3:

Development of a cell model of oxidant-induced mitochondrial DNA damage

3. Development of a cell model of oxidant-induced mitochondrial DNA damage

3.1 Introduction

To study the effects of mitochondrial DNA damage on cellular homeostasis, an *in vitro* system was established to enable the assessment of potential small molecule therapeutics. The cell model would enable a more thorough understanding on the significance that this type of DNA damage has on cell health and function. It was intended that this cell model would enable a better understanding of how mitochondrial DNA damage affects cellular function and to then develop treatment options that could successfully impact disease in a positive manner. To apply this hypothesis to respiratory disease, cigarette smoke was examined due to it being one of the most prevalent oxidants inducing DNA damage associated with respiratory disease (Deslee et al., 2009; Fischer et al., 2015).

Initially, primary lung cells were used in an attempt to establish this *in vitro* model of oxidative DNA damage. However, these cells can vary greatly in their response and they varied in facilitating a clear understanding of how mitochondrial DNA damage can affect cellular homeostasis. High content imaging was used, where detailed fluorescent images of cells are captured and analyzed; however, the data analysis from primary cells proved more difficult in part due to their non-uniform size and shape. Therefore, A549 cells, which are a transformed pulmonary epithelial Type II cell line, were used to develop and validate a cell model of oxidative DNA damage. A549 cells were initially tested for their response following cigarette smoke exposure. It will be shown that this stimulus induced an increase in ROS throughout the cell and within the mitochondria, which led to oxidative DNA damage within the mitochondria and the nucleus. This was disease relevant and enabled the data generated in the lab to be linked to clinical findings from patients who smoke. However, based on the hypothesis the stimulus needed to focus primarily on oxidative DNA damage within the mitochondria, meanwhile cigarette smoke affected the entire cell and had some variability concerns. For that reason, a different irritant was needed, which would due to its mechanism of action primarily impact the mitochondria of the cell. The literature had shown the herbicide paraquat, when exposed to cells in culture and to rats would preferentially move to the inner mitochondrial membrane space and utilize

the reducing equivalents from the electron transport chain to produce superoxide anions (Castello et al., 2007).

Once the cell culture conditions were optimal, it was confirmed paraquat induced ROS and was present both within the cell and more specifically within the mitochondria. It was observed following exposure to the herbicide, the cells did indeed have oxidative mitochondrial DNA damage, primarily as a result of increased ROS. This led to the elucidation of the negative impact increased ROS had on the mitochondrial membrane potential and membrane integrity.

The cell was found to respond to the rise in ROS through the up-regulation of MnSOD protein present within the cell to convert destructive superoxide radicals into hydrogen peroxide, which is ultimately converted to water by catalase. Moreover, the cells increased their expression or localization of OGG1 within the mitochondria to initiate DNA repair of the oxidized guanine residues. It was assumed the cellular repair mechanisms were activated, and this was confirmed by measuring changes in glutathione levels. Glutathione is a key antioxidant tasked with the removal of harmful reactive radicals capable of inducing macromolecule damage to the cell. Gluthathione-S-transferase is the enzyme responsible for catalyzing toxic compounds to glutathione to render them less harmful and for removal from the cell (Fletcher et al., 2015).

Finally, the mechanism of action for paraquat was confirmed in A549 cells devoid of mitochondrial DNA. Through chronic exposure to ethidium bromide, the mitochondrial DNA will become depleted and therefore the cell's electron transport chain is rendered non-functional. This lead to a decrease in reducing equivalents thereby barring paraquat from being reduced within the mitochondria, which blocked the production of superoxide anions upon oxidation in the presence of oxygen (Brar et al., 2012).

3.2 Results

3.2.1 Cigarette smoke exposure increases ROS and oxidative DNA damage

To develop a cell model of oxidative stress and to further understand the impact of cigarette smoke on ROS mediated mitochondrial DNA damage, A549 cells were exposed to the vapor phase of one cigarette as described in Chapter 2. ROS production was characterized using high-content imaging, despite the caveats known about fluorescence based ROS dyes (Winterbourn, 2014; Woolley et al., 2013). However, after testing several different dyes, the chloromethyl-version of the ROS detection dye DCF was selected based on its sensitivity and the necessary cell retention required for imaging. Cells exposed to the vapor phase from one cigarette for 5 min displayed a significant ($p < 0.01$) 1.5-fold increase in total ROS levels compared to room air control 2 hr post exposure (Fig. 3.1a). ROS levels continued to rise (8 hr) following the exposure, but reached a plateau and remained constant for up to 24 hr post exposure (Fig. 3.1a). Sample images from air (Fig. 3.1c) and cigarette smoke (Fig. 3.1d) exposed A549 cells depict increased DCF or green fluorescence post cigarette smoke exposure (24 hr). It can be observed there is a small, significant ($p < 0.0001$) change in the air exposure controls over time. This observation could be attributed to an elevation in ROS immediately following the air exposure. To test if the observed elevation in ROS following cigarette smoke exposure were predominately derived from the mitochondria, the mitochondria specific ROS dye, MitoSOX™ was utilized. Cells exposed to cigarette smoke were found to have about 125% increase in ROS levels compared to air controls 2 hr post exposure (Fig. 3.1b).

Oxidative DNA damage was found to be present within the mitochondria 24 hr following cigarette smoke exposure. To measure oxidative DNA damage, an immunofluorescence assay was optimized as discussed in Chapter 2 to quantify and localize the DNA lesion, 8-oxoguanine. The 8-oxoguanine assay detects the lesion throughout the cell and through the use of the image analysis software (Harmony v3.5.2, Perkin Elmer) the cell can be segmented. This enabled the quantification of the DNA lesion within both the nuclear and the mitochondrial DNA. As shown in Fig. 3.2a, 24 hr post cigarette smoke exposure trended toward an increase in mitochondrial DNA 8-oxoguanine. Cigarette smoke also affected nuclear DNA;

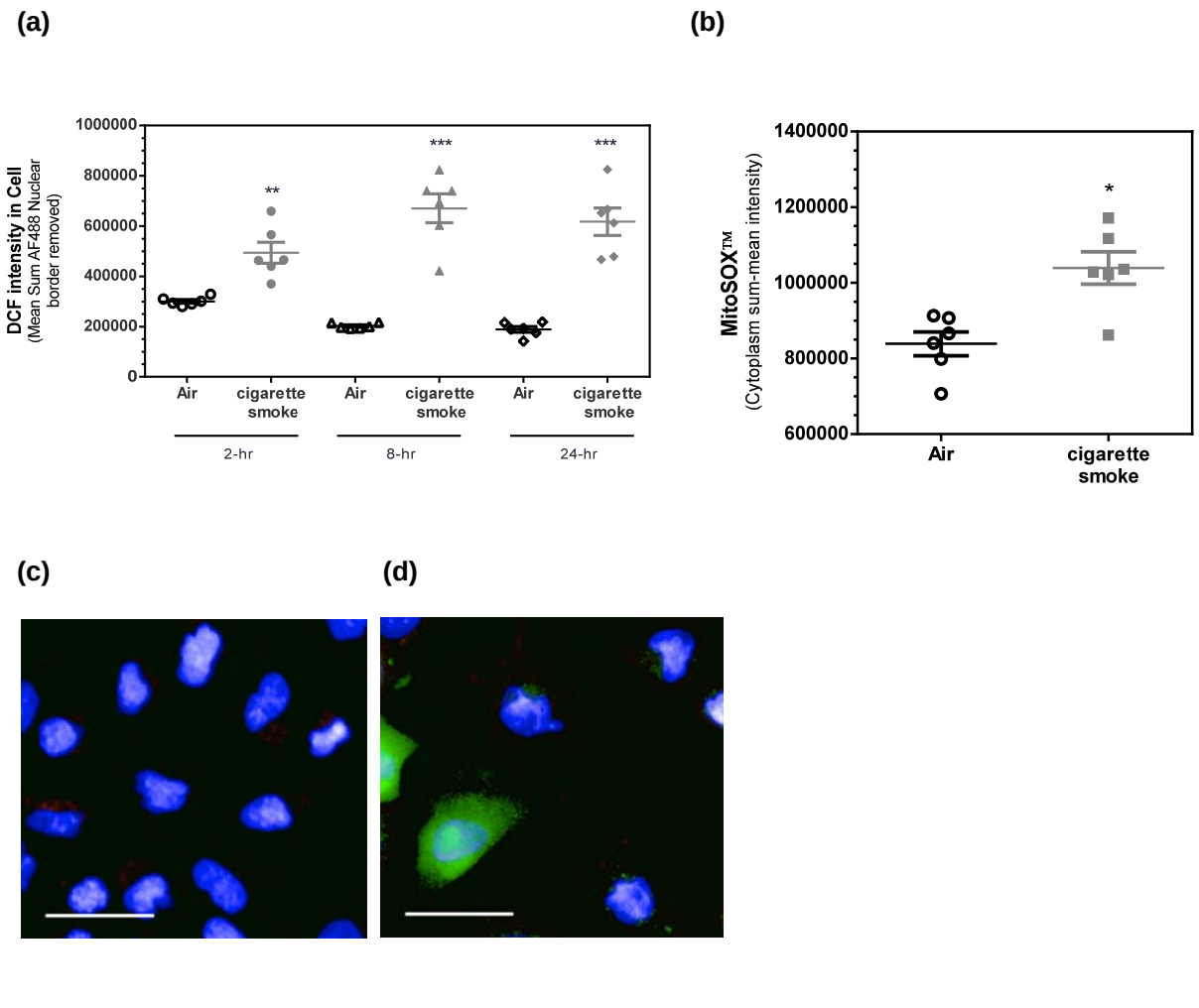

Figure 3.1 Effects of cigarette smoke exposure on ROS production over time in A549 cells.

Figure 3.1 Effects of cigarette smoke exposure on ROS production over time in A549 cells.

A549 cells were exposed to the vapor phase of 1 cigarette for 5 min. ROS was detected at varying time points using 5 μM CM-H2DCFDA (DCF) followed by identification of the plasma membrane (5 μg/mL CellMask™ deep red) and nuclei (5 μg/mL Hoechst 33342). Live cell imaging was performed with 20X magnification, 4 fields per well in triplicate. Fluorescence intensity of DCF within the cell was averaged based on the number of cells imaged. (a) Graphical representation of the changes in ROS detected at 2, 8, and 24 hr following 5 min cigarette smoke exposure. (b) Mitochondrial-specific ROS was detected by the changes in MitoSOX™ intensity 2 hr following 5 min cigarette smoke exposure. Sample images from air control (c) and cigarette smoke (d) exposed cells depicting changes in ROS 24 hr post exposure (Hoechst 33342, overlaid blue; CM-H2DCFDA, overlaid green; line = 40 μm). Data shown are from an independent experiment, with each condition tested in sextuplicate. Significance was determined using a paired, 2-tailed t-test (p<0.05, ** p<0.01, *** p<0.001). Significance for air controls (a) was determined using a 1-way ANOVA comparing the mean to the mean from each group (**** p <0.0001).*

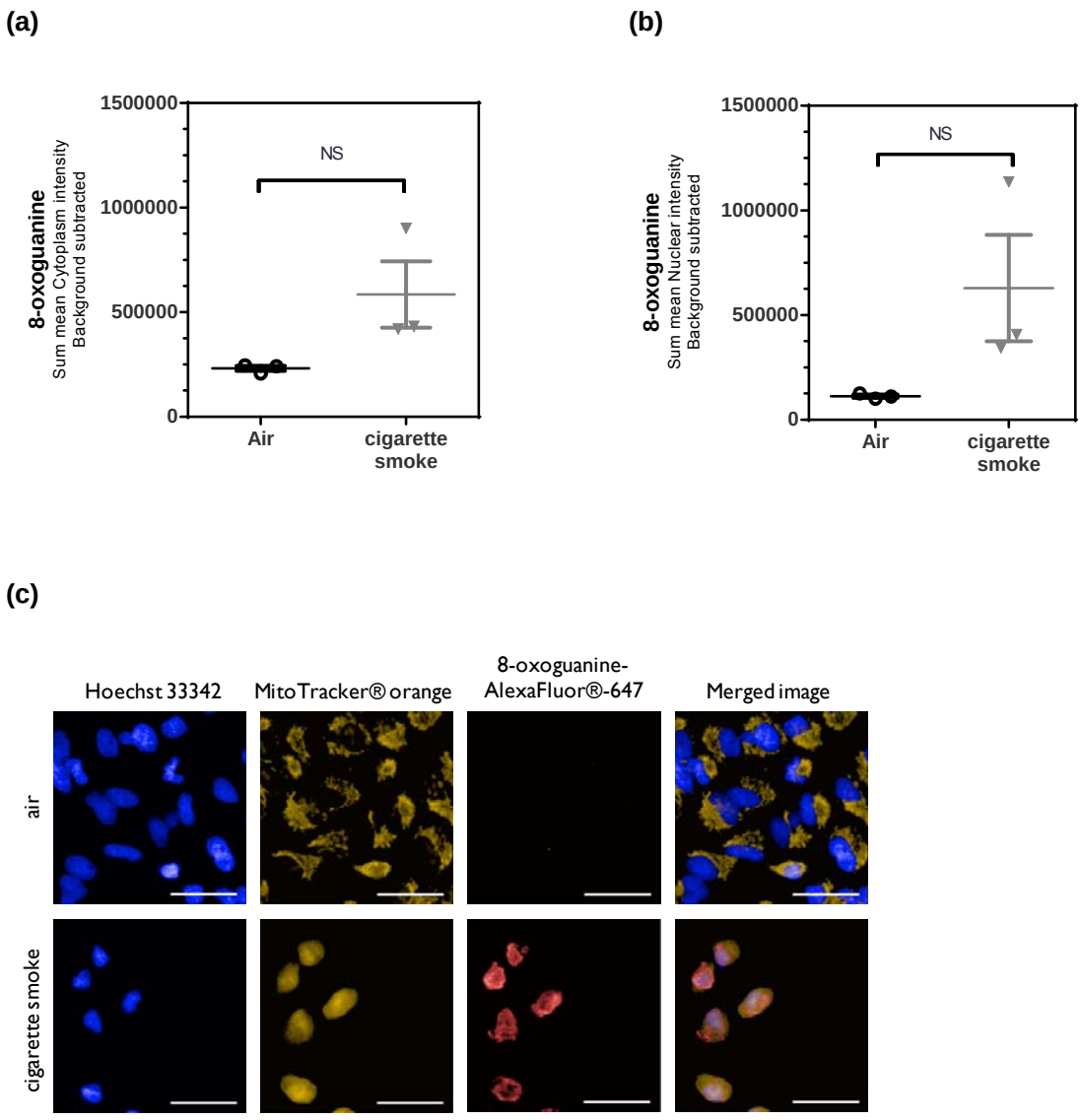

Figure 3.2 Effects of cigarette smoke exposure on oxidative DNA damage.

A549 cells were exposed to the vapor phase of 1 cigarette for 5 min. 8-oxoguanine was detected and images captured using methods in Chapter 2. The change in (a) cytoplasm and (b) nuclear fluorescence intensity was quantified 24 hr post cigarette smoke exposure (NS = non-significant). (c) Sample images from control and cigarette smoke exposed cells depicting changes in 8-oxoguanine intensity (Hoechst 33342, overlaid blue; MitoTracker® orange, overlaid orange; 8-oxoguanine, overlaid red; line = 40 μm) are shown. Data shown are from an independent experiment, with each condition tested in triplicate. Significance was determined using a paired, 2-tailed t-test ($p<0.05$, ** $p<0.01$, *** $p<0.001$).*

Fig. 3.2b shows the increased 8-oxoguanine detected within this cellular compartment. While the data reflects a three to four fold change following cigarette smoke exposure, the data did not reach statistical significance in part due to the variability observed across the triplicate test wells. Sample images are shown from both air and cigarette smoke exposed cells in Fig. 3.2c, and from these images it can be observed that there is increased 8-oxoguanine or red fluorescence both within the cytoplasm/ mitochondrial region and in the nuclear region of the cells following exposure to cigarette smoke.

3.2.2 Effect of paraquat on total and mitochondrial ROS

It has been shown previously that the herbicide paraquat stimulates ROS production via interaction with electron flow within the mitochondrial electron transport chain (Castello et al., 2007). The time- and concentration-dependence of the paraquat-induced ROS production were evident (Fig. 3.3a (24 hr) and b (48 hr)). At an early time point, i.e. 4 hr of paraquat exposure, there was negligible measureable increased ROS detected (data not shown). Cells treated with paraquat for 24 hr, however, displayed a concentration-dependent rise in ROS levels (Fig. 3.3a). As compared to untreated cells, significant accumulation of ROS began with a paraquat concentration of 1 mM ($p < 0.001$). The EC_{50} value for paraquat was 1.6 mM (calculated using a non-linear regression analysis with a variable slope and a sigmoid-dose response) and the maximal response nearly reached a 30-fold (3 mM) increase over baseline. Sample images of these data are shown in Fig. 3.3c, and depict a rise in green fluorescence intensity corresponding to enhanced ROS production with increments of paraquat up to about 10 mM. At this top concentration, the total cellular DCF intensity (Fig. 3.3a) decreased relative to the levels obtained with 3 mM. This effect could be attributed to paraquat-mediated cell death and this loss in cell number was measured by counting the number of nuclei within the imaged field of view (data not shown). By 48 hr as compared to 24 hr, ROS production began to shift as evidenced by the change in the EC_{50} value to 0.34 mM and the shift in the concentration response curve to the left. Paraquat concentrations of 0.3 and 0.6 mM resulted in an 11 and 30-fold increase, respectively

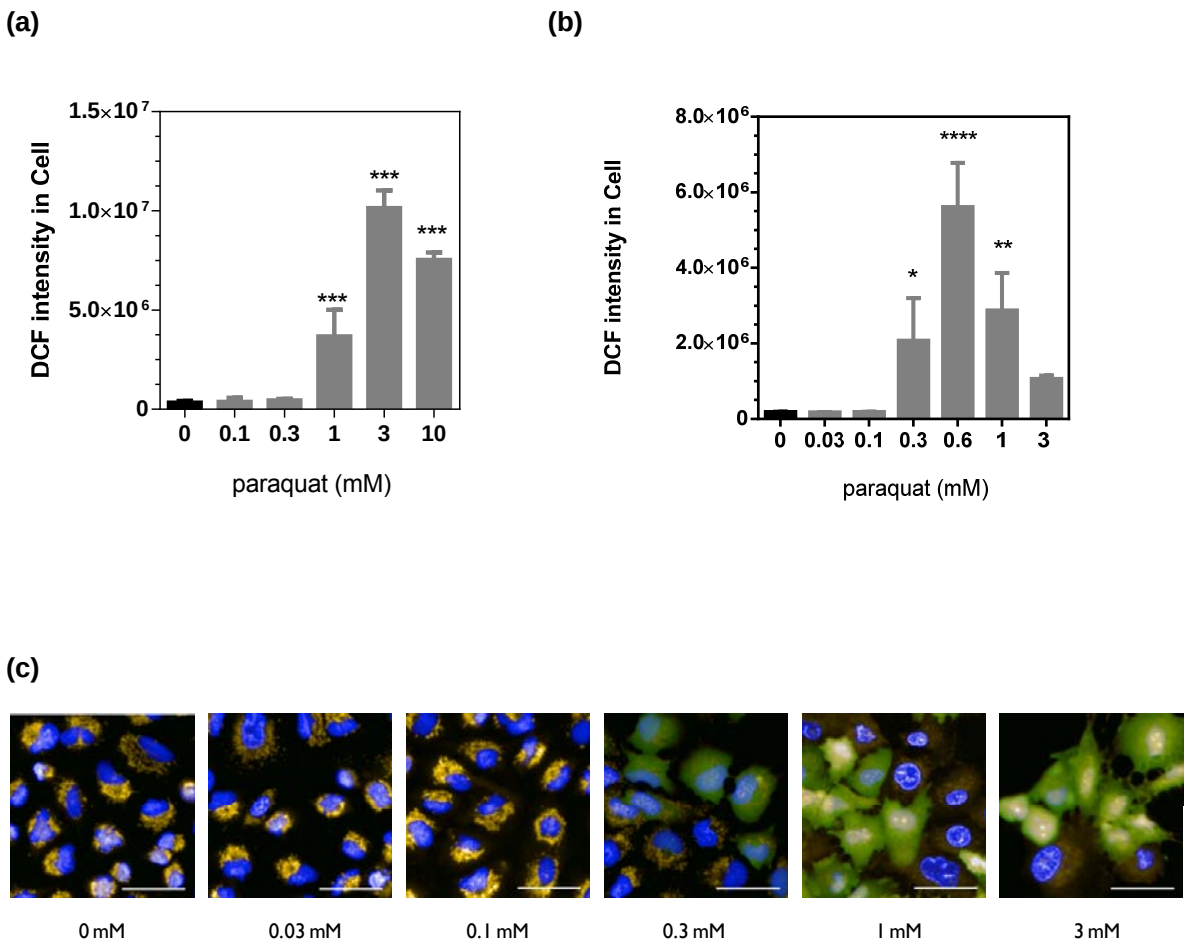

Figure 3.3 Effects of paraquat exposure on ROS production in A549 cells.

A549 cells were treated using various concentrations of paraquat for 24 hr. ROS was detected using 5 µM CM-H2DCFDA (DCF) followed by identification of mitochondria (250 nM MitoTracker® orange CMTMRos; overlaid orange) and nuclei (5 µg/mL Hoechst 33342; overlaid blue). Live cell imaging was performed with 20X magnification, 4 fields per well in triplicate. Fluorescence intensity of DCF within the cell was averaged based on the number of cells imaged. ROS levels are graphically illustrated following (a) 24 and (b) 48 hr paraquat exposure. Significance was determined using a 1-way ANOVA with a Dunnett's post test comparing treatment groups to untreated control (p<0.05, ** p<0.01, *** p<0.001). (c) Sample representative images from A549 cells exposed to increasing concentrations of paraquat (24 hr) depicting ROS (overlaid green) levels (line = 40 µm). Data shown are from a representative experiment.*

at this time (Fig. 3.3b). This was in contrast to the undetectable levels of ROS production from these paraquat test concentrations following 24 hr exposure.

Using the mitochondria specific ROS sensor MitoSOX™, it was observed under basal conditions in the absence of paraquat, A549 cells had little or no measureable mitochondrial ROS production (Fig. 3.4a). Consistent with the findings described above for total cellular ROS, paraquat exposure resulted in no detectable mitochondrial ROS after 4 hr of exposure. However, paraquat (0.03-3 mM) exposure for 24 hr provoked a concentration-dependent rise of mitochondrial ROS in A549 cells. A maximal intensification of 1.75-fold was obtained at the highest concentration (3 mM), with an EC_{50} value of 0.277 mM (Fig 3.4b). This value represents a log shift in potency compared to the EC_{50} value calculated for total ROS using DCF as the sensor. This shift in potency could be attributed to the more specific chemistry of the MitoSOX™ dye versus the DCF dye as discussed in a recent review of fluorescent ROS probes (Winterbourn, 2014).

3.2.3 Time and concentration-dependent effect of paraquat on mitochondrial oxidative DNA damage

Mitochondrial DNA (mtDNA) is encapsulated within the nucleoids that are physically tethered to the inner mitochondrial membrane (Scheibye-Knudsen et al., 2015). Given the close proximity of the mtDNA to the electron transport chain, oxidative DNA damage was likely in response to paraquat due to its interaction at Complex I and the production of superoxide radicals. Addition of paraquat to A549 cells for 24 hr resulted in elevated red fluorescence intensity (using AlexaFluor®-647) within the cytoplasm denoting an accumulation of the oxidized DNA lesion. Following paraquat treatment (24 hr), there was a concentration-dependent rise in 8-oxoguanine content (Fig. 3.5b) coinciding with the MitoTracker® stain. At 24 hr, this intensity was shown to co-localize to the

(a)

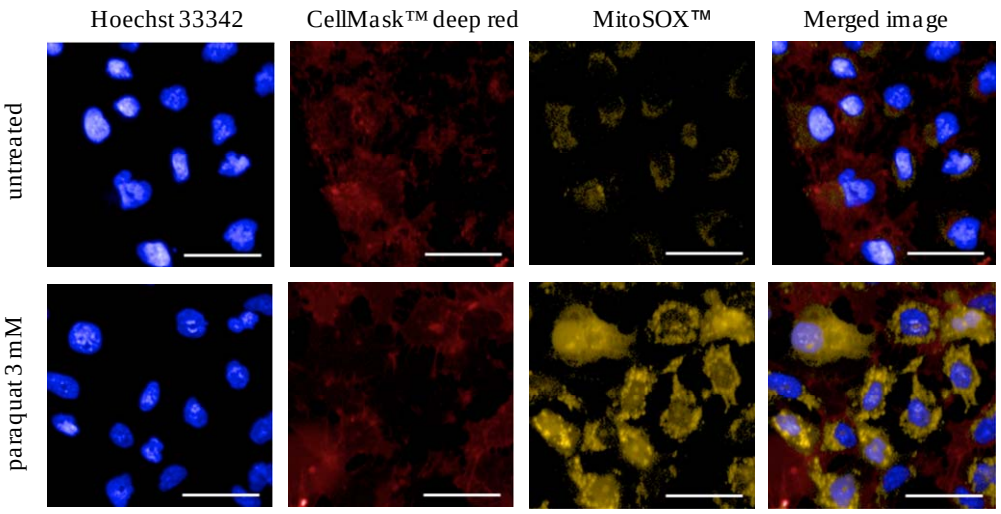

(b)

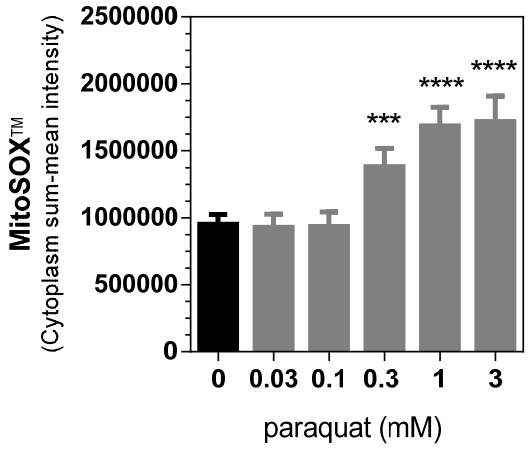

Figure 3.4 Effects of paraquat exposure on mitochondrial-specific ROS production in A549 cells.

Figure 3.4 Effects of paraquat exposure on mitochondrial-specific ROS production in A549 cells.

A549 cells were treated and imaged similarly to that described in Fig. 3.1. Mitochondrial-specific ROS was detected using 5 µM MitoSOX™ (overlaid orange). Stains for the nucleus (5 µg/mL Hoechst 33342; overlaid blue) and the plasma membrane (5 µg/mL CellMask™ deep red; overlaid red) were added prior to live cell imaging. Fluorescence intensity of MitoSOX™ within the cytoplasm region was averaged based on the number of cells imaged. (a) Sample images from control and paraquat (3 mM) treated cells (after 24 hr) depict mitochondrial-ROS. (b) Graphical representation of cells exposed to increasing concentrations of paraquat. Significance was determined using a 1-way ANOVA with a Dunnett's post test comparing treatment groups to an untreated control ($p<0.05$, ** $p<0.01$, *** $p<0.001$, **** $p<0.0001$). Data shown are from an independent experiment, with each condition tested in triplicate.*

(a)

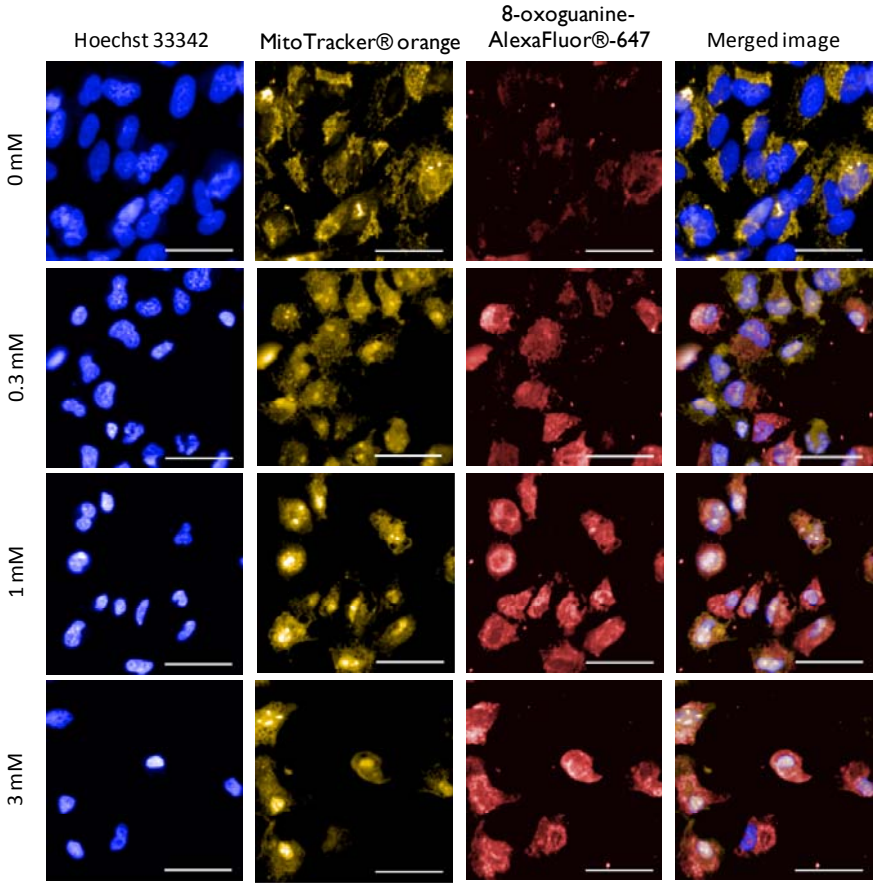

(b)

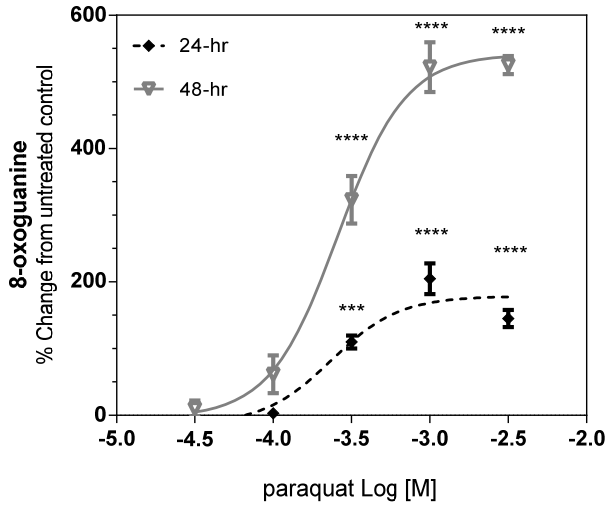

Figure 3.5 Effects of 24 and 48 hr paraquat exposure on mitochondrial oxidative DNA damage content in A549 cells.

Figure 3.5 Effects of 24 and 48 hr paraquat exposure on mitochondrial oxidative DNA damage content in A549 cells.

A549 cells were treated with paraquat for 24 or 48 hr and subjected to formaldehyde fixation prior to immunofluorescence detection of 8-oxoguanine as described in Chapter 2. (a) Changes in 8-oxoguanine are depicted in sample representative images (Hoechst 33342, overlaid blue; MitoTracker® orange, overlaid orange; 8-oxoguanine, overlaid red) from cells exposed to increasing concentrations of paraquat (48 hr, line = 40 μm). (b) The percent change in 8-oxoguanine intensity within the cytoplasm region following 24 and 48 hr treated cells with various concentrations of paraquat (Log M). Significance was determined using a 1-way ANOVA with a Dunnett's post test comparing treatment groups to an untreated control ($p<0.05$, ** $p<0.01$, *** $p<0.001$, **** $p<0.0001$). Data shown are from a representative experiment.*

mitochondria that were stained with MitoTracker® dye and visualized using laser confocal high-powered magnification (Appendix S3). A549 cells treated for 48 hr experienced a further accumulation of 8-oxoguanine; with over a 500% increase at 3 mM compared to control cells (Fig. 3.5b). As reflected in the sample images in Fig. 3.5a, after 48 hr of paraquat exposure, 8-oxoguanine does not solely reside within the mitochondria. However, the most concentrated fluorescent intensity of the 8-oxoguanine lesion remained within the mitochondria; despite the DNA adduct appearance within the nuclear compartment. Interestingly, the magnitude of the 8-oxoguanine intensity within the cytoplasm was boosted with time, but the EC_{50} value; i.e. 0.25 mM (calculated using a non-linear regression analysis with a variable slope and a sigmoid dose-response, bottom constrained at 0), remained constant from 24 to 48 hr.

3.2.4 Effects of paraquat on inducing dsDNA breaks

Over time, ROS generated within the mitochondria will begin to leak and induce damage to other regions of the cell including the nucleus. ROS can damage the sugar backbone of DNA leaving behind single and double strand DNA (dsDNA) breaks (Bacsi et al., 2015). Once a dsDNA break occurs, histone2-AX is rapidly phosphorylated at serine 139 signaling for the recruitment to the site of the break proteins involved in the repair of the DNA backbone. pH2AX due to its rapid recruitment and good correlation to the level of dsDNA breaks has largely become widely used as a sensitive marker of this type of DNA damage (Sharma et al., 2012). A549 cells when exposed to paraquat exposure for less than 24 hr, displayed little or no elevated levels of pH2AX (data not shown). This data suggests the ROS have not leaked out of the mitochondria in sufficient quantity to induce detectable oxidative dsDNA breaks in the nucleus. By 48 hr of paraquat exposure, there was a significant ($p < 0.001$) 2-fold rise in pH2AX detected at the highest concentration (3 mM), and was concentration-dependent (Fig. 3.6a). Elevated pH2AX was significant observed at 1 mM ($p<0.001$) and 0.1 mM ($p<0.01$) paraquat; however, 0.3 mM paraqaut had no significant impact on pH2AX levels. Sample representative images from these cells clearly depict an increase in pH2AX-DyLight™-550 (orange fluorescence) intensity within the nucleus of the cells exposed to 3 mM paraquat for 48 hr (Fig. 3.6c) compared to untreated control (Fig. 3.6b). These data suggest the ROS

(a)

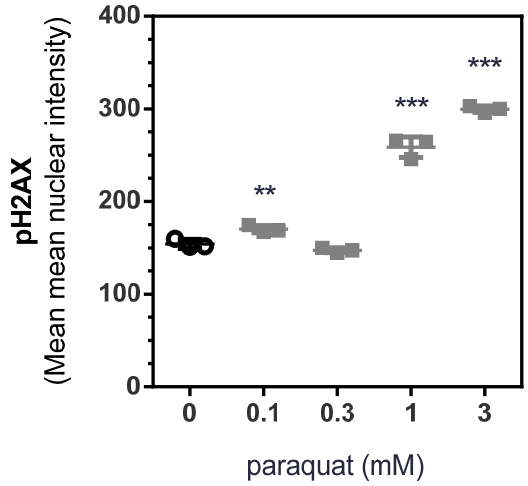

(b) **(c)**

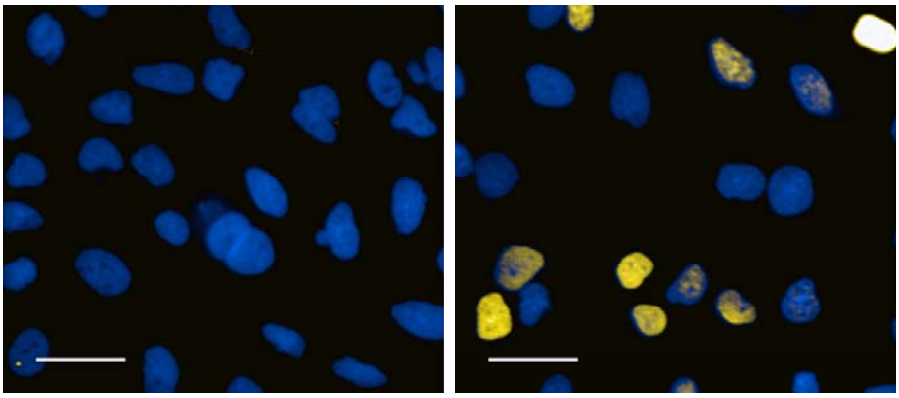

Figure 3.6 Effects of 48 hr paraquat exposure on induction of dsDNA breaks in A549 cells.

A549 cells were exposed to paraquat for 48 hr and subjected to formaldehyde fixation as part of immunofluorescence detection of pH2AX as described in Chapter 2. (a) The mean nuclear intensity of pH2AX from cells exposed to increasing concentrations of paraquat (mM). Significance was determined using a 1-way ANOVA with a Dunnett's post test comparing treatment groups to untreated control (p<0.05, ** p<0.01, *** p<0.001, **** p<0.0001). pH2AX is depicted in sample images (Hoechst 33342, overlaid blue; anti-pH2AX- DyLight™-550, overlaid yellow) from untreated (b) and 3 mM paraquat exposed cells (c, line = 40 µm). Data shown are from an independent experiment, with each condition tested in triplicate.*

have begun to leak from the mitochondria perhaps due to a compromised mitochondrial membrane, and exerting their influence throughout the cell.

3.2.5 Effects of paraquat on mitochondrial membrane potential and membrane integrity

Interruption of normal electron flow within the electron transport chain by paraquat was expected to result in a loss of mitochondrial membrane potential (Li et al., 2015). To validate this notion within the current *in vitro* model, the cationic, ratiometric dye JC-1 was used to determine the effect paraquat has on membrane potential. Mitochondria with an unaltered membrane potential exhibit an increase in the aggregate form of the dye versus the monomer form of the dye, which increases in intensity when the membrane potential is diminished. At less than 24 hr, little change in JC-1 fluorescence was noted (data not shown). Conversely, following the addition of paraquat (24 hr) there was almost a 100% loss of the mitochondrial membrane potential in response to varying concentrations of paraquat (Fig. 3.7a). Following 48 hr of exposure, the paraquat concentration-response curve was leftward shifted and was reflected in the respective EC_{50} values (Fig. 3.7a) from 237 μM (24 hr) to 130 μM (48 hr, calculated using a non-linear regression analysis with a variable slope and a sigmoid dose-response, top constrained at 0). There was a rise in green fluorescence intensity due to accrual of the monomer form of the dye from cells with increasing concentrations of paraquat at 48 hr (Fig. 3.7b). Paraquat exhibited a maximal effect of 100% loss of mitochondrial membrane potential across multiple concentrations compared to control cells at 48 hr, which was not observed at 24 hr.

The loss of mitochondrial membrane potential, could lead to decreased integrity of the mitochondrial membrane. To test this hypothesis, MitoTracker® orange CMTMRos was used because when added to live cells, the dye will accumulate inside energetically active mitochondria with an intact membrane. The staining pattern within the cells was stratified and quantified based on its appearance within the cells, with healthy, active mitochondria taking on a punctate appearance (Fig. 3.8a). The fluorescence pattern from paraquat treated cells appear diffuse and “leaky” (Fig. 3.8b), clearly different from the punctate appearance observed in untreated cells. A549 cells treated with increasing concentrations of paraquat show

(a)

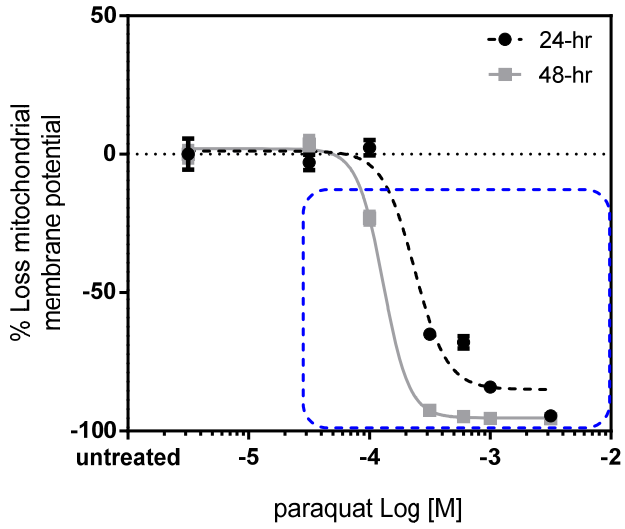

(b)

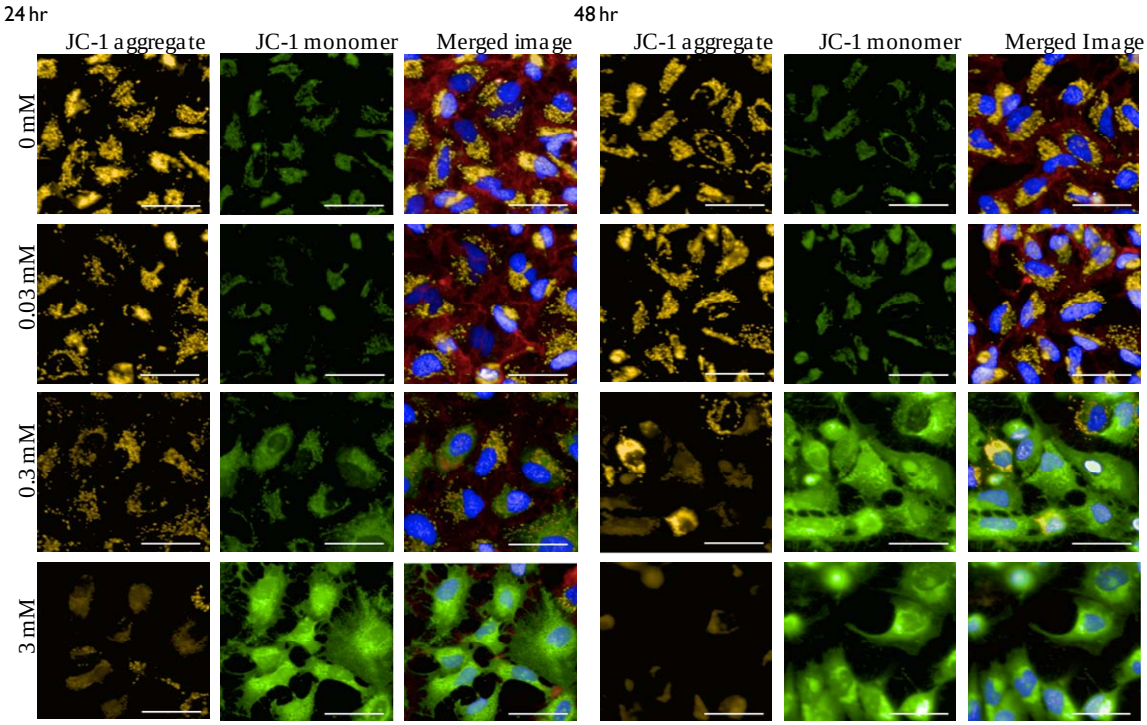

Figure 3.7 Effects of 24 and 48 hr paraquat exposure on mitochondrial membrane potential in A549 cells.

Figure 3.7 Effects of 24 and 48 hr paraquat exposure on mitochondrial membrane potential in A549 cells.

*A549 cells were treated with varying concentrations of paraquat for 24 or 48 hr. Mitochondrial membrane potential was detected using 2 µg/mL JC-1 and the transition from aggregate to monomer form was monitored by live cell imaging as described Chapter 2. Fluorescence intensity of the monomer (overlaid green) and the aggregate (overlaid orange) forms of JC-1 within the cell were averaged based on the number of cells imaged. A ratio was calculated from the average aggregate intensity/ average monomer intensity and a percent change from untreated cells was calculated. (a) The percent change of the JC-1 ratio with increasing concentrations of paraquat (Log M) at 24 and 48 hr. (b) Sample images (Hoechst 33342, overlaid blue; CellMask™ deep red, overlaid red) from cells exposed to increasing concentrations of paraquat at 24 hr and 48 hr post exposure (line = 40 µm). Significance was determined using a 1-way ANOVA with a Dunnett's post test comparing treatment groups to the untreated control, and all test concentrations within the blue dotted line were significant (**** $p<0.0001$). Data shown are from a representative experiment.*

(a) (b)

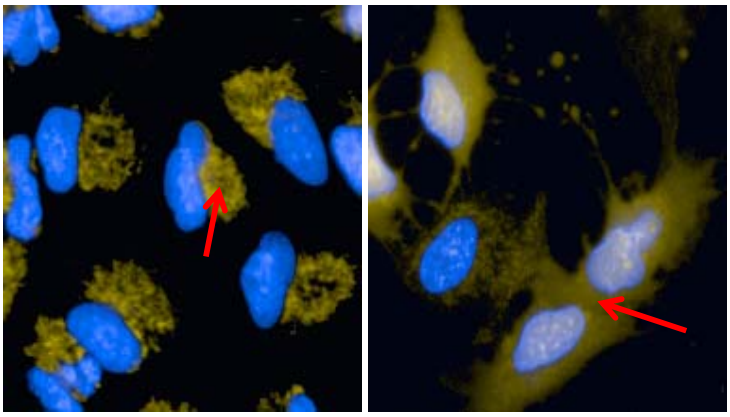

(c)

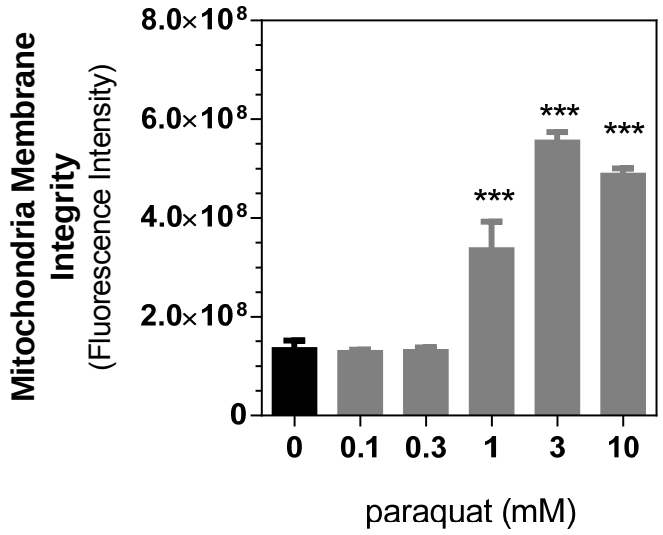

Figure 3.8 Effects of 24 hr paraquat exposure on mitochondria membrane integrity on A549 cells.

Figure 3.8 Effects of 24 hr paraquat exposure on mitochondria membrane integrity on A549 cells.

A549 cells were treated, stained, and imaged as previously described in Fig. 3.3. Fluorescence intensity pattern of the MitoTracker® orange dye (overlaid, orange) within the cell was assessed using PhenoLOGIC (machine learning-enabled software), where a punctate appearance was classified as functional and a diffuse appearance was classified as dysfunctional. Sample representative images from untreated (a) and 3 mM paraquat (b) treated cells with arrows indicating the functional pattern in the untreated image and the dysfunctional pattern in the paraquat image. (c) The average fluorescence intensity of the dysfunctional phenotype following 24 hr paraquat (mM) exposure. Significance was determined using a 1-way ANOVA with a Dunnett's post test comparing treatment groups to untreated control ($p<0.05$, ** $p<0.01$, *** $p<0.001$). Data shown are from a representative experiment.*

evidence of this leaky phenotype as detected by the surge at 24 hr in this phenotype's cellular fluorescence intensity by 400% at 3 mM compared to untreated cells (Fig. 3.8c). TheEC_{50} value of this effect was calculated to be 0.93 mM (calculated using a non-linear regression analysis with a variable slope and a sigmoid dose-response).

3.2.6 Effects of paraquat on cytochrome *c* translocation

It was observed that paraquat decreased A549 cell number with time compared to untreated controls. With a decrease in the mitochondrial membrane integrity, the cell's ability to produce energy for cell survival would also be affected (discussed in Chapter 5); thereby the likelihood the cell will undergo apoptosis would also be increased. The release of cytochrome *c* from the mitochondria is the initial step of the intrinsic apoptosis pathway, preceding caspase activation. Measured by immunofluorescence, cytochrome *c* translocation from the mitochondria to the nucleus can be monitored and quantified. The translocation of the protein was elevated in A549 cells exposed to increasing concentrations of paraquat. Cytochrome *c* translocation following paraquat exposure (48 hr) exhibited almost a 4-fold increase in translocation at the highest concentration (3 mM, Fig. 3.9a). Sample images (Fig. 3.9b) depict a nucleus devoid of yellow staining (cytochrome *c*) from untreated cells. With paraquat exposure the nuclear region has progressively elevated levels of yellow fluorescence suggesting an association between paraquat concentration and cytochrome *c* translocation.

3.2.7 Effects of paraquat on DNA repair and the anti-oxidant response

Thus far, it has been shown that paraquat increased oxidative DNA damage, specifically the 8-oxoguanine lesion when added to A549 cells (Fig. 3.5). To evaluate the cellular response to elevated oxidative DNA damage, an antibody was created to detect OGG1 for use in an immunofluorescence assay. As described above, OGG1 is the primary glycosylase responsible for the detection of 8-oxogaunine as part of the base excision repair pathway. While there are some commercially available antibodies for OGG1 (Novus Biologicals; Littleton, CO), several were tested and validated but over time began

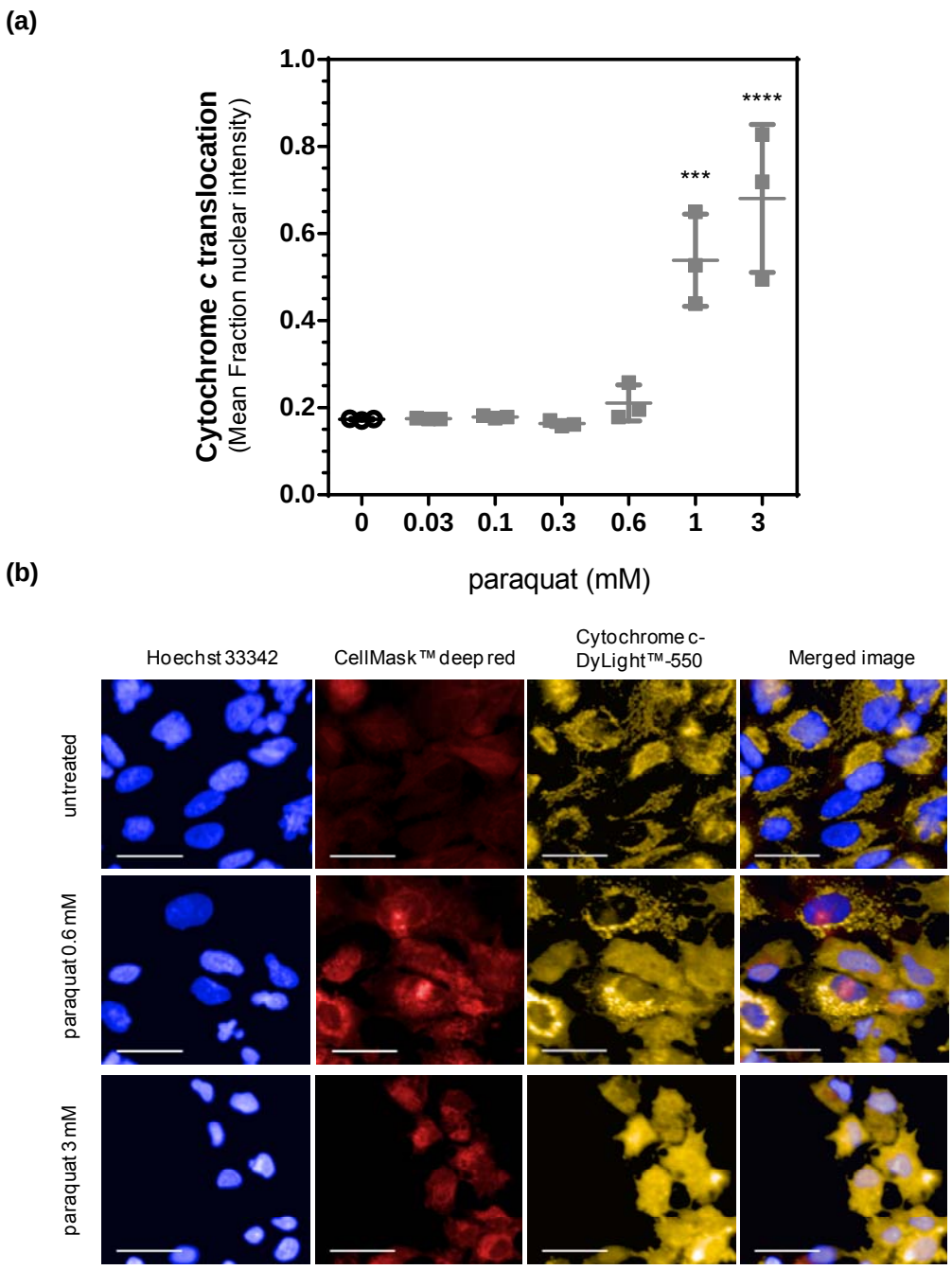

Figure 3.9 Effects of paraquat exposure on intrinsic apoptosis initiation: cytochrome c translocation.

Figure 3.9 Effects of paraquat exposure on intrinsic apoptosis initiation: cytochrome c translocation.

*A549 cells were exposed to paraquat for 48 hr and subjected to formaldehyde fixation as part of immunofluorescence detection of cytochrome c as described in Chapter 2. (a) Graphical representation of the mean fraction nuclear intensity of cytochrome c from cells exposed to increasing concentrations of paraquat (48 hr). Significance was determined using a 1-way ANOVA with a Dunnett's post test comparing treatment groups to untreated control (*** p<0.001, **** p<0.0001). (b) Translocation of cytochrome c is depicted in sample representative images (Hoechst 33342, overlaid blue; anti-cytochrome c-DyLight™-550, overlaid yellow; CellMask™ deep red, overlaid red) from control and paraquat exposed cells (line = 40 μm). Data shown are from a representative experiment.*

to display reduced specificity and inconsistent background staining. To permit superior detection of OGG1, four polyclonal antibodies were created by a contracted supplier and were tested by western blot analysis for the detection of OGG1. Clone 5981 (Appendix S2) demonstrated refined specificity over the other three antibodies tested in detection of the appropriate sized band by western blot analysis with limited background staining. Using this clone, A549 cells were exposed to increasing concentrations of paraquat and the cells were stained for OGG1 content changes in the mitochondrial space. As shown in Fig. 3.10a, paraquat exposure (24 hr) boosted OGG1 content in the mitochondria in a concentration-dependent manner with an EC_{50} value of about 300 μM. There was relatively no enhanced buildup of OGG1 protein levels detected between 24 and 48 hr paraquat exposure (Fig. 3.10b). The half maximal response was about 400 μM for paraquat-induced OGG1 in A549 cells (48 hr, calculated using a non-linear regression analysis with a variable slope and a sigmoid dose-response). Upon examination of the sample images from 3 mM paraquat exposed cells (Fig. 3.10c), it was observed there was a rise in green fluorescence (OGG1) in the mitochondrial space of the cells following 24 hr paraquat exposure relative to untreated cells.

Cells work to remove excess ROS and specifically superoxide anion by enzymatic conversion within the mitochondria by MnSOD (also referred to as SOD2) to form hydrogen peroxide. The resulting hydrogen peroxide is then converted to oxygen and water by a second enzyme catalase (Fig. 3.11a). To monitor the cellular detoxification in response to paraquat-induced superoxide anion production, high content image analysis demonstrated with increasing concentrations of paraquat (24 hr), MnSOD expression levels rose by 2-fold (Fig. 3.11b). It can be observed from the sample images there was elevated yellow fluorescence (MnSOD) from A549 cells exposed to paraquat (3 mM) relative to untreated control cells (Fig. 3.11c).

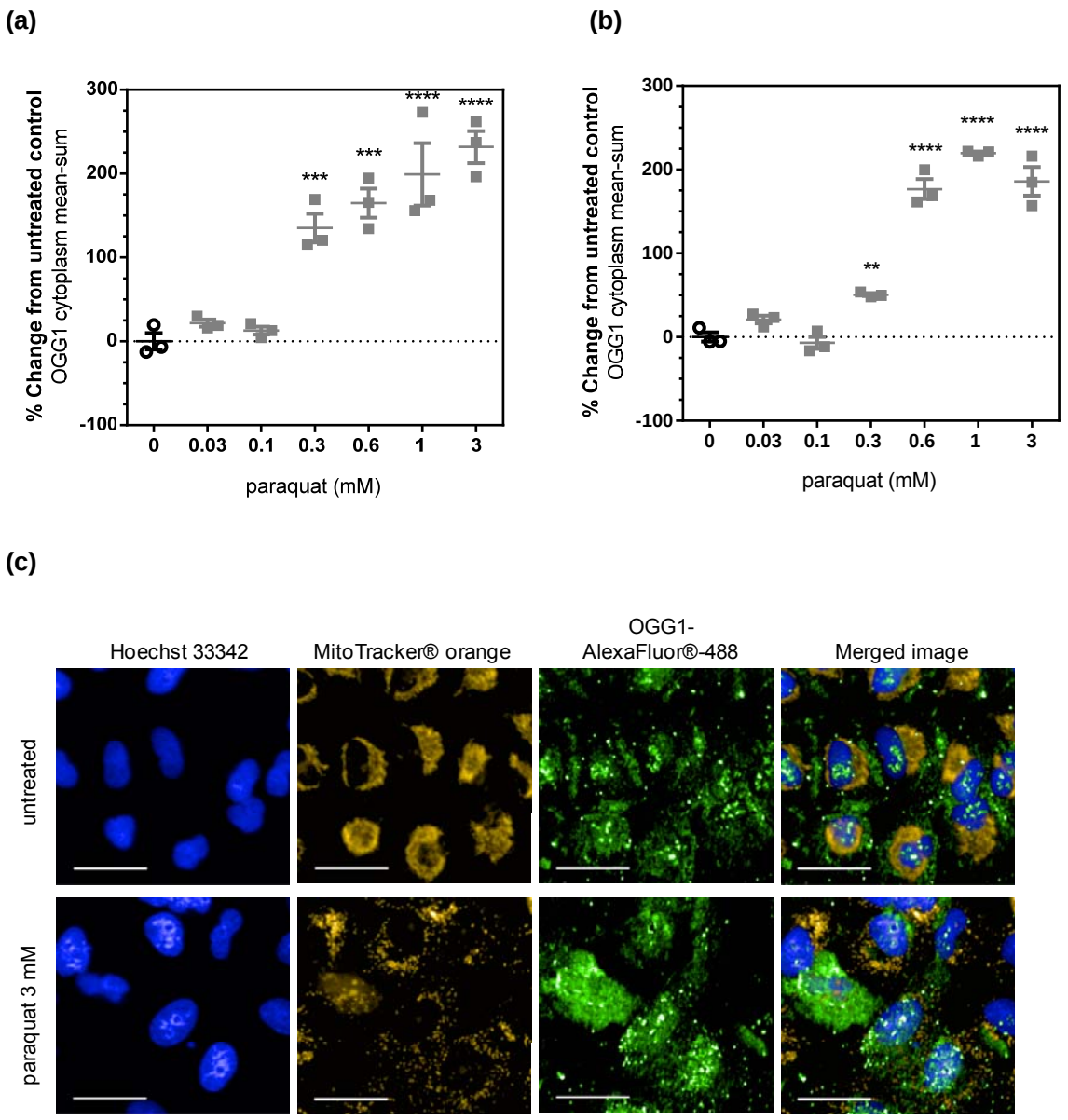

Figure 3.10 Effects of 24 and 48 hr paraquat exposure on mitochondrial OGG1 content in A549 cells.

Figure 3.10 Effects of 24 and 48 hr paraquat exposure on mitochondrial OGG1 content in A549 cells.

*A549 cells were exposed to paraquat for 24 or 48 hr and subjected to formaldehyde fixation prior to immunofluorescence detection of OGG1 using methods described in Chapter 2. Graphical representations of the percent change in OGG1 intensity within the cytoplasm region following 24 (a) or 48 hr (b) exposure of cells to increasing concentrations of paraquat (mM). Significance was determined using a 1-way ANOVA with a Dunnett's post test comparing treatment groups to untreated control (** p<0.01, *** p<0.001, **** p<0.0001). (c) Changes in OGG1 staining are depicted in samplerepresentative images (Hoechst 33342, overlaid blue; MitoTracker® orange, overlaid orange; anti-OGG1-AlexaFluor®-488, overlaid green) from control and paraquat treated cells (line = 40 μm). Data shown are from a representative experiment.*

(a)

$$2O_2^- + 2H^+ \xrightarrow[Superoxide\ \ dismutase\ \ (SOD)]{} O_2 + H_2O_2$$

$$2H_2O_2 \xrightarrow[Catalase]{} O_2 + 2H_2O$$

(b)

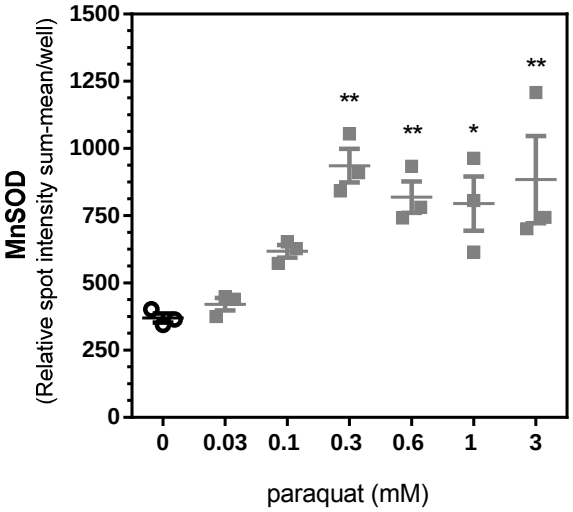

(c)

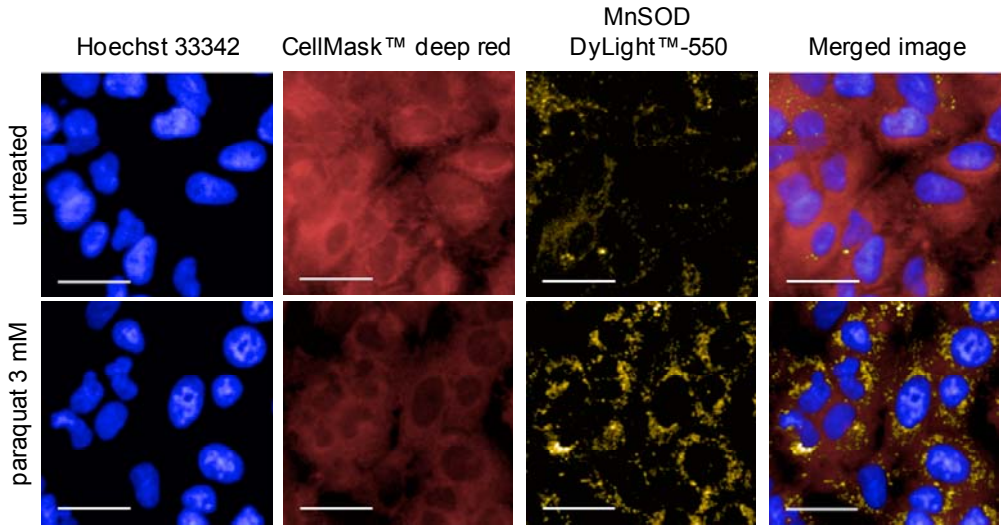

Figure 3.11 Effects of 24 hr paraquat exposure on MnSOD content in the mitochondria.

Figure 3.11 Effects of 24 hr paraquat exposure on MnSOD content in the mitochondria.

A549 cells were exposed to paraquat for 24 prior to immunofluorescence detection of MnSOD as described in Chapter 2. (a) The cellular response to superoxide anion is depicted along with a (b) graphical representation of the change in relative spot intensity of MnSOD within the cytoplasm region of the cells following exposure to increasing concentrations of paraquat (mM). Significance was determined using a 1-way ANOVA with a Dunnett's post test comparing treatment groups to untreated control ($p<0.05$, ** $p<0.01$). (c) Sample representative images (Hoechst 33342, overlaid blue; anti-MnSOD-DyLight™-550, overlaid yellow; CellMask™ deep red, overlaid red) from control and paraquat treated cells depict the change in MnSOD expression at 24 hr (line = 40 μm). Data shown are from a representative experiment.*

Conferring additional detoxification against ROS mediated damage; antioxidants such as glutathione, a non-protein thiol, are utilized by the cell to prevent oxidative damage to macromolecules (Fletcher et al., 2015). Glutathione serves as an electron donor in the presence of free radicals and is oxidized to glutathione disulfide (GSSG). Once oxidized, it is then reduced back to glutathione by glutathione reductase using NADPH as the electron donor. It is depicted in Fig. 3.12a that total glutathione levels decreased by 50% (3 mM) in A549 cells exposed to increasing concentrations of paraquat (24 hr). By 48 hr of exposure to paraquat (Fig. 3.12b), there was an 80% decline in total glutathione levels at the top test concentration (3 mM). These data indicate glutathione levels continue to decrease with time as a result of elevated ROS production from paraquat within the mitochondria of the cell. While the cell culture medium was supplemented with GlutaMAX to serve as an amino acid supplement and improves cell viability, there was no effect on the paraquat-induced changes in glutathione concentration by its presence in the culture medium (data not shown).

3.2.8 Effects of mtDNA deletion on paraquat-induced oxidative DNA damage

As described earlier, the mitochondrial genome encodes for 37 proteins, 13 of which are integral to subunits for the electron transport chain (Scheibye-Knudsen et al., 2015). It has been characterized that the mechanism of action for ROS generation by paraquat is through the siphoning of electrons from the electron transport chain (Dinis-Oliveira et al., 2006). To demonstrate this activity in the current cell model, the electron transport chain could be rendered dysfunctional through the deletion of the mitochondrial genome and thereby halting paraquat-induced superoxide anion production. The mitochondrial DNA from A549 cells were deleted with chronic ethidium bromide exposure, generating A549*rho*$^{\varphi}$ cells (Brar et al., 2012). Age matched A549 cells when exposed to increasing concentrations of paraquat produced a level of 8-oxoguanine similar to the data presented in Fig. 3.5, however, A549*rho*$^{\varphi}$ did not exhibit such as response. Sample images of untreated A549 (Fig. 3.13a) and A549*rho*$^{\varphi}$ (Fig. 3.13b) were compared to cells exposed to 3 mM paraquat for 24 hr (A549, Fig. 3.13c and A549*rho*$^{\varphi}$, Fig. 3.13d). In normal A549 cells, paraquat exposure was observed to produce a rise in the red fluorescence intensity depicting elevated levels of the oxidative DNA lesion

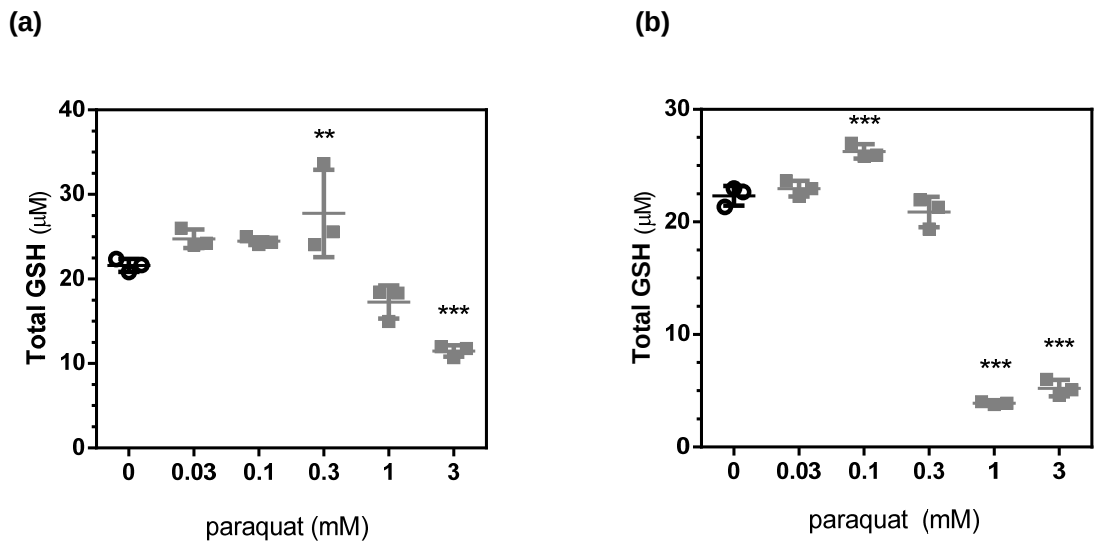

Figure 3.12 Effects of 24 and 48 hr paraquat exposure on total glutathione in A549 cells.

*A549 cells were treated with paraquat for 24 and 48 hr prior to glutathione analysis using a commercially available kit as described in Chapter 2. (a) Graphical representation of the change in total glutathione content in A549 cells exposed to increasing concentrations of paraquat (mM) for 24 hr and (b) after 48 hr of exposure. Significance was determined using a 1-way ANOVA with a Dunnett's post test comparing treatment groups to untreated control (** p<0.01, *** p<0.001). Data shown are from a representative experiment.*

8-oxoguanine, while similar images from A549*rho*$^{\varphi}$ depicted no rise in red fluorescence. These images and data corroborate the mechanism of action for paraquat and further attribute paraquat-induced 8-oxoguanine to the mitochondrial DNA damage.

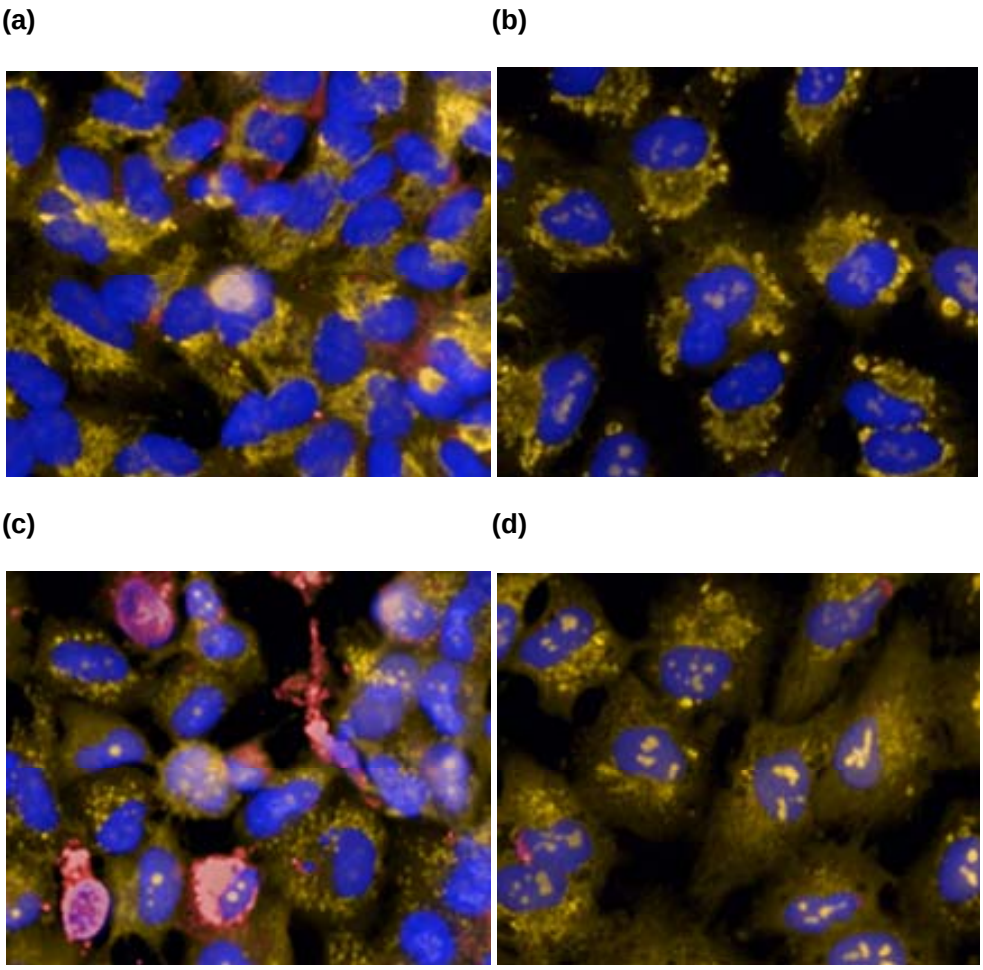

Figure 3.13 Effects of deleting mitochondrial DNA on paraquat-induced 8-oxoguanine.

A549 cells were treated with 50 ng/mL ethidium bromide for 14 population doublings to generate A549rho$^{\varphi}$ cells devoid of functional mitochondrial DNA. A549 and A549rho$^{\varphi}$ cells were treated with paraquat for 24 hr, and then stained for the oxidative DNA marker, 8-oxoguanine. (a) Untreated A549 cells (Hoechst 33342, overlaid blue; MitoTracker® orange, overlaid orange; 8-oxoguanine, overlaid red) and (b) untreated A549rho$^{\varphi}$ cells are compared to (c) A549 cells exposed to 3 mM paraquat (d) A549rho$^{\varphi}$ cells exposed to 3 mM paraquat for 24 hr (line = 40 μm). Data shown are from a representative experiment.

3.3 Discussion

In this chapter, it's been presented how cigarette smoke could be used as a stimulus in an *in vitro* cell based assay to mimic disease and the induction of oxidative stress. Following exposure of A459 cells to cigarette smoke, there was a 3-fold increase in ROS produced in a temporal manner, and could largely be attributed to ROS produced within the mitochondria based on staining of the cells with MitoSOX™. This increased ROS was associated with elevated levels of oxidative DNA damage, 8-oxoguanine. While this stimulus is relevant to respiratory disease and assisted in establishing a potential translation to the clinic, the stressor's impact was not localized to only the mitochondria, as cigarette smoke affected the DNA in both the nucleus and the mitochondria equally. Moreover, both cigarette smoke and cigarette smoke extract each exhibited variability in the cellular response elicited from the oxidant induced stress. The cigarette smoke extract was purchased from a commercial vendor (Murty Pharmaceuticals; Lexington, KY), and exhibited lot-to-lot variability in the response it elicited (data not shown). A recent review focused on the *in* vitro exposure of cells to cigarette smoke and how the various methods differed in the delivering of the smoke to the cells and the variability seen across the methods (Thorne and Adamson, 2013). A potential solution was to utilize a stimulus capable of localizing the ROS generation and thereby DNA damage to the mitochondria of the cell. Therefore, paraquat was used due to its mechanism of action specificity within the mitochondria of cells.

Paraquat elicited a robust concentration-dependent production of ROS in A549 cells, with a 30-fold surge (3 mM) over baseline. This rise in ROS can largely be associated with an increase in mitochondrial ROS. Unlike other ROS generators, time was required for paraquat-induced ROS being detected at 24 hr onwards, where as cigarette smoke demonstrated elevated ROS as early as 2 hr post smoke exposure. Another difference between cigarette smoke and paraquat was the observation that paraquat induced the oxidative DNA lesion, 8-oxoguanine predominately within the mitochondria of cells. There was a 20-fold rise following 24 hr exposure to 3 mM paraquat; however, this more than doubled after 48 hr of paraquat exposure resulting in a 50-fold accumulation in 8-oxoguanine. This observation was supported by the sample images showing a significant ($p<0.05$) increase in red fluorescence in the mitochondrial space of the cells.

While the DNA damage was intensifying within the mitochondria, there was a concomitant loss of the mitochondrial membrane potential over time with increasing paraquat concentration. Paraquat induced a half maximal response of 237 μM (24 hr), and 48 hr of exposure shifted this value to the left to 130 μM. The mitochondrial membrane integrity was also affected, with a shift toward a "leaky" membrane phenotype 24 hr post exposure to paraquat. Cytochrome *c* was examined as a measure of mitochondrial health, as will typically reside within the inner mitochondrial space as part of the electron transport chain. The leaking of this protein out of the mitochondria is a measure of poor membrane integrity, facilitating the activation of caspase 9, a key component in the apoptosis pathway. Following 48 hr paraquat (3 mM) exposure, there was almost a 4-fold upswing in cytochrome *c* translocation to the nucleus. These data support the concept that the mitochondria are compromised following paraquat exposure and could initiate the apoptosis pathway, perhaps leading to cell death.

The cell was found to respond to paraquat-induced ROS and oxidative DNA damage. OGG1, the enzyme responsible for detection and excision of the DNA lesion 8-oxoguanine was found to be elevated following paraquat exposure. There was a 2-fold increase in OGG1 content following paraquat (3 mM) exposure, with relatively unchanged EC_{50} values (300 to 400 μM) from 24 to 48 hr of paraquat exposure, respectively. These data suggest the level of OGG1 protein had maximally accumulated within the mitochondria. The cellular response was not only limited to oxidative DNA damage, but the cells responded to the rise in ROS as well by activating the anti-oxidant response. MnSOD was shown to have increased by 2-fold following addition of paraquat (24 hr). While ROS was only detected at the top test concentrations (1 and 3 mM), the MnSOD quantification reflected that the cells responded to low or undetectable ROS levels as observed by the elevated levels of MnSOD protein. Additionally, the key anti-oxidant protein glutathione was measured and was shown to be significantly ($p<0.001$) decreased following 24 hr paraquat exposure (3 mM). This decrease continued and by 48 hr, lower concentrations of paraquat (1 and 3 mM) have significantly decreased total glutathione levels ($p < 0.001$), suggesting a shift in the EC_{50} curve to the left. These data suggest, in part, that the cell does indeed mount a response to paraquat-induced ROS. Further, the data support the cell's attempt to correct the paraquat-induced 8-oxoguanine, but with increasing time these repair mechanisms were overwhelmed and the cell signals for the initiation of apoptosis.

Finally, the data support the mechanism of action for paraquat. Cells exposed to chronic ethidium bromide had their mitochondrial DNA deleted rendering the electron transport chain as dysfunction and depriving paraquat of a source of electrons to generate reactive radicals. Cells exposed to paraquat displayed a concentration-dependent rise as expected in the 8-oxoguanine lesion in age-matched A549 cells; however, A549*rho*$^{\varphi}$ cells were shown to be absent of the oxidative DNA lesion post paraquat exposure (24 hr). This established that the mechanism of action for paraquat was through the electron transport chain, facilitating the use of paraquat as a model to examine the role of mitochondrial oxidative DNA damage in disease for future work in identifying potential small molecule activators of the repair process (Chapter 4).

While paraquat and cigarette smoke were studied in additional cell types, the variable nature of cigarette smoke was not studied extensively in primary cells. Perhaps, moving to a different cell type and shifting from a transformed cell line to a primary human lung cell would provide a path forward for this stimulus. It would prove useful to compare future work to primary cells to help draw comparisons from *in vitro* data, to *in vivo* data, and eventually towards a clinical significance.

CHAPTER 4:

Characterization of modulating OGG1 enzyme activity

4. Characterization of modulating OGG1 enzyme activity

4.1 Introduction

An examination of OGG1 activity in human lung epithelial cells has shown that when the protein is transduced into cells it has a beneficial impact on cell viability and protection against oxidant-induced DNA damage (Yang et al., 2015). The converse was also observed in these cells; when the gene was silenced, DNA damage was elevated, resulting in a decline in cell viability (Yang et al., 2015). Further, it's been demonstrated that the activity of the OGG1 enzyme can be restored through binding sites on the protein, which are capable of activating the stalled enzyme due to a distortion in the active site caused by a mutation in C253I to C253L (Lukina et al., 2013). It had previously been demonstrated as well by Fromme et al. that the product (8-oxoguanine) generated through the removal of the damaged base pair mediated by OGG1 was capable of binding to OGG1 and increasing the catalytic activity of the enzyme (Fromme et al., 2003). The aim of the experiments presented in this chapter was to demonstrate that by modulating the activity of OGG1 there was a positive or negative effect on paraquat-induced 8-oxoguanine. Secondly, the OGG1 activators were tested to examine the effect they have on paraquat-induced DNA damage, but also on cell health.

Initial work focused on utilizing the paraquat-induced mtDNA damage model to characterize the modulation of OGG1 content within the cell. The cell model was modulated using baculovirus and siRNA to increase or decrease OGG1 content respectively, along with small molecule activators, which were tested for their effect *in* vitro on impacting oxidative stress-induced OGG1 activity. OGG1 activators were identified using a biochemical approach similar to that used for testing OGG1 activity in cell lysates (Siggens et al., 2012). Following identification of certain OGG1 activators, these tool compounds were tested for their ability to cause a reduction in paraquat-induced mitochondrial 8-oxoguanine levels. Additionally, the activators were tested for their ability to impact cellular function, which could be translated into cell health.

Recent evidence has suggested it could be the incomplete repair of the DNA lesion and the resulting single strand DNA break that causes an induction of the inflammatory response in airway epithelial cells in allergic lung inflammation (Bacsi et

al., 2013). Moreover, it was recently proposed that DNA Ligase III was a rate limiting step for base excision repair, indicating incomplete repair might be achieved if the activity of DNA Ligase III did not keep pace with OGG1 (Akbari et al., 2014). To examine whether the remaining steps of the base excision repair pathway were keeping pace with elevated OGG1 activity, DNA Ligase III protein levels were measured following pre-incubation of the small molecule OGG1 activators with A549 cells followed by exposure to paraquat. Finally, to examine the overall impact the OGG1 activators had on the enzyme itself, OGG1 protein concentrations were examined by immunofluorescence to determine if the content of OGG1 was altered within the mitochondria in the presence of the OGG1 activators.

4.2 Results

4.2.1 Effect of OGG1 BacMam on paraquat-induced mitochondrial DNA 8-oxoguanine

Paraquat has previously been shown to induce the oxidative DNA damage lesion, 8-oxoguanine in a concentration- and time-dependent manner (Chapter 3). The question arises as to whether enhanced DNA glycosylation capacity, i.e. Ogg1 activity, would offset the levels of paraquat-induced 8-oxoguanine lesion development. OGG1 BacMam was constructed (Chapter 2) to test the effects of increasing OGG1 protein content and whether this would lower the level of 8-oxoguanine present in particular within the mitochondria. A549 cells transduced with 5% v./ v. OGG1-BacMam were shown to be protective from paraquat-induced cell loss. There was a significant ($p<0.0001$) 70% rise in cell numbers from untreated OGG1 BacMam transduced cells compared to untreated cells transduced with null BacMam virus. The EC_{50} values for paraquat-induced cell death were similar for both the null (0.52 mM) and OGG1 BacMam (0.45 mM) transduced paraquat exposed cells (24 hr), but the two treatment groups were significantly ($p<0.0001$) different from one another. As shown in Fig. 4.1b, 5% v./ v. OGG1 BacMam reduced the magnitude of paraquat-induced change in 8-oxoguanine content. At 3 mM paraquat, the magnitude of change was decreased by almost 50% with the addition of the OGG1 BacMam as compared to the null BacMam virus. Further, the paraquat concentration needed to elicit a half maximal response was similar for both treatment groups with an EC_{50} value of about 0.5 mM, but the treatments were significantly ($p<0.001$) different from each other (calculated using a non-linear regression analysis with a variable slope and a sigmoid-dose response). Transduction efficiency was tested using null-virus with a green fluorescent protein tag to assist with transduction optimization (data not shown).

To understand in which cellular compartment, nuclear or mitochondrial, OGG1 was impacting the change in 8-oxoguanine, green fluorescent protein (GFP)-tagged OGG1 BacMam was constructed with a mitochondrial localization protein (manganese superoxide dismutase – MnSOD, utilizing only the localization sequence and not the full protein) MnSOD-OGG1-GFP BacMam. This construct was added to A549 cells for 48 hr

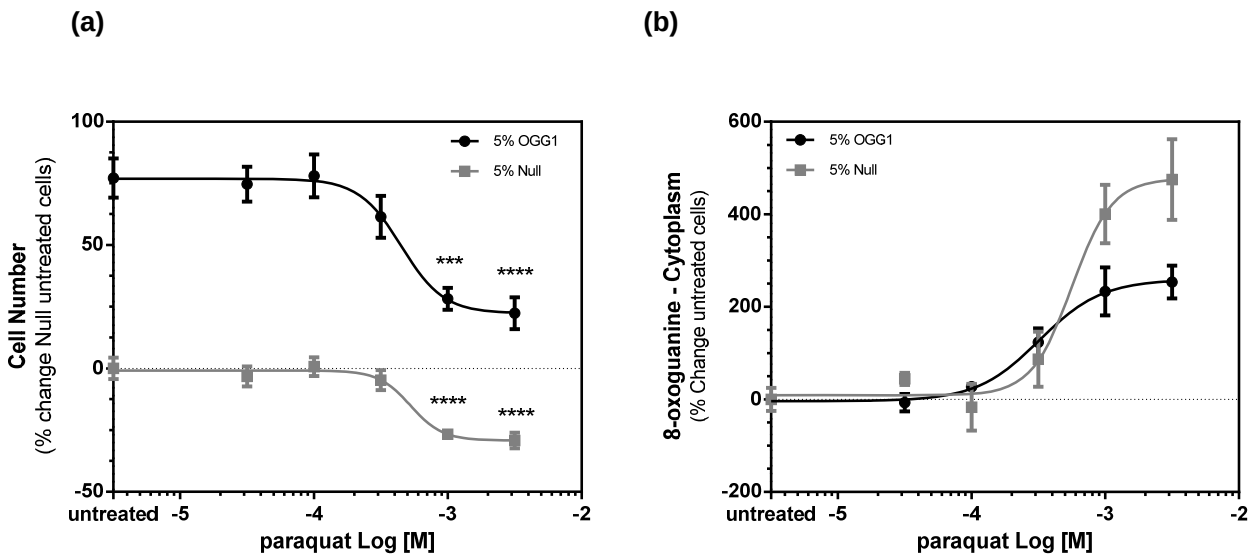

Figure 4.1 Effects of OGG1-BacMam following 24 hr paraquat-induced changes on cell number and 8-oxoguanine in A549 cells.

A549 cells were incubated with 5% v./v. OGG1-BacMam for 48 hr prior to treatment with varying concentrations of paraquat for 24 hr and stained for 8-oxoguanine as described in Chapter 2. (a) Change in cell number following exposure to varying concentrations of paraquat for 24 hr. Significance determined between the two untreated groups using an un-paired, 2-tailed t-test. (b) The percent change in 8-oxoguanine intensity within the mitochondria of the cells from varying concentrations of paraquat compared to control cells. Comparison between the non-linear fits performed using an extra sum of squares F-test (p = 0.05). The data are a summary of three independent experiments.

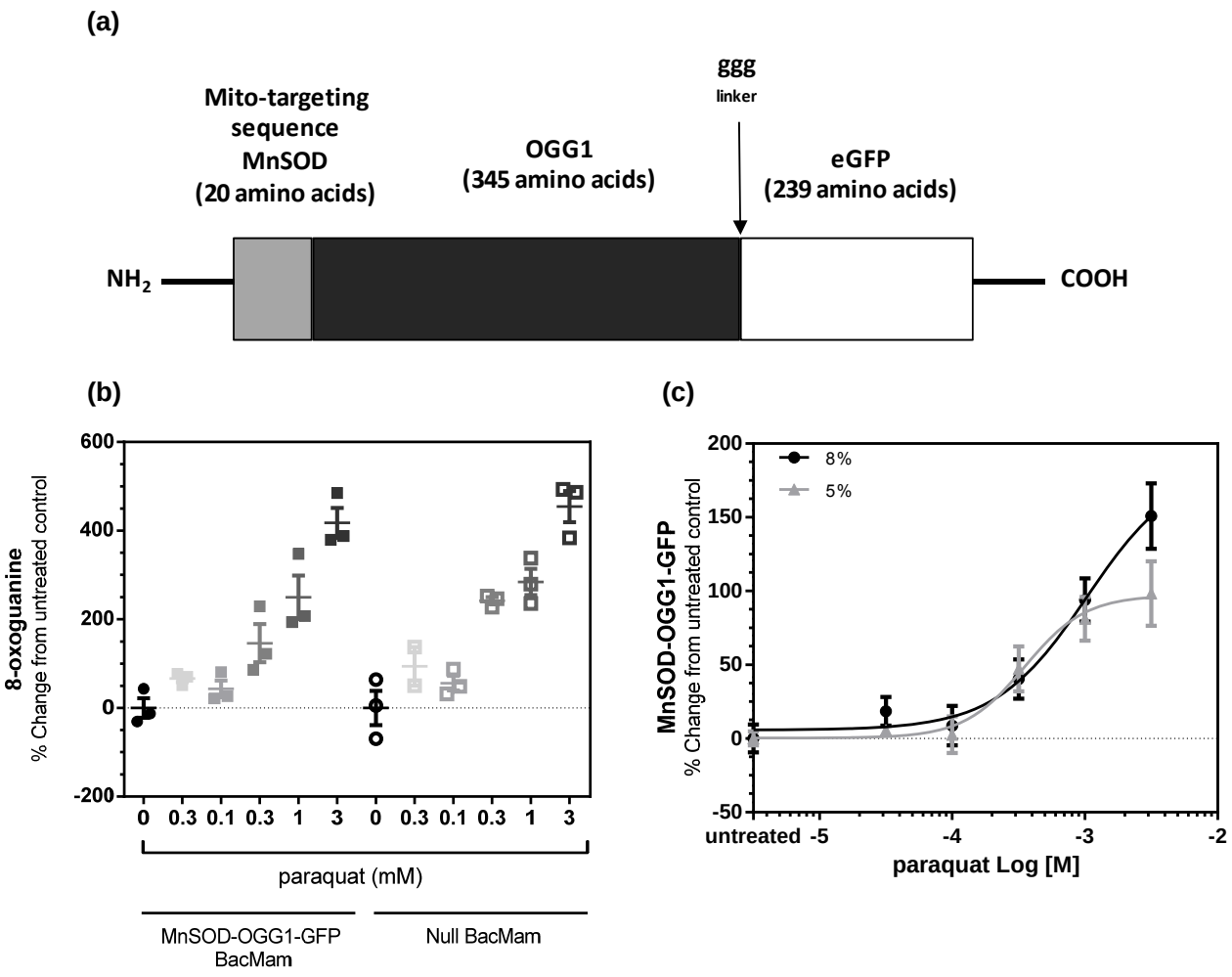

Figure 4.2 Effects of MnSOD-OGG1-GFP BacMam following paraquat exposure on 8-oxoguanine content in A549 cells.

Figure 4.2 Effects of MnSOD-OGG1-GFP BacMam following paraquat exposure on 8-oxoguanine content in A549 cells.

A549 cells were incubated with 8 or 5% v./ v. MnSOD- OGG1-GFP BacMam for 48 hr prior to treatment with varying concentrations of paraquat for 24 hr. The cells were stained and imaged for 8-oxoguanine as previously described (Fig. 4.1). (a) Map of the MnSOD-OGG1-GFP construct. (b) Percent change from the 8-oxoguanine intensity of control cells within the cytoplasm of cells treated with 8% v. /v. MnSOD-OGG1-GFP or null BacMam. (c) Percent change in GFP intensity within the cytoplasm region following A549 cells exposed to varying concentrations of paraquat (24 hr). (d) A sample image from cells treated with 3 mM paraquat is shown (Hoechst 33342, overlaid blue; MnSOD-OGG1-GFP, overlaid green; MitoTracker® Orange CMTMRos, overlaid orange; 8-oxoguanine, overlaid red) and (e) MnSOD-OGG1-GFP alone with all of the color overlays removed for the nucleus, mitochondria, and 8-oxoguanine. Data shown are from an independent experiment, with each condition tested in triplicate.

prior to paraquat exposure (24 hr). Unfortunately, the mitochondrial targeted OGG1 BacMam construct did not protect the cells against paraquat-induced changes in cell number (data not shown) or with 8-oxoguanine lesion accumulation relative to the null BacMam control (Fig. 4.2b). However, the images (Fig. 4.2d) show there was an increase in GFP intensity demonstrating the BacMam construct was transcribed and translated when added to cells. This was evident by the 150% increase in GFP signal detected in the cytoplasm of the cells in the presence of 3 mM paraquat (24 hr) when transduced with 8% MnSOD-OGG1-GFP BacMam (Fig. 4.2c).

Sample images shown in Fig. 4.2d and 4.2e are of the same field of view from A549 cells transduced with 8% v./ v. MnSOD-OGG1-GFP tagged BacMam construct and exposed to 3 mM paraquat (24 hr). The image in Fig. 4.2e has all of the color overlays removed except for the GFP, enabling the visualization and localization of the transduced OGG1 protein expressed within these cells following treatment with paraquat. While the images demonstrate that the BacMam construct was recruited to produce active OGG1, the resultant enzyme was not effective in lowering the levels of paraquat-induced 8-oxoguanine lesion relative to the null control (Fig 4.2b). Similar results were obtained with OGG1-GFP BacMam construct lacking the MnSOD leader localization protein; this protein also failed to alter paraquat-induced 8-oxoguanine (data not shown). However, the GFP signal from the OGG1-GFP construct was diminished compared to the MnSOD-OGG1-GFP version of the BacMam, and could suggest that without the mitochondrial localization signal the OGG1-GFP is not shuttled immediately to the mitochondria (data not shown). It was later surmised that the GFP tag on the C-terminus (Fig. 4.2a), which is close to the DNA binding pocket, negatively impacted OGG1 binding to the DNA strand due to the “bulky” nature of the tag. Thus, the ability of the GFP-tagged OGG1 to carry out effective DNA repair was compromised.

4.2.2 Effect of *OGG1* siRNA on paraquat-induced 8-oxoguanine

The use of gene silencing *OGG1* (siRNA) enabled the specific dissection of the pathway to examine how the cell compensates when the cell senses an increase in oxidative DNA damage. When A549 cells were transfected with 100 nM *OGG1* siRNA for 48 hr and then exposed to paraquat for 24 hr, the levels of 8-oxoguanine increased significantly. There was greater than a 1500% rise in 8-oxoguanine content with *OGG1* siRNA compared to about a 300% increase with transfection

reagents alone in response to paraquat (3 mM, Fig. 4.3). In the absence of paraquat, the number of surviving cells was about 25% lower with *OGG1* siRNA compared to the transfection reagent control (data not shown). It is important to note that in the absence of paraquat, cells treated with *OGG1* siRNA had about a 200% increase in 8-oxoguanine content compared to the transfection reagent controls. These data indicate that under non-stressed conditions, cells treated with *OGG1* siRNA have a higher starting level of 8-oxoguanine compared to non-transfected cells. The magnitude of the paraquat-induced 8-oxoguanine response was different with the *OGG1* siRNA, and was significantly ($p<0.0001$) different compared to the Dharmafect® control, but the Dharmafect® and media response curves were not statistically different from each other ($p<0.8$). Across the treatment groups, the EC_{50} values for the groups were relatively similar with media 0.16 mM, Dharmafect® 0.22 mM, and *OGG1* siRNA at 0.42 mM (calculated using a non-linear regression analysis with a variable slope and a sigmoid-dose response). It was confirmed by RT-PCR, *OGG1* siRNA was effective at silencing of *OGG1* gene expression (Appendix S1).

4.2.3 Effect of small molecule OGG1 activators on paraquat-induced mitochondrial DNA 8-oxoguanine

Given the findings above, this supported the hypothesis that increased OGG1 protein content attenuates the production of 8-oxoguanine more than basal levels of OGG1. Therefore, small molecule activators were sought to achieve similar effects. It has been shown previously that small molecules such as 8-bromoguanine can facilitate the activity of isolated OGG1 (Fromme et al., 2003; Lukina et al., 2013). In the present study however, 8-bromoguanine was not effective. When added to A549 cells prior to the addition of paraquat for 24 to 48 hr, 8-bromoguanine did not reduce mitochondrial 8-oxoguanine content (data not shown). To enable identification of small molecules

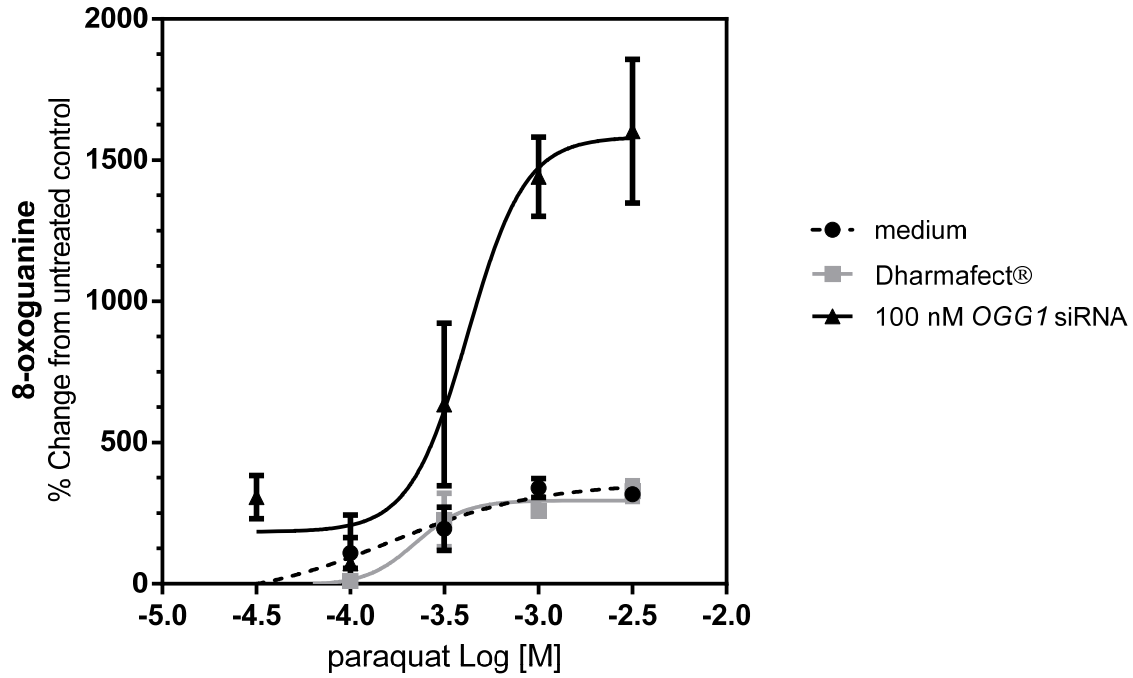

Figure 4.3 Effects of OGG1 siRNA on 8-oxoguanine content following paraquat exposure in A549 cells.

A549 cells were incubated with 100 nM OGG1 siRNA containing Dharmafect® at a dilution of 1:50 in serum-free conditions. Following 48 hr incubation, the medium was replaced to complete culture medium and the A549 cells were treated with increasing concentrations of paraquat for 24 hr. The cells were stained and imaged for 8-oxoguanine as described in Chapter 2. This figure represents the percent change in 8-oxoguanine intensity within the mitochondria of paraquat treated cells compared to the media control. Comparison between the non-linear fits performed using an extra sum of squares F-test (p = 0.05). Data shown are from an independent experiment, with each condition tested in triplicate.

capable of activating OGG1 enzyme activity, a high throughput screen was initiated within the Discovery Research group at GlaxoSmithKline. Several compounds were subsequently identified and tested in the paraquat-induced 8-oxoguanine assay (Table 4.1). For the present investigation, the compounds were evaluated for their effects on paraquat-induced 8-oxoguanine formation by varying the pre-incubation time with cells. When the compounds were added two to four hours prior to paraquat exposure, the compounds maximally reduced 8-oxoguanine (Appendix S8). When the compounds in Table 4.1 were pre-incubated (4 hr, 3 – 100 μM) with A549 cells prior to paraquat exposure (48 hr, 0.6 mM), the compound treated cells had (at particular concentrations of compound) lower 8-oxoguanine levels compared to paraquat exposed cells without the OGG1 activators (Fig. 4.4a and 4.4b). Compounds A, B, D, and F offered some protection, whereas Compound C exhibited no protective effect. An important point was that these compounds were not optimized and remain crude tools. For example, Compound A has a bell-shaped concentration response curve, possibly due to poor compound solubility as observed by the cloudy suspension (at high concentrations) noted when it was added to the cells.

Sample representative images depict an increase in 8-oxoguanine depicted as red fluorescence intensity (using AlexaFluor®-647) in the mitochondria from a concentration-response curve of paraquat in the absence of activators (Fig. 4.5a). An advantage of imaging is the ability to analyze additional cellular features such as cell size, cell shape, and the pattern of the fluorescence staining, all of which could be indicative of broader ongoing biological processes. For example, as cells begin to die either through apoptosis or necrosis, the nucleus will begin to condense. It was shown in Chapter 3 that paraquat exposure for 48 hr will induce cytochrome c translocation and thereby activate the intrinsic apoptosis pathway. Further, as observed above with increasing concentrations of paraquat, the nucleus begins to shrink and appears a brighter blue/ white (Fig. 4.5a). This color shift is due to the chromatin condensing, a step in the apoptosis pathway, permitting additional Hoechst dye to intercalate into the DNA. The nuclear size was quantified using the analysis software (Chapter 2) and paraquat was observed to induce a significant ($p<0.0001$) decrease in the overall area of the nucleus at 0.6 mM and above (Fig. 4.6a and 4.6b). This change in nuclear size can be observed in Fig. 4.5a as well.

NUMBER	NAME
COMPOUND A	(S)-2-((6-METHYL-2-(PHENYLAMINO)PYRIMIDIN-4-YL)AMINO)-N-PHENYLPROPANAMIDE
COMPOUND B	2-(4-FLUOROPHENYL)-N,1,7-TRIMETHYL-1H-PYRROLO[2,3-D]PYRIDAZIN-4-AMINE
COMPOUND C	N-CYCLOHEXYL-2-CYCLOPROPYLQUINAZOLIN-4-AMINE
COMPOUND D	2-(4-(4-(1H-IMIDAZOL-1-YL)PHENOXY)-5-METHYLPYRIMIDIN-2-YL)OCTAHYDROPYRROLO[1,2-A]PYRAZINE
COMPOUND F	1-CYCLOHEXYL-1-(2,4-DICHLOROPHENYL)-2-(1H-IMIDAZOL-1-YL)ETHANOL

Table 4.1 Tool OGG1 small molecule activators.

(a)

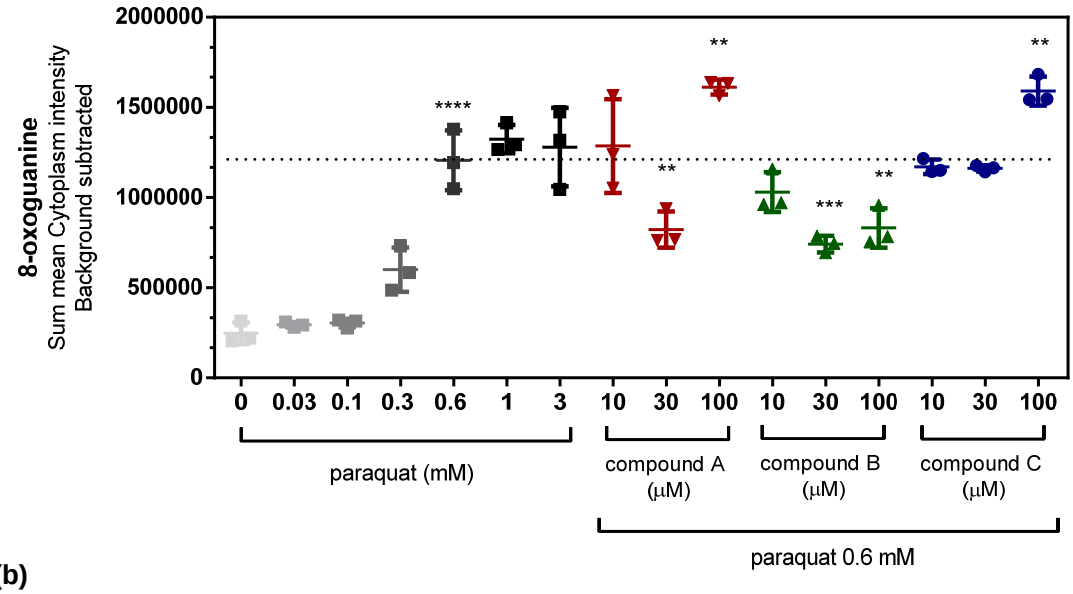

(b)

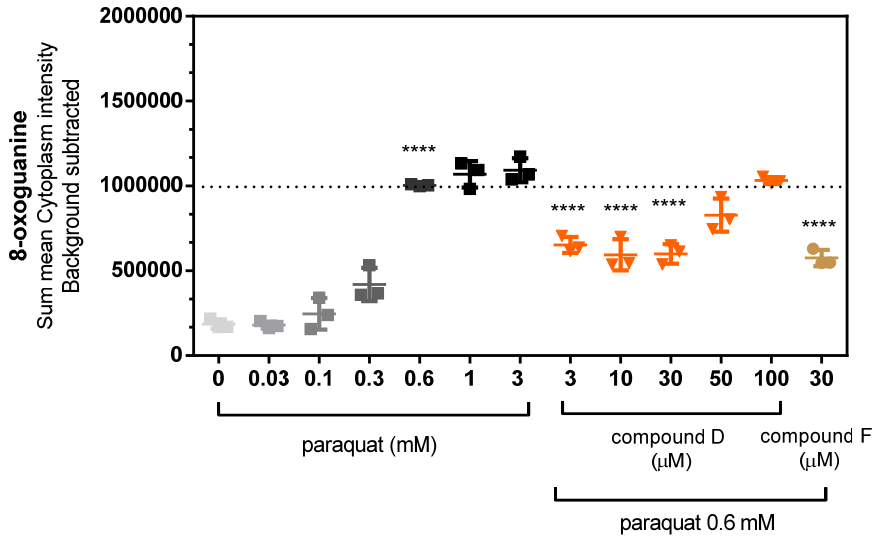

Figure 4.4 Effects of OGG1 small molecule activators on paraquat-induced 8-oxoguanine in A549 cells.

Figure 4.4 Effects of OGG1 small molecule activators on paraquat-induced 8-oxoguanine in A549 cells.

*A549 cells were pre-treated for 4 hr with small molecule OGG1 activators or 0.1% DMSO prior to addition of 0.6 mM paraquat for 48 hr. The cells were stained and imaged for 8-oxoguanine content as described in Chapter 2 and the average fluorescence intensity within the cell was normalized based on the number of cells imaged. (a) and (b) Graphical representations of the change in 8-oxoguanine intensity within the cytoplasm of cells compared to 0.6 mM paraquat treated cells. Significance was determined using a 1-way ANOVA with a Dunnett's post test comparing paraquat alone treated groups to untreated control (0 mM) and OGG1 activator treated groups to 0.6 mM paraquat control (** $p<0.01$, *** $p<0.001$, **** $p<0.0001$). Data shown are from a representative experiment, performed four times.*

When, OGG1 activators were pre-incubated (4 hr, 3 – 100 μM) prior to the addition of paraquat (0.6 mM), nuclear size was preserved (Fig. 4.6a and 4.6b), albeit with varying effectiveness. Compounds B and D appeared to demonstrate concentration-dependence and compound F restored the nuclear size when tested (30 μM). Compound C failed to restore nuclear size, consistent with its lack of effect on reducing paraquat-induced 8-oxoguanine.

The rise in paraquat-induced 8-oxoguanine was found to not be evenly distributed among the cells within a given well. Some cells were affected more than others and single cell analysis (Chapter 2) quantified this pattern as the shift in the mean distribution of 8-oxoguanine in each cell compared to the 8-oxoguanine mean from cells treated in the absence of paraquat. In untreated cells, about 10-15% of the cell population was classified as this high responder phenotype, but in response to increasing concentrations of paraquat, there was a concentration-dependent rise in this phenotype (Fig. 4.7a). When OGG1 activators were added 4 hr prior to paraquat exposure (0.6 mM), several Compounds (B and D) demonstrated a concentration-dependent lowering of 8-oxoguanine in this high responder cell population (Fig 4.7a and 4.7b). For example, sample images shown in Fig. 4.5b depict a decrease in this phenotype for Compound B even though 8-oxoguanine was still observed within the mitochondria. Compound F (30 μM) and the effective concentration of Compound A (30 μM) both reduced this population phenotype by almost 100%. Sample images from these two compounds are shown in Fig. 4.5b along with sample images for Compounds B, C, and D. These images not only depict a decrease in the number of cells expressing high levels of 8-oxoguanine, but also show that certain compounds protect against changes in nuclear area (Fig. 4.6a and b).

(a)

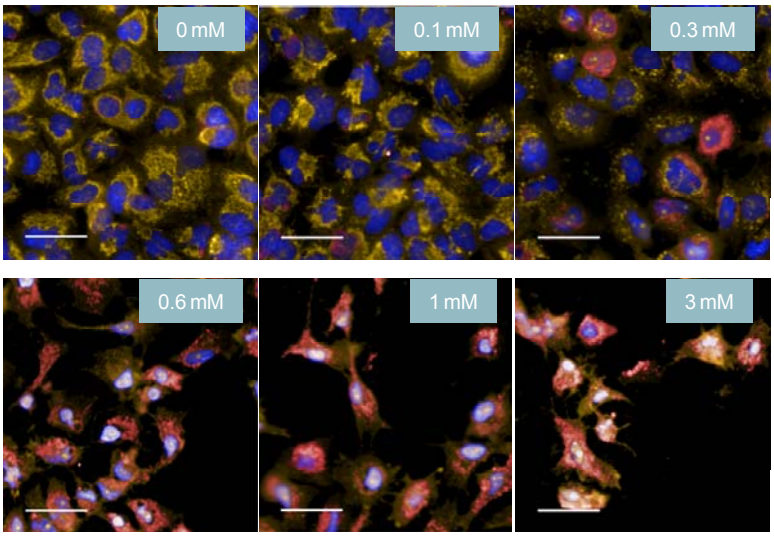

(b)

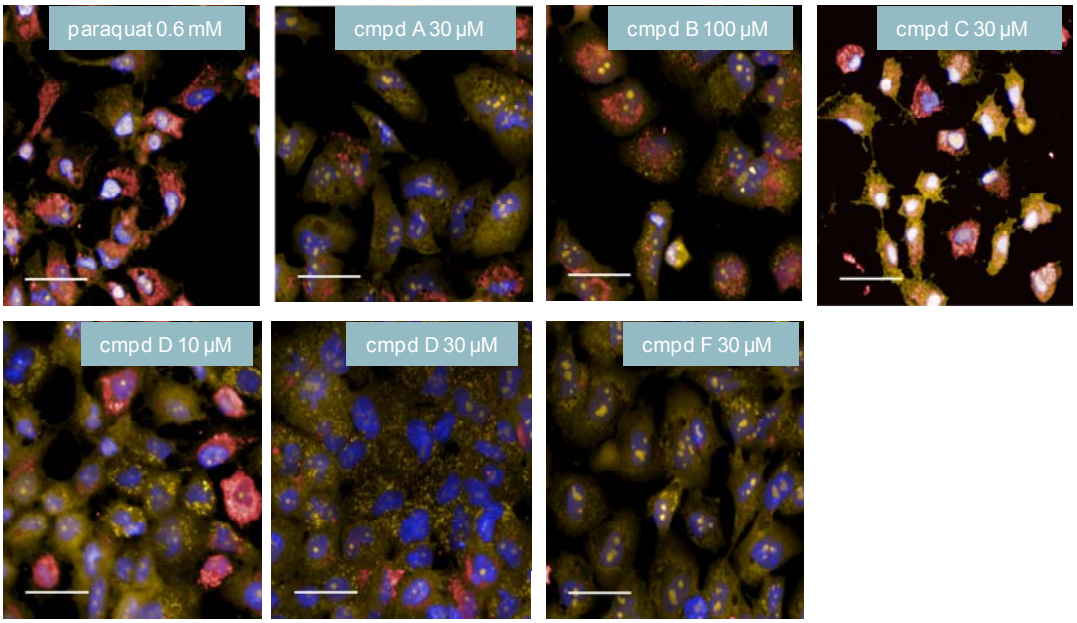

Figure 4.5 Sample images of paraquat-exposed A549 cells following 4 hr pre-treatment with OGG1 activators.

Figure 4.5 Sample images of paraquat-exposed A549 cells following 4 hr pre-treatment with OGG1 activators.

(a) Sample representative images from cells pre-incubated with 0.1% DMSO (4 hr) prior to exposure to increasing concentrations of paraquat for 48 hr (Hoechst 33342, overlaid blue; MitoTracker® orange, overlaid orange; 8-oxoguanine-AleaFluor®-647, overlaid red; line = 40 µm). (b) Sample images from cells pre-incubated with OGG1 activators (4 hr) prior to paraquat exposure at a single concentration (0.6 mM) for 48 hr. Data shown are from a representative experiment, performed four times.

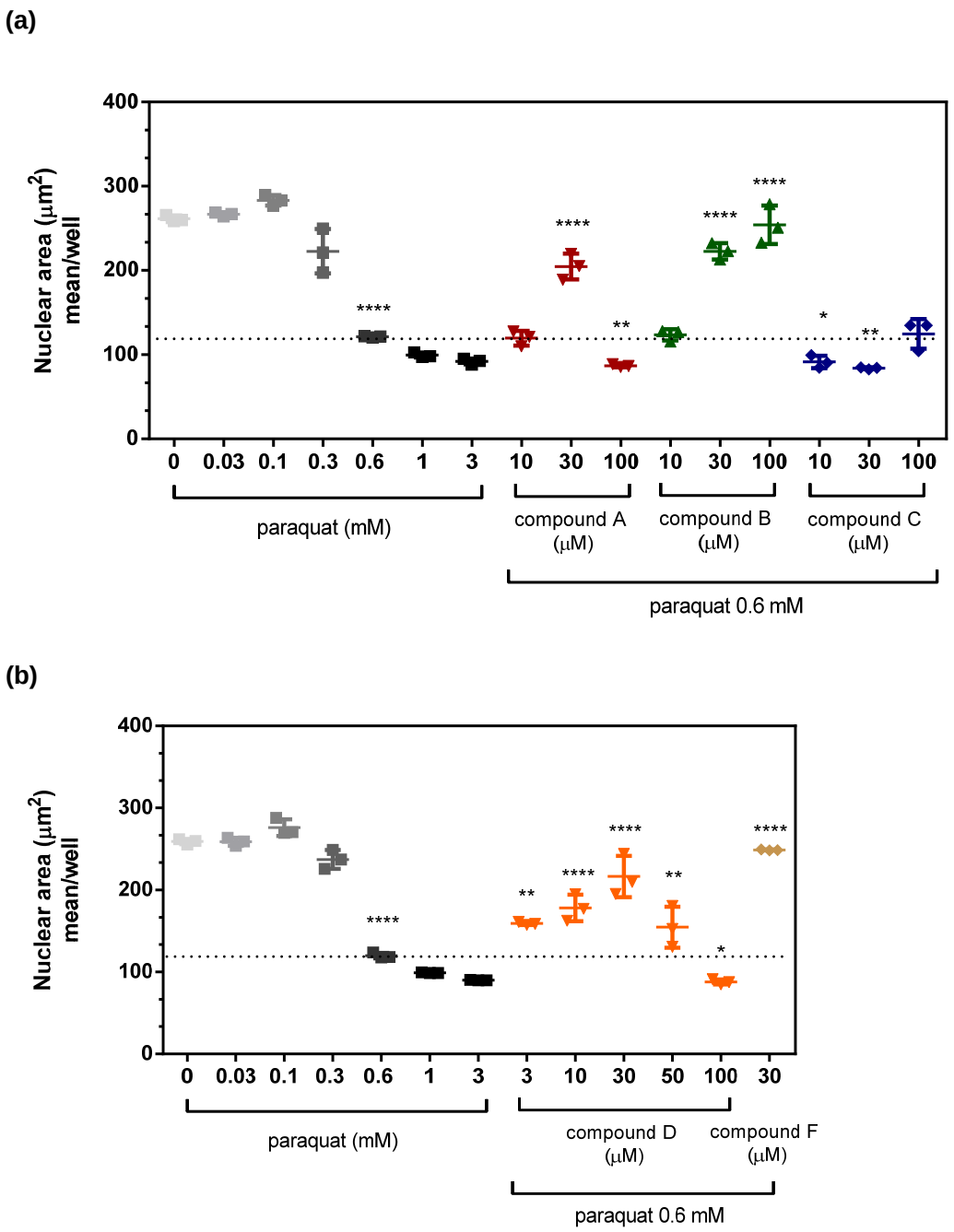

Figure 4.6 Effects of small molecule OGG1 activators on nuclear area in A549 cells.

Figure 4.6 Effects of small molecule OGG1 activators on nuclear area in A549 cells.

The images from Fig. 4.4 were analyzed further by examining morphology changes as described in Chapter2. (a) and (b) The mean nuclear area for A549 cells pre-incubated with OGG1 activators (4 hr) prior to exposure to a single concentration of paraquat (0.6 mM) for 48 hr. Significance was determined using a 1-way ANOVA with a Dunnett's post test comparing paraquat alone treated groups to untreated control (0 mM) and OGG1 activator treated groups to 0.6 mM paraquat control (p<0.05, ** p<0.01, *** p<0.001, **** p<0.0001). Data shown are from a representative experiment, performed three times.*

(a)

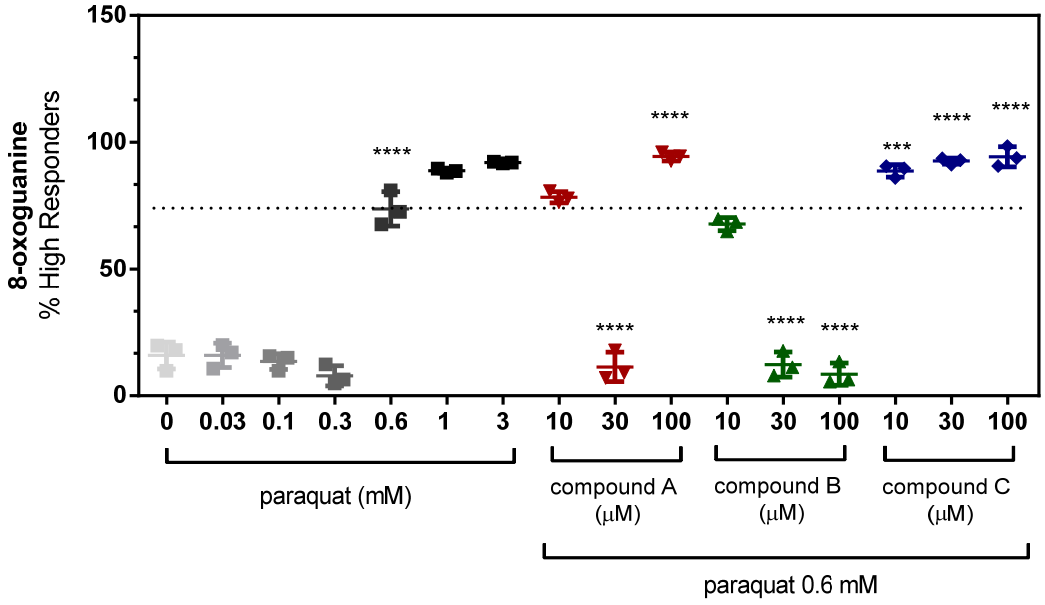

(b)

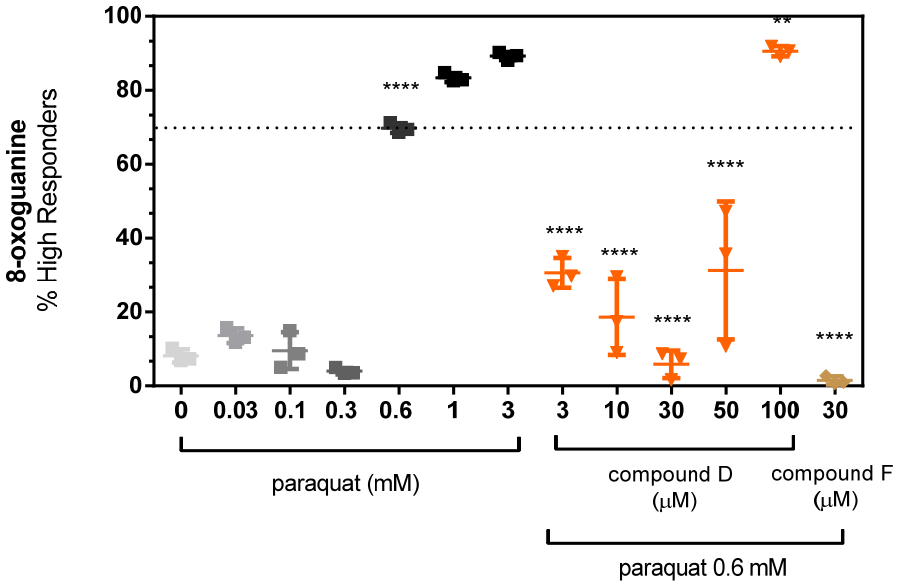

Figure 4.7 Effects of small molecule OGG1 activators on percent of A549 cell population classified as high responders.

Figure 4.7 Effects of small molecule OGG1 activators on percent A549 cell population classified as high responders.

*The images from Fig. 4.5 were analyzed further examining morphology changes as described in Chapter2. (a) and (b) The percent of the cell population as high responders is shown for A549 cells pre-incubated with OGG1 activators (4 hr) prior to exposure to a single concentration of paraquat (0.6 mM) for 48 hr. Significance was determined using a 1-way ANOVA with a Dunnett's post test comparing paraquat alone treated groups to untreated control (0 mM) and OGG1 activator treated groups to 0.6 mM paraquat control (** p<0.01, *** p<0.001, **** p<0.0001). Data shown are from a representative experiment, performed three times.*

4.2.4 Effect of small molecule OGG1 activators on paraquat-induced mitochondrial membrane depolarization

While the OGG1 activating compounds attenuated paraquat-induced oxidative DNA damage, the question arose whether this would lead to a beneficial, functional outcome on the mitochondria and the cell. Paraquat was shown to reduce the mitochondrial membrane potential (Fig. 3.7). After 4 hr pre-incubation, Compound D elicited a modest improvement as shown in Fig. 4.8a. Compound D (30 μM) restored about 50% of the paraquat induced loss of membrane potential. The remaining test compounds, including Compound F (Fig. 4.8a) were essentially without effect (data not shown). It can be observed with increasing concentration of paraquat exposure (24 hr), the JC-1 dye shifts from the aggregate to the monomer form of the dye (Fig. 4.8b, c, and d). Pre-incubation with compound D (30 μM) 4 hr prior to paraquat exposure prevented the dye shift from the aggregate to the monomer form (Fig. 4.8e).

4.2.5 Effect of OGG1 activators on paraquat-induced changes on down-stream base excision repair proteins

Although the OGG1 activators lowered paraquat-induced 8-oxoguanine levels, it was not clear whether the compounds initial effects were promoting base excision repair. In the absence of the base excision pathway, the content of the DNA Ligase III, a probable rate limiting step in base excision repair, was measured (Akbari et al., 2014). Imaged cells were selected based on a certain threshold of fluorescence intensity to identify cells based on their fluorescence staining pattern (similar to 8-oxoguanine analysis). In response to paraquat exposure (3 mM) for 48 hr, DNA Ligase III content within the mitochondria of A549 cells decreased by about 50% (Fig. 4.9a and 4.9b). OGG1 activators when added 4 hr prior to the addition of paraquat increased the fluorescence intensity of DNA Ligase III (using AlexaFluor®-488) towards untreated control levels (Fig. 4.9a and b). These data indicate there was an increase in enzyme content within the mitochondria of the cells. Compounds A, B, and D elevated DNA Ligase III content in a concentration-dependent manner when tested in the presence of a single

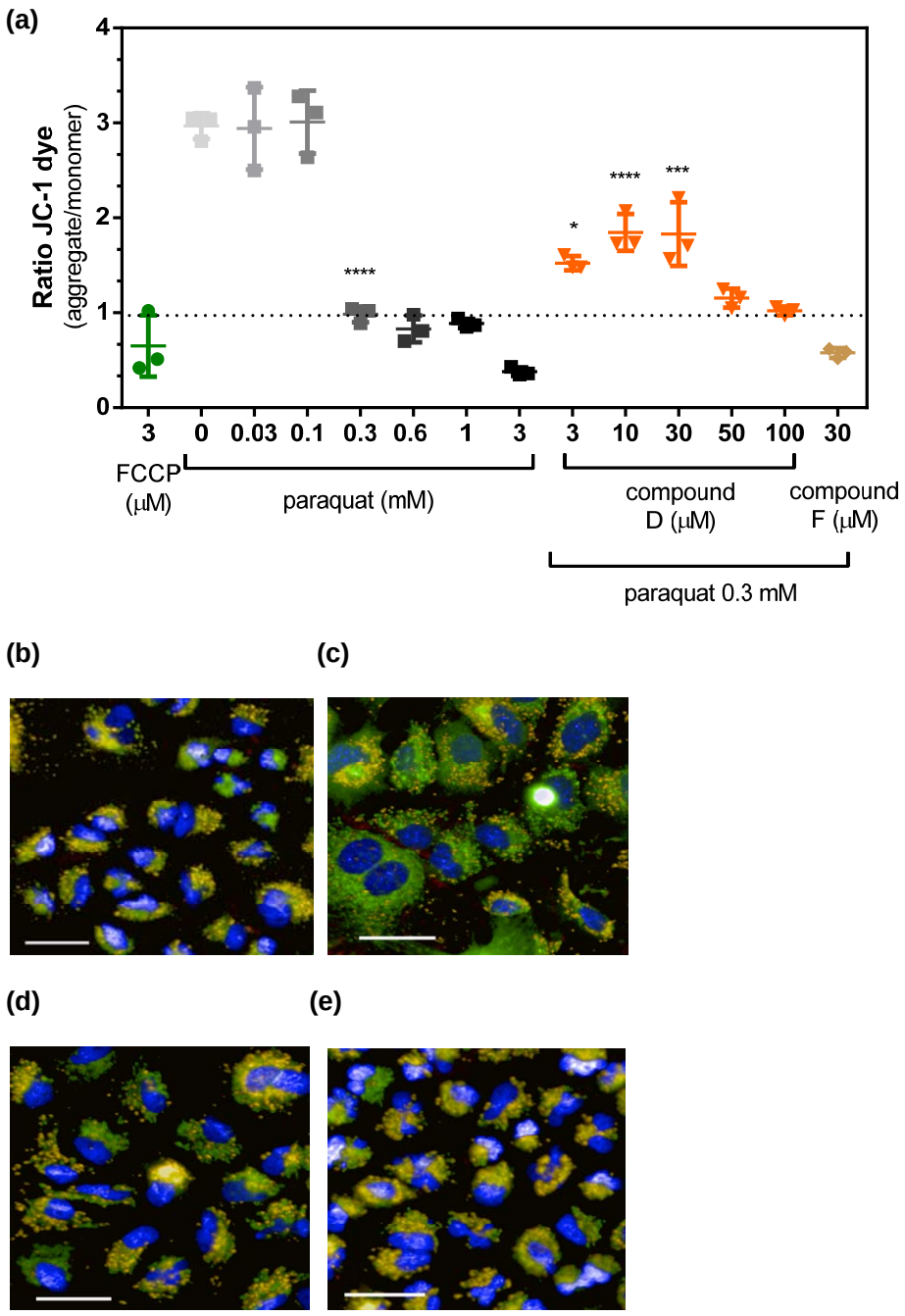

Figure 4.8 Effects of OGG1 activators on mitochondrial membrane potential in A549 cells.

Figure 4.8 Effects of OGG1 activators on mitochondrial membrane potential in A549 cells.

A549 cells were pre-treated for 4 hr with the OGG1 small molecule activators or 0.1% DMSO prior to exposure to 0.3 mM paraquat for 24 hr. Mitochondrial membrane potential was measured from images captured as described in the methods. (a) Graphical representation of the change in the JC-1 ratio with increasing concentration of paraquat and cells pre-treated with the OGG1 activators prior to exposure to a single concentration of paraquat (0.3 mM) for 24 hr. Sample representative images from (b) untreated, (c) 3 mM paraquat, (d) 0.3 mM paraquat , and (e) Compound D (30 μM) with 0.3 mM paraquat exposed cells (Hoechst 33342, overlaid blue; JC-1 monomer, overlaid green; JC-1 aggregate, overlaid orange; CellMask™ Deep Red, overlaid red; line = 40 μm). Significance was determined using a 1-way ANOVA with a Dunnett's post test comparing paraquat alone treated groups to untreated control (0 mM) and OGG1 activator treated groups to 0.3 mM paraquat control ($p<0.05$, ** $p<0.01$, *** $p<0.001$, **** $p<0.0001$). Data shown are from a representative experiment, performed four times.*

(a)

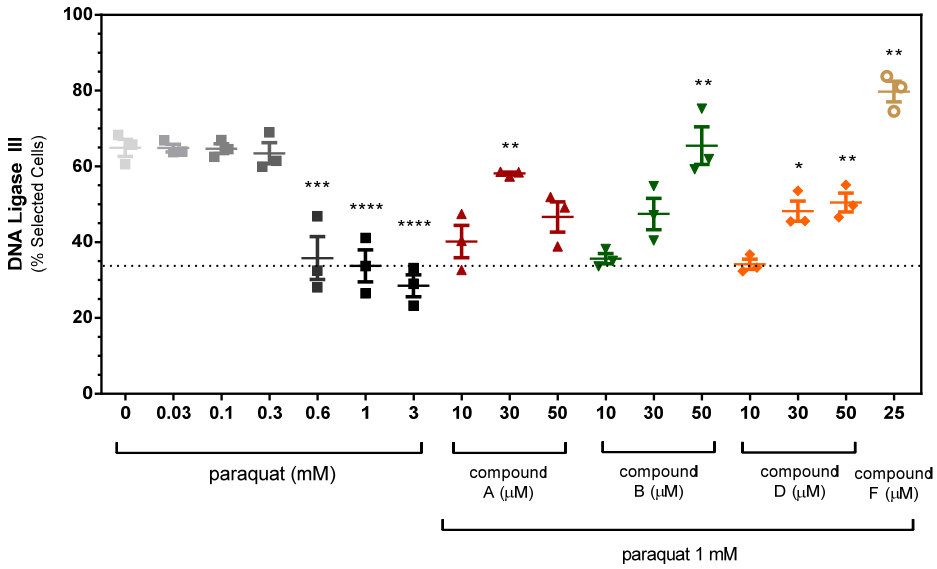

(b)

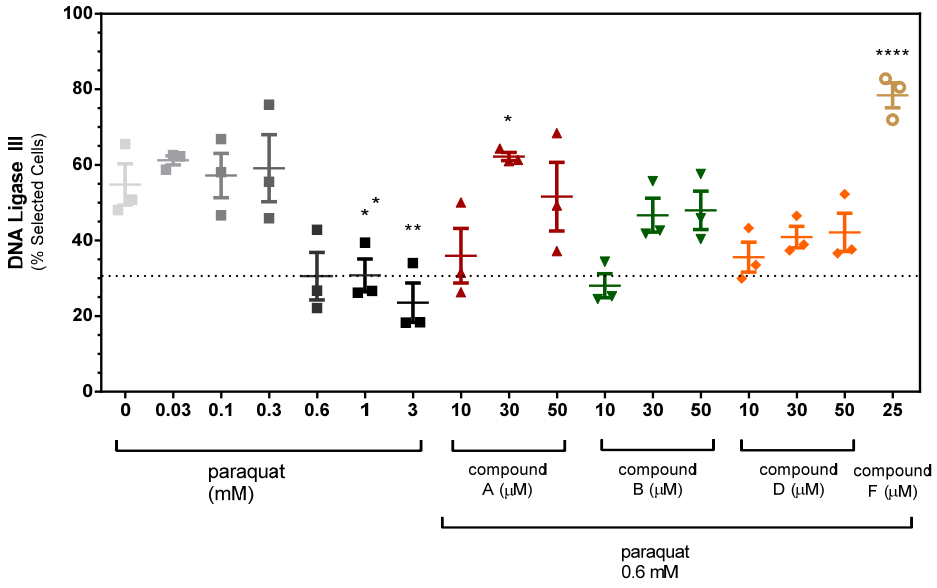

Figure 4.9 Effects of OGG1 tool activators on DNA Ligase III in A549 cells.

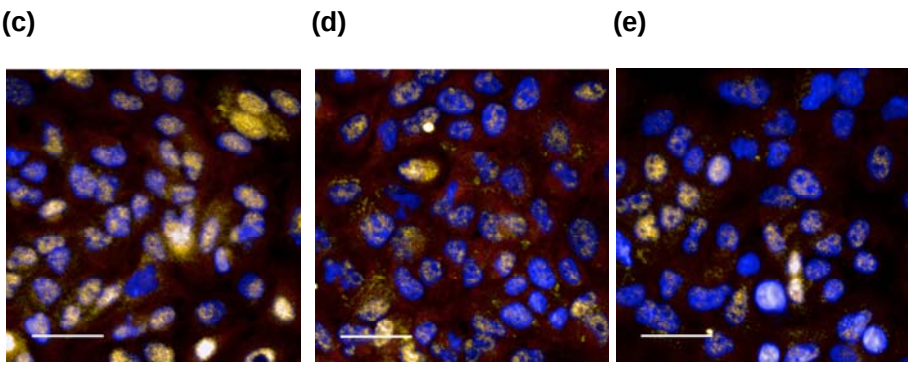

Figure 4.9 Effects of OGG1 activators on DNA Ligase III in A549 cells.

A549 cells were pre-treated for 4 hr with four OGG1 activators prior to addition of 0.6 and 1 mM paraquat for 48 hr and then subjected to immunofluorescence staining for DNA Ligase III (Chapter 2). Changes in DNA Ligase III protein content in the cytoplasm region of cells exposed to (a) 1 mM and (b) 0.6 mM paraquat exposure. Sample images depict the changes in DNA Ligase III (overlaid orange) content in (c) untreated, (d) 0.6 mM paraquat, and (e) 1 mM paraquat exposed cells (CellMask™ Deep Red; overlaid red and Hoechst 33342; overlaid blue, line = 40 µm). Significance was determined using a 1-way ANOVA with a Dunnett's post test comparing paraquat alone treated groups to untreated control (0 mM) and OGG1 activator treated groups to 0.6 or 1 mM paraquat control ($p<0.05$, ** $p<0.01$, *** $p<0.001$, **** $p<0.0001$). Data shown are from a representative experiment, performed two times.*

concentration of paraquat (1 mM). An important observation is that these compounds had reduced effectiveness at ameliorating 8-oxoguanine at this concentration of paraquat exposure (Appendix S7). When the OGG1 activators were tested in the presence of lower levels of paraquat concentration (0.6 mM), applications of the compounds were associated with an apparent restoration of complete (Compounds B and D) DNA Ligase III content (Fig 4.9b). Sample images from 0.6 and 1 mM paraquat exposed cells (Fig 4.9d and 4.9e) depict a reduction in fluorescence intensity (using DyLight™-550) of DNA Ligase III in the cytoplasm region of these cells relative to the untreated control (Fig. 4.9c).

4.2.6 Effect of OGG1 activators on paraquat-induced changes in mitochondrial OGG1 protein content

With the compounds impacting 8-oxoguanine through OGG1, the overriding question had been what effect the compounds had on OGG1 protein levels. As shown in Fig. 3.10, acute paraquat exposure increased OGG1 content within the mitochondria of the cells. Therefore, OGG1 activators were tested as previously described and in the presence of a single concentration of paraquat (0.6 and 0.3 mM). The compounds in a concentration-dependent manner increased OGG1 content in the mitochondria of the cells (Fig. 4.10a and b). The increase associated with Compound A (50 μM) was almost 100% over that obtained with paraquat (0.6 mM), with similar effects observed at 0.3 mM paraquat. Compounds B and F at their respective top concentrations (50 and 30 μM) significantly ($p < 0.05$) increased OGG1 in the cells when exposed to paraquat (0.3 mM). While effective at reducing 8-oxoguanine (Fig. 4.4b), Compound D did not alter OGG1 protein content in A549 cells (Fig. 4.10b). In the absence of paraquat, the OGG1 activators did not have an impact on OGG1 content within the mitochondria (data not shown). Taken together, these data suggest, based on the sample images, that paraquat (0.6 mM) induced OGG1 protein to potentially relocate out of the nucleus and into the mitochondria (Fig. 4.10d) when compared to untreated cells (Fig. 4.10c). A549 cells pre-incubated with Compound A (50 μM) and exposed to paraquat (0.6 mM) , caused a rise in OGG1 protein and was exemplified by the sample image detailing an increase in OGG1 associated green fluorescence (using AlexaFluor®-488, Fig. 4.10e).

(a)

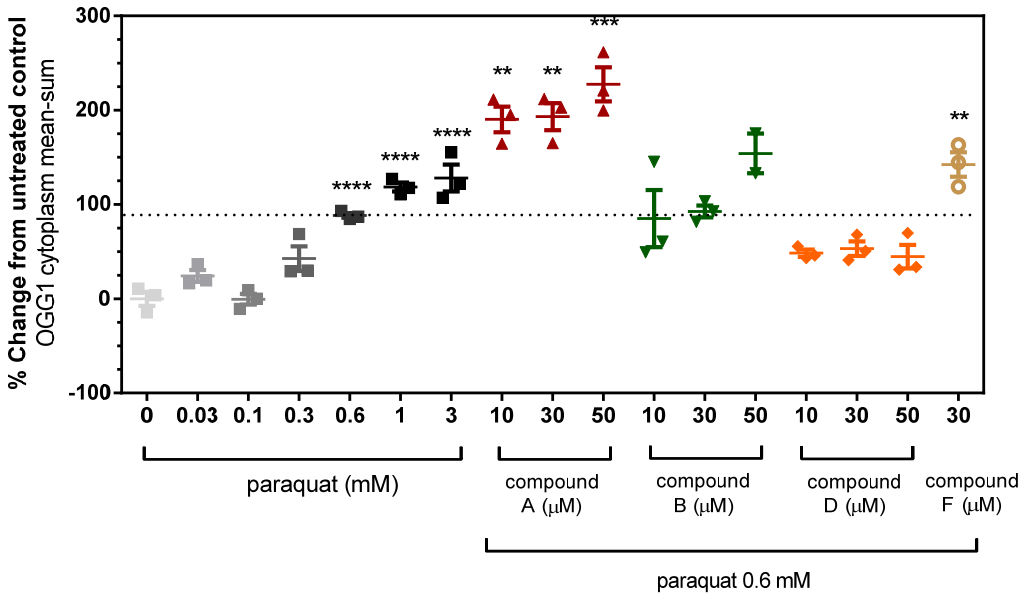

(b)

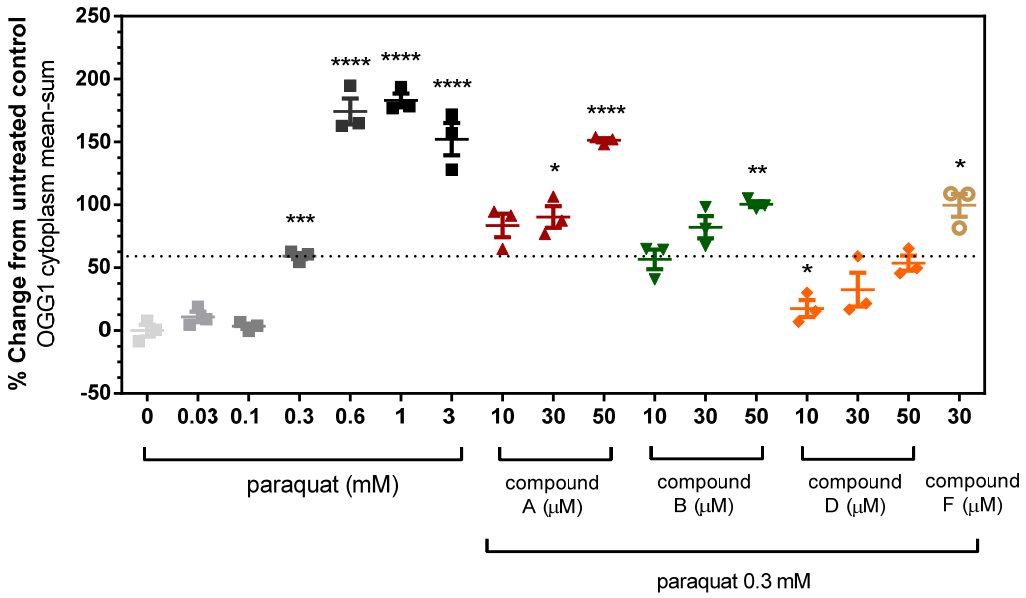

Figure 4.10 Effects of OGG1 activators on OGG1 in A549 cells.

(c) **(d)** **(e)**

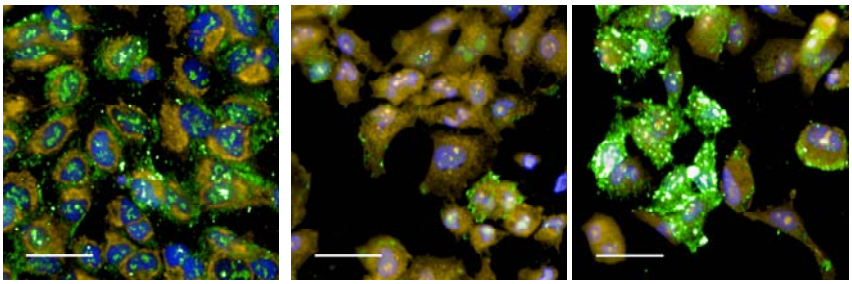

Figure 4.10 Effects of OGG1 activators on OGG1 in A549 cells.

A549 cells were pre-treated for 4 hr with OGG1 activators prior to addition of 0.3 or 0.6 mM paraquat for 48 hr and then subjected to immunofluorescence staining for OGG1 (Chapter 2). Percent change relative to untreated control in OGG1 content of the cytoplasm region of cells exposed to (a) 0.6 mM and (b) 0.3 mM paraquat exposure. Sample images depict the changes in OGG1 (overlaid green) content in (c) untreated, (d) 0.6 mM paraquat, and (e) 50 μM compound A with 0.6 mM paraquat exposed cells (MitoTracker® orange; overlaid orange and Hoechst 33342; overlaid blue, line = 40 μm). Significance was determined using a 1-way ANOVA with a Dunnett's post test comparing paraquat alone treated groups to untreated control (0 mM) and OGG1 activator treated groups to 0.3 or 0.6 mM paraquat control (p<0.05, ** p<0.01, *** p<0.001, **** p<0.0001). Data shown are from an independent experiment, with each condition tested in triplicate.*

4.3 Discussion

The data presented in this chapter demonstrates the ability to impact paraquat-induced mitochondrial oxidative DNA damage in a positive and negative manner. The addition of OGG1 protein to the cells through BacMam transduction enabled a 50% decrease in the overall magnitude of the paraquat-induced 8-oxoguanine response relative to control BacMam null transduced cells. Additionally, the OGG1 protein had a protective effect on overall cell survival. Through the use of various BacMam constructs, it was observed that paraquat induced oxidative DNA damage in the mitochondria and that OGG1 was recruited to the site of the DNA damage. Blocking translation of *OGG1* to active OGG1 protein through the use of *OGG1* siRNA demonstrated that the oxidative DNA lesion could be potentiated in both untreated (300%) and paraquat (1500%) exposed cells. It was observed that the half-maximal effective concentrations were similar across the OGG1 siRNA treatment groups. These data suggests that the mechanism of action for paraquat is unchanged but in the absence of OGG1, the 8-oxoguanine lesion begins to accumulate with time. These data support previously published reports demonstrating the beneficial and deleterious effects of, respectively, increasing or decreasing OGG1 content within the cell (Ruchko et al., 2011; Su et al., 2013).

While it has been shown previously that molecules such as 8-bromoguanine can exert a feed-forward effect by activating 8-oxoguanine DNA repair through OGG1, it has not been previously shown that a small molecule OGG1 activator could have an impact on reducing overall oxidative DNA damage (Fromme et al., 2003). Through a screening effort designed to identify potential OGG1 activators, several molecules were identified. While these compounds represent early leads and are classified as tool molecules, several compounds were found to be capable of activating and accelerating repair of paraquat-induced 8-oxoguanine by almost 60%. Moreover, several of the tool compounds (Compounds A, B, D, F) were capable of blocking phenotypic changes that are associated with paraquat-induced DNA damage such as changes in cell morphology and this high-responder phenotype. For these two parameters, Compounds A, B, D, and F could restore by 100% the paraquat-induced changes. Furthermore, Compound D was shown to have a functional impact by blocking paraquat-induced mitochondrial membrane depolarization as assessed by JC-1. This lent support for the OGG1 activators to have a functional impact, through the reduction of paraquat-induced mitochondrial DNA damage whereby mitochondrial membrane potential could remain intact.

Moreover, paraquat was shown to induce a reduction in DNA Ligase III which, as discussed earlier, is potentially the rate limiting enzyme in base excision repair. Paraquat was shown to reduce DNA Ligase III by about 50% and was shown to be reversed by the addition of the OGG1 activators (Compound A, B, D, and F). Finally, OGG1 protein was observed to rise in the mitochondria following paraquat exposure, with certain OGG1 activators (Compounds A, B, and F) enabling OGG1 to accumulate further. These data suggest that the OGG1 activators can reduce paraquat-induced oxidative mitochondrial DNA damage. It can be appreciated that the decline in 8-oxoguanine appears to coincide with an increase DNA Ligase III indicating full DNA repair was executed. These data also suggest that by reducing 8-oxoguanine there is a beneficial effect on the mitochondria. A summary of the compounds and their activity in the various assays discussed is presented in Table 4.2.

While additional work is needed to optimize the compounds and to confirm where on the OGG1 protein the small molecules bind, the tool compounds provide the beginnings for the identification of OGG1 activators that could be evaluated for the capability of modifying disease in patients. Initial test compounds were assayed in the paraquat-induced cytochrome c translocation assay; however, due to antibody supply the assay could not be repeated and would require additional assay validation and optimization. Early results suggest the OGG1 activators prevented paraquat-induced cytochrome *c* translocation, and in so doing, prevented intrinsic apoptosis.

Additional work is ongoing to confirm the data presented in this chapter relative to established methods presented in the literature such as long chain PCR. This method enables the relative quantification of the number of damaged base pairs in a given cell. Early results appear promising and confirm paraquat-induced mitochondrial DNA damage (Appendix S5). Finally, while later time points (48 hr) had initially been tested in the paraquat-induced JC-1 assay (Fig. 3.7), the OGG1 activators were not tested against this time point and highlight a potential path forward to examine their functional impact on mitochondrial health.

	Top Concentration (μM)	Reduced paraquat-induced 8-OG	Restored paraquat-induced nuclear size changes	Reduced paraquat-induced high responders	Restored paraquat-induced loss of mito-membrane potential	Restored paraquat-induced loss of DNA-Ligase III	Increased paraquat-induced OGG1 mito-content
Compound A	50	**Positive**	**Positive**	**Positive**	**No effect**	**Positive**	**Positive**
Compound B	50	**Positive**	**Positive**	**Positive**	**No effect**	**Positive**	**Positive**
Compound C	50	**No effect**	**No effect**	**No effect**	**No effect**	**Not Tested**	**Not Tested**
Compound D	50	**Positive**	**Positive**	**Positive**	**Positive**	**Positive**	**No effect**
Compound F	30/25	**Positive**	**Positive**	**Positive**	**Positive**	**Positive**	**Positive**

Table 4.2 Summary of activity for OGG1 activators.

mito, mitochondrial

8-OG, 8-oxoguanine

CHAPTER 5:

Examination of the role of mitochondrial DNA damage on cellular energy production and on mitochondrial dynamics

5. Examination of the role of mitochondrial DNA damage on cellular energy production and on mitochondrial dynamics

5.1 Introduction

An essential requirement for cell survival is a constant supply of energy, typically derived from the breakdown of glucose and through the electron transport chain. Oxidative DNA damage can lead to somatic mutations, enabling the translation of proteins with a genetic code modification typically rendering them non-functional (Chinnery and Hudson, 2013). As discussed earlier, oxidative DNA damage affected the mitochondrial DNA and this in turn could lead to reduced translation of the protein sub-units encoded by the mtDNA required for oxidative phosphorylation. Previously, it has been demonstrated that increasing concentrations of hydrogen peroxide increasingly destabilize the mitochondria leading to decreased ATP production (Small et al., 2014). Furthermore, Small and colleagues demonstrated that this increase in oxidative stress led to mitochondrial membrane depolarization, elevated superoxide formation, and a rise in mitophagy (a macroautophagy selecting mitochondria). Work with mitochondria-rich cardiomyocytes has suggested a possible association between nutrient deprivation resulting in a loss of ATP linked to a reduction in OGG1 protein content (Siggens et al., 2012). Increased ROS and mitochondrial DNA damage can lead to alterations in the outer mitochondrial membrane and this could in turn cause a decline in energy production, which has been shown to be a contributing factor to many chronic diseases and to aging (Paradies et al., 2010). Previous studies have shown that cells exposed to the chemotherapeutic agent bleomycin experience elevated levels of mtDNA damage, an increase in mitochondrial dysfunction, and a loss of ATP production (Brar et al., 2012). Further, it was demonstrated by Brar et al. that these changes in mitochondrial state led to a rise in apoptosis (Brar et al., 2012). Therefore, the aim of the following experiments was to examine the effect of 8-oxoguanine lesion accumulation within mtDNA has on fission and fusion and to assess whether the OGG1 activators would impact mitochondrial dynamics.

ATP and ADP were measured in A549 cells following exposure to cigarette smoke or paraquat, where the magnitude of change was larger for paraquat compared to cigarette smoke. To examine the effects that increased base excision repair might

have on ATP and ADP; the OGG1 activators were tested at a single concentration against a paraquat concentration-response curve. This showed that enhanced repair of the 8-oxoguanine DNA lesion partially prevented the loss of ATP but only marginally altered ADP levels.

Accumulation of ROS within the mitochondria and ensuing oxidative damage to various macromolecules initiates a survival mechanism. As Chauhan and colleagues reviewed, the mitochondria divide and join together through fission and fusion, respectively, to maintain cell survival and ATP levels (Chauhan et al., 2014). Therefore, measurement of the number of mitochondria, sometimes referred to as mitochondrial mass, was made using the surface marker TOM20 to determine whether the paraquat-induced reduction in ATP could be attributed to a loss in the number of mitochondria. Further, the effect of OGG1 activation on reducing oxidative DNA damage was scrutinized to determine if there was an association between reduced 8-oxoguanine and changes in mitochondrial mass.

Moreover, as was presented earlier (see Mitochondrial Dynamics 1.8), the mitochondria will activate fission and fusion in response to changes the cell senses in the levels of ROS, oxidative phosphorylation, ATP, and GSSG (Mishra and Chan, 2016). Therefore, the present studies examined the interaction of the mitochondria and their response to the oxidant stress inducer paraquat. Markers of fission (DRP1) and fusion (MFN1) were used to gauge the effects of paraquat-induced changes in mitochondrial dynamics. Predominately, fission enables a dilution of mitochondrial DNA damage, where as fusion concentrates the DNA in an effort to bring un-damaged DNA to two partially damaged organelles (Chauhan et al., 2014). As before with TOM20, the effect of OGG1 activation on the reduction of the 8-oxoguanine lesion within the mitochondrial genome was evaluated for its potential impact on mitochondrial dynamics. Additional markers such as the phosphorylation of DRP1 or OPA1 could have been examined, but the identification of changes in total DRP1 and MFN1 were designed as initial observations in the engagement of this dynamic process. These results suggest a possible association between a reduction in mtDNA 8-oxoguanine content and prevention of mitochondrial turnover, leading to an increase in cell health.

5.2 Results

5.2.1 Effect of cigarette smoke on cellular energetic state.

Previous studies have evaluated the acute effects of cigarette smoke exposure on the cellular energetic state. Hoffman and co-workers showed a rise in ATP concentration, whereas Kamp and colleagues found a loss of ATP concentration following cigarette smoke exposure (Hoffmann et al., 2013; Kamp et al., 1998). Exposure to cigarette smoke was used to provoke oxidative DNA damage. It was observed that ATP levels declined while ADP levels remained relatively constant. A549 cells exposed to the vapor phase of one cigarette for 5 min experienced a decline in ATP, which reached significance at 48 hr post exposure, where there was a significant 77% ($p<0.0001$) decline in ATP concentration relative to the air control (Table 5.1). Meanwhile, ADP concentration significantly decreased 24 hr post cigarette smoke exposure by 32% ($p<0.01$). By 48 hr post exposure, the decline in ADP did not reach significance (19%, $p<0.212$). The loss of significance could be due the observed increase in the standard error of the mean (SEM) for ADP, 48 hr cigarette smoke exposure (Table 5.1). The loss in ATP concentration was observed by a decrease in the ATP/ADP ratio (Fig. 5.1). As described above, A549 cells produce energy primarily through glycolysis and this observation could explain why if ATP concentrations decline, ADP levels should rise and that was not observed (Jantzen et al., 2012).

5.2.2 Effect of paraquat on cellular energetic state over time.

In chapters 3 and 4, it was established that mitochondrial function was altered by the loss of membrane potential from cells exposed to paraquat and cigarette smoke. Loss of membrane potential prevents the formation of the electro-chemical gradient required for ATP generation (Sureshbabu and Bhandari, 2013). In response to paraquat, changes in ATP production have been shown to vary depending on cell type (Forman et al., 1980; Palmeira et al., 1994). To examine the effect paraquat has on ATP and ADP, A549 cells were exposed to increasing concentrations for 24 and 48 hr. Paraquat induced a concentration- and time-dependent loss in cellular energy levels. Following 24 hr exposure to paraquat (3 mM), there was a 70% decrease in the ATP/ADP ratio compared to untreated cells (Fig 5.2). By 48 hr of exposure,

	24-hr		48-hr	
	air	**cigarette smoke**	**air**	**cigarette smoke**
ATP Average (µmoles/ g protein)	3.138	2.175	3.438	0.778
ATP SEM	0.404	0.305	0.123	0.158
t-test (p value)		0.1301		0.0002
% Change		30.68%		77.36%
ADP Average (µmoles/ g protein)	39.740	26.846	32.873	26.685
ADP SEM	1.995	0.842	1.721	3.794
t-test (p value)		0.0040		0.2117
% Change		32.45%		18.82%

Table 5.1 Summary of ATP and ADP concentrations 24 and 48 hr post air or cigarette smoke exposure.

SEM = standard error of the mean, n = 3

*Significance was determined using an un-paired, 2-tailed t-test (** p<0.01, *** p<0.001).*

Percent change calculated relative to the appropriate air control.

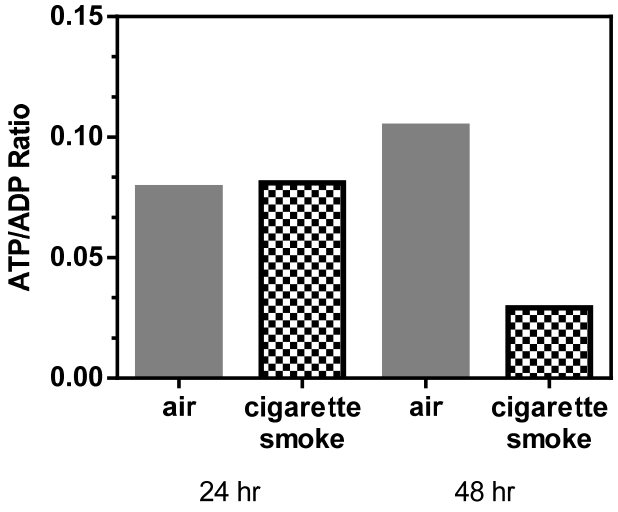

Figure 5.1 Effects of cigarette smoke-induced changes in ATP/ADP ratio over time.

A549 cells were exposed to air or cigarette smoke as described in Chapter 2. The cells were collected and lysed according to the manufacturer instructions for both assay kits, ATP and ADP. The respective concentrations were determined and normalized relative to the protein concentration of each test sample. The average ATP and ADP concentrations from an independent study, with each condition tested as an n=3 (Table 5.1), were then divided to create the ATP/ADP ratio and is represented as a single value.

paraquat (3 mM) caused a 97% decline in the ATP/ADP ratio (Fig. 5.2). These changes were due to the significant loss of 57% ($p<0.01$) in ATP levels and a significant rise of 18% ($p<0.05$) in ADP concentrations 24 hr post addition of paraquat (3 mM). These changes in ATP and ADP continued with time, where there was a significant loss of 87% ($p<0.001$) in ATP and a significant rise of 300% in ADP ($p<0.0001$) concentrations 48 hr post exposure to paraquat (Table 5.2). These data confirmed that paraquat affects the cellular energetic state of A549 cells. The decline in ADP from untreated cells from 24 to 48 hr could be associated with the observation that A549 cells are contact inhibited and will exit log phase growth and therefore the energy requirements of the cells will be altered. While it was observed that the ATP concentrations from the air treated groups in Table 5.1 are about 50% lower compared to the untreated ATP concentrations found in Table 5.2, this could be attributed to previous observations that the mechanical stimulation from the fan in the air control group has an effect on the cells.

5.2.3 Effect of OGG1 activators on paraquat-induced loss of ATP.

In the present studies, certain OGG1 activators mitigated paraquat-induced loss of mitochondrial membrane potential. Given the importance of maintaining the membrane potential for energy production, the more promising OGG1 activators (Compounds A, D, and F) were tested to determine their effect on the cellular energetic state. As shown in Fig. 5.2, paraquat-induced a concentration dependent decline in the ATP/ADP ratio at 24 and 48 hr. A549 cells were separately pre-incubated (4 hr) with several of the OGG1 activators at a single concentration (based on an effective concentration for reducing paraquat-induced 8-oxoguanine, Chapter 4), and then exposed to increasing concentrations of paraquat. In the absence of paraquat, Compounds A and F did not alter ATP or ADP concentrations relative to the untreated control (Table 5.3). However, Compound D elevated ATP concentrations by almost 50%, but had no effect on ADP levels and this led to a rise in the ATP/ADP ratio observed in Fig. 5.3b.

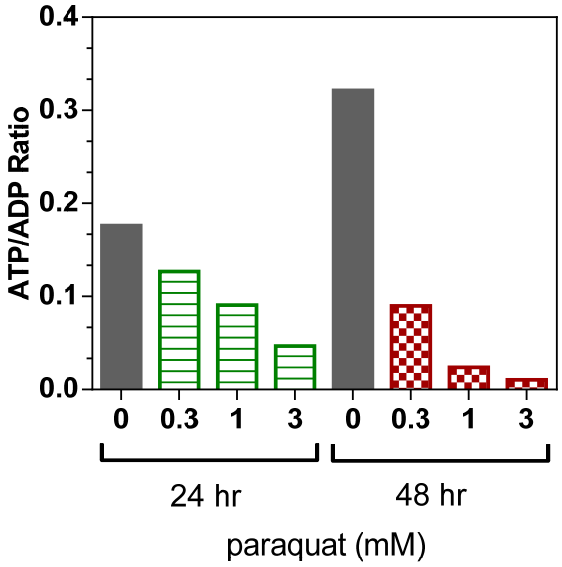

Figure 5.2 Effects of paraquat-induced changes in ATP/ADP ratio over time.

A549 cells were incubated with varying concentrations of paraquat for 24 or 48 hr as described in Chapter 2. The cells were collected and lysed according to the manufacturer instructions for both assay kits, ATP and ADP. The respective concentrations were determined and normalized relative to the protein concentration of each test sample. The average ATP and ADP concentrations from an independent study, with each condition tested as an n=6 (Table 5.2), were then divided to create the ATP/ADP ratio and is represented as a single value.

	24-hr				48-hr			
Paraquat [mM]	**0**	**0.3**	**1**	**3**	**0**	**0.3**	**1**	**3**
ATP Average (µmoles/ g protein)	6.295	3.126	2.488	1.990	5.522	2.202	1.169	0.730
ATP SEM	0.828	0.136	0.066	0.044	0.814	0.073	0.086	0.117
t-test (p value)		0.1001	0.0265	0.0094		0.0023	0.0003	0.0002
% Change		32.73%	46.46%	57.17%		60.13%	78.83%	86.79%
ADP Average (µmoles/ g protein)	35.750	24.633	27.383	42.505	17.176	24.485	49.195	68.686
ADP SEM	1.228	0.936	2.060	1.798	1.941	2.230	1.736	1.466
t-test (p value)		0.0000	0.0058	0.0112		0.0330	0.0000	0.0000
% Change		33.05%	23.40%	-18.90%		-42.56%	-186.42%	-299.90%

Table 5.2 Summary of ATP and ADP concentrations 24 and 48 hr post paraquat exposure.

SEM = standard error of the mean, n= 6

Significance was determined using a 1-way ANOVA with a Dunnett's post test comparing to untreated control

(p<0.05, ** p<0.01, *** p<0.001, **** p<0.0001).*

Percent change calculated relative to the appropriate untreated control.

Paraquat-induced changes in ATP/ADP were relatively consistent across the three independent experiments, except for the diminished levels of ADP from 0.3 mM paraquat in Fig. 5.3b (Table 5.3). Compound A partially prevented the paraquat-induced fall of ATP/ADP (Fig. 5.3a). Moreover, the compound induced a significant 2-fold ($p<0.05$) rise in ATP compared to paraquat (3 mM) alone (Table 5.3). ADP concentrations appear unaltered with this compound. Similarly, compound F (Fig. 5.3c) partially prevented the decline in the ATP/ADP ratio. Compound F also induced a significant 2.8-fold ($p<0.01$) rise in ATP concentration compared to similarly 3 mM paraquat exposed cells (Table 5.3). However, with this compound there was a measureable significant 54% ($p<0.01$) increase in ADP concentration when compared to paraquat-exposed cells in the absence of compound (Table 5.3).

By contrast to the findings above, compound D only had a marginal effect on the ATP/ADP ratio in response to paraquat treatment (Fig. 5.3b). This was also suggested by the individual ATP and ADP values (Table 5.3). Compound D had a varied effect on ATP levels and a trend reaching significance ($p<0.01$) at 1 mM paraquat for increasing ADP concentrations. The data presented in Fig. 5.2 and Table 5.2 demonstrates that the OGG1 activators, Compounds A and F, partially protected cells from the paraquat-induced energy loss; whereas Compound D was the exception, offering no protection.

						compound A 30 µM				
Paraquat [mM]	**0**	**0.3**	**0.6**	**1**	**3**	**0**	**0.3**	**0.6**	**1**	**3**
ATP Average (µmoles/ g protein)	3.177	1.887	1.187	1.021	0.626	3.926	2.896	2.890	2.666	1.314
ATP SEM	1.017	0.060	0.080	0.062	0.047	0.028	0.228	0.243	0.054	0.107
t-test							0.0129	0.0026	0.0000	0.0042
Fold Change							1.53	2.43	2.61	2.10
ADP Average (µmoles/ g protein)	11.547	19.723	39.714	46.802	53.455	11.083	29.202	37.954	35.400	58.119
ADP SEM	1.166	2.171	3.968	1.480	4.832	0.656	1.423	2.964	0.873	1.557
t-test							0.0217	0.7402	0.0027	0.4102
Fold Change							1.48	0.96	0.76	1.09

						compound D 30 µM				
Paraquat [mM]	**0**	**0.3**	**0.6**	**1**	**3**	**0**	**0.3**	**0.6**	**1**	**3**
ATP Average (µmoles/ g protein)	4.601	2.564	1.430	1.469	0.955	2.857	2.587	2.224	2.201	1.374
ATP SEM	0.680	0.100	0.126	0.154	0.103	0.086	0.046	0.063	0.139	0.304
t-test							0.8421	0.0048	0.0245	0.2612
Fold Change							1.01	1.56	1.50	1.44
ADP Average (µmoles/ g protein)	7.493	1.490	13.538	22.336	40.479	7.798	13.605	31.289	32.169	45.916
ADP SEM	0.403	0.149	0.764	0.902	0.907	0.636	0.523	2.400	0.418	3.358
t-test							0.0000	0.0021	0.0006	0.1931
Fold Change							9.13	2.31	1.44	1.13

Table 5.3 Summary of ATP and ADP concentrations following pre-treatment with an OGG1 activator in the presence of varying concentrations of paraquat for 48 hr.

						compound F 25 µM				
Paraquat [mM]	**0**	**0.3**	**0.6**	**1**	**3**	**0**	**0.3**	**0.6**	**1**	**3**
ATP Average (µmoles/ g protein)	4.936	2.835	1.668	0.922	0.607	4.658	3.237	3.224	2.876	1.728
ATP SEM	0.278	0.071	0.109	0.061	0.087	0.210	0.031	0.171	0.275	0.084
t-test							0.0065	0.0015	0.0023	0.0007
Fold Change							1.14	1.93	3.12	2.85
ADP Average (µmoles/ g protein)	12.638	7.864	19.201	27.620	41.326	13.023	25.699	36.234	42.044	63.471
ADP SEM	0.763	0.504	0.657	1.657	3.056	0.352	1.183	1.471	0.757	1.856
t-test							0.0002	0.0005	0.0014	0.0035
Fold Change							3.27	1.89	1.52	1.54

Table 5.3 Summary of ATP and ADP concentrations following pre-treatment with an OGG1 activator in the presence of varying concentrations of paraquat for 48 hr.

SEM = standard error of the mean, n= 3

Significance was determined using an un-paired, 2-tailed t-test comparing compound to paraquat/ without compound control (p<0.05, ** p<0.01, *** p<0.001, **** p<0.0001).*

Percent change calculated relative to the appropriate untreated control.

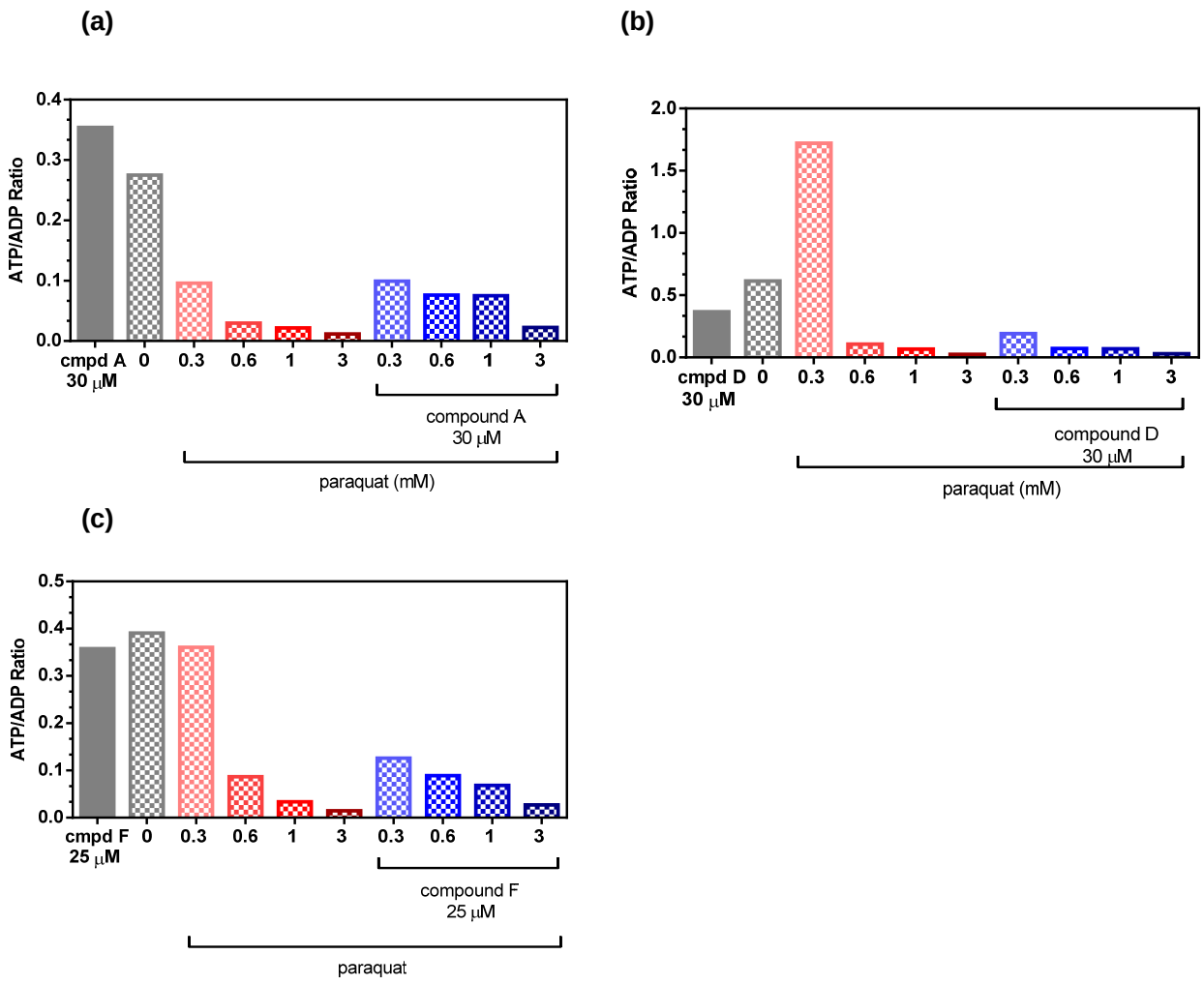

Figure 5.3 Effects of OGG1 activators on paraquat-induced changes in ATP/ADP ratio.

Figure 5.3 Effects of OGG1 activators on paraquat-induced changes in ATP/ADP ratio.

A549 cells were pre-incubated (4 hr) with a single concentration of an OGG1 activator prior to the addition of varying concentrations of paraquat for 48 hr as described in Chapter 2. The cells were collected and lysed according to the manufacturer instructions for both assay kits, ATP and ADP. The respective concentrations were determined and normalized relative to the protein concentration for each test sample. The average ATP and ADP concentrations from independent studies, with each condition tested as an n=3 (Table 5.3), these values were then divided to create the ATP/ADP ratio and is represented as a single value. Graphical representation of the ATP/ADP ratio of A549 cells exposed to increasing concentrations of paraquat (mM) for 48 hr following pretreatment with (a) Compound A 30 μM, (b) Compound D 30 μM, or (c) Compound F 25 μM.

5.2.4 Effect of paraquat and OGG1 activators on mitochondrial mass.

Chauhan and coworkers have suggested that a cell will compensate by increasing the number of mitochondria present within a cell as superoxide anions accumulate within the inner mitochondrial membrane space, which in turn adversely affect mtDNA (Chauhan et al., 2014). In the present studies, TOM20 was used to qualitatively assess mitochondrial number. This mitochondrial surface protein, which is a subunit of the mitochondrial import receptor, has been shown to be a suitable marker of mitochondrial mass (Rehman et al., 2012). Thus, Tom20 expression is a reflection on the number of mitochondria present within the cell. A549 cells were exposed to increasing concentrations of paraquat, and TOM20 expression was quantified by fluorescence imaging. After 48 hr of exposure to paraquat, high concentrations significantly reduced TOM20 expression by 25% ($p < 0.001$) at 3 mM (Fig. 5.4a). Reduced TOM20 expression continued in a non-concentration dependent manner for 1 and 0.6 mM and then returned to baseline at 0.3 mM paraquat. However, lower concentrations of paraquat (0.1 and 0.03 mM) significantly elevated TOM20 by about 20% ($p<0.01$, Fig. 5.4a). It can be observed in Fig. 5.4b, that TOM20 expression was co-localized with MitoTracker® orange, supporting TOM20 as a fluorescent protein marker for the number of mitochondria.

To determine whether OGG1 activation and base excision repair would influence TOM20 expression, the cells were pretreated with selected OGG1 activators for 4 hr prior to addition of a single concentration of paraquat (0.6 mM). The cells were incubated for 48 hr and then evaluated for TOM20 protein expression. The OGG1 activators had a limited effect on TOM20 expression (Fig. 5.4c). The dotted line in the graph represents the level of TOM20 expression detected from the 0.6 mM paraquat, with values above the line representing an improvement and below the line representing a decline in mitochondrial mass. The data trend in the presence of Compound A was to mitigate the decline in paraquat-induced TOM20 expression; however, the variability in the data prevents the data from reaching statistical significance. Compounds D and F appear to significantly assist in a concentration dependent manner (Compound D)

(a)

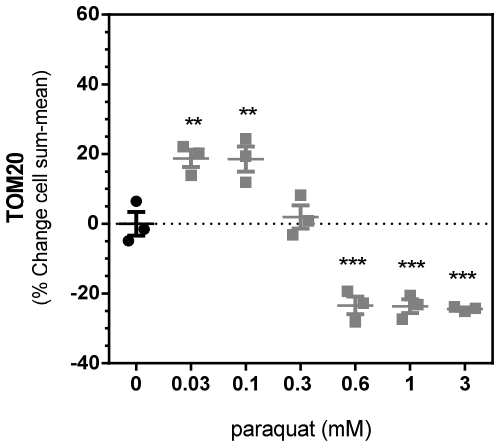

(b)

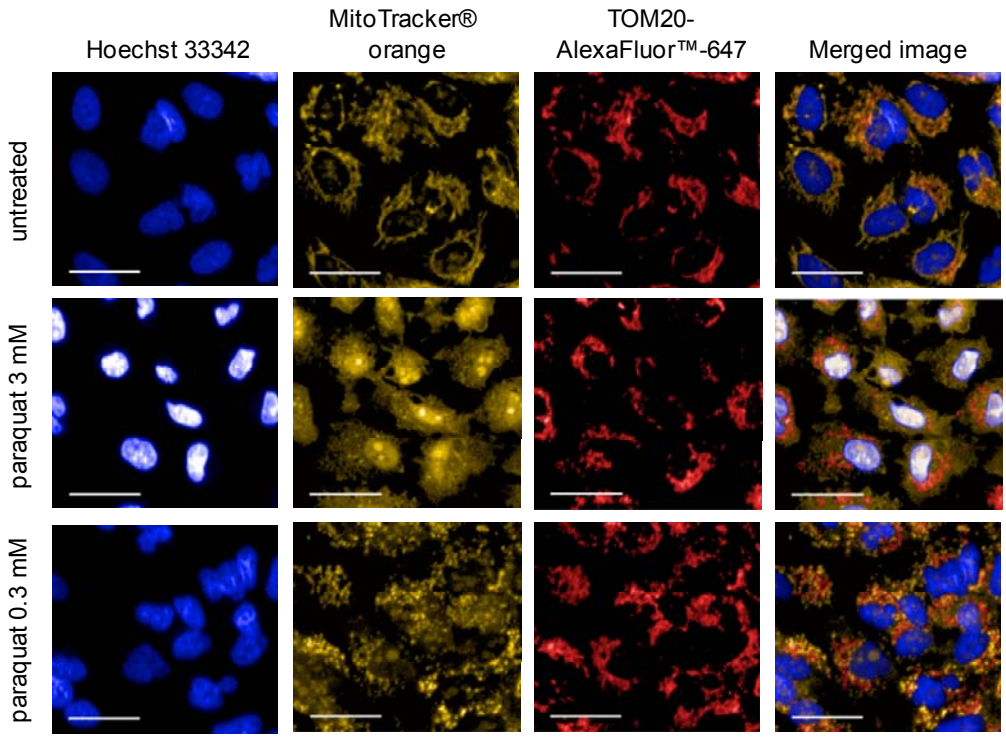

Figure 5.4 Effects of paraquat and OGG1 activators on mitochondrial mass in A549 cells.

(c)

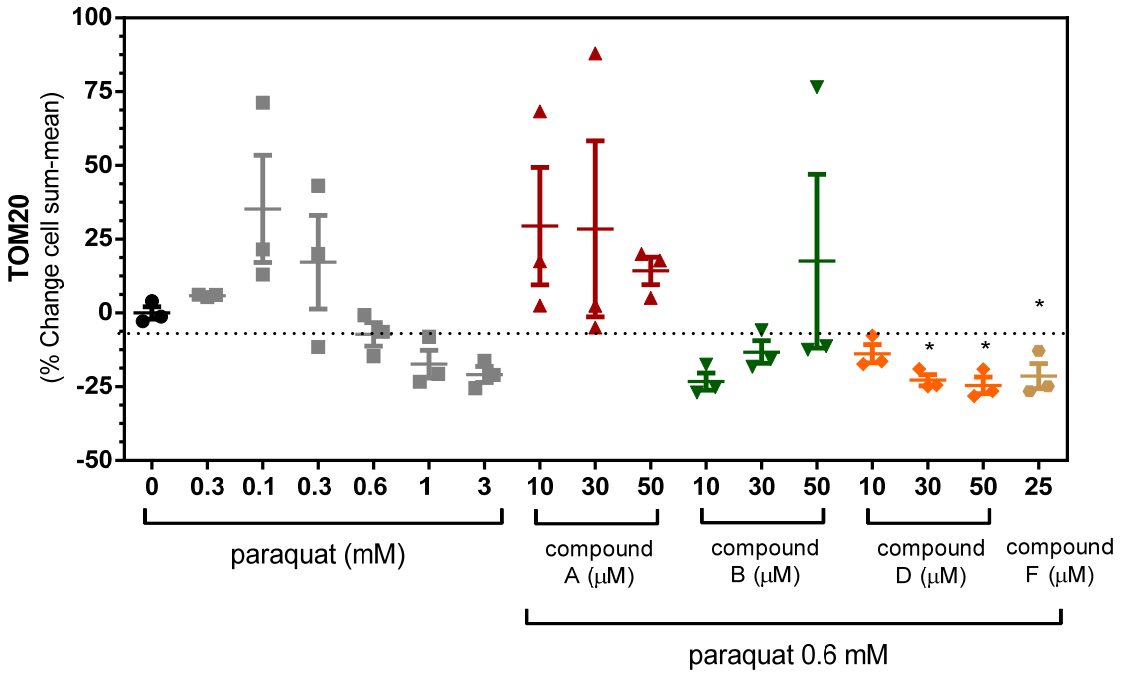

Figure 5.4 Effects of paraquat and OGG1 activators on mitochondrial mass in A549 cells.

Figure 5.4 Effects of paraquat and OGG1 activators on mitochondrial mass in A549 cells.

A549 cells were exposed to (a) and (b) varying concentrations of paraquat (mM) or (c) pre-treated (4 hr) with OGG1 tool activators prior to addition of a single concentration of paraquat (0.6 mM) for 48 hr. The cells were subjected to formaldehyde fixation for immunofluorescence detection of TOM20, with images acquired and analyzed as described in Chapter 2. (a) Graphical representation of the changes in TOM20 protein content in the cytoplasm region of cells exposed to increasing concentrations of paraquat. (b) Sample representative images from A549 cells exposed to increasing concentrations of paraquat (48 hr) are shown with color overlays (Hoechst 33342, overlaid blue; MitoTracker® orange, overlaid yellow; anti-TOM20-AlexaFluor®-647, overlaid red; line = 40 μm). (c) Changes in TOM20 expression from A549 cells pre-treated (4 hr) with OGG1 activators (10-50 μM) prior to paraquat (0.6 mM) exposure for 48 hr. Significance was determined using a 1-way ANOVA with a Dunnett's post test comparing paraquat alone treated groups to untreated control (0 mM) and OGG1 activator treated groups to 0.6 mM paraquat control ($p<0.05$, ** $p<0.01$, *** $p<0.001$). Data shown are from two independent experiments, with each condition tested in triplicate.*

with paraquat-induced decline ($p<0.05$) of TOM20 protein expression. Compound B was not statistically different from 0.6 mM paraquat control. Additional work is required to further understand whether improving overall base excision repair impacts oxidative stress-induced changes on mitochondrial mass.

5.2.5 Effect of paraquat and the OGG1 activators on mitochondrial fission.

In response to increased levels of oxidative stress and decreased energy production, the mitochondria will undergo fission and fusion (Chauhan et al., 2014). During fission, the mitochondria split apart to separate off sections of the organelle that have been damaged by ROS. A common marker for fission is DRP1, a protein that is recruited at the point of division for the mitochondria was used as a marker of mitochondrial fission (Ahmad et al., 2015; Aravamudan et al., 2014; Hoffmann et al., 2013; Willems et al., 2015). To monitor this activity in cells, a DRP1 immunofluorescence assay was validated using commercially available antibodies . Following paraquat (3 mM) exposure for 18 hr, DRP1 content within the cells increased by about 60% ($p<0.05$, Fig. 5.5a), with the remaining paraquat concentrations trending toward an increase but did not reach statistical significance. DRP1 expression continued to rise over time, and at 24 hr of exposure to 0.3 – 3mM paraquat there was a significant ($p< 0.0001$) concentration-dependent rise within the cells (Fig. 5.5b). However, by 30 hr DRP1 content began to return toward baseline for the top test concentration of 3 mM (Fig. 5.5c) and by 48 hr, there was a 25% ($p<0.05$) decrease in DRP1 content (Fig. 5.5d). However, DRP1 expression remained elevated at 48 hr post exposure in cells treated with 0.3 mM paraquat.

To examine whether accelerated repair of oxidative DNA damage would alter mitochondrial fission, selected OGG1 activators were tested for their effect on DRP1 expression. A549 cells were pre-incubated (4 hr) with the compounds (10-50 μM) prior to 48 hr exposure to a single concentration of paraquat (0.6 mM), which was chosen because of the ability of the selected compounds to block paraquat-induced 8-oxoguanine. All of the compounds significantly prevented DRP1 loss (48 hr, Fig. 5.6a).

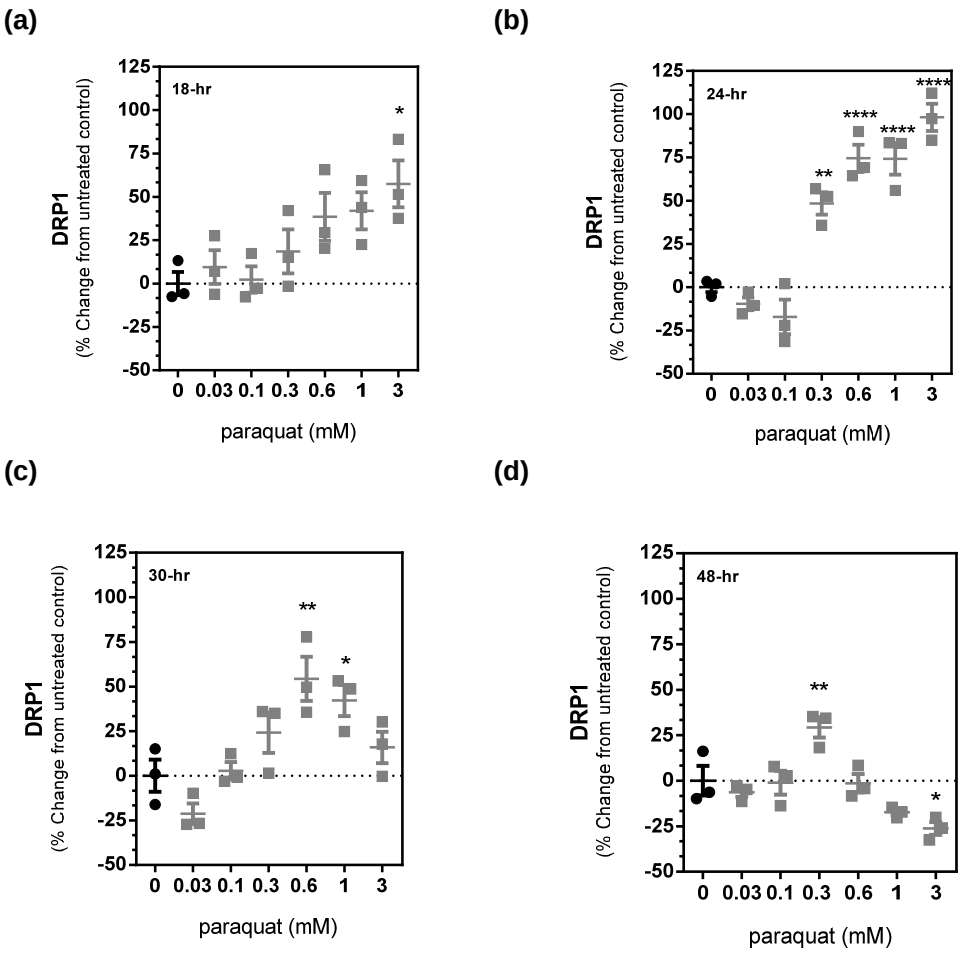

Figure 5.5 Effects of paraquat on mitochondrial fission in A549 cells over time.

A549 cells were exposed to varying concentrations of paraquat (mM) over time. The cells were subjected to formaldehyde fixation for immunofluorescence detection of DRP1; images were acquired and analyzed as described in Chapter 2. Graphical representation of the changes in DRP1 protein content in the cytoplasm region of cells exposed to paraquat are shown following (a) 18 hr, (b) 24 hr, (c) 30 hr, and (d) 48 hr exposure. Significance was determined using a 1-way ANOVA with a Dunnett's post test comparing treatment groups to untreated sample (p<0.05, ** p<0.01, *** p<0.001, **** p<0.0001). Data shown are from a single, independent experiment, with each condition tested in triplicate.*

(a)

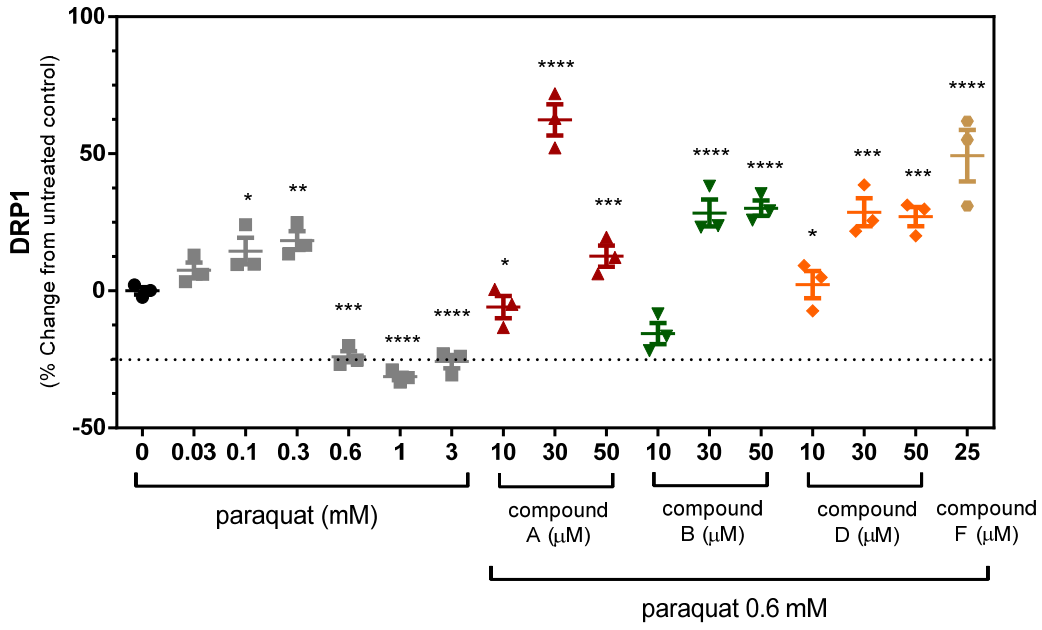

Figure 5.6 Effects of OGG1 activators on paraquat-induced changes on mitochondrial fission in A549 cells.

(b)

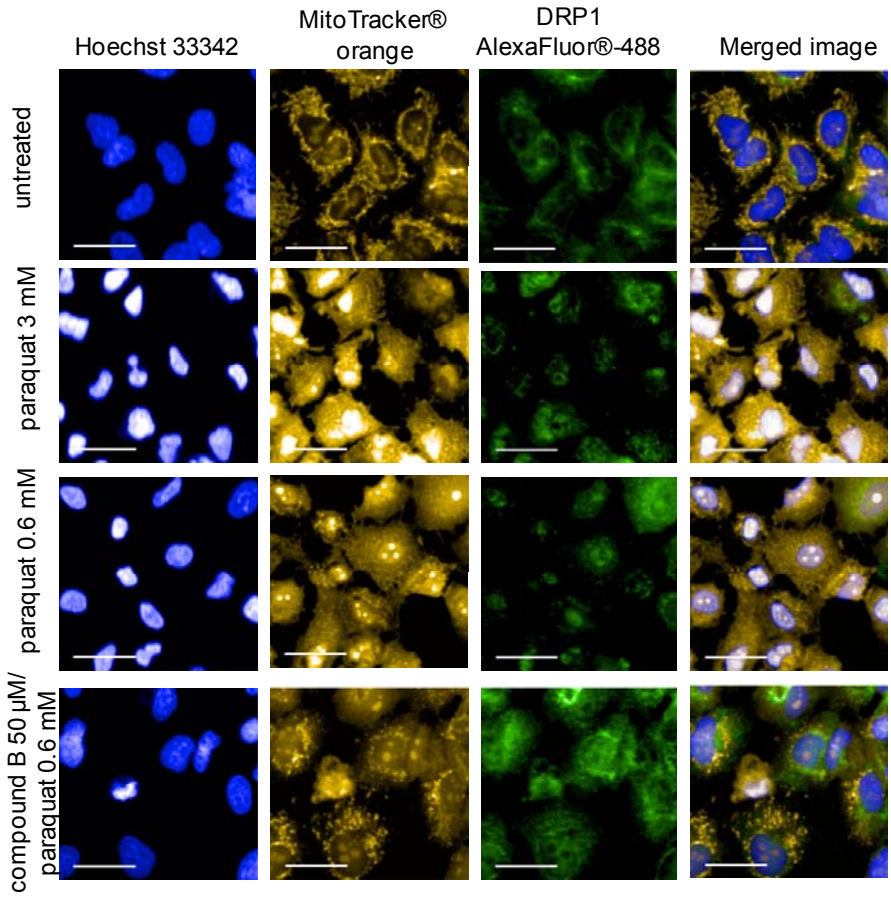

Figure 5.6 Effects of OGG1 activators on paraquat-induced changes on mitochondrial fission in A549 cells.

Figure 5.6 Effects of OGG1 activators on paraquat-induced changes on mitochondrial fission in A549 cells.

A549 cells were pre-treated (4 hr) with an OGG1 activator prior to exposure to a single concentration of paraquat (0.6 mM) for 48 hr. The cells were subjected to formaldehyde fixation for immunofluorescence detection of Drp1 and analyzed as described in Chapter 2. (a) Graphical representation of the percent change in DRP1 protein content from cells pretreated with the OGG1 activators. (b) Sample representative images from DRP1 stained cells are shown with color overlays (Hoechst 33342, overlaid blue; anti-DRP1-AlexaFluor®-488, overlaid green; MitoTracker® orange, overlaid yellow; line = 40 μm). Significance was determined using a 1-way ANOVA with a Dunnett's post test comparing paraquat alone treated groups to untreated control (0 mM) and OGG1 activator treated groups to 0.6 mM paraquat control ($p<0.05$, ** $p<0.01$, *** $p<0.001$, **** $p<0.0001$). Data shown are from a representative experiment, performed two times.*

Compounds B and D demonstrated a concentration-dependent response, whereas Compound A precipitated during use and may have contributed to the bell-shaped concentration response data (Fig. 5.6a). Application of Compound F was associated with a 50% increase of DRP1 levels above the untreated control. These data were confirmed through the sample images that depict paraquat reduced DRP1 as observed by a decrease in the green fluorescence (using AlexaFluor®-488) intensity of the images (Fig. 5.6b). Restoration of DRP-1 content was observed with compound B as indicated in the elevated green fluorescence intensity (Fig. 5.6b).

5.2.6 Effect of paraquat and the OGG1 activators on mitochondrial fusion.

Mitochondria can also reorganize by fusion, where mitochondria will dilute out the damaged mtDNA in an effort to restore energy production (Chauhan et al., 2014). Similar to DRP1, MFN1 is a surface protein that is recruited to the mitochondria at the junction of where two mitochondria will merge as part of mitochondrial fusion (Agarwal et al., 2012; Ashley and Poulton, 2009; Torres-Gonzalez et al., 2014). In the present studies, mitochondrial fusion within the cell was monitored using an immunofluorescence assay validated from the manufacturer suggested protocol to detect changes in MFN1 protein. In the presence of paraquat (3 mM) for 24 hr, there was a significant 200% ($p<0.0001$) rise in MFN1 content (Fig. 5.7a). MFN1 levels continued to rise, and by 30 hr, there was a 300% ($p<0.001$) concentration-dependent accumulation (Fig. 5.7b). As was observed with DRP1, paraquat-induced a small non-significant loss in MFN1 content of about 20% following prolonged exposure (48 hr) (Fig. 5.7c).

To determine whether activation of OGG1 influenced mitochondrial fusion, several OGG1 activators were evaluated at their respective effective concentration for reducing paraquat-induced 8-oxoguanine (see Fig. 4.4). As before, the OGG1 activators (10-50 μM) were added 4 hr prior to exposure of A549 cells to paraquat (0.6 mM, 24 and 48 hr). Following 24 hr paraquat (0.6 mM) exposure, the compounds had little impact on MFN1 cellular content (Fig. 5.8a). The exception was Compound F, which significantly increased by almost 100% ($p<0.01$) MFN1 protein expression.

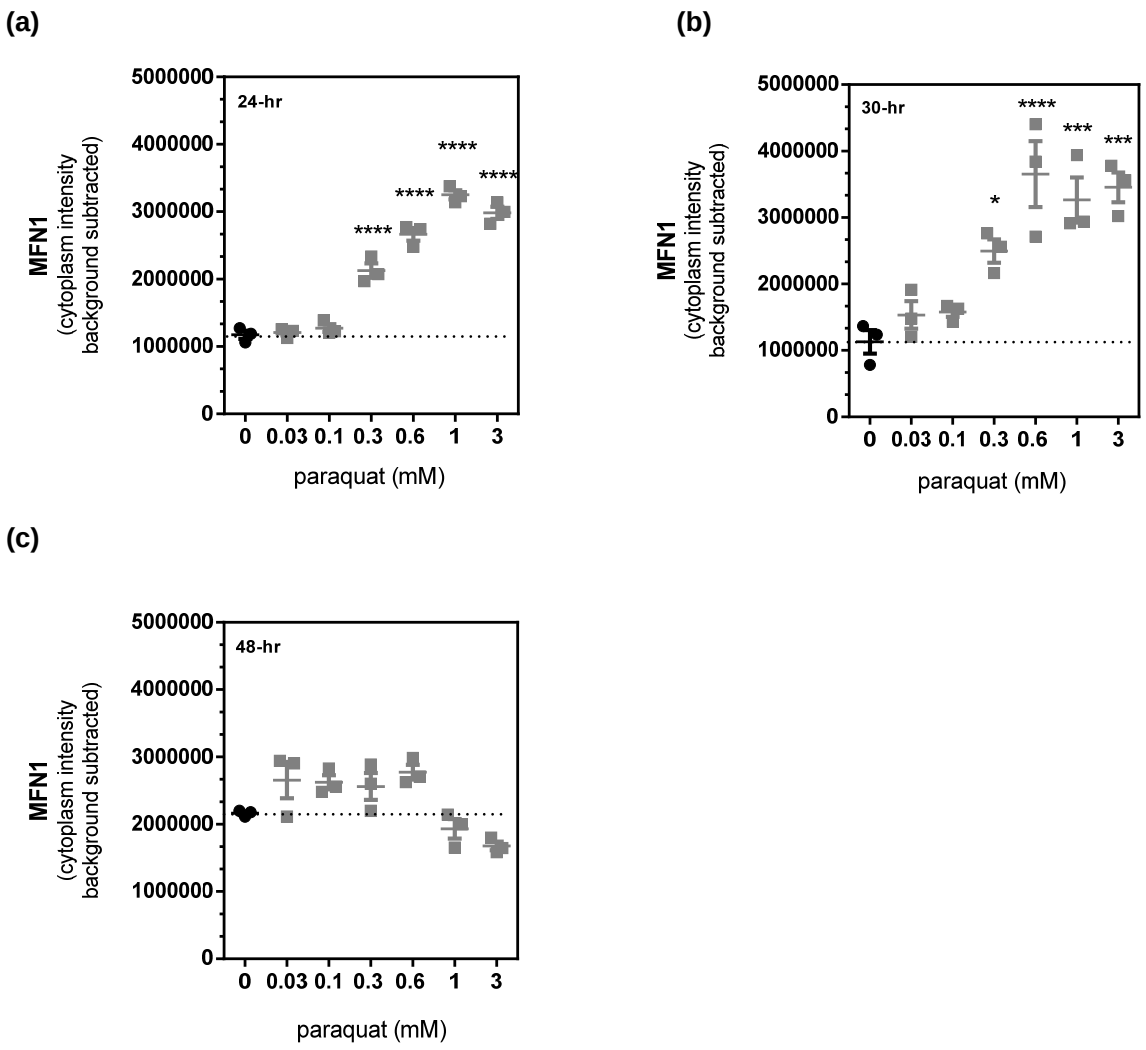

Figure 5.7 Effects of paraquat on mitochondrial fusion in A549 cells over time.

A549 cells were exposed to varying concentrations of paraquat (mM) over time. The cells were subjected to formaldehyde fixation for immunofluorescence detection of MFN1; images were acquired and analyzed as described in Chapter 2. Graphical representation of the changes in MFN1 protein content in the cytoplasm region of cells exposed to increasing concentrations of paraquat are shown following (a) 24 hr, (b) 30 hr, and (c) 48 hr exposure. Significance was determined using a 1-way ANOVA with a Dunnett's post test comparing treatment groups to untreated control (0 mM) (p<0.05, *** p<0.001, **** p<0.0001). Data shown are from a single, independent experiment, with each condition tested in triplicate.*

However, at 48 hr exposure, MFN1 expression was decreased by paraquat treatment alone, the OGG1 activators had a significant effect ($p<0.05$) and maintained MFN1 levels (Fig. 5.8b). Compounds B and D increased MFN1 in a concentration-dependent manner; meanwhile Compound F increased MFN1 expression by 100% ($p<0.0001$) above baseline control. Compound A showed a possible trend of an increase in MFN1 expression at 30 μM, but did not reach statistical significance due to the unequal variance present across the three samples. The sample images reflect that MFN1 protein (green fluorescence) was present in untreated cells (Fig5.8c). However, in the presence of paraquat (0.6 mM or 0.3 mM) it was observed there was a loss of green fluorescence intensity (using AlexaFluor®-488), which was blocked when the cells were pre-incubated with compound F (25 μM) before paraquat (0.6 mM).

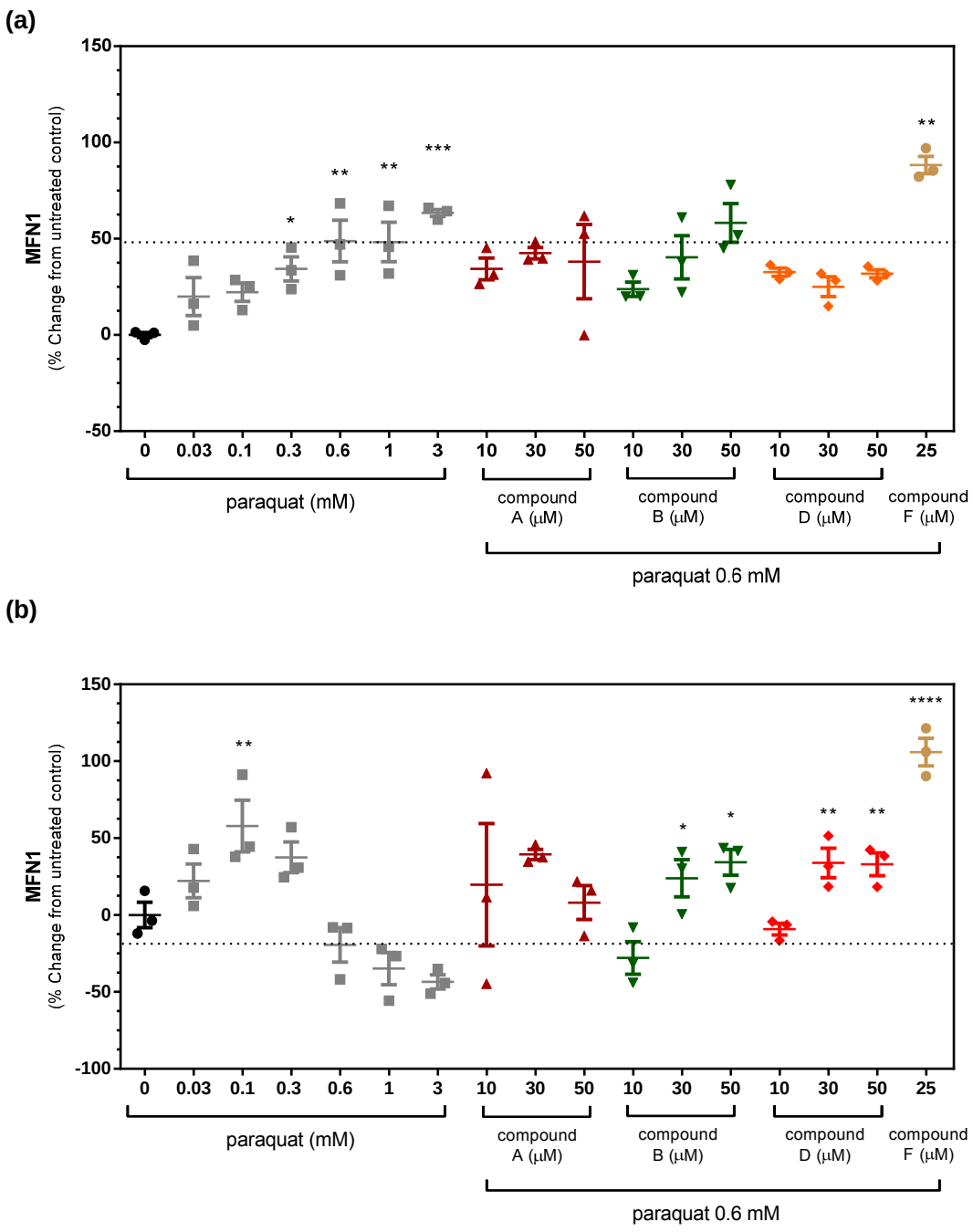

Figure 5.8 Effects of OGG1 activators on paraquat-induced changes on mitochondrial fusion in A549 cells.

(c)

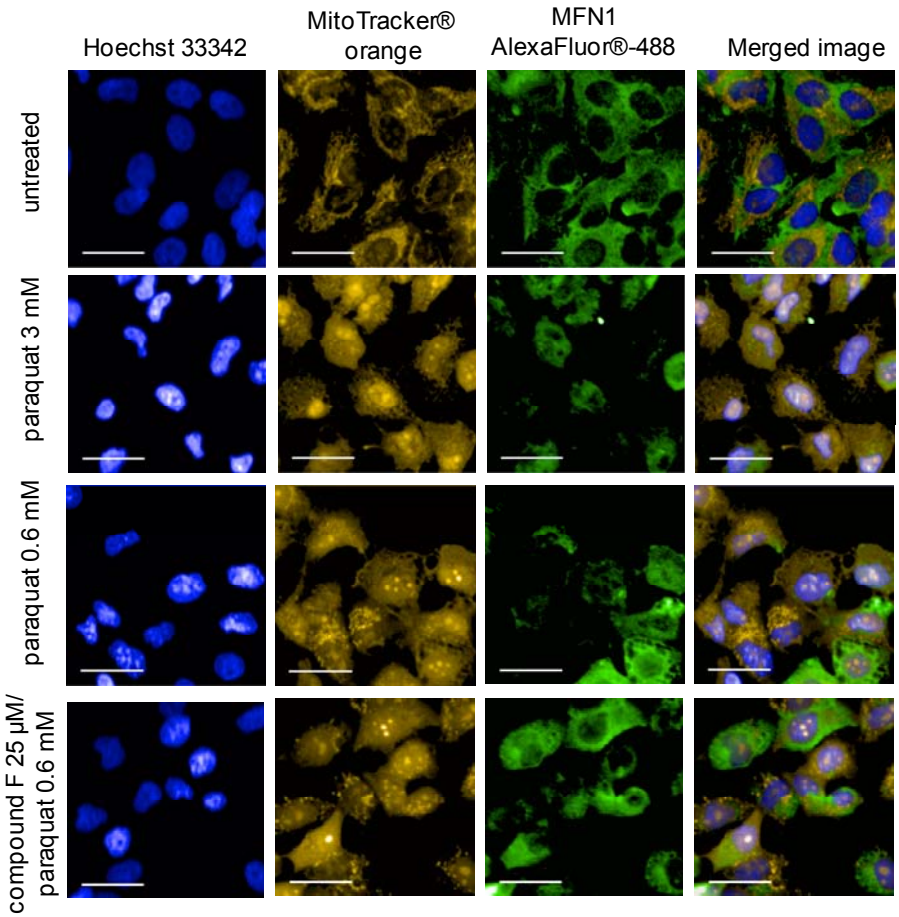

Figure 5.8 Effects of OGG1 activators on paraquat-induced changes on mitochondrial fusion in A549 cells.

Figure 5.8 Effects of OGG1 activators on paraquat-induced changes on mitochondrial fusion in A549 cells.

A549 cells were pre-treated with an OGG1 activator for 4 hr prior to exposure to a single concentration of paraquat (0.6 mM) for 48 hr. Graphical representation of the percent change in MFN1 protein content in the cytoplasm region of cells pretreated with the OGG1 activators and exposed to paraquat (0.6 mM) for (a) 24 hr and (b) 48 hr. (c) Sample representative images are shown with color overlays (Hoechst 33342, overlaid blue; anti-MFN1-AlexaFluor®488, overlaid green; MitoTracker® orange, overlaid yellow; line = 40 μm). Significance was determined using a 1-way ANOVA with a Dunnett's post test comparing paraquat alone treated groups to untreated control (0 mM) and OGG1 activator treated groups to 0.6 mM paraquat control ($p<0.05$, ** $p<0.01$, *** $p<0.001$, **** $p<0.0001$). Data shown are from two independent experiments, with each condition tested in triplicate.*

5.3 Discussion

The data presented demonstrate that cigarette smoke exposed A549 cells have decreased ATP concentrations at 48 hr post exposure (Fig. 5.1). These data lend support for the hypothesis that mitochondrial DNA damage adversely affects cellular homeostasis and cell health. Paraquat at concentrations producing the 8-oxoguanine lesion induced a 70% decline in the ATP/ADP ratio, 24 hr post exposure to A549 cells. This change in energy state continued to deteriorate, and by 48 hr post paraquat exposure (3 mM) there was a 97% reduction in the ATP/ADP ratio. In contrast to cigarette smoke exposure, as expected there was an increase in ADP concentration with paraquat (over a 3-fold rise at 48 hr). A possible method to understand the differences observed with the two different stimuli would be to substitute galactose for glucose in the culture medium, thereby forcing the cells into generating ATP from mitochondrial respiration, so changes in ATP could be associated to changes in mtDNA (Benard et al., 2007; Trian et al., 2007). Interestingly, when the OGG1 activators A and F were added prior to paraquat exposure, there was a partial protection of paraquat-induced ATP loss. Both compounds had a 2-fold increase in ATP concentration when normalized for protein concentration; however, Compound A had no effect on overall ADP levels and Compound F appears to exacerbate paraquat-induced ADP accumulation. Compound D did not have an effect on paraquat-induced changes in ATP and ADP. These data suggest a possible relationship where effective repair of oxidative DNA damage through the addition of a small molecule OGG1 activator, could improve mitochondrial function. Further, these data suggest ATP and ADP concentrations are affected by paraquat in A549 cells. The observation by Forman and colleagues that exposure of primary rat alveolar macrophages to paraquat did not alter ATP levels could be due to differences between a primary tissue derived cell and a transformed cell line such as A549 cells (Forman et al., 1980). While not presented here, similar observations using primary airway derived cells have demonstrated differing sensitivities to paraquat and the use of a transformed cancer cell line is a limitation of the current work.

The number of mitochondria within a cell will fluctuate as they undergo mitogenesis and mitophagy. Further while once thought of as discrete organelles, mitochondria form a network throughout the cell that constantly undergoes fission and fusion in an attempt to maintain cellular function (Benard et al., 2007). To evaluate these events in response to paraquat exposure, mitochondrial mass was measured using the

mitochondrial surface marker TOM20. A549 cells exposed to various concentrations of paraquat had 20% reduction in TOM20 protein expression. However, addition of OGG1 activators had no protective effect on TOM20 levels. These data indicate that while paraquat did impact overall mitochondrial mass, the activation of OGG1 to induce DNA repair did not alter TOM20 expression, at least as measured under the current conditions.

To further understand the effects of oxidative stress-induced DNA modifications, additional mitochondrial dynamic events were measured. To monitor fission (DRP1) and fusion (MFN1) events, immunofluorescence assays were developed to monitor the changes in two mitochondrial surface markers. When added to cells, paraquat had a biphasic effect. Initially, there was a concentration dependent rise in the fission marker protein at early time points (18 and 24 hr); however, by 30 hr the high concentration (3 mM) resulted in a return of DRP1 levels to baseline values. Moreover, extended paraquat exposure (48 hr) caused a 20% decrease in DRP1 content. The addition of OGG1 activators to paraquat exposed cells prevented the decline of DRP1 protein. It can be surmised from these data there is a possible association with increased efficiency of DNA repair from paraquat-induced oxidative DNA damage and an in increase mitochondrial fission.

The current findings also suggest that the mitochondria underwent fusion in response to the presence of paraquat. A549 cells exposed to paraquat also experienced a biphasic effect on MFN1 protein levels with an initial increase (24 hr), followed by a decline with extended exposure. The latter response may be due to prolonged ROS generation and mitochondrial DNA damage, forcing the cells into a situation where they could not successfully repair the DNA. This notion is supported by the observation that there is increased cytochrome *c* translocation observed at this time point (48 hr) at high concentrations of paraquat (Fig. 3.9a), suggesting the cells have become apoptotic. Following 24 hr paraquat exposure, there was little or no effect of the compounds on MFN1. At this time, paraquat has modest effects on 8-oxoguanine levels. Longer exposure however produced a 20% decrease in MFN1 protein levels and all of the compounds restored MFN1 to untreated control levels. The OGG1 activators when added prior to paraquat treatment trended toward an increase of mitochondrial fusion at 48 hr. From the present studies, it is unclear why the OGG1 activators restore mitochondrial fission and fusion, but do not impact

overall mitochondrial mass. It could be postulated that the compounds require additional time to complete DNA repair, reinvigorate fission and fusion ultimately leading to an increase in the number of mitochondria. It is important to note, that more sensitive markers of mitochondrial dynamics such as mitochondrial fragmentation and elongation were not examined and could be altered by accelerated repair of oxidative DNA damage by the OGG1 activators.

From the findings described above, additional work is required to understand the muted and delayed decrease in ATP following cigarette smoke exposure. Because A549 cells are a transformed cell line and mainly produce energy through glycolysis and not through oxidative phosphorylation, the use of a primary cell could yield additional evidence on this observation. Additionally, while the data presented here yields compelling evidence for a possible association between oxidative stress-induced DNA damage modulating mitochondrial fission and fusion, future work should focus on transferring these observations to primary cells. Further work is also needed to delineate which signaling pathways impact mitochondrial mass, specifically TOM20. Protein kinase D1, which acts as an oxidant sensor, has been shown to signal between the nucleus and the mitochondria and could be evaluated in the paraquat-induced oxidative DNA damage assay in A549 cells as a measure of apoptosis (Brar et al., 2012). The use of antioxidants, such as N-acetylcysteine, may assist in defining whether DNA repair or ROS elimination is the driver behind having a beneficial impact on mitochondrial mass.

CHAPTER 6:

General Discussion

6.1 General Discussion

The current body of work demonstrates that paraquat is a useful tool in the examination of ROS-mediated mtDNA damage. As discussed above (Chapter 1) the mechanism of action for paraquat is such that it enables ROS to accumulate within mitochondria at the site of the electron transport chain, in close proximity to mtDNA (Cochemé and Murphy, 2008; Hegde et al., 2012). Elevated levels of paraquat-induced ROS within the mitochondria led to a rise in the DNA oxidation damage base, 8-oxoguanine. The use of paraquat as a tool for model development is supported by work published by Wang and colleagues where these investigators addressed the challenge of deciphering events solely associated with the mitochondria when a stimulus impacts both the nuclear and mitochondrial compartments (Wang et al., 2011). These observations support the use of paraquat as a model of a chemically more pure oxidant compared to cigarette smoke, which is disease relevant, but interfered with the cell on multiple levels (Fig. 3.2). Similarly, other investigators have demonstrated an increase in oxidative DNA damage following paraquat exposure (Cai et al., 2012; Zerin et al., 2012). However, a limitation of the methods these investigators used was in the detection of the DNA damage, which captured changes to both the nuclear and mitochondrial compartments. To this author's knowledge, only a limited number of publications have shown specific changes in mitochondrial function in response to paraquat (He et al., 2012; Kuck et al., 2015; Li et al., 2015). Taken together, these published studies highlight the need for a model or system that allows for the assessment of DNA damage specifically in the mitochondrial compartment.

In the current studies, immunofluorescence staining of 8-oxoguanine and image analysis was utilized to measure DNA damage specifically in the mitochondria, thereby circumventing the limitations cited above. Imaging of fluorescently labeled cells enabled the sub-cellular segregation and identification of biochemical and molecular events. Mitochondrial lesions as opposed to nuclear ones were segmented using mitochondrial specific dyes. In the work presented here, the high content imaging captured other notable changes, such as the rise in ROS-mediated 8-oxoguanine was associated with cytochrome *c* translocation, increased MnSOD protein expression, apoptosis, loss of mitochondrial membrane integrity, changes in nuclear size, and increased double strand nuclear DNA breaks. Accumulation of 8-oxoguanine was associated with mitochondrial membrane depolarization and a loss of membrane integrity. These changes in mitochondrial membrane polarization were

also associated with cytochrome *c* translocation, which is the initial step of the intrinsic apoptosis pathway. The cellular response to the elevated levels of ROS and 8-oxoguanine was evaluated, and the appropriate repair pathways to counteract these two events were measured as elevated MnSOD and OGG1 protein within the mitochondria. The present results are consistent with those of Li et al., who also showed a loss of mitochondrial membrane polarization following paraquat exposure in A549 cells (Li et al., 2015).

The present work also demonstrated that the transduction with OGG1 baculovirus was able to protect against paraquat-induced 8-oxoguanine formation, and conversely, gene silencing using *OGG1* siRNA, exacerbated the oxidant-induced DNA damage lesion. Through a biochemical screen conducted at GlaxoSmithKline, activators of OGG1 were identified. These compounds protected cells from paraquat-mediated damage. The decline of mitochondrial membrane potential was attenuated in A549 cells pre-treated with the small molecule activators. Moreover, the cells maintained their nuclear size when the OGG1 activators were present, suggesting that the activity of these compounds offer a benefit to cell health. OGG1 activity was shown to be positively affected by the small molecule activators as measured by cleavage of the radioactive labeled strand of DNA in the 8-oxoguanine excision assay (Appendix S5). Specific enzymes of the base excision repair pathway such as OGG1 and DNA Ligase III, were also elevated within the mitochondria in cells pre-treated with the OGG1 activators followed by oxidant-induced mitochondrial stress. The increase in DNA Ligase III could be associated with an increase in the appropriate downstream repair enzymes as a result of increased demand for base excision repair. These data further demonstrate that there were increased levels of OGG1 protein in the mitochondria following addition of the small molecule OGG1 activators, resulting in reduced amounts of 8-oxoguanine lesion within the cell; decreased concentrations of the lesion correlate with improved cell

health. To gain further understanding of how the activators of base excision repair affect the mitochondria, the energy level of the cells was examined. In concentration- and time-dependent studies, paraquat caused the ATP concentrations to decline, while ADP levels rose within the cells. However, OGG1 activators were only partially protective for paraquat-induced ATP changes and did not modify paraquat-induced ADP accumulation. It was expected that return of ATP to normal levels would result

in a reduction of ADP levels. However, this did not occur and these observations could be a consequence of using single cells in culture or could be associated to reduced mitochondrial respiration, which has been observed in the A549 cells (Jantzen et al., 2012). As reported by Jantzen and colleagues; measuring mitochondrial respiration in A549 cells is challenging due to the high rate of glycolysis, and it is possible that this accounts for the lack of change in ADP concentrations. Finally, in response to changes in the energy state of the cell, mitochondria will reorganize through fission and fusion in an effort to maintain ATP levels. Paraquat-induced alterations to mitochondrial dynamics were examined and while initially fission and fusion were activated, these pathways declined with increasing time of paraquat exposure. OGG1 activators were shown to partially or fully prevent a decline in fission and fusion, but did not alter the paraquat-induced decline in mitochondrial mass. These observations suggest accelerated base excision repair might be associated with modifying how the mitochondria react to a toxic stimulus and provide further support for a more detailed study on OGG1 activators as potential therapeutic agents.

6.2 Activation of Base excision repair

The absolute deletion of *OGG1* can have negative consequences on cell health. Evidence has shown that removal of the entire base excision pathway is not compatible with life (Klungland et al., 1999). By contrast, mice deficient in *ogg1-/-* are not embryonic lethal but markedly accumulate 8-oxoguanine lesions in their DNA (Klungland et al., 1999). While these animals exhibited an increase in mutation frequency, this change did not result in an increased incidence of tumor development. While an increased cancer risk was not observed in mice, there has been an association identified between an increased risk with certain cancers and specific human *OGG1* SNP variants, specifically Ser326Cys (Zhou et al., 2015).

Modulation of OGG1 content or activity may decrease 8-oxoguanine lesions in diseases where oxidative stress plays a role. In turn, a reduction in the level of DNA damage and mutation frequency could be beneficial in cancer, Parkinson's, Alzheimer's, and diseases of the aging process (Hegde et al., 2012; Zhou et al., 2015). Studies have shown that supplementing OGG1 is beneficial for reducing 8-oxoguanine in cells and tissues (Ruchko et al., 2011). Studies have also shown that the enzymatic activity of OGG1 can be modified through product-assisted catalysis

(Fromme et al., 2003; Lukina et al., 2013). The current studies suggest a small molecule can enhance catalytic activity of OGG1 and improve cell health.

While there is still conflicting evidence on the relative influence of the polymorphism variant OGG1 Ser326Cys when compared to OGG1 wild type on DNA repair activity, it is not believed to account for the differences between the two genotypes with respect to DNA damage under non-stressed conditions (Soares et al., 2015). Data presented in Appendix S6 suggests that OGG1 activation by the small molecule activators can occur in both wild type and in constructs bearing the variant Ser326Cys. These data suggest that while there are differences in excision activity with the OGG1 Ser326Cys, the OGG1 activators can have a beneficial impact on both OGG1 wild type and the SNP variant. It is important to note, in that assay the OGG1 variant does exhibit a lower excision activity as evidenced by the requirement to use higher quantities of the OGG1 enzyme in the assay compared to wild type.

While there are some differing views over precisely which enzyme of the base excision repair pathway constitutes the rate limiting step, several groups have shown that over expression of DNA Ligase III has a beneficial impact on mitochondrial base excision repair (Akbari et al., 2014; Ruchko et al., 2011; Tomkinson et al., 2013). While DNA Ligase III content was examined in the current study, future studies examining single strand mtDNA breaks would prove beneficial to determine whether increased OGG1 activity was sufficient to execute complete repair.

Previous reports in rodents have demonstrated that Nrf2 has a binding site in the *ogg1* promoter, suggesting that a rise in Ogg1 transcription to ensure DNA integrity is part of the cyto-protective effects mediated by Nrf2 (Singh et al., 2013). Cai et al. have shown that increasing *NRF2* expression via an adenoviral vector protected A549 cells from paraquat-induced apoptosis activation (Cai et al., 2012). However, these authors did not examine whether this treatment had an impact on mtDNA damage and they were unable to detect any changes in SOD protein, the enzyme required for removal of superoxide anion accumulation, which would be present following paraquat exposure (Cai et al., 2012). Kim and colleagues were able to demonstrate that treatment with 7,8-dihydroxyflavone (DHF), which has been shown to scavenge ROS, inhibited hydrogen peroxide-induced 8-oxoguanine in Chinese

hamster lung fibroblast cells (Kim et al., 2013). In this study, the mechanism of action was likely mediated through Nrf2 activation, resulting in an increase in the anti-oxidant and cytoprotective cellular responses. This in turn lead to Ogg1 activation through the binding to the promoter sequence by Nrf2. Moreover, these data suggest that elevating endogenous OGG1 levels through NRF2 activation can result in a decline in oxidized DNA. Interestingly, Zerin and colleagues demonstrated quercetin (3,3',4'5,7-pentahydroxyflavone) increased NRF2 in paraquat-exposed A549 cells; however, the impact on oxidative DNA damage was not examined in this study (Zerin et al., 2012). These data support that activation of the anti-oxidant activities through NRF2 could lead to an increase in OGG1-mediated base excision repair.

However, not all instances of increasing the activity and/or elevating the expression of OGG1 have been shown to be protective against oxidative stress. In a transgenic mouse model over-expressing human OGG1, elevated levels of mtDNA damage and accumulation of intracellular free radicals were observed under non-stressed conditions (Zhang et al., 2011). These observations are in contrast to a review suggesting increased OGG1 under conditions of oxidative stress had a positive effect (Sampath, 2014). While differences in experimental design could have resulted in these varied observations, it is clear that further work is needed to understand how the process of targeting various OGG1 isoforms to the mitochondria could impact base excision repair under conditions of oxidative stress.

However, the activity of OGG1 can be directly inhibited by various heavy metals and pesticides. Many of the these inhibitors such as chromium, arsenic, cadmium, and cyanide are found in the vapor of cigarette smoke (Adad et al., 2015; Bravard et al., 2006; Hodges and Chipman, 2002; van der Toorn et al., 2007). These compounds have been shown to block the electron transport chain, increase ROS levels, and lead to the formation of the 8-oxoguanine lesion and increase the propensity for somatic mutations.

6.3 Effects of OGG1 activation on mitochondrial function

Mitochondrial network fragmentation in diseases such as Parkinson's, Alzheimer's, and other mitochondrial-associated diseases, coupled with the observation that this

fragmentation can be reversed, suggest that pharmacological intervention could have an impact on disease progression (Willems et al., 2015). In the current study, the OGG1 activators had a positive impact on fission and fusion, resulting in partial restoration of mitochondrial function as reflected by preservation of ATP levels. These data suggest that, a pharmacological intervention could occur at the DNA level and that the resultant decrease in DNA damage has a positive effect on mitochondrial health. While mitochondrial mass as assessed by TOM20 was not improved by the OGG1 activators, the changes observed in DRP1 and MFN1 protein levels could indicate that the compounds had an impact on paraquat-induced changes to the mitochondrial network. A similar study has also demonstrated a positive effect on mitochondrial membrane potential using adenoviral addition of OGG1 under menadione-induced oxidative stress conditions in a cardiomyocyte cell line (Torres-Gonzalez et al., 2014). These authors were able to demonstrate a reduction in activation of apoptosis and a restoration of mitochondrial membrane integrity following the addition of the OGG1 adenoviral vector. These observations suggest a limited association between TOM20 expression and oxidative base excision repair under the current test conditions. An alternative explanation is that the compounds differentially activate OGG1, or exhibit some off target activity. A limitation of the current study is that it is not completely understood where on the OGG1 protein the activators bind to activate the catalytic activity; it is possible that differential binding sites by the various activators could confer differing activity. Another possible explanation for the lack of effect of pharmacologically-induced OGG1 activation on mitochondrial mass could be an increased rate of mitophagy under the experimental conditions. Mitochondrial turnover was not quantified in this work and the absence of this information is therefore a limitation in the understanding of the potential impact of OGG1 activation on improving mitochondrial function.

Fragmented mitochondria have been observed in COPD patient-derived bronchial epithelial cells and this observation has been reproduced in cells chronically exposed to cigarette smoke (Hoffmann et al., 2013). Furthermore, an elevated mitochondrial mass has been observed in bronchial smooth muscle cells from asthmatic patients, while no such differences were observed in the same cell type from COPD patients when compared to healthy controls (Trian et al., 2007). These observations could be explained by differences in the pathophysiology of these diseases; for example, asthma is associated with a significant impact on the smooth muscle tissue, and mitochondrial biogenesis has been linked to changes in calcium levels in the study by

Trian and colleagues (Trian et al., 2007). Altogether these studies suggest that alterations in mitochondrial biogenesis could be linked to airway remodeling as part of the pathophysiology of both COPD and asthma.

6.4 Potential therapeutic options for OGG1 activators

In the current study, the data revealed that small molecule activation of OGG1 was plausible and could result in decreased levels of superoxide anion-induced mtDNA damage. Likewise, there was an overall benefit on the cellular energetic state as assessed by prevention of paraquat-induced decline in ATP levels. This could translate to a benefit in the maintenance of the mitochondrial network within cells.

In the past, there have been efforts to identify DNA repair inhibitors as a method for improving chemotherapeutic effectiveness (Damia and D'Incalci, 2007; Ding et al., 2006). However, recent research has shifted to increase the understanding of how a decline in base excision repair is linked to certain cancers and whether restoration of this repair pathway could lead to disease improvement. In mouse models of breast cancer, researchers were able to demonstrate that elevated levels of mtDNA damage correlated with decreased levels of Ogg1 activity; importantly, the increase in DNA damage was corrected with the addition of a human OGG1 construct (Yuzefovych et al., 2016). The authors noted that the decline in breast cancer progression was a possible benefit from increased OGG1 expression. Additional clinical studies have shown that there is a significant down regulation of OGG1 gene expression in tumors compared to healthy nearby tissue in patients presenting with head and neck squamous cell carcinoma (Mahjabeen and Kayani, 2016).

Similarly, a meta-analysis of over 34,000 case studies concluded there was a possible association of an increased cancer risk in patients with the OGG1 Ser326Cys variant specifically for cancers of the lung, digestive system, and head and neck (Zhou et al., 2015). Data presented in Appendix S6 demonstrated the OGG1 activators successfully increased the activity of the Ser326Cys OGG1 variant in a biochemical assay, suggesting OGG1 activators could prove useful in the prevention or reduction of the risk associated with this polymorphism in certain cancers. While there is an association of the Ser326Cys OGG1 polymorphism and cancer, there exists as well a possible association with COPD disease progression

due to decreased repair of the 8-oxoguanine lesion (da Silva et al., 2013). Lung cancer is the leading cause of cancer-related deaths in the world, with non-small cell lung cancer having only a 15% five-year survivability (Peng et al., 2014). Studies in these patients have shown a significant association between progression free survival and certain OGG1 polymorphisms of Ser326Cys (Peng et al., 2014). In COPD patients, the repair activity of the polymorphism was measured using an *ex vivo* oxidant-induced stress and the comet assay; however, there are some limitations in conceptualizing the data and drawing broader conclusions about the impact of this polymorphism on COPD (da Silva et al., 2013). These data suggest that additional studies should be performed to understand the effect of this *OGG1* SNP in COPD and whether DNA repair could be affected by novel therapeutics. Interestingly, recent work has shown that the Ogg1 Ser326Cys variant of the enzyme is inactivated under hydrogen peroxide-induced oxidative stress and TNF-α mediated inflammation conditions in mouse embryonic fibroblasts (Morreall et al., 2014). Because COPD is a disease characterized by increased inflammation and oxidative stress, these data suggest that COPD patients with this polymorphism would have a higher risk of inactivated OGG1 and impaired DNA repair, which could contribute to the progression of oxidant-induced DNA damage in this disease.

An examination of DNA damage in peripheral blood mononuclear cells (PBMCs) from patients with COPD demonstrated a positive correlation to the level of DNA damage measured within the lung tissue (Yang et al., 2014). Furthermore, DNA damage in PBMCs negatively correlated with lung function in these patients, supporting the hypothesis that increased OGG1 activity could decrease 8-oxoguanine lesion content, thereby leading to potential disease improvement. Pre-clinical data generated in a rat model of cigarette smoke exposure, where increased levels of 8-oxoguanine were correlated with decreased expression of Ogg1, further support the hypothesis stated above (Chen et al., 2015).

However, the recent observation of a possible association between excision of 8-oxoguanine lesion by OGG1 and lung remodeling points to a level of caution required for the use of OGG1 activators *in vivo* (Aguilera-Aguirre et al., 2015). Because the lesion molecule 8-oxoguanine was exogenously added to the lungs of mice independent of the activity of OGG1, it is not clear whether small molecule activation of OGG1 would produce a comparable outcome. Finally, while most of the data

presented and discussed thus far have focused around patients exposed to cigarette smoke, exposure to smoke from cooking with biomass fuels presents a similar problem. In India, women cooking with this type of fuel were shown to have elevated levels of 8-oxoguanine and reduced levels of OGG1 protein expression in lung epithelium (Mukherjee et al., 2014). Mukherjee and colleagues used immunofluorescent and immunohistochemical methods, in a similar format to the current study, to examine the changes in the base excision repair proteins and the rise in 8-oxoguanine. These data validate the methods used in the current study to examine the functional effect of OGG1 activation on improving cell health following oxidative stress-induced mtDNA damage.

6.5 Summary

The present findings were enabled by the characterization of a cell-based model of mitochondrial specific oxidative stress, which has proven very useful to draw associations to more disease relevant systems, such as cigarette smoke exposure, as well as to generate novel hypotheses on the role of mitochondrial dysfunction in diseases such as COPD. This work has led to the identification and validation of small molecules capable of activating base excision repair of the oxidative stress-induced mtDNA damage. Examination of how mitochondria respond to oxidant stress led to the findings of the potential benefit of facilitating efficient repair of the mitochondrial genome. Ensuring adequate repair of oxidized DNA damage prevented the loss of mitochondrial membrane polarization. Mitochondria are in a constant state of flux to ensure cellular energy stores are maintained. Reducing the 8-oxoguanine lesion facilitated the partial restoration of ATP levels and the resurgence of fission and fusion as part of mitochondrial dynamics. Moreover, this study led to the further understanding of how mtDNA damage impacts overall mitochondrial function. The literature suggests that patients may have to be screened for various polymorphisms in *OGG1* to further understand the potential implications these polymorphisms have on disease. However, to fully realize the potential of this mechanism as a new therapy, the data presented here provide compelling evidence in support of the identification and further characterization of OGG1 activators for the treatment of COPD, diseases of aging, and diseases driven by mitochondrial oxidative stress. Furthermore, this work has established novel models and assays, thus opening new avenues of research to identify and validate novel therapeutic targets for the treatment of mitochondrial dysfunction in disease.

CHAPTER 7:

REFERENCES

7. References

Adad, L.M.D.M., Andrade, H.H.R. De, Kvitko, K., Lehmann, M., Cavalcante, A.A.D.C.M., Dihl, R.R., 2015. Occupational exposure of workers to pesticides: Toxicogenetics and susceptibility gene polymorphisms. Genet. Mol. Biol. 38, 308–315.

Agarwal, A.R., Zhao, L., Sancheti, H., Sundar, I.K., Rahman, I., Cadenas, E., 2012. Short-term cigarette smoke exposure induces reversible changes in energy metabolism and cellular redox status independent of inflammatory responses in mouse lungs. Am. J. Physiol. Lung Cell. Mol. Physiol. 303, L889–98.

Aguilera-Aguirre, L., Hosoki, K., Bacsi, A., Radák, Z., Sur, S., Hegde, M.L., Tian, B., Saavedra-Molina, A., Brasier, A.R., Ba, X., Boldogh, I., 2015. Whole transcriptome analysis reveals a role for OGG1-initiated DNA repair signaling in airway remodeling. Free Radic. Biol. Med. 89, 20–33.

Agustí, A., Barnes, P.J., 2012. Update in chronic obstructive pulmonary disease 2011. Am. J. Respir. Crit. Care Med. 185, 1171–6.

Ahmad, T., Sundar, I.K., Lerner, C. a., Gerloff, J., Tormos, a. M., Yao, H., Rahman, I., 2015. Impaired mitophagy leads to cigarette smoke stress-induced cellular senescence: implications for chronic obstructive pulmonary disease. FASEB J. 29, 2912–2929.

Akbari, M., Keijzers, G., Maynard, S., Scheibye-Knudsen, M., Desler, C., Hickson, I., Bohr, V.A., 2014. Overexpression of DNA ligase III in mitochondria protects cells against oxidative stress and improves mitochondrial DNA base excision repair. DNA Repair (Amst). 16, 44–53.

Akhmedov, A.T., Marin-Garcia, J., 2015. Mitochondrial DNA Maintenance: an appraisal. Mol. Cell. Biochem. 409, 283–305.

Aravamudan, B., Kiel, A., Freeman, M., Delmotte, P., Thompson, M., Vassallo, R., Sieck, G.C., Pabelick, C.M., Prakash, Y.S., 2014. Cigarette smoke-induced mitochondrial fragmentation and dysfunction in human airway smooth muscle. Am. J. Physiol. Lung Cell. Mol. Physiol. 306, L840–54.

Aravamudan, B., Thompson, M.A., Pabelick, C.M., Prakash, Y.S., 2013. Mitochondria in Lung Diseases. Expert Rev. Respir. Med. 7, 631–646.

Ashley, N., Poulton, J., 2009. Anticancer DNA intercalators cause p53-dependent mitochondrial DNA nucleoid re-modelling. Oncogene 28, 3880–91.

Ba, X., Bacsi, A., Luo, J., Aguilera-Aguirre, L., Zeng, X., Radak, Z., Brasier, A.R., Boldogh, I., 2014. 8-oxoguanine DNA glycosylase-1 augments proinflammatory gene expression by facilitating the recruitment of site-specific transcription factors. J. Immunol. 192, 2384–94.

Bacsi, A., Aguilera-aguirre, L., Szczesny, B., Radak, Z., Hazra, T.K., Sur, S., Ba, X., Boldogh, I., 2013. Down-regulation of 8-oxoguanine DNA glycosylase 1 expression in the airway epithelium ameliorates allergic lung inflammation. DNA Repair (Amst). 12, 18–26.

Bacsi, A., Pan, L., Ba, X., Boldogh, I., 2015. Pathophysiology of bronchoconstriction: role of oxidatively damaged DNA repair. Curr. Opin. Allergy Clin. Immunol. 16,

59–67.

Ballweg, K., Mutze, K., Konigshoff, M., Eickelberg, O., Meiners, S., 2014. Cigarette smoke extract affects mitochondrial function in alveolar epithelial cells. Am. J. Physiol. Lung Cell. Mol. Physiol. 307, L895–L907.

Bardwell, G.C., Pastukh, V. V, Alexeyev, M.F., Mark, N., 2013. Perinuclear Mitochondrial Clustering Creates an Oxidant-Rich Nuclear Domain Required for Hypoxia-Induced Transcription. Sci. Signal 5, 1–20.

Barker, B.L., Brightling, C.E., 2013. Phenotyping the heterogeneity of chronic obstructive pulmonary disease. Clin. Sci. 387, 371–387.

Barnes, P.J., 2010. Inhaled corticosteroids in COPD: a controversy. Respiration. 80, 89–95.

Bauer, M., Goldstein, M., Christmann, M., Becker, H., Heylmann, D., Kaina, B., 2011. Human monocytes are severely impaired in base and DNA double-strand break repair that renders them vulnerable to oxidative stress. Proc. Natl. Acad. Sci. U. S. A. 108, 21105–10.

Ben Anes, A., Fetoui, H., Bchir, S., Ben Nasr, H., Chahdoura, H., Chabchoub, E., Yacoub, S., Garrouch, A., Benzarti, M., Tabka, Z., Chahed, K., 2014. Increased oxidative stress and altered levels of nitric oxide and peroxynitrite in tunisian patients with chronic obstructive pulmonary disease: correlation with disease severity and airflow obstruction. Biol. Trace Elem. Res. 161, 20–31.

Benard, G., Bellance, N., James, D., Parrone, P., Fernandez, H., Letellier, T., Rossignol, R., 2007. Mitochondrial bioenergetics and structural network organization. J. Cell Sci. 120, 838–848.

Berndt, A., Leme, A.S., Shapiro, S.D., 2012. Emerging genetics of COPD. EMBO Mol. Med. 4, 1144–55.

Birben, E., Sahiner, U.M., Sackesen, C., Erzurum, S., Kalayci, O., 2012. Oxidative stress and antioxidant defense. World Allergy Organ. J. 5, 9–19.

Brar, S.S., Meyer, J.N., Bortner, C.D., Van Houten, B., Martin, W.J., 2012. Mitochondrial DNA-depleted A549 cells are resistant to bleomycin. Am. J. Physiol. Lung Cell. Mol. Physiol. 303, L413–24.

Bravard, A., Vacher, M., Gouget, B., Coutant, A., de Boisferon, F.H., Marsin, S., Chevillard, S., Radicella, J.P., 2006. Redox regulation of human OGG1 activity in response to cellular oxidative stress. Mol. Cell. Biol. 26, 7430–6.

Brooks, S.C., Adhikary, J., Rubinson, E.H., Eichman, B.F., 2013. Recent advances in the structural mechanisms of DNA glycosylases. Biochim. Biophys. Acta, 1834, 247–271.

Cai, Q., Hong, G., Jiang, X., Wu, Z., Zheng, J., Song, Q., Chang, Z., 2012. Recombinant adenovirus Ad-RUNrf2 reduces paraquat-induced A549 injury. Hum. Exp. Toxicol. 31, 1102–1112.

Castello, P.R., Drechsel, D.A., Patel, M., 2007. Mitochondria are a major source of paraquat-induced reactive oxygen species production in the brain. J. Biol. Chem. 282, 14186–14193.

Chakraborty, A., Wakamiya, M., Venkova-Canova, T., Pandita, R.K., Aguilera-Aguirre, L., Sarker, A.H., Singh, D.K., Hosoki, K., Wood, T.G., Sharma, G.,

Cardenas, V., Sarkar, P.S., Sur, S., Pandita, T.K., Boldogh, I., Hazra, T.K., 2015. Neil2-null mice accumulate oxidized DNA bases in the transcriptionally active sequences of the genome and are susceptible to innate inflammation. J. Biol. Chem. 290, 24636–24648.

Chauhan, A., Vera, J., Wolkenhauer, O., 2014. The systems biology of mitochondrial fission and fusion and implications for disease and aging. Biogerontology 15, 1–12.

Chen, H., Chan, D.C., 2015. Mitochondrial dynamics-fusion, fission, movement, and mtophagy-in neurodegenerative diseases. Hum. Mol. Genet. 18, R169–R176.

Chen, Z., Wang, D., Liu, X., Pei, W., Li, J., Cao, Y., Zhang, J., An, Y., Nie, J., Tong, J., 2015. Oxidative DNA damage is involved in cigarette smoke-induced lung injury in rats. Environ. Health Prev. Med. 20, 318–324.

Cheresh, P., Kim, S.-J., Tulasiram, S., Kamp, D.W., 2013. Oxidative stress and pulmonary fibrosis. Biochim. Biophys. Acta 1832, 1028–1040.

Chinnery, P.F., Hudson, G., 2013. Mitochondrial genetics. Br. Med. Bull. 106, 135–159.

Cline, S.D., 2012. Mitochondrial DNA damage and its consequences for mitochondrial gene expression. Biochim. Biophys. Acta 1819, 979–91.

Cochemé, H.M., Murphy, M.P., 2008. Complex I is the major site of mitochondrial superoxide production by paraquat. J. Biol. Chem. 283, 1786–98.

Cooke, M.S., Evans, M.D., Dizdaroglu, M., Lunec, J., 2003. Oxidative DNA damage: mechanisms, mmutation, and disease. FASEB J. 17, 1195–1214.

Cooper, C.E., Brown, G.C., 2008. The inhibition of mitochondrial cytochrome oxidase by the gases carbon monoxide, nitric oxide, hydrogen cyanide and hydrogen sulfide: chemical mechanism and physiological significance. J. Bioenerg. Biomembr. 40, 533–539.

da Silva, A.L.G., da Rosa, H.T., Karnopp, T.E., Charlier, C.F., Ellwanger, J.H., Moura, D.J., Possuelo, L.G., R de Moura Valim, A., Guecheva, T.N., Pegas Henriques, J.A., 2013. Evaluation of DNA damage in COPD patients and its correlation with polymorphisms in repair genes. BMC Med. Genet. 14, 1–8.

Dai, Y., Zheng, K., Clark, J., Swerdlow, R.H., Pulst, S.M., Sutton, J.P., Shinobu, L. a, Simon, D.K., 2014. Rapamycin drives selection against a pathogenic heteroplasmic mitochondrial DNA mutation. Hum. Mol. Genet. 23, 637–47.

Damia, G., D'Incalci, M., 2007. Targeting DNA repair as a promising approach in cancer therapy. Eur. J. Cancer 43, 1791–801.

Deslee, G., Adair-Kirk, T.L., Betsuyaku, T., Woods, J.C., Moore, C.H., Gierada, D.S., Conradi, S.H., Atkinson, J.J., Toennies, H.M., Battaile, J.T., Kobayashi, D.K., Patterson, G.A., Holtzman, M.J., Pierce, R. a, 2010. Cigarette smoke induces nucleic-acid oxidation in lung fibroblasts. Am. J. Respir. Cell Mol. Biol. 43, 576–84.

Deslee, G., Woods, J.C., Moore, C., Conradi, S.H., Gierada, D.S., Atkinson, J.J., Battaile, J.T., Liu, L., Patterson, G.A., Adair-Kirk, T.L., Holtzman, M.J., Pierce, R. a, 2009. Oxidative damage to nucleic acids in severe emphysema. Chest 135, 965–74.

Ding, J., Miao, Z.-H., Meng, L.-H., Geng, M.-Y., 2006. Emerging cancer therapeutic opportunities target DNA-repair systems. J. Chem. Inf. Model. 27, 338–344.

Dinis-Oliveira, R.J., Remião, F., Carmo, H., Duarte, J. a, Navarro, a S., Bastos, M.L., Carvalho, F., 2006. Paraquat exposure as an etiological factor of Parkinson's disease. Neurotoxicology 27, 1110–1122.

Dolle, C., Rack, J.G.M., Ziegler, M., 2013. NAD and ADP-ribose metabolism in mitochondria. FEBS J. 280, 3530–3541.

El-Zein, R. a, Monroy, C.M., Cortes, A., Spitz, M.R., Greisinger, A., Etzel, C.J., 2010. Rapid method for determination of DNA repair capacity in human peripheral blood lymphocytes amongst smokers. BMC Cancer 10, 1–9.

Finkel, T., 2011. Signal transduction by reactive oxygen species. J. Cell Biol. 194, 7–15.

Fischer, B., Voynow, J., Ghio, A., 2015. COPD: balancing oxidants and antioxidants. Int. J. Chron. Obstruct. Pulmon. Dis. 10, 261.

Fletcher, M.E., Boshier, P.R., Wakabayashi, K., Keun, H.C., Smolenski, R.T., Kirkham, P. a., Adcock, I.M., Barton, P.J., Takata, M., Marczin, N., 2015. Influence of glutathione- *S* -transferase (GST) inhibition on lung epithelial cell injury: role of oxidative stress and metabolism. Am. J. Physiol. - Lung Cell. Mol. Physiol. 308, L1274–L1285.

Flora, S.J.S., 2011. Arsenic-induced oxidative stress and its reversibility. Free Radic. Biol. Med. 51, 257–81.

Forman, H.J., Nelson, J., Fisher, A.B., 1980. Rat alvelar macrophages require NADPH for superoxide production in the respiratory burst. J. Biol. Chem. 255, 9879–9883.

Forman, H.J., Torres, M., 2002. Reactive Oxygen Species and Cell Signaling Respiratory Burst in Macrophage Signaling. Am. J. Respir. Crit. Care Med. 166, S4–S8.

Forman, H.J., Torres, M., 2001. Redox signaling in macrophages. Mol. Aspects Med. 22, 189–216.

Fromme, J.C., Bruner, S.D., Yang, W., Karplus, M., Verdine, G.L., 2003. Product-assisted catalysis in base-excision DNA repair. Nat. Struct. Biol. 10, 204–211.

Furda, A., Marrangoni, A.M., Lokshin, A., Van Houten, B., 2012. Oxidants and not alkylating agents induce rapid mtDNA loss and mitochondrial dysfunction. DNA Repair (Amst). 11, 684–692.

Furda, A., Santos, J.H., Meyer, J.N., Van Houten, B., 2014. Quantitative PCR-Based Measurement of Nuclear and Mitochondrial DNA Damage and Repair in Mammalian Cells. Methods Mol. Biol. 1105, 419–437.

Gould, N.S., Min, E., Gauthier, S., Chu, H.W., Martin, R., Day, B.J., 2010. Aging adversely affects the cigarette smoke-induced glutathione adaptive response in the lung. Am. J. Respir. Crit. Care Med. 182, 1114–22.

Grabiec, A., Hussell, T., 2016. The role of airway macrophages in apoptotic cell clearance following acute and chronic lung inflammation. Semin. Immunopathol. 1–15.

Green, D.R., Galluzzi, L., Kroemer, G., 2011. Mitochondria and the Autophagy-Inflammation-Cell Death axis in organismal aging. Science (80-.). 333, 1109–1112.

Gross, N.J., 2012. Novel antiinflammatory therapies for COPD. Chest 142, 1300–7.

Hashiguchi, K., Stuart, J.A., DeSouza-Pinto, N.C., Bohr, V.A., 2004. The C-termincal aO helix of human Ogg1 is essential for 8-oxoguanine DNA glycosylase activity: the mitochondrial B-Ogg1 lacks this domain and does not have glycosylase activity. Nucleic Acids Res. 32, 5596–5608.

Hashizume, M., Mouner, M., Chouteau, J.M., Gorodnya, O.M., Ruchko, M. V, Potter, B.J., Wilson, G.L., Gillespie, M.N., Parker, J.C., 2013. Mitochondrial-targeted DNA repair enzyme 8-oxoguanine DNA glycosylase 1 protects against ventilator-induced lung injury in intact mice. Am. J. Physiol. Lung Cell. Mol. Physiol. 304, 287–297.

He, X., Wang, L., Szklarz, G., Bi, Y., Ma, Q., 2012. Resveratrol inhibits paraquat-induced oxidative stress and fibrogenic response by activating the nuclear factor erythroid 2-related factor 2 pathway. J. Pharmacol. Exp. Ther. 342, 81–90.

Hegde, M.L., Mantha, A.K., Hazra, T.K., Bhakat, K.K., Mitra, S., Szczesny, B., 2012. Oxidative genome damage and its repair: implications in aging and neurodegenerative diseases. Mech. Ageing Dev. 133, 157–68.

Hill, J.W., Hu, J.J., Evans, M.K., 2008. Ogg1 is degraded by calpain following oxidative stress and cisplatin exposure. DNA Repair (Amst). 7, 648–654.

Hodge, S., Hodge, G., Ahern, J., Jersmann, H., Holmes, M., Reynolds, P.N., 2007. Smoking alters alveolar macrophage recognition and phagocytic ability. Am. J. Respir. Crit. Care Med. 37, 748–755.

Hodges, N.J., Chipman, J.K., 2002. Down-regulation of the DNA-repair endonuclease 8-oxo-guanine DNA glycosylase 1 (hOGG1) by sodium dichromate in cultured human A549 lung carcinoma cells. Carcinogenesis 23, 55–60.

Hoffmann, R.F., Zarrintan, S., Brandenburg, S.M., Kol, A., de Bruin, H.G., Jafari, S., Dijk, F., Kalicharan, D., Kelders, M., Gosker, H.R., Ten Hacken, N.H., van der Want, J.J., van Oosterhout, A.J., Heijink, I.H., 2013. Prolonged cigarette smoke exposure alters mitochondrial structure and function in airway epithelial cells. Respir. Res. 14, 97.

Holmuhamedov, E., Lewis, L., Bienengraeber, M., Holmuhamedova, M., Jahangir, A., Terzic, A., 2002. Suppression of human tumor cell proliferation through mitochondrial targeting. FASEB J. 16, 1010–6.

Hurst, J.R., Vestbo, J., Anzueto, A., Locantore, N., Mullerova, H., Tal-Singer, R., Miller, B., Lomas, D., Agusti, A., MacNee, W., Calverley, P., Rennard, S., Wouters, E., Wedzicha, J.A., 2010. Susceptibility to exacerbation in chronic obstructive pulmonary disease. N. Engl. J. Med. 363, 1128–1138.

Ishida, T., Hippo, Y., Nakahori, Y., Matsushita, I., Kodama, T., Nishimura, S., Aburatani, H., 1999. Structure and chromosome location of human OGG1. Cytogenet. Cell Genet. 85, 232–236.

Ishida, T., Hirono, Y., Yoshikawa, K., Hutei, Y., Miyagawa, M., Sakaguchi, I., Pinkerton, K.E., Takeuchi, M., 2009. Inhibition of immunological function mediated DNA damage of alveolar macrophages caused by cigarette smoke in

mice. Inhal. Toxicol. 21, 1229–35.

Ishihara, T., Kohno, H., Ishihara, N., 2015. Physiological roles of mitochondrial fission in cultured cells and mouse development. Ann. N. Y. Acad. Sci. 1350, 77–81.

Jaeschke, H., McGill, M.R., Ramachandran, A., 2012. Oxidant stress, mitochondria, and cell death mechanisms in drug-induced liver injury: lessons learned from acetaminophen hepatotoxicity. Drug Metab. Rev. 44, 88–106.

Jantzen, K., Roursgaard, M., Desler, C., Loft, S., Rasmussen, L.J., Møller, P., 2012. Oxidative damage to DNA by diesel exhaust particle exposure in co-cultures of human lung epithelial cells and macrophages. Mutagenesis 27, 693–701.

Kamenisch, Y., Fousteri, M., Knoch, J., von Thanler, A.-K., Fehrenbacher, B., Kato, H., Becker, T., Dolle, M.E.T., Kuiper, R., Majora, M., Schaller, M., van der Horst, G.T.J., van Steeg, H., Rocken, M., Rapaport, D., Krutmann, J., Mullenders, L.H., Berneburg, M., 2010. Proteins of nucleotide and base excision repair pathways interact in mitochondria to protect from loss of subcutaneous fat, a hallmark of aging. J. Exp. Med. 207, 379–390.

Kamp, D.W., Greenberger, M.J., Sbalchierro, J.S., Preusen, S.E., Weitzman, S.A., 1998. Epithelial Cell Injury : Role of Free Radicals. Free Radic. Biol. Med. 25, 728–739.

Karahalil, B., Bohr, V. a, De Souza-Pinto, N.C., 2010. Base excision repair activities differ in human lung cancer cells and corresponding normal controls. Anticancer Res. 30, 4963–71.

Kaur, M.P., Guggenheim, E.J., Pulisciano, C., Akbar, S., Kershaw, R.M., Hodges, N.J., 2014. Cellular accumulation of Cys326-OGG1 protein complexes under conditions of oxidative stress. Biochem. Biophys. Res. Commun. 447, 12–18.

Kelsen, S.G., 2012. Respiratory epithelial cell responses to cigarette smoke: the unfolded protein response. Pulm. Pharmacol. Ther. 25, 447–52.

Kim, H.S., Kim, B.-H., Jung, J.E., Lee, C.S., Lee, H.G., Lee, J.W., Lee, K.H., You, H.J., Chung, M.-H., Ye, S.-K., 2015. Potential role of 8-oxoguanine DNA glycosylase 1 as a STAT1 coactivator in endotoxin-induced inflammatory response. Free Radic. Biol. Med. 93, 12–22.

Kim, I., Rodriguez-Enriquex, S., Lemasters, J.J., 2007. Minireview: Selective degradation of mitochondria by mitophagy. Arch. Biochem. Biophys. 462, 245–253.

Kim, K.C., Lee, I.K., Kang, K.A., Cha, J.W., Cho, S.J., Na, S.Y., Chae, S., Kim, H.S., Kim, S., Hyun, J.W., 2013. 7,8-Dihydroxyflavone Suppresses Oxidative Stress-Induced Base Modification in DNA via Induction of the Repair Enzyme 8-Oxoguanine DNA Glycosylase-1. Biomed Res. Int. 2013, 1–10.

Kim, S.-J., Cheresh, P., Jablonski, R., Williams, D., Kamp, D., 2015. The Role of Mitochondrial DNA in Mediating Alveolar Epithelial Cell Apoptosis and Pulmonary Fibrosis. Int. J. Mol. Sci. 16, 21486–21519.

Kim, S.-J., Cheresh, P., Williams, D., Cheng, Y., Ridge, K., Schumacker, P.T., Weitzman, S., Bohr, V. a, Kamp, D.W., 2014. Mitochondria-targeted Ogg1 and aconitase-2 prevent oxidant-induced mitochondrial DNA damage in alveolar epithelial cells. J. Biol. Chem. 289, 6165–6176.

Kim, V., Criner, G.J., 2013. Chronic bronchitis and chronic obstructive pulmonary

disease. Am. J. Respir. Crit. Care Med. 187, 228–37.

Kirkham, P.A., Barnes, P.J., 2013. Oxidative Stress in COPD. Chest 144, 266–273.

Klungland, A., Bjelland, S., 2007. Oxidative damage to purines in DNA: Role of mammalian Ogg1. DNA Repair (Amst). 6, 481–488.

Klungland, A., Rosewell, I., Hollenbach, S., Larsen, E., Daly, G., Epe, B., Seeberg, E., Lindahl, T., Barnes, D.E., 1999. Accumulation of premutagenic DNA lesions in mice defective in removal of oxidative base damage. PNAS 96, 13300–13305.

Kost, T. a, Condreay, J.P., Ames, R.S., Rees, S., Romanos, M. a, 2007. Implementation of BacMam virus gene delivery technology in a drug discovery setting. Drug Discov. Today 12, 396–403.

Kovacs, K., Erdelyi, K., Hegudus, C., Lakatos, P., Regdon, Z., Bai, P., Hasko, G., Szabo, E., Virag, L., 2012. Poly (ADP-riboyl)ation is a survival mechanism in cigarette smoke-induced and hydrogen peroxide-mediated cell death. Free Radic. Biol. Med. 53, 1680–1688.

Kuck, J.L., Obiako, B.O., Gorodnya, O.M., Pastukh, V.M., Kua, J., Simmons, J.D., Gillespie, M.N., 2015. Mitochondrial DNA damage-associated molecular patterns mediate a feed-forward cycle of bacteria-induced vascular injury in perfused rat lungs. Am J Physiol Lung Cell Mol Physiol. 308, L1078–85. doi: 10.1152/ajplung.00015.2015. Epub 20.

Kunkel, T.A., Erie, D.A., 2015. Eukaryotic Mismatch Repair in Relation to DNA Replication. Annu. Rev. Genet. 49, 291–313.

Kyaw, M., Yoshizumi, M., Tsuchiya, K., Izawa, Y., Kanematsu, Y., Tamaki, T., 2004. Atheroprotective effects of antioxidants through inhibition of mitogen-activated protein kinases. Acta Pharmacol. Sin. 25, 977–985.

Lascano, R., Munoz, N., Robert, G., Rodriguez, M., Melchiorre, M., Trippi, V., Quero, G., 2012. Paraquat: An Oxidative Stress Inducer, in: Hasaneen, M.N. (Ed.), Herbicides - Properties, Synthesis and Control of Weeds. InTech, pp. 135–148.

Lee, C.F., Qiao, M., Schröder, K., Zhao, Q., Asmis, R., 2010. Nox4 is a novel inducible source of reactive oxygen species in monocytes and macrophages and mediates oxidized low density lipoprotein-induced macrophage death. Circ. Res. 106, 1489–97.

Li, G., Yuzhen, L., Yi, C., Xiaoxiang, C., Wei, Z., Changqing, Z., Shuang, Y., 2015. DNaseI Protects against Paraquat-Induced Acute Lung Injury and Pulmonary Fibrosis Mediated by Mitochondrial DNA. Biomed Res. Int. 2015, 1–10.

Liu, M., Doublié, S., Wallace, S.S., 2013. Neil3 , the final frontier for the DNA glycosylases that recognize oxidative damage. Mutat. Res. - Fundam. Mol. Mech. Mutagen. 743-744, 4–11.

Liu, P., Demple, B., 2010. DNA Repair in Mammalian Mitochondria : Much More Than we Thought? Environ. Mol. Mutagen. 51, 417–426.

Livak, K.J., Schmittgen, T.D., 2001. Analysis of relative gene expression data using real-time quantitative PCR and the 2(-Delta Delta C(T)) Method. Methods 25, 402–8.

Lúcia G da Silva, A., Helen, T., Charlier, C.F., Salvador, M., Dinara, J., R de Moura

Valim, A., Guecheva, T., Pegas Henriques, J.A., 2013. DNA Damage and Oxidative Stress in Patients with Chronic Obstructive Pulmonary Disease. Open Biomark. J. 6, 1–8.

Lukina, M. V., Popov, a. V., Koval, V. V., Vorobjev, Y.N., Fedorova, O.S., Zharkov, D.O., 2013. DNA Damage Processing by Human 8-Oxoguanine-DNA Glycosylase Mutants with the Occluded Active Site. J. Biol. Chem. 288, 28936–28947.

Luo, J., Hosoki, K., Bacsi, A., Radak, Z., Hegde, M.L., Sur, S., Hazra, T.K., Brasier, A.R., Ba, X., Boldogh, I., 2014. 8-Oxoguanine DNA glycosylase-1-mediated DNA repair is associated with Rho GTPase activation and α-smooth muscle actin polymerization. Free Radic. Biol. Med. 73, 430–8.

Ma, W., Hou, C., Zhou, X., Yu, H., Xi, Y., Ding, J., Zhao, X., Xiao, R., 2013. Genistein alleviates the mitochondria-targeted DNA damage induced by B-amyloid peptides 25-35 in C6 glioma cells. Neurochem. Res. 38, 1315–1323.

MacNee, W., 2005. Oxidants and COPD. Curr. drug targets - Inflamm. allergy 4, 627–41.

Mahjabeen, I., Kayani, M.A., 2016. Loss of Mitochondrial Tumor Suppressor Genes Expression Is Associated with Unfavorable Clinical Outcome in Head and Neck Squamous Cell Carcinoma: Data from Retrospective Study. PLoS One 11, 1–12.

Mainwaring, G., Lim, F.L., Antrobus, K., Swain, C., Clapp, M., Kimber, I., Orphanides, G., Moggs, J.G., 2006. Identification of early molecular pathways affected by paraquat in rat lung. Toxicology 225, 157–72.

Mandal, S.M., Hegde, M.L., Chatterjee, A., Hegde, P.M., Szczesny, B., Banerjee, D., Boldogh, I., Gao, R., Falkenberg, M., Gustafsson, C.M., Sarkar, P.S., Hazra, T.K., 2012. Role of human DNA glycosylase Nei-like 2 (NEIL2) and single strand break repair protein polynucleotide kinase 3'-phosphatase in maintenance of mitochondrial genome. J. Biol. Chem. 287, 2819–29.

Marella, M., Seo, B.B., Matsuno-Yagi, A., Yagi, T., 2007. Mechanism of cell death caused by complex I defects in a rat dopaminergic cell line. J. Biol. Chem. 282, 24146–56.

Marteijn, J.A., Lans, H., Vermeulen, W., Hoeijmakers, J.H.J., 2014. Understanding nucleotide excision repair and its roles in cancer and ageing. Nat. Rev. 15, 465–481.

Martin, S.A., 2011. Mitochondrial DNA Repair, in: Storici, F. (Ed.), DNA Repair - On the Pathways to Fixing DNA Damage and Errors. pp. 313–338.

Matsuda, S., Kitagishi, Y., Kobayashi, M., 2013. Function and Characteristics of PINK1 in Mitochondria. Oxid. Med. Cell. Longev. 1–6.

Medical Look [WWW Document], 2016March. URL www.medicalook.com/lung_diseases/emphysema.html

Melis, J.P.M., von Steeg, H., Luijten, M., 2013. Oxidative DNA Damage and Nucleotide Excision Repair. Antioxidants Redox Signal. 18, 2409–2419.

Meyer, A., Zoll, J., Charles, a. L., Charloux, A., de Blay, F., Diemunsch, P., Sibilia, J., Piquard, F., Geny, B., 2013. Skeletal muscle mitochondrial dysfunction during chronic obstructive pulmonary disease: central actor and therapeutic

target. Exp. Physiol. 98, 1063–1078.

Miller, M.L., Andringa, A., Hastings, L., 1995. Relationships between the nuclear membrane, nuclear pore complexes, and organelles in the type II pneumocyte. Tissue Cell 27, 613–619.

Mishra, P., Chan, D.C., 2016. Metabolic regulation of mitochondrial dynamics. J. Cell Biol. 212, 379–387.

Mittal, M., Siddiqui, R.S., Tran, K., Reddy, S.P., Malik, A.B., 2014. Reactive Oxygen Species in Inflammation and Tissue Injury. Antioxidants Redox Signal. 20, 1126–1167.

Mizumura, K., Cloonan, S.M., Nakahira, K., Bhashyam, A.R., Cervo, M., Kitada, T., Glass, K., Owen, C.A., Mahmood, A., Washko, G.R., Hashimoto, S., Ryter, S.W., Choi, A.M.K., 2014. Mitophagy-dependent necroptosis contributes to the pathogenesis of COPD. J. Clin. Invest. 1–17.

Moiseeva, O., Bourdeau, V., Roux, A., Deschênes-Simard, X., Ferbeyre, G., 2009. Mitochondrial dysfunction contributes to oncogene-induced senescence. Mol. Cell. Biol. 29, 4495–507.

Morán, M., Moreno-Lastres, D., Marín-Buera, L., Arenas, J., Martín, M. a, Ugalde, C., 2012. Mitochondrial respiratory chain dysfunction: implications in neurodegeneration. Free Radic. Biol. Med. 53, 595–609.

Morreall, J., Limpose, K., Sheppard, C., Kow, Y.W., Werner, E., Doetsch, P.W., 2014. Inactivation of a common OGG1 variant by TNF-alpha in mammalian cells. DNA Repair (Amst). 26, 15–22.

Mortusewicz, O., Rothbauer, U., Cardoso, M.C., Leonhardt, H., 2006. Differential recruitment of DNA Ligase I and III to DNA repair sites. Nucleic Acids Res. 34, 3523–3532.

Muftuoglu, M., Mori, M., Souza-pinto, N.C. De, 2014. Formation and repair of oxidative damage in the mitochondrial DNA. Mitochondrion 17, 164–181.

Mukherjee, B., Bindhani, B., Saha, H., Ray, M.R., 2014. Increased oxidative DNA damage and decreased expression of base excision repair proteins in airway epithelial cells of women who cook with biomass fuels. Environ. Toxicol. Pharmacol. 38, 341–52.

Nauseef, W.M., 2014. Detection of superoxide anion and hydrogen peroxide production by cellular NADPH oxidases. Biochim. Biophys. Acta 1840, 757–767.

Neofytou, E., Tzortzaki, E.G., Chatziantoniou, A., Siafakas, N.M., 2012. DNA Damage Due to Oxidative Stress in Chronic Obstructive Pulmonary Disease (COPD). Int. J. Mol. Sci. 13, 16853–64.

Niso-Santano, M., Bravo-San Pedro, J.M., Gómez-Sánchez, R., Climent, V., Soler, G., Fuentes, J.M., González-Polo, R. a, 2011. ASK1 overexpression accelerates paraquat-induced autophagy via endoplasmic reticulum stress. Toxicol. Sci. 119, 156–68.

Ogawa, A., Watanabe, T., Shoji, S., Furihata, C., 2015. Enzyme Kinetics of an Alternative Splicing Isoform of Mitochondrial 8-oxoguanine DNA Glycosylase, Ogg-1b and Compared with the Nuclear Ogg-1a. J. Biochem. Mol. Toxicol. 29, 49–56.

Palmeira, C.M., Moreno, A.J., Madeira, V.M.C., 1994. Metabolic alterations in hepatocytes promoted by the herbicides paraquat, dinoseb and 2,4-D. Arch. Toxicol. 24–31.

Panduri, V., Liu, G., Surapureddi, S., Kondapalli, J., Soberanes, S., Souza-pinto, N.C. De, Bohr, V.A., Budinger, G.R.S., Schumacker, P.T., Weitzman, S.A., Kamp, D.W., de Souza-Pinto, N.C., Bohr, V.A., Budinger, G.R.S., Schumacker, P.T., Weitzman, S.A., Kamp, D.W., 2009. Role of mitochondrial hOGG1 and aconitase in oxidant-induced lung epithelial cell apoptosis. Free Radic. Biol. Med. 47, 750–759.

Paradies, G., Giuseppe, P., Paradies, V., Reiter, R.J., Ruggiero, F.M., 2010. Melatonin , cardiolipin and mitochondrial bioenergetics in health and disease. J. Pineal Res. 297–310.

Paz-Elizur, T., Krupsky, M., Blumenstein, S., Elinger, D., Schechtman, E., Livneh, Z., 2003. DNA repair activity for oxidative damage and risk of lung cancer. J. Natl. Cancer Inst. 95, 1312–1319.

Peng, Y., Zhang, S., Xiong, Y., Cun, Y., Qian, C., Li, M., Ren, T., Xia, L., Cheng, Y., Wang, D., 2014. Association of DNA base excision repair genes (OGG1, APE1 and XRCC1) polymorphisms with outcome to platinum-based chemotherapy in advanced nonsmall-cell lung cancer patients. Int. J. Cancer 135, 2687–2696.

Persson, H.L., Vainikka, L.K., 2010. TNF-alpha preserves lysosomal stability in macrophages: a potential defense against oxidative lung injury. Toxicol. Lett. 192, 261–7.

Pickett, G., Seagrave, J., Boggs, S., Polzin, G., Richter, P., Tesfaigzi, Y., 2010. Effects of 10 cigarette smoke condensates on prmary human airway epithelial cells by comparative gene and cyokine expression studies. Toxicol. Sci. 114, 79–89.

Pierrou, S., Broberg, P., O'Donnell, R.A., Pawlowski, K., Virtala, R., Lindqvist, E., Richter, A., Wilson, S.J., Angco, G., Mooler, S., Bergstrand, H., Koopmann, W., Wieslander, E., Stromstedt, P.-E., Holgate, S.T., Davies, D.E., Lund, J., Djukanovic, R., 2007. Expression of Genes Involved in Oxidative Stress Responses in Airway Epithelial Cells of Smokers with Chronic Obstructive Pulmonary Disease. Am. J. Respir. Crit. Care Med. 175, 577–586.

Pinto, M., Moraes, C.T., 2015. Mechanisms Linking mtDNA Damage and Aging. Free Radic. Biol. Med. 85, 250–258.

Powers, S.K., Jackson, M.J., 2008. Exercise-Induced Oxidative Stress: Cellular Mechanisms and Impact on Muscle Force Production. Physiol. Rev. 88, 1243–1276.

Prakash, A., Doublie, S., 2015. Base Excision Repair in the Mitochondria. J. Cell Biochem. 116, 1490–1499.

Radak, Z., Bori, Z., Koltai, E., Fatouros, I.G., Jamurtas, A.Z., Douroudos, I.I., Terzis, G., Nikolaidis, M.G., Chatzinikolaou, A., Sovatzidis, A., Kumagai, S., Naito, H., Boldogh, I., 2011. Age-dependent changes in 8-oxoguanine-DNA glycosylase activity are modulated by adaptive response to physical exercise in human skeletal muscle. Free Radic. Biol. Med. 51, 417–423.

Rehman, J., Zhang, H.J., Toth, P.T., Zhang, Y., Marsboom, G., Hong, Z., Salgia, R., Husain, A., Wietholt, C., Archer, S.L., 2012. Inhibition of mitochondrial fission

prevents cell cycle progression in lung cancer. FASEB J. 26, 2175–2186.

Reyes, G.X., Schmidt, T.T., Kolodner, R.D., Hombauer, H., 2015. New Insights into the Mechanism of DNA Mismatch Repair. Chromosoma 124, 443–462.

Richardson, T., McCanse, W., Casale, G.P., Huang, D., Tian, J., Elkahwaji, J.E., Lele, S., Hemstreet, G.P., 2009. Tissue-based quantification of 8-hydroxy-2'-deoxyguanosine in human prostate biopsies using quantitative fluorescence imaging analysis. Urology 74, 1174–9.

Rovina, N., Koutsoukou, A., Koulouris, N.G., 2013. Inflammation and Immune Response in COPD : Where Do We Stand? Mediators Inflamm. 2013, 1–9.

Ruchko, M. V, Gorodnya, O.M., Zuleta, A., Pastukh, V.M., Gillespie, M.N., 2011. The DNA glycosylase Ogg1 defends against oxidant-induced mtDNA damage and apoptosis in pulmonary artery endothelial cells. Free Radic. Biol. Med. 50, 1107–13.

Rumsey, W., Larminie, C., Miller, B., Riley, J.H., Tal-Singer, R., Mayer, R.J., 2013. Gene Expression of Mitochondrial Oxidative Phosphorylation and Oxidative Stress Pathways are Negatively Affected by Disease Progression in the ECLIPSE COPD Cohort. Am. J. Respir. Crit. Care Med. 187, A1510.

Rycroft, C.E., Heyes, A., Lanza, L., Becker, K., 2012. Epidemiology of chronic obstructive pulmonary disease: a literature review. Int. J. Chron. Obstruct. Pulmon. Dis. 7, 457–94.

Safdar, A., Bourgeois, J.M., Ogborn, D.I., Little, J.P., Hettinga, B.P., Akhtar, M., Thompson, J.E., Melov, S., Mocellin, N.J., Kujoth, G.C., Prolla, T. a, Tarnopolsky, M. a, 2011. Endurance exercise rescues progeroid aging and induces systemic mitochondrial rejuvenation in mtDNA mutator mice. Proc. Natl. Acad. Sci. U. S. A. 108, 4135–40.

Sampath, H., 2014. Oxidative DNA damage in disease-Insights gained from base excision repair glycosylase-deficient mouse models. Environ. Mol. Mutagen. 55, 689–703.

Sampath, H., Vartanian, V., Rollins, M.R., Sakumi, K., Nakabeppu, Y., Lloyd, R.S., 2012. 8-Oxoguanine DNA glycosylase (OGG1) deficiency increases susceptibility to obesity and metabolic dysfunction. PLoS One 7, e51697.

Scheibye-Knudsen, M., Fang, E.F., Croteau, D.L., Wilson III, D.M., Bohr, V. a, 2015. Protecting the mitochondrial powerhouse. Trends Cell Biol. 25, 158–170.

Schumacker, P.T., Gillespie, M.N., Nakahira, K., Choi, A.M.K., Crouser, E.D., Piantadosi, C.A., Bhattacharya, J., 2014. Mitochondria in lung biology and pathology: more than just a powerhouse. Am. J. Physiol. - Lung Cell. Mol. Physiol. 306, L962–L974.

Seo, A.Y., Joseph, A.-M., Dutts, D., Hwang, J.C., Aris, J.P., Leeuwenburgh, C., 2010. New insights into the role of mitochondria in aging: mitochondrial dynamics and more. J. Cell Sci. 123, 2533–2542.

Sethi, S., Mahler, D. a, Marcus, P., Owen, C. a, Yawn, B., Rennard, S., 2012. Inflammation in COPD: implications for management. Am. J. Med. 125, 1162–70.

Sharma, A., Singh, K., Almasan, A., 2012. Histone H2AX Phosphorylation: A Marker for DNA damage, in: DNA Repair Protocols. Humana Press, pp. 613–626.

Siggens, L., Figg, N., Bennett, M., Foo, R., 2012. Nutrient deprivation regulates DNA damage repair in cardiomyocytes via loss of the base-excision repair enzyme OGG1. FASEB J. 26, 2117–24.

Singh, B., Chatterjee, A., Ronghe, A.M., Bhat, N.K., Bhat, H.K., 2013. Antioxidant-mediated up-regulation of OGG1 via NRF2 induction is associated with inhibition of oxidative DNA damage in estrogen-induced breast cancer. BioMed Cent. Cancer 13.

Small, D.M., Morais, C., Coombes, J.S., Bennett, N.C., Johnson, D.W., Gobe, G.C., 2014. Oxidative stress-induced alteations in PPAR-gamma and associated mitochondrial destabilization contribute to kidney cell apoptosis. Am. J. Physiol. Ren. Physiol. 307, F814–F822.

Soares, J.P., Silva, A.I., Silva, A.M., Almeida, V., Matos, M., Teixeira, J., Gaivão, I.O., Mota, M.P., 2015. Effects of physical exercise training in DNA damage and repair activity in humans with diffeent genetic polymorphisms of hOGG1 (Ser326Cys). Cell Biochem. Funct. 33, 519–524.

Soulitzis, N., Neofytou, E., Psarrou, M., Anagnostis, A., Tavernarakis, N., Siafakas, N., Tzortzaki, E.G., 2012. Downregulation of lung mitochondrial prohibitin in COPD. Respir. Med. 106, 954–61.

Stefanatos, R., Sanz, A., 2011. Mitochondrial Complex I. Cell Cycle 10, 1528–1532.

Steiling, K., van den Berge, M., Hijazi, K., Florido, R., Campbell, J., Liu, G., Xiao, J., Zhang, X., Duclos, G., Drizik, E., Si, H., Perdomo, C., Dumont, C., Coxson, H., Alekseyev, Y., Sin, D., Pare, P., Hogg, J., McWillams, A., Hiemstra, P., Sterk, P., Timens, W., Chang, J., Sebastiani, P., O'Connor, G., Bild, A., Postma, D., Lam, S., Spira, A., Lenburg, M., 2013. A dynamic bronchial airway gene expression signature of chronic obstructive pulmonary disease and lung function impairment. Am. J. Respir. Crit. Care Med. 187, 933–942.

Su, Y., Lee, Y., Chen, S., Lee, Y., Hsieh, Y., Tsai, J., Hsu, J., Tian, W., 2013. Essential Role of b -Human 8-Oxoguanine DNA Glycosylase 1 in Mitochondrial Oxidative DNA Repair. Environ. Mol. Mutagen. 54, 54–64.

Sureshbabu, A., Bhandari, V., 2013. Targeting mitochondrial dysfuntion in lung diseases: emphasis on mitophagy. Front. Physiol. 4, 1–8.

Taricani, L., Shanahan, F., Pierce, R.H., Guzi, T.J., Parry, D., 2010. Phenotypic enhancement of thymidylate synthetase pathway inhibitors following ablation of Neil1 DNA glycosylase/lyase. Cell Cycle 9, 4876–4883.

Taylor, A.E., Finney-Hayward, T.K., Quint, J.K., Thomas, C.M.R., Tudhope, S.J., Wedzicha, J. a, Barnes, P.J., Donnelly, L.E., 2010. Defective macrophage phagocytosis of bacteria in COPD. Eur. Respir. J. 35, 1039–1047.

Thimmulappa, R.K., Gang, X., Kim, J.-H., Sussan, T.E., Witztum, J.L., Biswal, S., 2012. Oxidized phospholipids impair pulmonary antibacterial defenses: evidence in mice exposed to cigarette smoke. Biochem. Biophys. Res. Commun. 426, 253–9.

Thorne, D., Adamson, J., 2013. A review of in vitro cigarette smoke exposure systems. Exp. Toxicol. Pathol. 65, 1183–93.

Tissenbaum, H.A., 2015. Using C. elegans for aging research. Invertebr. Reprod. Dev. 59, 59–63.

Tomkinson, A.E., Howes, T.R., Wiest, N.E., 2013. DNA ligases as therapeutic targets. Transl. Cancer Res. 1–17.

Torres-Gonzalez, M., Gawlowski, T., Kocalis, H., Scott, B.T., Dillmann, W.H., 2014. Mitochondrial 8-oxoguanine glycosylase decreases mitochondrial fragmentation and improves mitochondrial function in H9C2 cells under oxidative stress conditions. Am. J. Physiol. Cell Physiol. 306, C221–9.

Trian, T., Benard, G., Begueret, H., Rossignol, R., Girodet, P.-O., Ghosh, D., Ousova, O., Vernejoux, J.-M., Marthan, R., Tunon-de-Lara, J.-M., Berger, P., 2007. Bronchial smooth muscle remodeling involves calcium-dependent enhanced mitochondrial biogenesis in asthma. J. Exp. Med. 204, 3173–3181.

Tuder, R.M., Petrache, I., 2012. Review series Pathogenesis of chronic obstructive pulmonary disease. J. Clin. Invest. 122, 2749–2755.

van der Toorn, M., Slebos, D.-J., de Bruin, H.G., Leuvenink, H.G., Bakker, S.J.L., Gans, R.O.B., Koëter, G.H., van Oosterhout, A.J.M., Kauffman, H.F., 2007. Cigarette smoke-induced blockade of the mitochondrial respiratory chain switches lung epithelial cell apoptosis into necrosis. Am. J. Physiol. Lung Cell. Mol. Physiol. 292, L1211–8.

Vinnakota, C.V., Peetha, N.S., Perrizo, M.G., Ferris, D.G., Oda, R.P., Rockwood, G.A., Logue, B.A., 2012. Comparison of cyanide exposure markers in the biofluids of smokers and non-smokers. Biomarkers 17, 625–633.

Vlahos, R., Bozinovski, S., 2014. Role of alveolar macrophages in chronic obstructive pulmonary disease. Front. Immunol. 5, 1–7.

Vogel, K.W., Zhong, Z., Bi, K., Pollok, B. a, 2008. Developing assays for kinase drug discovery - where have the advances come from? Expert Opin. Drug Discov. 3, 115–29.

Wallace, K.B., Eells, J.T., Madeira, V.M.C., Cortopassi, G., Jones, D.P., 1997. Mitochondria-Mediated Cell Injury. Toxicol. Sci. 38, 23–37.

Wang, J., Wang, Q., Watson, L.J., Jones, S.P., Epstein, P.N., Wang, J., Wang, Q., Lj, W., Sp, J., Cardiac, E.P.N., 2011. Cardiac overexpression of 8-oxoguanine DNA glycosylase 1 protects mitochondrial DNA and reduces cardiac fibrosis following transaortic constriction. Am. J. Physiol. Hear. Circ. Physiol. 301, H2073–H2080.

Wiegman, C.H., Michaeloudes, C., Haji, G., Narang, P., Clarke, C.J., Russell, K.E., Bao, W., Pavlidis, S., Barnes, P.J., Kanerva, J., Bittner, A., Rao, N., Murphy, M.P., Kirkham, P. a., Chung, K.F., Adcock, I.M., 2015. Oxidative stress–induced mitochondrial dysfunction drives inflammation and airway smooth muscle remodeling in patients with chronic obstructive pulmonary disease. J. Allergy Clin. Immunol. 136, 769–780.

Willems, P.H., Rossignol, R., Dieteren, C.E., Murphy, M.P., Koopman, W.J., 2015. Redox Homeostasis and Mitochondrial Dynamics. Cell Metab. 22, 207–218.

Winterbourn, C.C., 2014. The challenges of using fluorescent probes to detect and quantify specific reactive oxygen species in living cells. Biochim. Biophys. Acta 1840, 730–738.

Woolley, J.F., Stanicka, J., Cotter, T.G., 2013. Recent advances in reactive oxygen species measurement in biological systems. Trends Biochem. Sci. 38, 556–565.

www.slideteam.net [WWW Document], 2015. . 76360787 Style Med. 1 Integumentary 1 Piece Powerpoint Present. Diagr. Infographic Slide. URL http://www.slideteam.net/business_powerpoint_diagrams/76360787-style-medical-1-integumentary-1-piece-powerpoint-presentation-diagram-infographic-slide.html

Xiang, M., Fan, J., Fan, J., 2010. Association of Toll-like receptor signaling and reactive oxygen species: a potential therapeutic target for posttrauma acute lung injury. Mediators Inflamm. 2010.

Yamamoto, M., Chapman, A., Schiestl, R., 2013. Effects of side-stream tobacco smoke and smoke extract on glutathione-and oxidative DNA damage repair-deficient mice and blood cells. Mutat. Res. 749, 58–65.

Yang, L., Wang, Y., Lin, Z., Zhou, X., Chen, T., He, H., Huang, H., Yang, T., Jiang, Y., Xu, W., Yao, W., Liu, T., Liu, G., 2015. Mitochondrial OGG1 protects against PM2.5-induced oxidative DNA damage in BEAS-2B cells. Exp. Mol. Pathol. 99, 365–373.

Yang, S., Wu, H., Zhao, J., Wu, X., Zhao, J., Ning, Q., Xu, Y., Xie, J., 2014. Feasibility of 8-OHdG formation and hOGG1 induction in PBMCs for assessing oxidative DNA damage in the lung of COPD patients. Respirology 19, 1183–90.

Yang, W., Tiffany-Castiglioni, E., Koh, H.C., Son, I.-H., 2009. Paraquat activates the IRE1/ASK1/JNK cascade associated with apoptosis in human neuroblastoma SH-SY5Y cells. Toxicol. Lett. 191, 203–10.

Yuzefovych, L. V., Kahn, A.G., Schuler, M.A., Eide, L., Arora, R., Wilson, G.L., Tan, M., Rachek, L.I., 2016. Mitochondrial DNA repair through Ogg1 activity attenuates breast cancer progression and metastasis. Cancer Res. 76, 30–34.

Zerin, T., Kim, Y., Hong, S., Song, H., 2012. Quercetin reduces oxidative damage induced by paraquat via modulating expression of antioxidant genes in A549 cells. J. Appl. Toxicol. 33, 1460–7.

Zhang, H., Xie, C., Spencer, H.J., Zuo, C., Higuchi, M., Ranganathan, G., Kern, P.A., Chou, M.W., Huang, Q., Szczensy, B., Mitra, S., Watson, A.J., Margison, G.P., Fan, C.Y., 2011. Obesity and hepatosteatosis in mice with enhanced oxidative DNA damage processing in mitochondria. Am. J. Pathol. 178, 1715–1727.

Zhi, Q., Sun, H., Qian, X., Yang, L., 2011. Edaravone , a novel antidote against lung injury and pulmonary fi brosis induced by paraquat? Int. Immunopharmacol. 11, 96–102.

Zhou, P.-T., Li, B., Ji, J., Wang, M.-M., Gao, C.-F., 2015. A systematic review and meta-analysis of the association between OGG1 Ser326Cys polymorphism and cancers. Med. Oncol. 32, 1–16.

APPENDIX:

SUPPLEMENTAL DATA

APPENDIX: SUPPLEMENTAL DATA

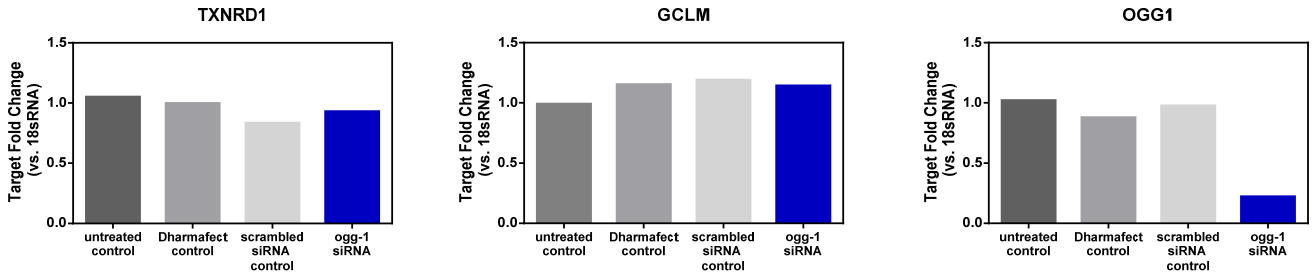

Figure S1 Effects of OGG1 siRNA on OGG1 gene expression.

A549 cells were incubated with 100 nM OGG1 siRNA containing Dharmafect® at a dilution of 1:50 in serum-free conditions. Following 48 hr incubation, the medium was replaced to complete culture medium and the A549 cells were incubated for an additional 24 hr. Cells were then lysed and RNA collected using the Cells-to-Ct kit according to manufacturer's instructions (Thermo; Waltham, MA). RT-PCR was performed using 10 µL of RNA solution and this product was used to determine gene expression of OGG1 related genes using 18s RNA as the endogenous control, in a multiplex format. The primer/probe sets were selected from Life Technologies (Carlsbad, CA) using the criteria of best coverage and inventoried; excluding sets compatible with genomic DNA. Data was calculated using the Livak method (Livak and Schmittgen, 2001) *and is from an independent experiment, with each condition performed in triplicate. Data was provided with permission courtesy of Alicia Davis, GlaxoSmithKline.*

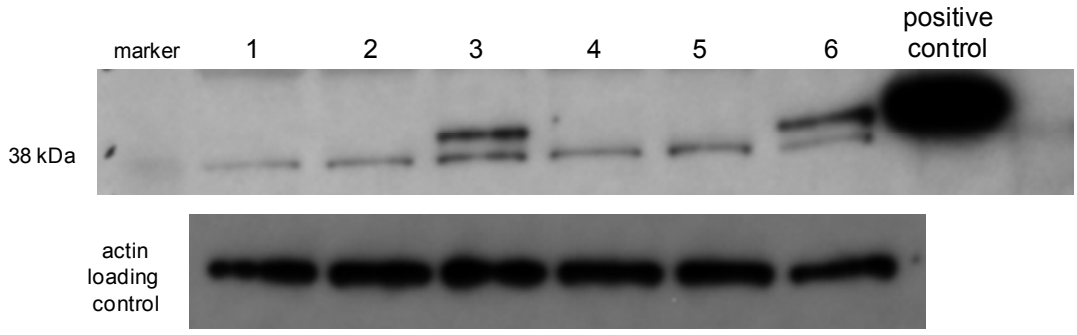

Figure S2 Validation of OGG1 antibody detection of appropriate protein band.

A549 cells were incubated with 8% v./ v. OGG1 BacMam for 48 hr prior to paraquat exposure (24 hr). Cells were lysed, protein was quantified and (1) untreated, (2) untreated and incubated with 8% null BacMam, (3) untreated with 8% OGG1 BacMam, or (4-6) 3 mM paraquat exposed cells and exposed to none, null, or OGG1 BacMam, respectively were subjected to electrophoresis. A positive control of human OGG1 was included on the gel, and corresponds to the predicted molecular weight of 39kDa (could vary depending on isoform). The blot was probed for OGG1 expression using 1 µg/mL of clone 5983 and then stripped and re-probed for actin for use as a loading control. Data shown is from an independent experiment, with each condition tested in triplicate.

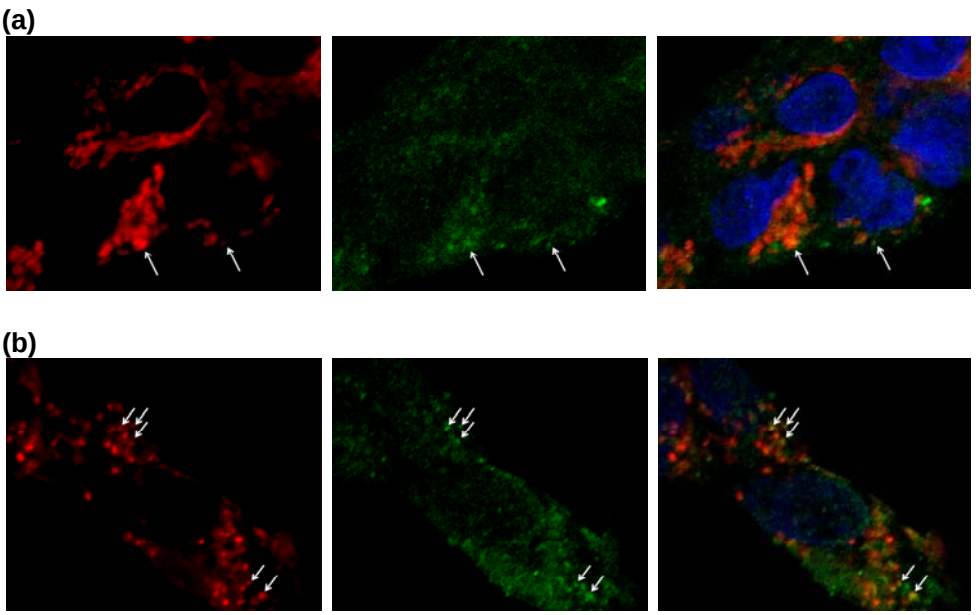

Figure S3 Examination of co-localization of paraquat-induced 8-oxogaunine to the mitochondria.

A549 cells were grown on poly-L-lysine cover slips (BD Biosciences; San Jose, CA) and stained for 8-oxoguanine as described in Chapter 2. Changes were made to the protocol for fluorescent probe selection, due to confocal instrument requirements: MitoTracker® red was substituted for MitoTracker® orange, a 1:100 dilution of the 8-oxoguanine detection antibody, 1:4000 dilution of Alexa Fluor® 488, and DRAQ™ 5 was substituted for Hoechst 33342. Sample images were acquired from (a) untreated and (b) 3 mM paraquat (24 hr) cells using an oil immersion 63X objective on a Leica TCS SP2 fluorescence microscope (Buffalo Grove, IL). The color overlays represent Draq5, overlaid blue; MitoTracker® red, overlaid red; 8-oxoguanine-AlexaFluor®-488, overlaid green, and orange represents co-localization of the red and green dyes. The arrows on the images represent mitochondria with 8-oxoguanine staining. Data shown is from an independent experiment, with each condition tested in triplicate. Data was provided with permission courtesy of William Fieles, GlaxoSmithKline.

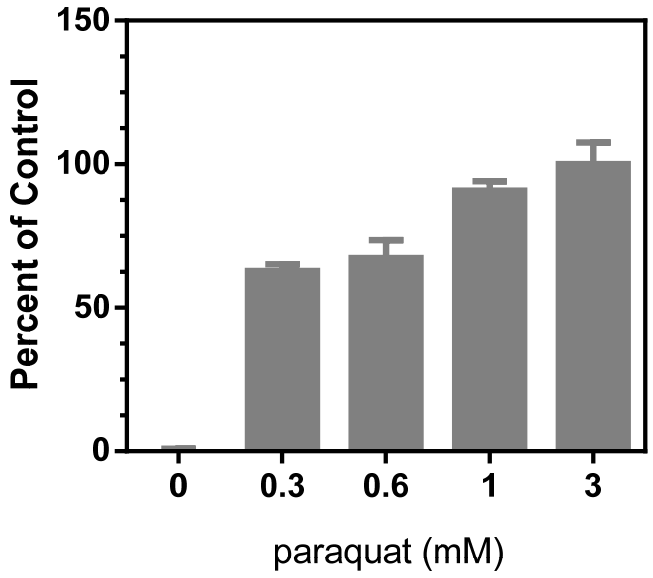

Figure S4 Effects of paraquat on mitochondrial DNA damage in A549 cells.

A549 cells were treated with paraquat for 48 hr and subjected to cell lysis using Cells-to-Ct kit (Thermo; Waltham, MA) per the manufacturer's instructions. The DNA was isolated and quantified, and then long and short chain PCR was conducted according to published methods (Furda et al., 2014). *Long-chain PCR was conducted using the 8.9 kilo-bases mitochondrial fragment (primers with accession numbers 14841 and 5999) along with short-chain PCR using a small mitochondrial fragment (accession numbers 14620 and 14841)* (Furda et al., 2014). *The product from the PCR reaction was quantified using PicoGreen® (Life Technologies; Carlsbad, CA), and the fluorescence intensity of the long-chain was subtracted from the intensity of the short-chain. A percent of control was then calculated and graphed relative to increasing concentrations of paraquat (mM) on the x-axis. These data indicate that with increasing concentrations of paraquat there was an increase in damage associated with the sequence of the long chain PCR primers. Data shown is from an independent experiment, with each condition tested in triplicate. Data was provided with permission courtesy of Alicia Davis, GlaxoSmithKline.*

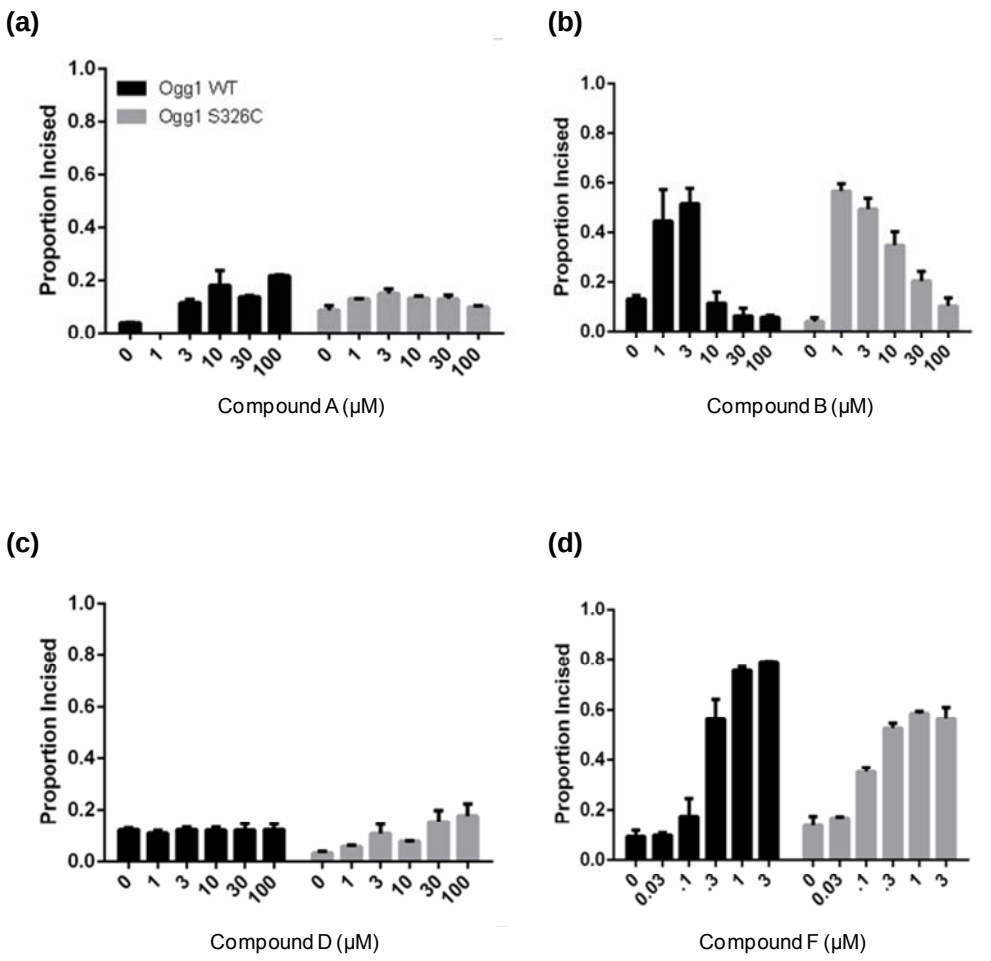

Figure S5 Effects of OGG1 activators on OGG1 incision activity.

Purified OGG1 enzyme (wild type – black bars; or S326C OGG1 – gray bars) was incubated with increasing concentrations of the OGG1 activators (µM) (a) compound A, (b) compound B, (c) compound D, or (d) compound F for 1 hr at 37°C along with a P^{32}, 5'-tagged oligonucleotide fragment containing an 8-oxoguanine lesion. The reaction was terminated by heating the reaction to 95°C for 5 min and the products were then separated using electrophoresis. Densitometry was performed and the proportion incision was calculated using the area for the value from the excised product, divided by the sum of the excised and non-excised products in each lane. Data shown is from an independent experiment. Data was provided with permission courtesy of Dr. Beverly Baptiste, National Institutes of Aging (manuscript preparation in progress).

(a)

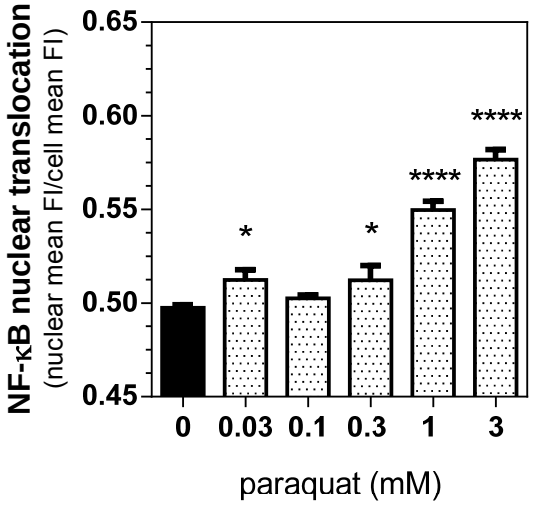

(b)

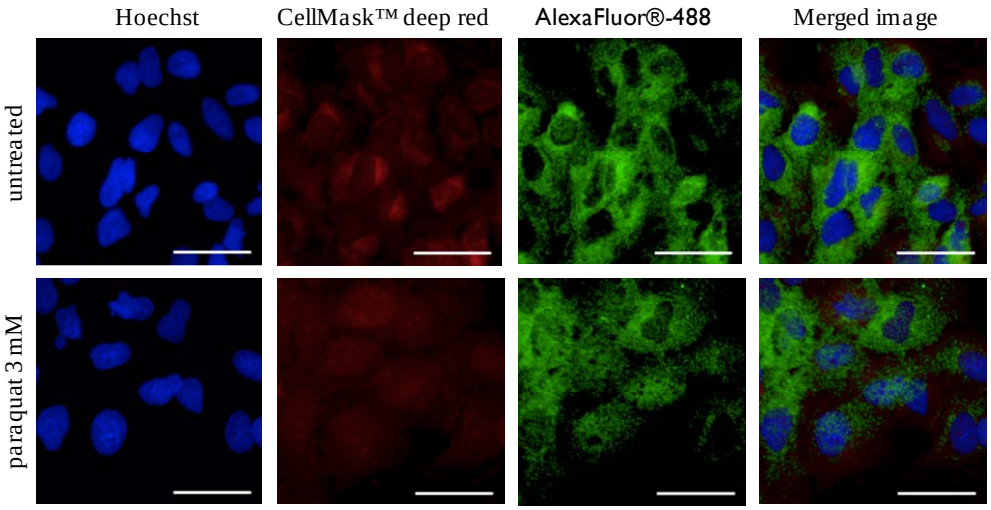

Figure S6 Effects of paraquat on markers of inflammation – NF-κB translocation.

Figure S6 Effects of paraquat on markers of inflammation – NF-κB translocation.

A549 cells were treated with paraquat for 24 hr and subjected to formaldehyde fixation prior to immunofluorescence detection of NF-κB as described in Chapter 2. (a) The translocation of NF-κB was quantified following exposure to a concentration-response curve of paraquat. (b) Changes in NF-κB are depicted in sample representative images (Hoechst 33342, overlaid blue; anti- NF-κB-AlexaFluor®-488; overlaid green, CellMask™ Deep Red, overlaid red) from cells exposed to 3 mM paraquat (24 hr, line = 40 μm). Significance was determined using a 1-way ANOVA with a Dunnett's post test comparing treatment groups to an untreated control ($p<0.05$, **** $p<0.0001$). Data shown is from an independent experiment, with each condition tested in triplicate.*

(a)

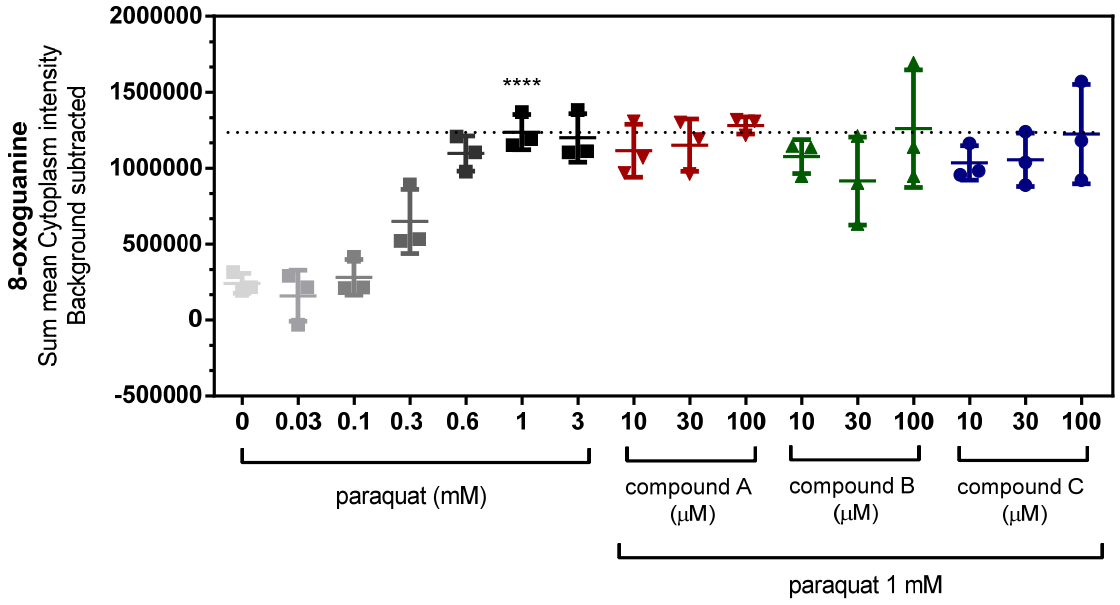

(b)

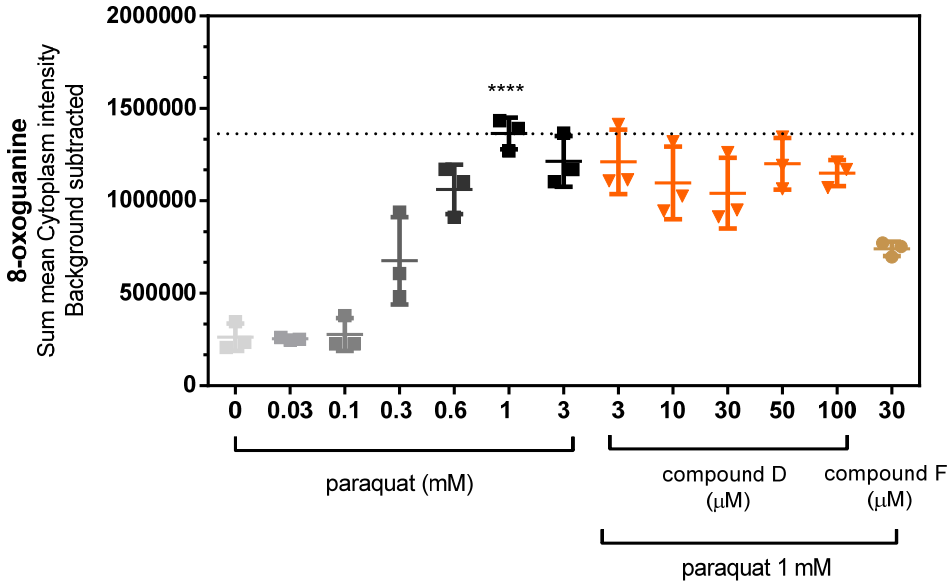

Figure S7 Effects of OGG1 small molecule activators on paraquat-induced 8-oxoguanine in A549 cells.

Figure S7 Effects of OGG1 small molecule activators on paraquat-induced 8-oxoguanine in A549 cells.

*A549 cells were pre-treated for 4 hr with small molecule OGG1 activators or 0.1% DMSO prior to addition of 1 mM paraquat for 48 hr. The cells were stained and imaged for 8-oxoguanine content as described in Chapter 2. (a) and (b) Graphical representations of the change in 8-oxoguanine intensity within the cytoplasm of cells compared to 1 mM paraquat treated cells. Significance was determined using a 1-way ANOVA with a Dunnett's post test comparing paraquat alone treated groups to untreated control (0 mM) and OGG1 activator treated groups to 1 mM paraquat control (** p<0.01, *** p<0.001, **** p<0.0001). Data shown are from a representative experiment, performed four times.*

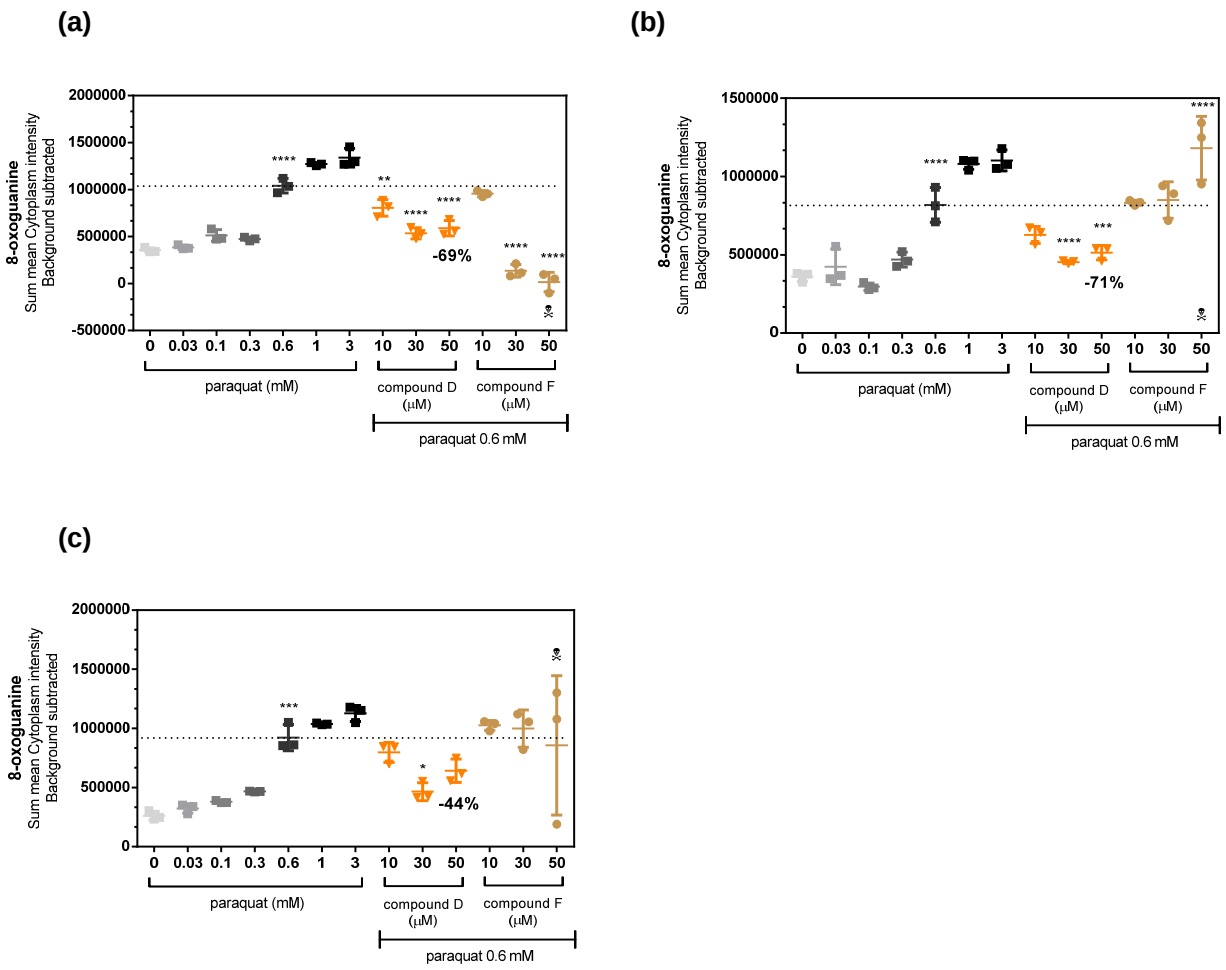

Figure S8 Effects of time of addition of OGG1 small molecule activators on paraquat-induced 8-oxoguanine in A549 cells.

Figure S8 Effects of time of addition of OGG1 small molecule activators on paraquat-induced 8-oxoguanine in A549 cells.

*A549 cells were pre-treated for (a) 4 hr, (b) 2 hr, and (c) 0 hr with select small molecule OGG1 activators or 0.1% DMSO prior to addition of 0.6 mM paraquat for 48 hr. The cells were stained and imaged for 8-oxoguanine content as described in Chapter 2. Graphical representations of the change in 8-oxoguanine intensity within the cytoplasm of cells compared to 0.6 mM paraquat treated cells. Significance was determined using a 1-way ANOVA with a Dunnett's post test comparing paraquat alone treated groups to untreated control (0 mM) and OGG1 activator treated groups to 0.6 mM paraquat control (*p<0.05, ** p<0.01, *** p<0.001, **** p<0.0001). Data shown is from an independent experiment, with each condition tested in triplicate.*